HIGH-THROUGHPUT STUDIES OF METAL OXIDE THIN FILMS FOR FUEL CELL APPLICATIONS

A Dissertation

Presented to the Faculty of the Graduate School

of Cornell University

in Partial Fulfillment of the Requirements for the Degree of

Doctor of Philosophy

by

Marc James Murphy

August 2018

HIGH-THROUGHPUT STUDIES OF METAL OXIDE THIN FILMS FOR FUEL CELL APPLICATIONS

Marc James Murphy, Ph.D.

Cornell University 2018

Low temperature fuel cells and hydrogen-generating electrolyzers are clean energy technologies with far reaching potential. However, performance is bottlenecked by the slow electrochemical reaction kinetics of oxygen reduction and oxygen evolution. Accelerating the reaction of oxygen currently requires precious metal electrocatalysts, stifling the prospect of widespread fuel cell and electrolyzer proliferation. Consequently, there has been a concerted effort in discovering alternative bifunctional oxygen electrocatalysts, most notably from inexpensive and naturally abundant materials. In particular, complex metal oxides represent a major class of promising new catalyst materials, demonstrating strong catalytic activity and tunability. The sheer breadth of metal oxide systems, underscored by their nearly limitless structural and compositional degrees of freedom, motivates high-throughput synthesis and experimental approaches to expedite and maximize the efficacy of materials discovery. In this study, we performed a range of high-throughput oxygen catalysis measurements on composition-spread libraries of co-sputtered metal oxide thin films. Catalytically active oxides were discovered using a combination of electrochemical screening (cyclic voltammetry, rotating disk electrode, electrochemical impedance, etc.) and versatile high-throughput characterization techniques for structural and compositional mapping. The information from the screening results narrowed the library of potential oxygen catalysts, while identifying novel oxide compounds and structures. The effective translation from thin film to high-surface-area nanoparticle catalysts not only validates the methods utilized in this study, but demonstrates high-throughput electrochemistry as a crucial and complementary approach to catalysis research.

BIOGRAPHICAL SKETCH

I dedicated the last 6.5 years of my life focused on making a positive contribution to science, however small it may have been. Although I am always motivated to further expand the reaches of my research, I am fully content with the overall quality of my work. I had the privilege of growing up in a supportive household amongst a family that deeply instilled the values and virtues that exemplify my tireless drive to make a positive impact on society.

I dedicate this work to my family for their unwavering and unconditional support.

ACKNOWLEDGEMENTS

I would like to thank my friends/colleagues, my adviser (van Dover), my committee (Professors DiSalvo and Abruña), and everyone (in CCMR, CHESS, CNF) else who helped me along the way.

TABLE OF CONTENTS

CHAPTER 1

FUEL CELLS

1.1 Prologue

This research is primarily focused on oxygen electrocatalysis, a vital chemical process for a number of applications, namely catalytic converters, metal-air batteries, hydrogen fuel production, solar-to-fuel production, and combinations thereof. Although there are many branching applications to oxygen electrocatalysis, fuel cells have always been the impetus behind this work. Therefore, this chapter will discuss some of the key fundamentals, operating components, and types of fuel cells. This chapter will also briefly discuss the current state and future projections of commercial fuel cells based on industry trends, federal and global initiatives.

1.2 Introduction

Fuel cells are among the principal technologies being propelled to the energy forefront as part of the long-term global initiative to lower pollution levels, improve energy consumption efficiency, and reduce global carbon emissions. Fuel cells are highly efficient, zero-emission electrochemical devices that generate electricity from the reaction of hydrogen (H_2) and oxygen (O_2). Consequently, many have sought to incorporate fuel cell technology into several commercial applications, namely electric vehicles, stationary power systems, and portable devices. Although fuel cells have slowly gained traction in various niche markets, the prospect of widespread growth is still hindered by high production costs, relatively low durability, and the high logistical threshold in establishing an infrastructure for hydrogen-fuel delivery. Nonetheless, fuel cells continue to play an indispensable role in fully integrating clean energy globally.

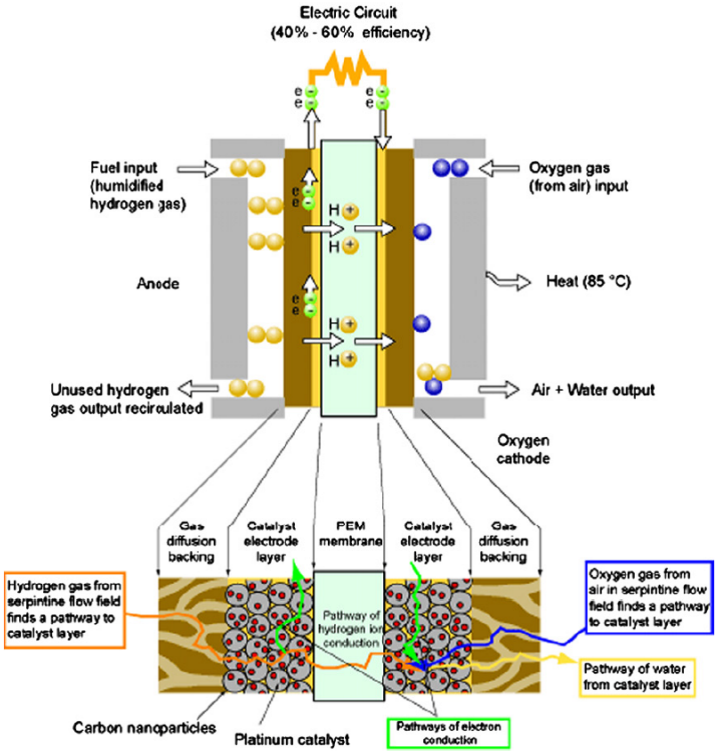

Figure 1.1: A schematic of a prototypical hydrogen proton-exchange fuel cell. The core fuel cell device consists of an anode and cathode separated by an ionically conductive electrolyte membrane. The illustration shows the detailed composite of the membrane electrode assembly (MEA), which consists of catalyst layers, gas diffusion layers, and bipolar plates.[264]

1.3 Fuel Cell Reaction

A fuel cell is a galvanic electrochemical cell that converts chemical energy into electricity by the reduction/oxidation (redox) reaction of hydrogen (H_2) and oxygen (O_2). Figure 1.1 shows an illustration of a basic fuel cell architecture, consisting of two electrodes (i.e. anode and cathode) separated by an ionically conductive electrolyte membrane. During operation, H_2 is supplied to the anode and oxidized (i.e. loss of electrons) into protons (H^+):

$$Anode : H_2 \rightarrow 2H^+ + 2e^- \tag{1.1}$$

The electrons released from the oxidation half-reaction spontaneously conduct through an external circuit towards the cathode in the form of electrical current. The incoming electrons reduce the O_2 molecules, forming O^{2-} anions, or some variant (e.g. OH^-, H_2O) depending on the electrolyte

membrane.

$$Cathode: \frac{1}{2}O_2 + 2e^- \rightarrow 2O^{2-} \tag{1.2}$$

When both half-reactions are combined, the net reaction becomes:

$$Cell\,Reaction: \frac{1}{2}O_2 + H_2 \rightarrow H_2O \tag{1.3}$$

For charge balance, the H^+ ions transport through the ionically conductive electrolyte membrane towards the cathode, combining with O^{2-} to form water (H_2O) as the main byproduct.

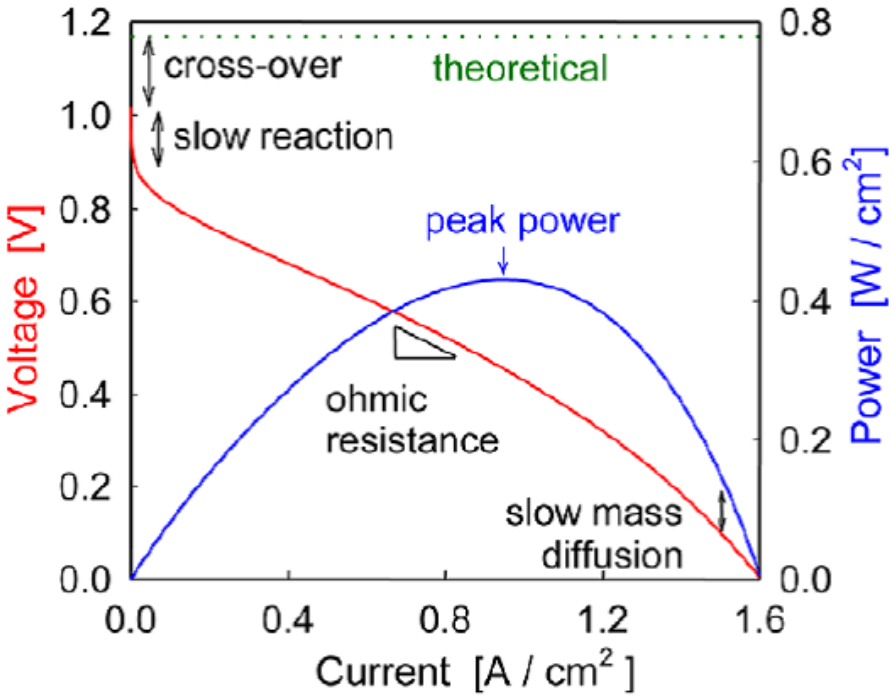

Figure 1.2: Voltage (V)-current (A/cm^2) curve, and a power density (W/cm^2) of a typical fuel cell device. The overpotentials with resepect to the theoretical potential (green dotted line) across different regimes of the V-I curve are identified by the rate-limiting mechanisms that induce energy loss.[82]

1.4 Fuel Cell Operation

Figure S.2 shows the output of a typical fuel cell, showcasing the operating voltage (V) versus the electrical current density (A/cm^2) (red curve), and the overall power density (blue curve).

The dashed line across the figure is the theoretical redox potential, or open-circuit voltage (OCV). The power density curve is the product of the operating voltage and current density, which peaks at some intermediate voltage and corresponding current density.

Fuel cell performance is generally characterized by the overpotential, η, which is the difference between the operating voltage and the OCV, and the power density. Both are important metrics for operating efficiency, and the rate of energy transfer, which is essential for dynamic and distributive applications. However, the superimposed curves underscore the major trade-off between high operating at efficiency near the onset voltage, and peak power density at greater overpotentials. Although the OCV is the theoretical redox potential, in practice, the redox current does not activate until reaching a certain overpotential of ~300 mV as a result of energy loss attributed to a combination of slow reaction kinetic kinetics, ohmic losses from the fuel cell components, and limited mass transport of the redox species. Thus, the working potential must be adjusted relative to the OCV (E_{eq}). Equation A.4 shows the adjusted potential, which now incorporates systematic leakage (E_L) due to fuel crossover across the electrolyte, as well as partitioned overpotentials (i.e. η_{act}, η_{iR},η_{diff}) that correspond reaction kinetics, Ohmic losses, and mass-transport.

$$E = E_{eq} - E_L - \eta_{act} - \eta_{iR} - \eta_{diff} \tag{1.4}$$

The voltage-current curve can be defined by the different regimes corresponding to the rate-limiting mechanism. For instance, while factoring in systematic losses from fuel crossover, the overpotential preceding the onset of current is predominately limited by the reaction kinetic threshold, which is notably attributed to sluggish oxygen reduction kinetics at the cathode. Increasing the overpotential drives the redox kinetics to increase exponentially, but the current output is now limited by the Ohmic resistance of the components due to the increase in the iR drop. As a result, the current-potential curve follows a more linear progression, characteristic of Ohm's Law. At even greater current densities, the cell now reaches a point where the consumption rate of H_2 and O_2 at the electrodes exceeds the rate of supply, causing fuel depletion that is now governed by mass-transport (i.e. diffusion, migration).

Efficiency is defined as the fraction of energy that can be converted into useable work (i.e. electrical work, mechanical work, etc.), and thus, is one of the critical benchmarks for energy consumption. Practical fuel cells have the notable advantage of operating at much higher efficiencies than conventional heat engines (i.e. internal combustion), which are restricted by a relatively low heat-to-work conversion efficiency imposed by the Carnot limit. In contrast, fuel cell efficiency is predicated on the conversion of chemical energy released from the redox reaction of H_2 and O_2 into useful electrical work. To illustrate, Equation A.5 represents maximum efficiency as a ratio of the maximum possible work that can be extracted from the free-energy, ΔG, of the reaction, and the enthalpy, ΔH.

$$Ideal\ \eta = \frac{\Delta G}{\Delta H} = 1 - \frac{T\Delta S}{\Delta H} \tag{1.5}$$

Depending on the sign of the entropy change (ΔS), which is expected to be negative, the maximum efficiency can approach almost 100%. However, a more practical metric is the voltage efficiency, which is the ratio of the cell voltage divided by the Nernst potential (E_{eq})-See Appendix I to learn more about the Nernst equation.

$$\eta = \frac{V_{Cell}}{E} \tag{1.6}$$

In practice, fuel cell efficiencies are around 40-60% due to energy losses induced by heat loss and the aforementioned rate-limiting mechanisms (i.e. sluggish reaction kinetics, Ohmic losses, fuel crossover, mass-transport), though fuel cells that operate on the cogeneration of heat and electricity can reach efficiencies as high as 85%. Nevertheless, commercial fuel cell efficiencies generally exceed conventional internal combustion engines, which only operate at around 20%.

The I-V behavior of a fuel cell is explicitly expressed by the Butler-Volmer (BV) equation (Equation A.7).

$$I = I_O \left\{ exp\left[\frac{\alpha n F \eta}{RT}\right] - exp\left[\frac{(1-\alpha)\, F\eta}{RT}\right] \right\} \tag{1.7}$$

The BV equation is an exponential relationship between the current density and the overpotential, and is directly derived from the intrinsic rates of reaction of the redox species. Each exponential term corresponds to the forward and reverse direction of the net cell reaction. However, at greater

overpotentials, the back-reaction term becomes negligible, and the BV equation can be approximated as a single exponential corresponding to the forward reaction. Additional details about the BV equation are discussed in Appendix I.

1.5 Membrane Electrode Assembly

The core assembly of the fuel cell, known as the membrane electrode assembly (MEA), consists of the anode, cathode and the electrolyte membrane. Materials selection and MEA design studies have looked extensively at optimizing and satisfying the often far-reaching property requirements of each component, most notably the electrolyte membrane, electrocatalysts and catalyst supports, all while maintaining cross compatibility and high durability during operation.

The electrolyte membrane facilitates fast conduction of select ionic species from one electrode to the other. In addition to being ionically conductive, the electrolyte must be electronically insulating to prevent electrical shorting, and impermeable to fuel crossover. For operational longevity, electrolytes must be chemically inert, thermally robust, and strongly compatibility with the adjoined components during operation. Choosing a suitable electrolyte material depends on the fuel cell type and application. The most common electrolytes generally include aqueous solutions, solid polymers and solid oxides.

The typical morphology of the cathode and anode is a porous composite consisting of a thin catalyst layer (CL) and a gas diffusion layer (GDL). The CL, which has a thickness on the order of 10 μm, is comprised of an intimate mixture of widely dispersed high surface area electrocatalyst nanoparticles supported by an ionically and electronically conductive support.[264, 82, 156, 24] Electrocatalysts are materials designed to accelerate the rates of oxygen reduction reaction (ORR) and hydrogen oxidation reaction (HOR) at the cathode and anode, respectively. Both reactions take place at the triple phase boundary within the CL, the junction between electrocatalyst, conductive

support, and electrolyte where the reactants (H_2, O_2), ions (H^+, OH^-, O^{2-} , etc.), and electrons meet. Because ORR and HOR are heterogeneous reactions, synthesizing the electrocatalyts as nanoparticles ensures a large distributive reactive surface area. Additionally, mixing electrocatalysts with a high surface area, chemically inert conductive support ensures good electron mobility to the active sites, which is necessary for completing the full redox. While electrocatalyst research has been one of the most active research areas, it remains as one of the most challenging in terms of overcoming performance, cost, and durability limitations. The GDL backing of the CL is a porous matrix that provides permeable channels to facilitate sufficient flow of H_2 and O_2 to the CL. Moreover, the GDL material must be conductive in order to function as a current collector, and robust enough to provide mechanical support, heat/water removal, and protection from corrosion and erosion. GDLs for low temperature fuel cells are commonly made from porous carbon fiber, often woven together to form a cloth, or bonded together by resins to form a paper.[264] Additionally, GDLs are sometimes wetted with Teflon (PTFE) to increase hydrophobicity, thereby increasing the transport of water. Micro-porous layers composed of carbon black powder are sometimes situated at the junction between the CL and GDL for better water drainage.

1.6 Fuel Cell Types

There are various types of fuel cells that are optimized for certain applications. For instance, the prototypical fuel cell depicted in Figure 1.1 is known as a proton exchange membrane fuel cell (PEMFC), which uses a H^+ conductive polymeric electrolyte membrane. Fuel cell types are primarily distinguished by the electrolyte, conductive ionic species (e.g. H^+, O^{2-} , OH^-, etc.), operating temperatures, and fuel type (i.e. H_2, CH_3OH). Table 8.1 shows a list of key fuel cells and their operating parameters.

Fuel Cell Type	Abbreviation	Temperature Range (°C)	Output Range	Efficiency	Common Electrolyte
Proton Exchange Membrane	PEMFC	70-110	<250kW	50-60% electric	Sulfonated Polymer
Alkaline	AFC	100-250	10kW-100kW	50-70% electric	Aqueous KOH
Phosphoric Acid	PAFC	150-250	50kW-1MW	80-85% CHP	H_3PO_4
Molten Carbonate	MCFC	500-700	<1MW	85% CHP	$(Na,K)_2CO_3$
Solid Oxde	SOFC	700-1000	5kW-3MW	85% CHP	$(Zr,Y)O_{2-\delta}$

Table 1.1: List of prominent fuel cell types and associated operating temperatures, power density range, efficiency range, and common electrolyte materials

1.6.1 Proton Exchange Membrane Fuel Cells

The proton exchange membrane fuel cell (PEMFC) is the most prolific type of fuel cell, and currently the most commercially viable. As the name suggests, the PEMFC consists of an electrolyte membrane that ionically conducts H^+ from the anode to the cathode. With electrical efficiencies that range from ~40-60%, PEMFCs also exhibit excellent power densities while operating at relatively low temperatures (~80 °C, see Table 8.1).[264, 82, 156, 24] The ability to operate at near ambient conditions is critical for applications that require fast startup times (e.g. portal power, electric vehicles) while minimizing degradation after several power cycles. Although PEMFCs yet to fully reach the necessary cost and performance benchmarks for widespread use in markets against competing technologies such as Li-ion batteries and combustion engines, academic and industrial research still remains very active.

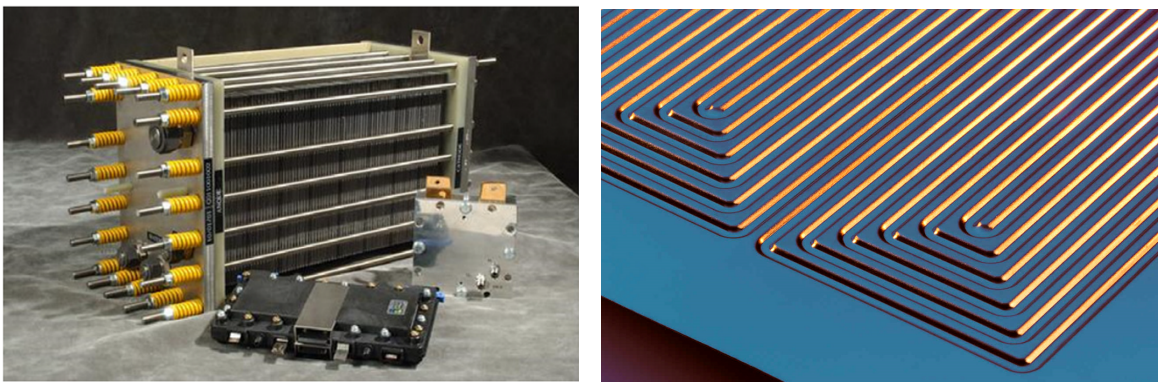

(a) (b)

Figure 1.3: (b) PEM fuel cell stack.[264] (a) Gas flow channel (http://change-florida.com/fuelcells.html on 03/09/2018).

Proton exchange membrane (PEM) electrolytes are thin ionomer membranes (10-100 μm) containing conductive hydrated channels for proton flow.[264, 164] Common electrolyte materials are derived from a solid polymer containing sulfonic functional groups tethered to a perfluorinated backbone (PTFE) that provides mechanical support; the most well-known PEM is Nafion, which was developed by Dupont in the 1960s. Proton transport through the PEM is a combination of proton site hopping from one sulfonic group to another, and vehicular diffusion of hydronium (H_3O^+) ions, which is governed by both water diffusivity and electro-osmotic drag.[264] In order to optimize proton transport (i.e. ionic conductivity), PEM electrolytes must maintain a certain level of hydration. If the water content decreases, the membrane is susceptible to defect formation and cracking. Conversely, excess water can swell the membrane, as well as flood the cathode, reducing the fuel delivery rate to the active sites, consequently starving the CL of oxygen. The PEM electrolyte must also maintain a low pH, which induces a highly acidic environment for the surrounding materials. This is particularly problematic for the electrocatalysts and conductive supports.

Another key PEMFC component is the bipolar plate, which is interfaced with the outward faces of the GDLs. Bipolar plates are used as separators that allow multiple MEAs to be stacked in series to increase the operating potential-a single MEA is typically limited to ~1V) (Figure 1.3a).[264, 256] Bipolar plates supply and distribute H_2 and O_2 using distributive patterned gas

flow channels (GFCs), providing uniform convective flow throughout.[90] Figure 1.3b shows a picture of a typical flow field design, which can vary depending on the specifications of the application. In addition to uniform fuel distribution, bipolar plates are current collectors that provide mechanical support, fast heat conduction, and a high impermeability of H_2 and O_2 to minimize cross-over and leakage. Bipolar plates make up a large fraction of both the stack weight (80%) and cost (45%), prompting efforts to seek lighter weight, inexpensive materials.[90] Common materials currently used as bipolar plates include graphite and/or graphite-composites. While these graphite-based materials are chemically inert and conductive, they are also mechanically brittle and expensive. Thus, many have sought aluminum, iron, stainless steel, titanium, and nickel as viable bipolar plate materials.[90]

Upon the discovery of H^+ conductive (~0.01-0.25 S/cm)[90, 129] ionomer electrolytes, many have sought to integrate PEMFCs into portable and automotive technologies. However, high material costs and limited durability still preclude widespread proliferation. Hydration maintenance of the PEM membrane along with a restricted library of corrosion-resistant electrocatalysts, such as Pt and/or Pt alloys, continue to be major cost burdens. Nonetheless, the utility of PEMFCs continue to grow in various niche markets, even breaking into large competitive markets with the recent launch of commercial fuel cell electric vehicles (FCEV) (within the last 2 years) by Toyota and Hyundai.

1.6.2 Alkaline Fuel Cells

Alkaline fuel cells (AFCs) were one of the earliest commercial prototypes, first incorporated into NASA space shuttles for a number of Apollo missions. Like PEMFCs, AFCs operate at low temperatures (< 100 °C), but their distinguishing feature is the use of alkaline electrolytes that transport hydroxide ions (OH^-) from the cathode to anode. Although they have been slowly displaced by conventional PEMFCs, interests in AFCs have reemerged within the

last decade due to advances in the performance and durability of polymeric alkaline electrolyte membranes.[279, 153, 108]

Early AFC electrolytes were composed of a porous matrix of gel-like material saturated with a strongly basic aqueous potassium hydroxide (KOH) solution. Under alkaline conditions, the anodic and cathodic half-reactions involve the hydroxide anions.

$$Cathode : \frac{1}{2}O_2 + H_2O + 2e^- \rightarrow 2OH^- \tag{1.8}$$

$$Anode : H_2 + 2OH^- \rightarrow 2H_2O + 2e^- \tag{1.9}$$

Alkaline fuel cells are highly efficient, reaching values as high as 70%, much of which is largely attributed to faster ORR kinetics under alkaline conditions.[225] Compared to PEMFCs, there is a larger library of materials that are stable under alkaline conditions.[33, 107, 167] Thus, AFCs are not limited to using expensive precious metal electrocatalysts such as Pt or Pt-alloys, though they are still among the most catalytically active materials even in alkaline environments.[225] The potential use of cheaper non-precious metal electrocatalysts combined with a simple KOH electrolyte in contrast to highly expensive Nafion and/or any other fluoropolymer-based electrolyte bolsters AFCs as less-expensive alternatives to PEMFCs.

Despite its advantages, AFCs suffer from irreversible carbonate formation. Trace amounts of carbon sourced from CO_2 mixed with oxygen/hydrogen, and leached carbon support reacts to form carbonate (CO_3^{2-}) anions. The carbonate combines with the potassium (K^+) cations, precipitating potassium carbonate (K_2CO_3) salt that consequently expedites fuel cell degradation by clogging the electrode pores, subsequently flooding and blocking fuel supply.

$$Anode : CO_2 + 2OH^- + K^+ \rightarrow K_2CO_32 + H_2O \tag{1.10}$$

Common techniques such as cycling the KOH solution continuously, and/or using high purity gas feeds can decrease the rate of K_2CO_3 formation, prolonging the operating lifetime, though these processes are very costly. In order to mitigate the lingering issues with leakage and the

formation of a K_2CO_3 precipitate, research in alkaline electrolytes have shifted towards polymer anion exchange membrane (AEM) materials. Common AEMs consist of cationic functional groups (e.g. pyridinium, guanidinium, ammonium, phosphonium, sulfonium, etc.) containing hydroxyl counter anions, which act as the anion-exchange sites.[37, 153, 108] These membranes also consist of a polymeric backbone that supports the cationic groups, much like the PTFE material in Nafion.

One of the contemporary challenges with AFCs is finding suitable AEM materials that facilitate comparable ionic transport properties to PEMs. Reaching this benchmark is far less tenable given the intrinsic difficulty of transporting the fairly large and bulky hydroxyl species in comparison to the smaller and mobile protonic species. Additionally, current AEMs contain cationic groups that are susceptible to degradation reactions with the hydroxyl counter-anions, drawing concerns regarding chemical stability during operation. The extent of degradation varies depending on the degree of hydration and temperature. The polymeric backbone (i.e. polysulfones, fluorinated polymers, etc.) is also susceptible to degradation. To circumvent the pervasive issues with degradation, different synthesis routes (i.e. crosslinking, irradiation/grafting, etc.) and AEM materials, including fluoropolymers, polysulfones, polyarylenes, and poly(ether-imide)s, have been evaluated, many of which are linked to ammonium cations.[153] Overall, the sharp rise in the number of AEM studies has been encouraging, which may spawn a significant revitalization of commercial AFCs.

1.6.3 Solid Oxide Fuel Cells

Solid oxide fuel cells (SOFCs) are high temperature (600-1200 °C) devices that utilize an ionically conductive solid oxide membrane as the electrolyte for the transport of oxygen anions (O^{2-}) from the cathode to anode.[82] When SOFCs operate continuously, they demonstrate outstanding stability, good fuel flexibility, and high operating efficiencies. Solid oxide fuel cells are primarily composed of ceramics, a class of materials known for being highly robust within a wide

high temperature range. In contrast to low temperature fuel cells (PEMFCs, AFCs), SOFCs are not limited by issues associated with leakage and hydration maintenance. Performance is largely governed by the transport properties of O^{2-} across the oxide membrane (conductivity is exponentially dependent on temperature). Commercial SOFCs commonly use yttria stabilized zirconia (YSZ) and/or ceria (Ce)-based oxides as the electrolytic membranes due to their strong chemical stability at high temperatures.[82, 263] The electrodes are ceramic composites (i.e. cermets) composed of the solid oxide electrolyte mixed with catalytically active materials. Operating at very high temperatures significantly reduces the kinetic redox reaction threshold, eliminating the need for precious metal electrocatalysts. For instance, an SOFC anode is typically a porous composite containing transition metal electrocatalysts such as nickel (Ni) mixed with YSZ. In addition to exhibiting fast oxidation kinetics, the anode is an active steam reformer to make hydrogen fuel.[82] It is typically the thickest layer of the MEA stack, providing mechanical support. Cathode materials commonly consist of lanthanide-based and perovskite-based oxides such as lanthanum strontium manganite ($La_{1-x}Sr_xMnO_{3-\delta}$, 0.15 ¡ x ¡ 0.25), or LSM.[2] Because many cathode materials such as LSM are fairly poor ionic conductors, the design of the SOFC minimizes the thickness of the cathode layer on top of the stack to minimize polarization losses.

A major limitation with SOFCs is that they must operate at high temperatures in order to thermally activate all of the processes (i.e. catalysis, ionic conductivity, electronic conductivity, etc.) needed to maintain practical power and efficiency. Consequently, SOFCs are chiefly utilized as primary and/or auxiliary stationary power systems for small and large-scale installations. Operating at high temperatures also imposes a limit on the library of ceramics that are chemically and thermally stable at extremely high temperatures. Even for ceramics that fit all of the property requirements, many are still susceptible to chemical degradation, thermal stress buildup, and thermal-induced cracking.

As more businesses and even certain households incorporate SOFC technology into off-grid stationary power generation systems, research continues to be an active area, with a heavy

emphasis on lowering the operating temperatures within an intermediate range (500-600 °C). This can significantly reduce startup times, insulation costs, component costs, and extend the operating lifetimes.

1.6.4 Additional Fuel Cell Types

Although PEMFCs, AFCs, and SOFCs are the most ubiquitous commercially, there exist several other types of fuel cells. Each offers their own set of unique properties, operating conditions, and limitations. Other types include phosphoric acid fuel cells (PAFCs), direct methanol fuel cells (DMFCs), and molten carbonate fuel cells (MCFCs). Phosphoric acid fuel cells (PAFCs) operate between 150 and 200 °C using highly concentrated H^+ condutive liquid phosphoric acid as the electrolyte.[264, 1]. PAFCs offer the additional benefit of operating with a variety of fuel types (i.e. hydrogen, methanol, ethanol), as well as operating as a combined heat and power source, converting expelled water into steam. While PAFCs are not as efficient as PEMFCs, they are comparatively less expensive. However, PAFCs operate under harsh acidic conditions, limiting the available materials for redox catalysis to precious metals. Moreover, the use of liquid electrolytes introduces complications with leakage. Direct-methanol fuel cells (DMFCs), which operate on the consumption of methanol fuel as opposed to hydrogen, have recently gained significant interest. Methanol has a higher energy density than hydrogen, with a clear logistic advantage of easier handling and distribution, though the presence of carbon makes DMFCs less environmentally friendly (CO_2 and CO are common byproducts). Molten carbon fuel cells (MCFCs) are intermediate temperature (600-700 °C) devices that use a molten carbonate salt mixture suspended in a ceramic matrix as the electrolyte, which ionically conducts carbonate (CO_3^{2-}) ions. They are commonly used to generate electricity from natural gas, biogas from anaerobic digestion, and coal-based sources.[24] While MCFCs are far from being zero-emission devices, they are highly efficient (~70%), and are suitable internal reformers capable of converting energy dense sources such as methane into hydrogen fuel. Overall, it is recommended that the reader seek literature that goes

into greater depth on all of these fuel cells systems. While this summary is limited in length and detail, it should not undercut their significance in terms of operational efficacy, research activity, and commercial value on a wider scale.

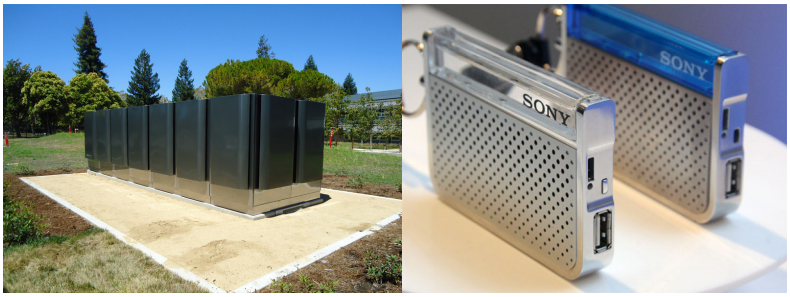

(a) (b)

(c)

Figure 1.4: (a) Stationary SOFC (http://www.fchea.org/stationary/ on 03/09/2018). (b) Portal fuel cell (https://www.slashgear.com/sony-demo-hybrid-fuel-cell-concepts-2535678/ on 03/09/2018). (c) Fuel cell electric vehicle (http://www.thetruthaboutcars.com/2013/11/hyundai-says-fuel-cells-will-be-cheaper-than-batteries-will-debut-hydrogen-fuel-cell-cuv-next-year-for-sale-in-2015/ on 03/09/2018)

1.7 Applications and Market Landscape

Commercial fuel cells are integrated in several applications (Figure x) associated with stationary, transportation, and portable power.[40] Stationary fuel cells include alternative off-grid primary and backup power generation, as well as combined heat and power (CHP) generation

for homes, businesses, telecommunications networks, and utilities. Transportation applications include fuel cell electric vehicles (FCEVs), and specialty vehicles such as buses, off-road vehicles, and material handling equipment (MHE) such as forklifts. The utility of fuel cell technology has also expanded towards portable power devices such as personal electronics, auxiliary power, and military equipment.

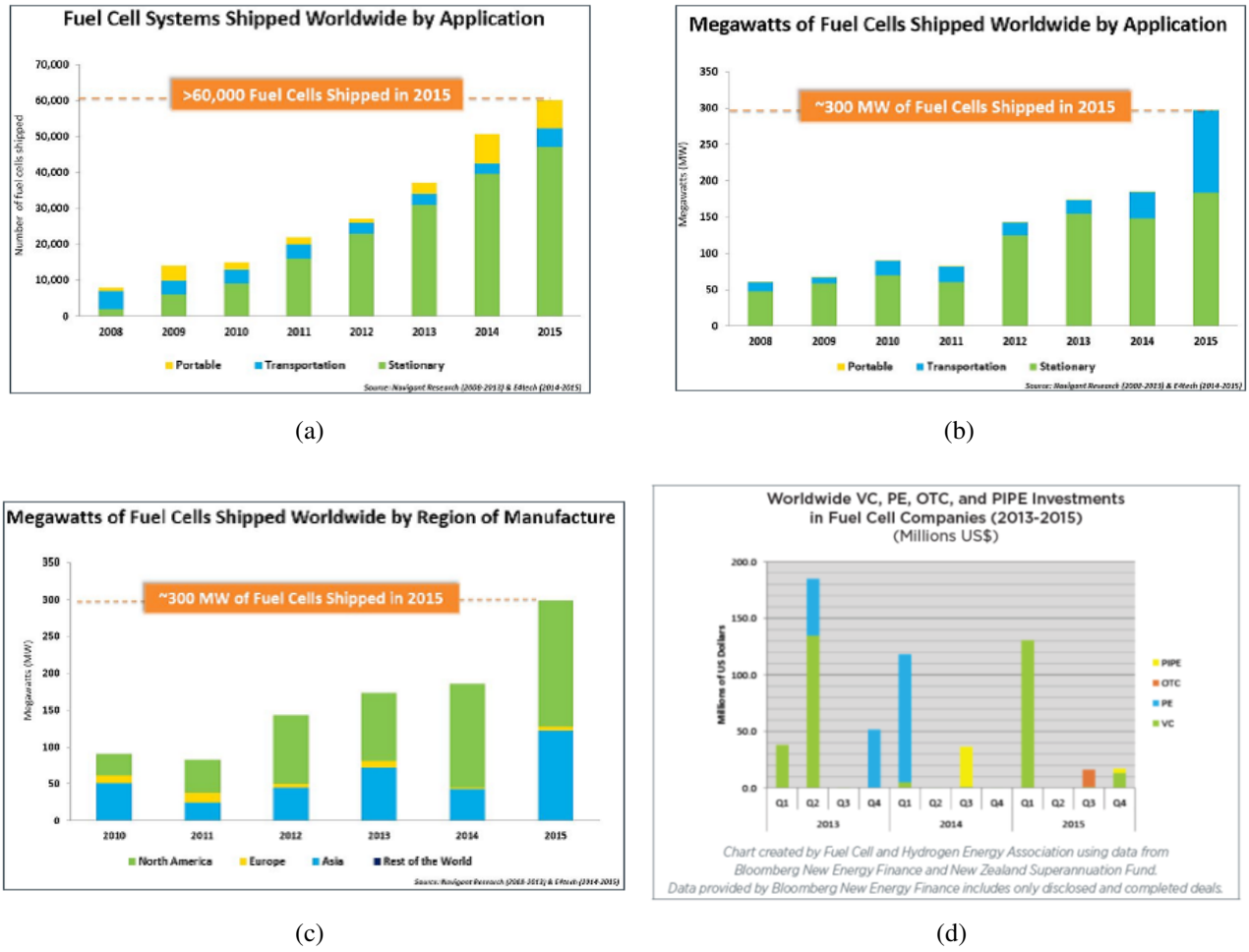

Figure 1.5: (a) Total fuel cell shipped year-by-year. (b) Total fuel cell megawattage year-by-year. (c) Megawatts shipped by region. (d) Worldwide fuel cell investment.[40]

According to the Fuel Cell Technologies Market Report published in August of 2016 by the U.S. Department of Energy (DOE), more than 60,000 fuel cells were shipped globally in 2015, which totaled to more than 300 megawatts (MW)-more than 65% increase from 2014 (Figure

1.5a,b).[40] The largest fuel cell market was in North America, with shipments around 30% more than Europe and Japan combined (see Figure 1.5c). The increase in wattage comes largely from recent market growth in both stationary power and transportation. Recent activities in stationary power included large-scale installations of fuel cell power parks in both the U.S. and South Korea, along with steady a growth in residential fuel cell systems in Japan.[40, 41, 178] Steady growth in transportation is attributed to increased deployment of specialty vehicles such as MHE and buses. Moreover, FCEVs developed by Toyota and Hyundai were recently made available as of 2015 in parts of California, Europe and Japan.[40, 41]

The fuel cell industry, which includes all technologies related to hydrogen and fuel cells, reported approximately $2 billion in total revenue (roughly consistent with 2014).[40, 41] However, there reported figure varies between less than $1 billion and over $3 billion due to uncertainties and discrepancies when factoring additional revenue sources from private and government project funding, as well as fuel cell sales for educational purposes.[40] Additionally, multi-faceted companies and conglomerates do not always disclose revenue from the sales of fuel cell units separately from other products.

During the period between 2013 and 2015, cumulative global investment in fuel cell companies from venture capitalists (VCs), private equity (PE), over-the-counter (OTC) and private investment in public equities (PIPE) totaled to around $592.7 million (Figure 1.5d).[40] The U.S. constitutes around 58% of the total investment. Despite commercial growth in certain fuel cell markets, total investment was comparatively lower than the $736.2 million invested between 2012 and 2014, and $1.038 billion between 2011 and 2013. More specifically, total investment was around $163.6 million in 2015, slightly above the $154.6 million figure in 2014, but down from $274.5 million in 2013. However, there was a notable increase in total investment in U.S.-based fuel cell companies, which estimated to $131.1 million compared to $40 million in 2014.

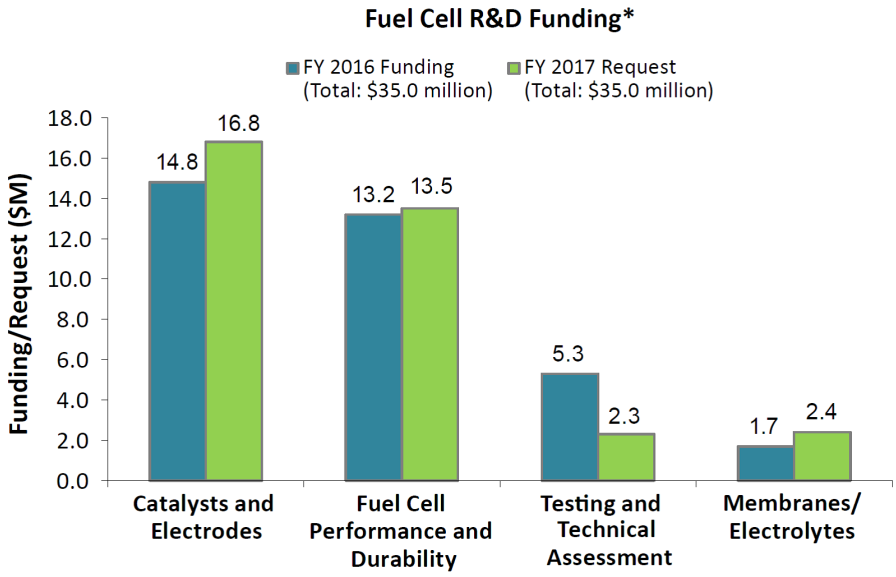

(a)

Figure 1.6: 2016 and 2017 R&D fuel cell funding in key areas.[178]

1.7.1 Federal Activities

Within the last 15 years, the federal government has taken a more active role towards building an infrastructure for clean and renewable energy through legislation, federal research funding, and consumer/corporate subsidies.[40, 210] For instance, Title VIII of the Energy Policy Act (EPAct) of 2005, a bill signed by George W. Bush, establishes research and development on technologies relating to the production, purification, distribution, storage, and use of hydrogen energy, fuel cells, and related infrastructure.[40] In 2015, a major milestone for EPAct was reached when Hyundai and Toyota released a line of commercial fuel cell electric vehicles (FCEV), meeting one of the stated program goals, to enable a commitment by automakers no later than year 2015 to offer safe, affordable, and technically viable hydrogen fuel cell vehicles in the mass consumer market. Furthermore, Honda is slated to release a new FCEV during 2017.[40]

Then-President Obama issued an Executive Order, *Planning for Federal Sustainability in the Next Decade*. This order outlined sustainability goals for federal agencies to incorporate clean energy technologies (encompassing fuel cells and related technologies) into federal buildings and

vehicles. Obama also signed a Transportation bill, which includes a Section 1413, which designates alternative fueling corridors for hydrogen, propane, and natural gas fueled vehicles. Additionally, Congress retroactively extended tax credit of up to $8,000 for the purchase of FCEVs, extending beyond the original expiration year of 2014.[40, 210] In the Fiscal Year of 2015, Congress appropriated approximately $97 million for the DOE Office of Energy Efficiency and Renewable Energy (EERE), Fuel Cell Technologies Office (FCTO), and $30 million for solid oxide fuel cell (SOFC)-related activities within the Office of Fossil Energy.[40, 210] While including funding for the Advanced Research Projects Agency-Energy (ARPA-E) and Office of Science (SC), the total U.S. DOE funding for hydrogen production/storage and fuel cells was approximately $150 million.[40] The DOE funding through the FCTO was distributed to various R&D projects within several proposals and programs, most notably Small Business Innovation Research and Small Business Technology Transfer (SBIR/STTR); Advanced Hydrogen Storage Systems Awards and Research; and Development and Demonstrations Funding Awards.[40] Lastly, FCTO also allocated resources towards market transformation efforts to expedite the commercialization of hydrogen and fuel cell technologies.

Other federal agencies that provided funding to hydrogen and fuel cell technologies included the Department of Transportation's Federal Transit Administration (FTA), and the Defense Department's Defense Logistics Agency (DLA), which funds several transportation technologies. The fiscal year 2017 budget requested $35 million for the Fuel Cells program, equal to the 2016 appropriation. Figure 1.6 shows the breakdown of the distributed funding for the key areas of fuel cell R&D.

1.8 Benchmarks

The commercial growth and sustainability of fuel cell technology is predicated on reaching certain target performance benchmarks, both short-term and long-term, while continually re-

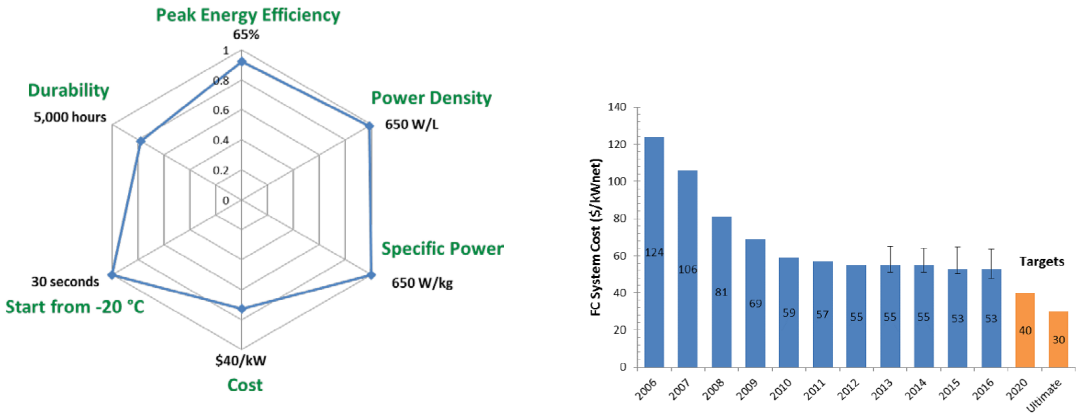

(a) (b)

Figure 1.7: (a) Key fuel cell benchmarks compared to current performance standards.[210] (b) Year-by-year cost/kW and target benchmarks.[178]

ducing production costs. Efforts to reduce cost, improve power output, efficiency, and durability are ongoing, and essential for widespread integration into competitive energy markets. Figure S.7 shows the year-by-year production cost of PEM fuel cells along with the projected and target cost. Consequently, various performance benchmarks have been projected by the DOE [210], which are dependent upon the specific application and fuel cell type. For instance, low temperature fuel cells for automotive applications are benchmarked to reach 65% peak efficiency and 5000-hour lifetime at a production cost of $40/kW a by the year 2020, but long-term competiveness will require operation lifetimes that exceed 8,000-h, and productions costs approaching $30/kW.[210] Based on the 2016 DOE annual progress report, the preliminary projected cost of automotive PEMFCs operating at 80 kW is around $53/kW at a manufacturing volume of at least 500,000 units/year, and $59/kW at a volume of 100,000 units/year. However, the cost did not change from 2015, and current PEMFCs manufactured at an output of around 1000 units/year costs around $230/kW. As of late 2016, the operating lifetime of a commercial PEMFC is around 3,900-h.[210]

Most recently, there has been a concerted effort to directly and indirectly improve fuel cell performance through Fuel Cell Performance and Durability (FC-PAD) Consortium initiative. Launched in 2015, FC-PAD consolidates and coordinates research in several areas related to fuel cell technology, spanning across industry, academia, and national laboratories. The organization

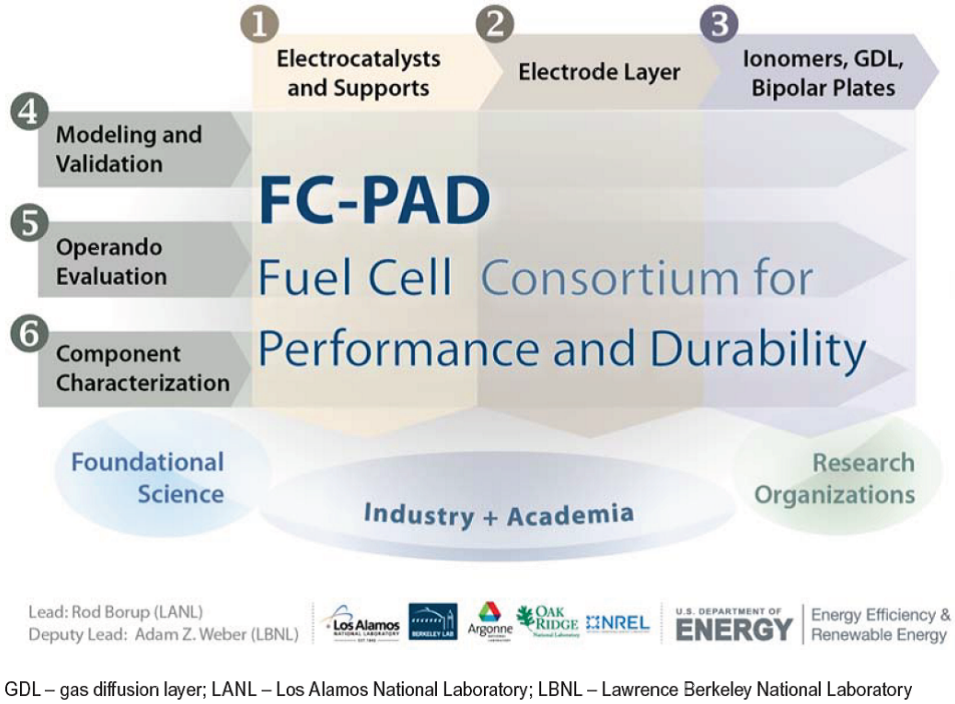

GDL – gas diffusion layer; LANL – Los Alamos National Laboratory; LBNL – Lawrence Berkeley National Laboratory

(a)

Figure 1.8: Key components and research methodologies of FC-PAD. [210]

partitions research in FC-PAD into three general areas: electrocatalysts and supports; electrode layers; ionomers, gas diffusion layers, bipolar plates, interfaces. Research on each of these components is also organized by methodologies using the latest approaches in modeling and validation; operando evaluation; benchmarking, accelerated stress tests, and contaminants; and component characterization and diagnostics. Other facets related to fuel cell research also include studies on hydrogen production, delivery, and storage; basic research; manufacturing R&D; technology validation; market transformation; education, safety, codes, and standards.

Additionally, a second consortium was established in 2016 called the Electrocatalysis Consortium (ElectroCat), which focuses on high-performance, low cost platinum group metal (PGM)-free catalysts for automotive fuel cells. However, the scope of ElectroCat extends to research areas corresponding to high-throughput combinatorial methodologies, computational methods, nano-structured thin films, and PGM-free catalysts. Primarily, ElectroCat aims to minimize

PGM loading while optimizing the catalytic activity through alloying and core-shell synthesis.

1.9 Closing Summary

As the climate continues to change as a consequence of unchecked carbon emission, we have reached a critical juncture where coordinated efforts scientifically and legislatively are more important than ever to upend this existential threat of climate change. Fuel cells play a critical role towards building a sustainable infrastructure powered exclusively by clean energy technologies. However, the high production costs, coupled with longstanding challenges in optimizing redox catalysis and durability, continue to be the limiting factors that preclude large-scale distribution. But despite these limitations, fuel cell utilization in certain markets continues to grow. Thus, fuel cell research will continue to be an active and critical facet to clean energy.

CHAPTER 2

OXYGEN REDUCTION AND EVOLUTION CATALYSIS

2.1 Introduction

The transition from fossil fuels to large-scale sustainable clean energy storage and conversion continues to be a major scientific and industrial challenge. The performance (i.e. efficiency, power density) of low temperature electrochemical cells, such as fuel cells[264, 263, 24], electrolyzers[262, 23, 43, 151, 143], photocatalytic water splitters[43, 116, 261], and metal-air batteries[26], all of which operate on the consumption and/or production of oxygen, is limited predominantly by the sluggish kinetics of oxygen reduction/evolution reaction (ORR/OER). Even for systems that use "state-of-the-art" components, ORR/OER at low temperatures still suffer from ~400 mV overpotentials upon reaching practical current density outputs (Figure S.1).[264]

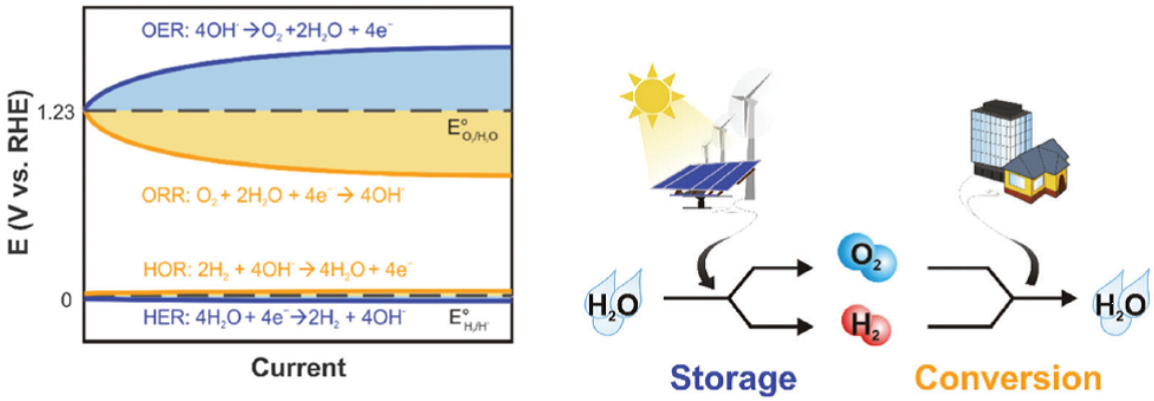

(a) (b)

Figure 2.1: (a) The cell potential at a given output current for ORR/OER and HOR/HER. Comparatively, HOR/HER is far more facile than ORR/OER. The area under the curves correspond to energy lost due to the limited kinetics of ORR/OER. (b) Illustrations of the role of oxygen and hydrogen during conversion and storage.[94]

Summarized in chapter 1, ORR/OER is a half-reaction that takes place at the cathode(ORR)/anode(OER). During ORR, oxygen molecules adsorb onto the reactive sites at the cathode, undergoing a series of heterogeneous electron-transfer reduction reactions. Under acidic con-

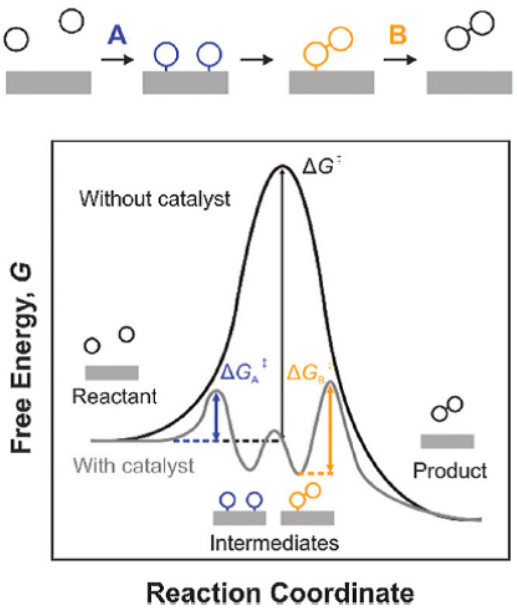

Figure 2.2: The change in the transition state when catalysts are incorporated. The change is induced by a lower-energy reaction pathway through the formation of heterogeneous oxygen intermediates at the catlayst surface[94]

ditions, the reaction of oxygen is shown as:

$$O_2 + 4H^+ + 4e^- \rightarrow 2H_2O \tag{2.1}$$

Conversely, reversing the direction of the reaction initiates OER, where water is oxidized to evolve O_2. Despite the natural ubiquity of both ORR and OER, efforts to elucidate the underlying factors that influence the reaction mechanisms and kinetics is still limited. Most importantly, optimizing the ORR/OER reaction rates to reach competitive performance benchmarks continues to be a major challenge.

2.2 Oxygen Electrocatalysts

High surface area electrocatalysts, which are uniformly embedded within a composite layer that makes up the anode and cathode (See Chapter 1), are used to accelerate the reaction kinetics of ORR/OER. The breadth of research devoted to oxygen catalysis using a wide range

of systematic, experimental, and theoretical approaches, has led to the discovery of several novel active catalyst materials. Currently, platinum (ORR) or iridium (OER) are among the standard catalysts in commercial proton-exchange membrane fuel cells (PEMFCs) and electrolyzers, respectively. However, these materials are among the rarest and most expensive noble metals, incurring a large fraction of the overall manufacturing cost, and severely limiting the production throughput. In addition to several studies that focus on reducing the material loading of Pt and Ir, many researchers have sought to eventually replace them with less expensive and more abundant alternative (non-Pt and non-Ir) catalysts, without compromising the overall catalytic activity. Although many have reported a wide range of catalyst systems that showcase very promising results, there has been limited success in implementing them commercially, thereby replacing the current noble metal standards.

The search for alternative oxygen catalysts is the primary motivation behind this research. Thus, this chapter will convey the massive scope of oxygen catalysis, generalizing previous studies on notable catalyst systems, particularly metal oxides for alkaline fuel cells and electrolyzers. With regards to this research, two key oxide systems will be discussed in Chapters 5 and 6: manganese-doped ruthenium oxide ($Mn_xRu_{1-x}O_{2-y}$) and pyrochlores ($(Bi,Pb)_2(Ir,Ru)_{2-x}(Bi,Pb)_xO_{7-y}$). Both systems were evaluated as bifunctional catalysts using combinatorial high-throughput techniques derived from methodologies established by previous graduate students within the van Dover group, as well as prolific electrocatalyst researchers (e.g. Goodenough, Stamenkovic, Abruña, Gasteiger, etc.).[182, 242, 74]

2.2.1 The Role of Oxygen Catalysts

The performance bottleneck from sluggish ORR and OER is induced by the high kinetic activation thresholds for oxygen redox (See Appendix I summary on Transition State Theory). Catalytically active materials contain reactive surface sites that unlock faster reaction pathways involv-

ing heterogeneously formed intermediates (Figure S.2).[94] These pathways are generally characterized by a reaction sequence of steps consisting of molecular and ionic adsorption/desorption; protonation; production of oxygen intermediates, and oxygen bond-breaking.[84, 170, 215, 131] However, the predicted reaction sequence and rate-limiting step(s) are highly dependent on the catalyst material and environment, often becoming a major source of discord amongst electocatalyst researchers. But as *in*-situ and *ex*-situ electrochemical and characterization techniques become increasingly more sophisticated, and when combined with the latest theoretical models, the confluence of these methods help further expound the factors that drive specific reaction mechanisms in relation to key operating conditions (e.g. pH, temperature, electrolyte, etc.) and catalyst material properties (i.e. electronic, surface chemistry, structure, surface morphology, etc.).

2.2.2 Oxygen Reduction

The most prolific class of catalysts for oxygen reduction, as well as hydrogen oxidation/evolution is platinum (Pt) and platinum alloys (Pt-M, M=Co, Ir, Cr, Ni, Cu, etc.).[94, 70, 251, 160, 159, 61] In addition to consistently exhibiting the highest catalytic activities for ORR, Pt is chemically inert, and highly robust against corrosive environments. Consequently, applications such as proton-exchange membrane fuel cells (PEMFCs), which operate under highly acidic conditions, employ Pt-based materials as the standard catalysts for both the anode (hydrogen oxidation) and cathode (oxygen reduction). However, Pt is one of, if not the most expensive precious metal in the market due to its wide ranging application value and natural scarcity. Thus, the incorporation of Pt constitutes a significant fraction of the overall production cost of PEMFCs, ultimately stifling large-scale manufacturing and any subsequent long term growth.

Despite the need for less-expensive alternative catalyst materials, Pt continues to be the most heavily studied catalyst, establishing an comprehensive network of research focused on different aspects to engineering Pt particles, including surface structure[231, 148, 147],

alloying[70, 160, 159, 230, 252], and particle morphology[147, 282, 165], all of which converge towards optimizing catalytic activity while minimizing volumetric and/or mass Pt loading. Prominent studies related to Pt ORR catalysis have attempted to reconcile theoretical models built on molecular simulations and density functional theory (DFT) with systematic *ex*-situ and *in*-situ experimentation. For instance, Stemankovic et al. among several other researchers modeled ORR selectivity and activity on various faces of Pt (e.g. (111), (110), and (100)), reporting the (111) face as the most active.[230, 229] Other consequential studies have used kinetic and thermodynamic models to identify key descriptors that govern ORR activity.[94, 160, 159, 230, 84] These models correlate with the Sabatier principle, which identifies an optimizal binding energy of oxygen and hydroxyl groups on the catalyst surface for maximum catalytic ORR activity.[230, 84, 229] The binding energy descriptor is governed by the electronic properties of the catalyst, particularly the interactions between the metallic d-band center with the molecular orbitals of the oxygen adsorbates. When the binding energy is too high, the Pt surface becomes poisoned by the accumulation of bound oxygen intermediates due to a low rate of oxide dissociation; conversely, when the binding energy is too low, partially reduced intermediates desorb, producing partially reduced byproducts (i.e. H_2O_2) that can have adverse effects on the surrounding components.[84, 131]

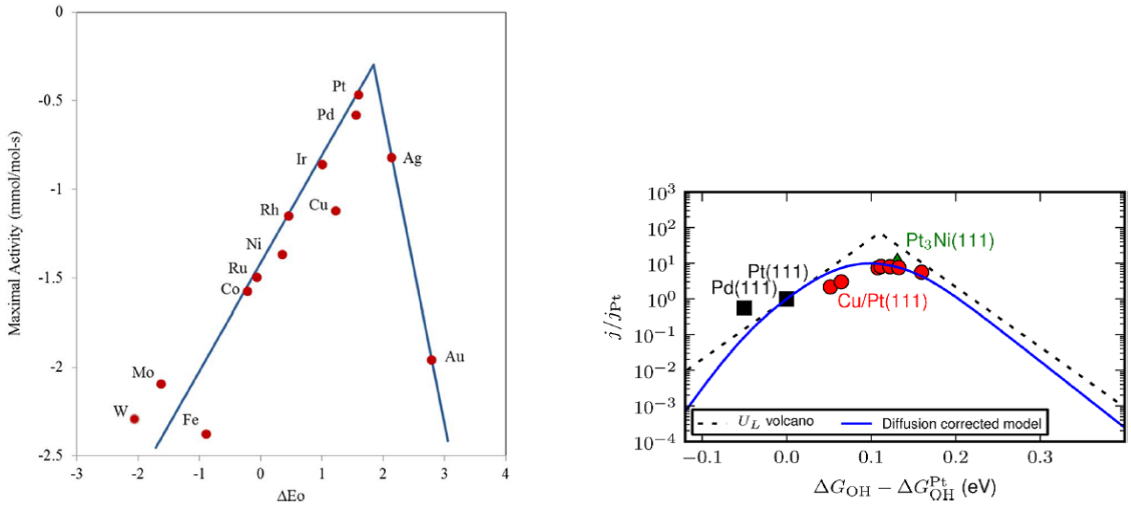

(a) (b)

Figure 2.3: (a) Volcano plot of metal catalysts. (b) Volcano plot of Pt-metal alloys at the (111) plane.[23]

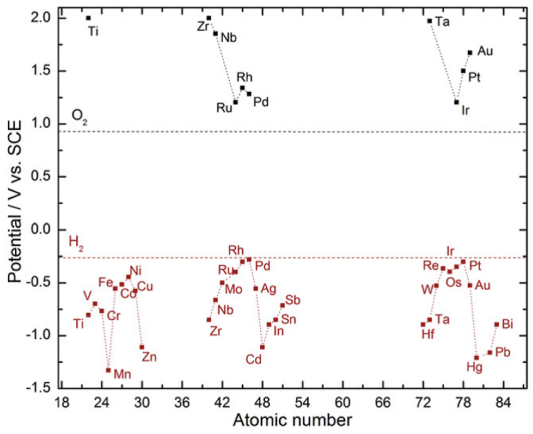

Figure 2.4: (a) Potential vs. atomic number volcano plot relative to the theoretcial potentials for the reaction of hydrogen and oxygen.[23]

Consequently, the catalytic activity with respect to the binding energy descriptor establishes a ”volcano” trend (Figures S.3a), resolving an activity peak. This model has led to several other studies that focused on adjusting the oxygen binding energy (tuning the d-band center) through alloying-induced strain effects (Figure S.3b) using a number of different noble and transition metals. Alloying brings the additional benefit of reduced cost by reducing Pt-loading when alloyed with cheaper metals. Alloying has also been used to engineer the nanostructure of Pt-based catalysts through the design of core-shell bimetallic Pt particles, composed of a monolayer shell of Pt and a non-Pt core made of precious and/or transition metals (Ir, Pd, Au, Ni FeCu, etc.).[112, 274, 209, 198, 271, 235] These approaches optimize Pt use, while using the nanostructured core as a template for maximizing the preferential orientation of the highly active (111) face. While a more in depth summary of Pt catalysts is warranted, it is well beyond the necessary scope of this thesis. Thus, I encourage the reader to explore this massive sphere independently.

2.2.3 Oxygen Evolution

In addition to proliferating energy conversion applications such as fuel cells, it is critical to establish an infrastructure that can facilitate large-scale generation and storage of hydrogen fuel.

Efficient electrochemical systems for generating hydrogen fuel through water oxidation have been highly sought, most prominently through electrical electrolysis and systems that facilitate solar-to-fuel conversion. However, current electrolysis systems suffer from low efficiencies and current outputs imposed by the large kinetic threshold of oxidizing water to generate oxygen. Efforts to optimize OER efficiencies have culminated into several studies on bulk and molecular catalyst systems for photo and electrical electrolysis.[23, 43, 143, 116, 261]

In the same fashion as PEMFCs, the harsh acidic environment in proton-exchange membrane electrolyzers severely limits the availability of compatible catalysts to a select group of noble metals (e.g. Pt, Rh, Ir, Au).[23] Iridium (Ir) and IrO_2 are considered the benchmark catalysts for PEM electrolyzers due to their high stability and strong catalytic activity.[42, 32, 31, 100, 59] However, Ir is among the rarest and most expensive noble metals within the earths crust (less abundant than both Pt and Au). Accordingly, ongoing research has focused on minimizing Ir loading by mixing with less expensive elements.[168, 169, 278] Ruthenium (Ru) and RuO_2 are another set of highly active catalysts that exhibit even stronger OER activities than Ir/IrO_2.[119, 31] Despite this, Ru and RuO_2 are susceptible to corrosion in acidic media, resulting in the formation of RuO_4 compounds, which can subsequently react further to form various other undesired complexes with the surrounding reactants.[23, 119, 43, 30] Regardless, many have sought to better stabilize RuO_2, mostly through mixing.[6, 154, 142]

2.3 Alternative Alkaline Oxygen Catalysts

Given the high cost and scarcity of Pt and Ir, their long-term commercial application as oxygen catalysts is unsustainable. Recently, efforts to replace Pt and Ir with alternative electrocatalysts, while limited for applications associated with proton-exchange membrane (PEM)-based systems, have rapidly expanded for alkaline-based electrochemical systems due to the large library of materials that are chemically stable at higher pH environments. Although research

on traditional alkaline fuel cells (AFCs), which relied on aqueous KOH electrolyte, have been largely displaced by PEMFCs due to severe durability issues associated with irreversible carbonate degradation,[24, 78] growing interests in modern AFCs that use ionomer-based anion-exchange membranes[91, 254, 253] have consequently revitalized interests in non-Pt ORR/OER catalysts.

2.4 Alkaline ORR/OER

In alkaline media, the reduction of oxygen reaction (direct or series) is now shown as:

$$O_2 + H_2O + 4e^- \rightarrow 4OH^- \qquad \textit{Direct Pathway} \tag{2.2}$$

$$\begin{aligned} O_2 + 2H^+ + 2e^- &\rightarrow 2H_2O_2 \qquad \textit{Series Pathway} \\ H_2O_2 + 2H^+ + 2e^- &\rightarrow 2H_2O \end{aligned} \tag{2.3}$$

Catalytic behavior can drastically change when the pH of the electrolyte increases due to the shift in the working potential, which can affect the rate-limiting mechanisms of ORR and OER.[226] Based on the Nernst equation, the potential shifts by -0.059 V per unit pH with respect to the standard hydrogen electrode (SHE) as the relative concentrations of H^+ and OH^- change. A shift in the working potential can change the local double layer structure and electric field at the electrode/electrolyte interface, affecting the adsorption strengths of charged and uncharged species.[226] For instance, in the case of Pt, the more negative working potential under alkaline conditions lowered the binding energy of the non-reactive support anions, resulting in faster ORR kinetics.[226] Conversely, an acidic environment induced greater surface coverage of adsorbed support anions, reducing the active area and overall catalytic activity.

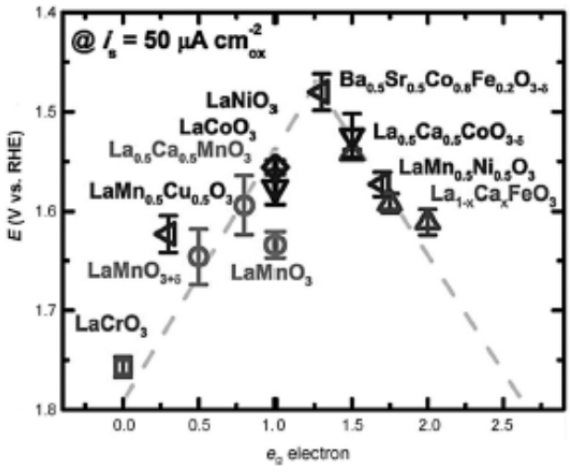

Figure 2.5: Volcano plot fo lanthanum and barium-based perovskites.[81]

2.5 Metal-Oxide Catalysts

Metal oxides represent a major class of materials found in several applications in areas related to energy, electronics, medicine, infrastructure, and aerospace. They exhibit properties that span a wide spectrum due to their high structural complexity, tunability, high degree of mixing, and tolerance for disorder. Among several subclasses of metal oxides include systems that are strongly active for ORR/OER. The subset of potential metal oxide catalysts includes binary oxides (MnO_x, NiO, Co_3O_4)[68, 110, 136], and complex bimetallic oxides with perovskite[283, 81, 238], spinel[122], and pyrochlore[95] structures. For example, select substituted perovskites ($A_{1-x}A_xB_{1-y}BO_3$) (A=La, Ca, Ba; B = Fe, Co, Mn, Ni, Sr, etc.) have been reported as active oxygen catalysts, most notably lanthanum ($LaMO_3$, M=Fe, Co, Mn, Ni, Sr, Ca, etc.) and barium-based ($BaMO_3$, M=Fe, Co, Mn, Ni, Sr, Ca) oxides.[81, 238, 239, 2, 243] Many of these oxides have also demonstrated some degree of cataltyic tunability through doping and defect formation. For instance, Sunitivich et al. demonstrated the catalytic tunability of several La-perovskites based on Sabatiers principle, showcasing the effects of B-site doping on the occupation of the e_g orbital descriptor, identifying optimal activities (volcano plot).[238]

Other oxide catalysts of interest include transition-metal spinels (AB_2O_4). In particular,

cobalt-based spinels such as Co_3O_4, $NiCo_2O_4$, and $Co_xMn_{3-x}O_4$ have received attention for their reportedly strong bifunctional activities.[122, 106] Other notable oxide catalysts include manganese oxide (MnO_x)[92, 195], manganese-containing bimetallic oxide systems and composites[50, 49], and Pb-containing pyrochlores ($A_2B_2O_6O'_x$), most notably $Pb_2Ru_2O_{6.5}$.[95, 97]

Despite some promising features associated with metal oxides, there are some notable limitations. Although many prominent metal oxides show promising catalytic properties for ORR and OER, most have yet to consistently reach the catalytic performance of Pt and Ir. Moreover, with the exception of a few oxides that exhibit some metallic behavior, such as IrO_2 and RuO_2, most oxides are poor electronic conductors. Consequently, most oxides rely on a well-dispersed conductive support such as carbon, though carbon is relatively unstable in alkaline media.[140] Oxide nanoparticles also have a relatively low active surface areas, though maximizing and tuning the specific surface area has been extensively explored through different synthesis methods, yielding particle systems consisting of microspheres, urchin-like, nanowire arrays, rod-like, and 3D hierarchical porous structures.[238] But despite these current set of challenges, metal oxides continue to be one of major areas of interest in catalysis research.

2.6 Bifunctional Catalysts: Oxide Pyrochlores and Mn-Ruthenates

As previously mentioned, this research is centered on two oxide systems that were evaluated as bifunctional catalysts: pyrochlores ($(Bi,Pb)_2(Ir,Ru)_{2-x}(Bi,Pb)_xO_6\ O'_y$), and Mn-doped RuO_2 ($Mn_xRu_{1-x}O_{2-y}$). In particular, $Mn_xRu_{1-x}O_{2-y}$ demonstrated remarkably strong bifunctional activity comparable to Pt for ORR and RuO_2 for OER. Lead (Pb)-iridium (Ir) pyrochlores ($Pb_2Ir_{2-x}Pb_xO_6O'_y$) were evaluated to demonstrate and validate our combinatorial high-throughput methodologies for screening ORR/OER catalytic activity.

2.6.1 Manganese-Ruthenates

We evaluated thin film composition libraries of manganese-ruthenium oxide as bifunctional catalysts using a set of high-throughput electrochemical and characterization techniques. As previously summarized, both MnO_x and RuO_2 are highly active for ORR/OER. RuO_2 is regarded as one of the most active OER catalysts, while different compounds and polymorphs of MnO_x has been widely reported to exhibit bifunctional activity. The combination of both, unsurprisingly, showcased synergistic catalytic enhancements relative to pure RuO_2 and MnO_x (See chapter 5 for manuscript). More specifically, the combination of both materials formed a highly active single-phase $Mn_xRu_{1-x}O_{2-y}$ ($0.02 < x < 0.45$), which has never been previously reported up to this point.

Manganese oxide (MnO_x) is an attractive bifunctional catalyst for its high abundance, low toxicity, and low cost.[110, 127, 22, 29, 68, 173, 234, 221, 163, 276, 45, 275, 28, 21, 50, 92] Previous studies reported promising, but widely disparate activity results based on the different valence states, phase structure, polymorphic structure, composition, and morphology of various MnO_x compounds.[45, 149] For instance, α-Mn_2O_3, MnOOH, Mn_3O_4, and certain polymorphs of MnO_2 have been identified as active ORR catalysts while MnO is comparatively inactive.[127, 146, 128] Cheng et al. describes various structures of pure MnO_2 and their catalytic activities[28] while Gorlin et al. found nanostructured Mn_2O_3 to be particularly active for both ORR and OER. Furthermore, interests in Mn-based catalysts also extend to ternary Mn-metal oxides (spinel, perovskites)[122, 106, 133, 27, 238], Mn-oxide/metal composites[179, 50, 49], and Mn-doped carbon nanomaterials.[250] Li et al. among several others reported highly active cobalt manganese oxide spinel ($CoMn_2O_4$) catalysts deposited on reduced graphene oxide.[122] Physical mixtures of MnO_x with other oxides, carbon nanostructures, and metals (e.g. Pd, Ag)[179] have also been shown to exhibit synergistic enhancements attributed to combinations of dual active sites of the constituent materials, improved electron transfer, and electronic coupling effects.[238]

Ruthenium oxide, which has a tetragonal rutile unit cell structure (Figure S.6), in addition

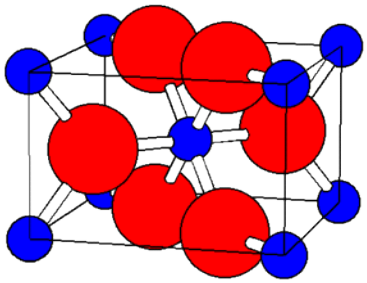

Figure 2.6: Rutile atomic structure. *Saved from https://cbc-wb01x.chemistry.ohio-state.edu/ woodward/ch754/struct/TiO2.htm on 12/04/2017*

to being one of the most active OER catalysts, is one of the few oxides that exhibits metallic behavior.[216] Although RuO_2 is relatively scarce, it is comparatively less expensive than several precious metal catalysts including Pt, Pd, Ir, and Au. Without compromising its catalytic activity and electronic conductivity, there have been interests in using RuO_2 as a host material to different transition metals (e.g. Ni, Co, Fe, Zn)[184, 183, 122]. However, few have studied mixed Mn-Ru oxide as potential bifunctional electrocatalysts.[158, 157, 79, 102] One study not related to catalysis explored Mn as one of the theoretical dopants for stabilizing a high-pressure fluorite-cubic polymorph of RuO_2.[98] However, there is currently no known phase database or reports of an atomically mixed Mn-oxide and RuO_2 system. Jang et al. synthesized and evaluated a physically separated mixture of α-MnO_2 and RuO_2 as evidenced by the distinct set of XRD patterns corresponding to the aforementioned phases.[102] Guo et al. also describes an oxide catalyst system containing γ-MnO_2 and RuO_2 which also showed no evidence of atomic mixing.[79] The absence of any study or phase database on a mixed Mn-Ru oxide system strongly suggests that the two systems are immiscible, which is bolstered by the resulting samples synthesized in Guo and Jangs work. Thus, this system, under certain fabrication methods, yields a likely metastable mixed Mn-doped rutile system.

2.6.2 Pyrochlores

While not as prolific as perovskites and spinels, pyrochlores represent another major oxide system of interest for a number of different applications, including oxygen catalysis. Pyrochlore catalysts were first identified by Dr. Horrowitz et al., who discovered a series of specific compounds ($Bi_2Ru_{2-x}Bi_xO_{7-y}$ and $Pb_2Ru_{2-x}Pb_xO_{7-y}$) and combinations thereof that exhibited remarkably strong catalytic properties for ORR and OER.[95] Consequently, their uniquely tunable structure and catalytic properties continues to spur a consistent output of catalyst research.

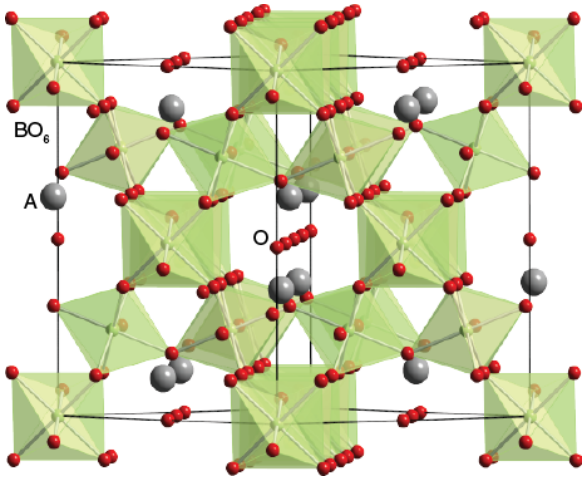

Figure 2.7: Pyrochlore structure ($A_2B_2O_7$). *Saved from http://www.chemtube3d.com/solidstate/SS-Pyrochlore.htm on 12/04/2017*

Pyrochlore Structure

A pyrochlore is a ternary oxide with an ideal formula of $A_2B_2O_7$, belonging to a family of phases iso-structurally based on the $(NaCa)(NbTa)O_6F/OH$ mineral.[236] Figure S.7 shows an illustration of a typical pyrochlore structure. There are around 150 distinct pyrochlore compounds, which are predominantly cubic and ionic in nature. The A-site cations (~1 Å radii), which are generally larger than the B-site cations (~0.6 Å radii), range from rare earth elements to elements with inert lone-pair electrons, while B-site cations range from transition metals to post-transition metals, with oxidation states ranging from +2 to +5.[236] The pyrochlore structure, much like per-

ovskites, has a high tolerance for disorder and defect formation, which includes oxygen vacancies and cation substitution, both of which have been found to affect several material properties.[67] The unit cell of an ideal pyrochlore structure contains 8 compounds (88 atoms) with a cubic space group of Fd3m, and a lattice constant ranging from ~10 to ~11 Å depending on the size of the cationic species, and the degree of disorder due to lattice distortion, cationic substitution, and defect concentration. Pyrochlores contain four crystallographically non-equivalent atomic sites, which includes 2 non-equivalent oxygen anionic sites. To distinguish the 2 anionic sites, many represent the formula as $A_2B_2O_6O'$, illustrating O and O′ as non-equivalent sites. This representation is often convenient for non-stoichiometric pyrochlores containing oxygen vacancies, which are almost exclusively located at the O′ sites within the sublattice.

Many describe the pyrochlore structure as an interpenetrating network of corner sharing BO_6 octahedra and linear A_2O' chains. The structure has a network of 8-fold and 6-fold coordinated oxygen anion polyhedral around each A and B-site, respectively. Others have described the structure as an anion deficient fluorite unit cell.[3] The A-site polyhedral is a scalenohedra (distorted cube), and contains 6 equally spaced O anions and 2 equally spaced O′ anions, which are slightly closer in distance to the A-cation, though the A-O′ and A-O distances are equal if the A-site polyhedra conforms to a cubic coordination. The smaller B-site cations generally have a trigonal antiprism coordination with the O anions, which are equally spaced from the central cations. The B-O-B bond angles are buckled at around 120-140° in contrast to the perovskite's B-O-B angle of 180°, while the A_2O' is a linearly coordinated network to a tetrahedrally shared O′ atoms within the A_2O' network.

To elaborate more on the pyrochlore structure, one previously inferred feature is the variation in the coordination geometry around the A and B-sites depending on the placement of the O-sites within the crystal structure. The distribution of the O-sites is quantified by the x-parameter, which is limited between 0.3125 and 0.375. For instance, at 0.3125, the B-site polyhedra conforms to a perfect octahedral geometry while the A-site polyhedra are distorted to form hexagons of six

O anions, whose plane is perpendicular to the A-O′ axis. For x = 0.375, the A-site polyhedra have a perfect cubic coordination while the B-site polyhedra have a trigonal antiprism geometry. Consequently, both the A-site and B-sites cannot simultaneously have an octahedral coordination and a cubic coordination polyhedral.

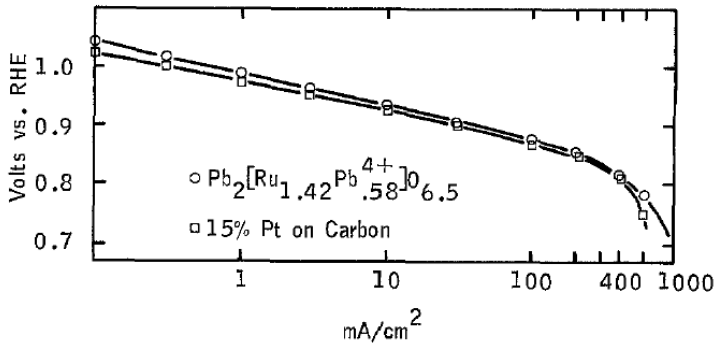

Figure 2.8: Polarization curve comparison between $Pb_2[Ru_{1.42}Pb^{4+}_{0.58}]O_{6.5}$ and 15% Pt on carbon.[95]

Oxygen Catalysis

The most attractive pyrochlore feature is the ability to ostensibly tune a wide range of physical properties due to their high degree of structural distortion, defection formation, and cationic doping, underscoring their substantial application value. For instance, pyrochlores have been shown to be insulating, semiconducting, and even metallic in behavior. Other examples include pyrochlores that are strong refractories, and lanthanide-containing pyrochlores that are fluorescent and phosphorescent. In the case of oxygen catalysis, a series of pyrochlores compounds ($[Pb,Bi]_2[Ru,Ir]_{2-x}[Pb,Bi]O_6O'_y$) have demonstrated strong catalytic activity, as well as high electronic and ionic conductivity, which are enabled by the conductive RuO_6/IrO_6 network, and high oxygen vacancy (O′-sites) concentration, respectively.[277, 240, 190, 186, 144, 135, 95, 97, 60, 51, 48] Consequently, this became one of my major material systems of interest for combinatorial high-throughput electrochemical testing (See Chapter 6).

Initial oxygen catalyst studies on pyrochlores as cathode catalysts for fuel cells were

performed by Horowitz et al. in the early 1980s.[95, 97] He first reported $Bi_2Ru_{2-x}Bi_xO_{7-y}$ and $Pb_2Ru_{2-x}Pb_xO_{7-y}$ as active catalysts for ORR and OER in alkaline conditions.[95, 97], which were synthesized using his patented co-precipitation synthesis method. Figure 5.8 shows a polarization curve of a Pb^{4+}-doped $Pb_2[Ru_{1.42}Pb^{4+}{}_{0.58}]O_{6.5}$, demonstrating slightly better performance compared to a 15 wt.% Pt carbon black mixture.[95] Since then, many have sought to integrate pyrochlores into existing fuel cells systems, often citing $Pb_2Ru_{2-x}Pb_xO_{7-y}$ as being the most active pyrochlore compound.[277, 190, 185] In more specific cases, researchers studied the effects of pyrochlore B-site substitution[277, 96], vacancy concentration[60], and pH[67] on the catalytic activity and mechanistic behaviors. For instance, Goodenough et al. indirectly demonstrated the effects of pH on the oxygen reaction pathways, inferred by the degree of surface protonation measured by the mean surface-charge density, which provided some evidence of changing active sites.[67] For composition, Zen et al. studied the effects of both pH and B-site doping composition of $Pb_2Ru_{2-x}Pb_xO_{7-y}$ and $Bi_2Ru_{2-x}Bi_xO_{7-y}$ on ORR and OER catalytic activity.[277] They found an optimum concentration of x~0.26 for the $Pb_2Ru_{2-x}Pb_xO_{7-y}$, postulating the Ru-O_b-Pb bridging oxygen as the active site under acidic conditions.[277] Although pyrochlores have been shown to suffer stability issues under aqueous acidic conditions, some have reported better chemical stability when bonded to Nafion, or ostensibly any polymer-based proton-exchange membrane.[277, 67]

In this study, we evaluated a Pb-Ir oxide composition spread system, which encompasses the $Pb_2Ir_{2-x}Pb_xO_{7-y}$ compound over a certain composition range, which has also been reported as a fairly activite bifunctional catalyst.[115, 135, 111] Despite the greater economic incentive in evaluating $Pb_2Ru_{2-x}Pb_xO_{7-y}$ due to the lower cost of the constituent materials (Ru and Pb) and the high scarcity of Ir, $Pb_2Ir_{2-x}Pb_xO_{7-y}$, or more broadly a Pb-Ir oxide composition spread, became a suitable sample for study using the available high-throughput electrochemical and characterization methods. Chapter 6 discusses the work done on this material system.

2.7 High-Throughput Electrocatalyst Research

Systematic discovery of new catalyst materials represents an overwhelmingly daunting task given the sheer breadth of existing materials, especially when conventional test methods impose considerable time and resource constraints. Accelerating the process of evaluating new catalyst materials while navigating through nearly limitless material combinations, coupled with their own set of unique structural and chemical properties, highlights the full necessity of employing high-throughput combinatorial techniques as a complementary approach to catalysis research. Initially confined to areas centered on rapid drug testing, high-throughput research has branched off to other scientific disciplines, becoming a major paradigm in experimental and theoretical[72] materials science, most notably for the materials discovery initiative.

Consider a new material system composed of 2 or more compounds. This unknown material may (or may not) yield interesting catalytic properties, which may (or may not) be optimized within a narrow composition band. For a traditional electrochemist, exploring this material′s composition space requires synthesis of separate sample batches that incrementally span a set composition range, which will invariably incur substantial time and energy. Not only is the approach woefully inefficient, the material system in question throughout the measured composition space may turn out to be catalytically inactive, thus completely undercutting the entire effort. In contrast, a high-throughput approach facilitates rapid synthesis of sample forms comprised of material combinations that span highly resolved and wide-ranging composition libraries (e.g. composition spreads, discrete material libraries). These composition libraries undergo modified electrochemical techniques designed to simultaneously or serially measure the catalytic activity of the entire library, identifying the most active compositions. Unsurprisingly, high-throughput electrochemistry has become an effective and crucial approach to screening and discovering new catalyst materials.[152, 187, 213, 162]

2.7.1 High-Throughput Synthesis

There are several approaches to synthesizing material systems conducive to high-throughput electrochemical testing.[152] While high-throughput research is broadly applicable to material libraries distinguished by one or multiple parameter(s) (e.g. composition, grain size, particle size, film thickness, defect concentration, etc.), the bulk of combinatorial research centers on composition libraries, where new material combinations are concieved and synthesized, with composition being the primary tunable parameter. Thus, various combinatorial sample forms have been explored, including powders, liquids, thin films, and bulk materials.

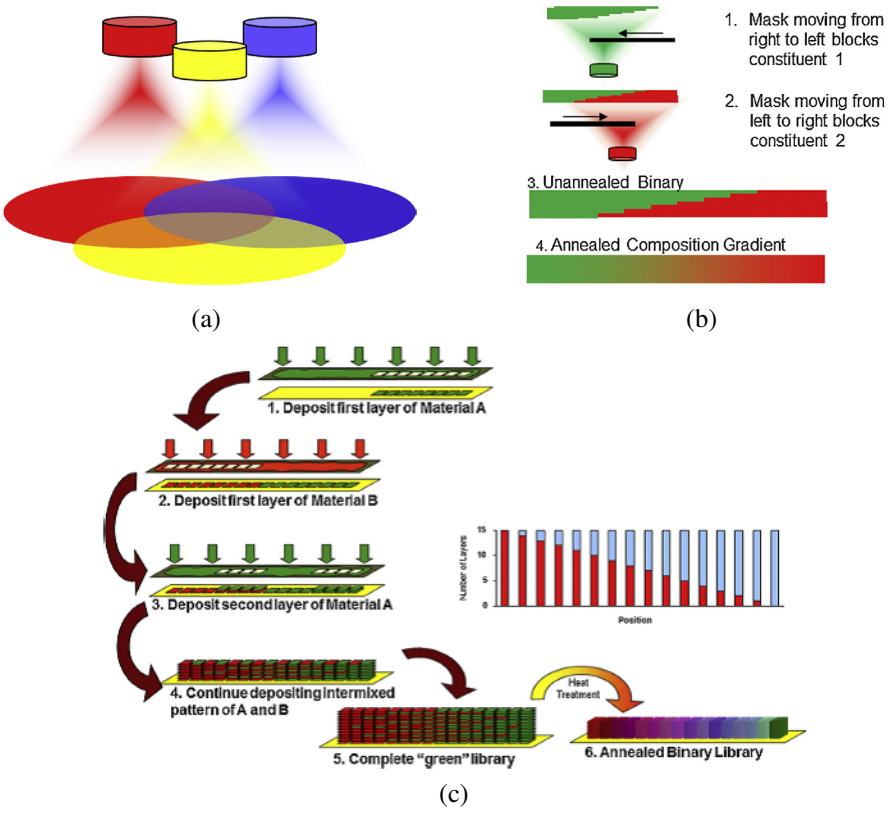

Figure 2.9: Composition spreads fabricated from (a) co-sputtering, (b) pulsed laser deposiition. (c) Discrete binary composition library fabricated from shadow masks.[152]

For thin films, several known techniques have been used to create composition libraries, including co-sputtering, pulsed laser deposition (PLD), evaporation, and chemical vapor deposition (CVD). One common sample form is a composition spread thin film, where the entire

film is composed of an intermixed system with a continuous composition gradient across the substrate.[152, 76, 74] One of the more common ways to fabricate composition spreads is co-sputtering (Figure 4.9a) from multiple sources simultaneously onto a single substrate. The formation of the composition gradient is facilitated by the configuration of the sputter sources, which are oriented in a manner that ensures non-uniform deposition across the substrate. Another method involves PLD, where deposition is achieved using a high-powered excimer laser. Some PLD systems have a dual excimer laser system to facilitate simultaneous deposition, but most systems are limited to sequential deposition (Figure 4.9b) accompanied by moveable masks designed to create thickness wedges.[152] Another method that is worth mentioning is evaporation from multiple sources using shadow masks to create that spatially uneven deposition.[152] One of the major benefits of evaporation relative to co-sputtering is greater control of the deposition conditions.

In addition to composition spreads, sample forms may be comprised of an array of discrete composition libraries, which are formed using specially designed masks. For instance, figure 4.9c shows a discrete binary composition library synthesized sequentially using a series of shadow masks. Fabricating discrete libraries is most commonly achieved through liquid deposition from inkjet printing or pipettes due to their relatively low cost and simple implementation.[193, 211, 205] The liquid medium renders an intimate mixture between constituent precursors, which crystallize in conjunction with full evaporation annealing. These approaches are generally applicable to a wide range of materials, even metal oxides.[132, 120]

2.7.2 High-throughput Electrochemical Testing

Since the adoption of high-throughput electrochemistry, there have been a number of ingenious cell designs built either for serial or parallel catalytic screening. For parallel screening, optical electrochemical techniques have become the popular method for measuring cataltyic activities of various known electrochemical processes, including methanol, hydrogen, and ethanol

oxidation; oxygen reduction and evolution; and photocatalytic.[76, 193, 130, 63] Moreover, optical screening was one of the flagship techniques within the van Dover laboratory, used by many of the previous graduate students.[182, 242, 77] Optical screening, which will be discussed in greater detail in Chapter 3, incorporates an indicator that fluoresces under a certain chemical process within the diffusion layer of the sample surface. The fluorescence is then captured by a CCD camera, spatially resolving areas of high catalytic activity depending on the lifetime and intensity of the fluorescence. Smotkin and Mallouk pioneered this clever way of capturing catalysis-activated fluorescence using a quinine compound as the indicator, demonstrating its utility on several active materials for methanol oxidation.[193]

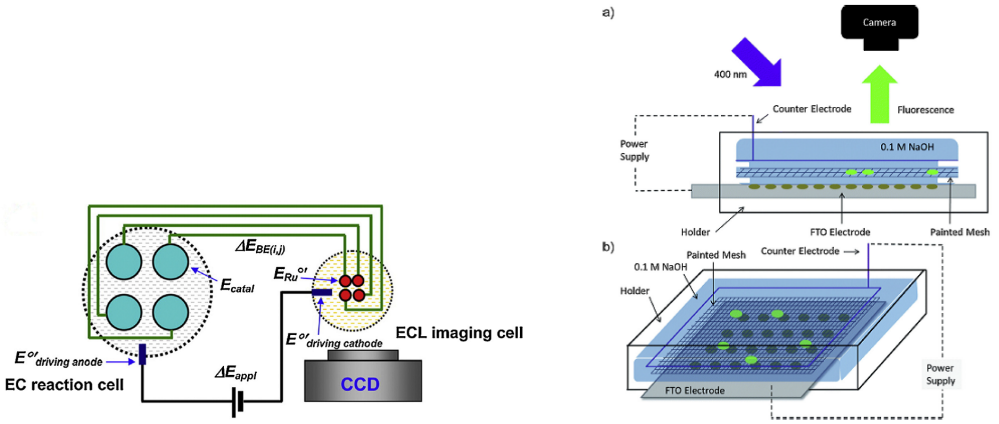

(a) (b)

Figure 2.10: Combinatorial fluorescence test for oxgyen evolution catalysis.[63, 64]

Another variation of fluorescence, particularly for ORR imaging, captures electrochemiluminescence (ECL) at the anode to image the anodic currents in response to the reduction reaction at the cathode array.[130] They measured the ECL intensity of an array of Pt anodes submerged in electrolyte mixed with a Ru(II)+tripropylamine complex. Figure 4.10a shows the array of ORR catalysts coated on glassy carbon, each connected to a Pt anode. At an overpotential within the mass-transport-limited cathodic regime, the ECL intensity of the anode array is measured and contrasted by a CCD camera. Other researchers have used fluorescence to spatially resolve oxygen evolution catalysis.[63, 64] In one study, Gerken et al. employed a stainless steel mesh situated parallel to the catalyst array, which were deposited onto conductive FTO coated glass. The mesh,

which was coated with a special paint used to visualize the air flow across the aerodynamic surfaces, contained a fluorescence compound sensitive to oxygen (Figure 4.10b).

One of the major challenges with electrochemical fluorescence is measuring in analyte with a narrow and near-neutral pH window. This is problematic for most catalysts, because a neutral pH is not applicable to real systems (i.e. fuel cells, batteries), which operate under more extreme conditions (high or low pH). Moreover, catalytic reaction pathways have been known to change when transitioning from acidic to basic conditions, resulting in disparities in catalytic activity between high and low pH. Thus, a particular catalyst library, while highly active under a fluorescence test, may ostensibly be less active when incorporated into a lower pH environment, such as a PEM fuel cell.

Non-fluorescent optical methods have also been explored. For instance, Fosdick et al. evaluated ORR and HER catalysis of inkjet printed catalyst libraries by measuring the degree of dissolution of Cr micro-bands, which dissolve under anodic potentials that are dependent on the cathodic loading of the catalyst.[58, 57] The number of micro-bands dissolved corresponded to how active the catalyst is. For OER, Xiang et al. used a camcorder to measure and record the oxygen bubbles evolving from the catalyst library, which he demonstrated on a (Ni-Fe-Co)O_x library.[273]

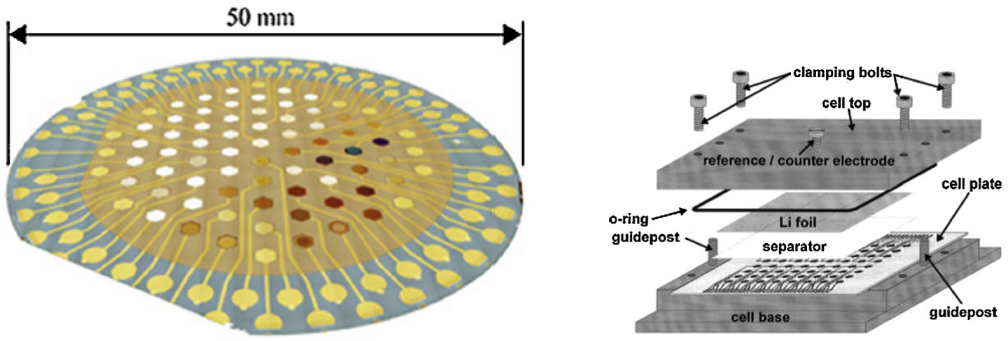

(a) (b)

Figure 2.11: (a) Multi-electrode array for oxygen reduction.[36] (b) Multi-electrode cathode array for lithium-ion batteries.[39, 56]

Another common parallel cell designed is a multi-electrode array connected to a multi-channel potentiostat (Figure 4.11a).[36] In general, these methods offer a more quantitative approach to catalysis screening. The cell design generally consists of discrete composiition libraries deposited onto and array of conductve pads, which can be tested independently as isolated cells, or simultaneously within a common electrolyte. Several catalyst researchers have adopted some form of the multi-electrode array design.[35, 280, 88] For instance, Dahn et al. designed a multi-electrode array of sputtered cathode materials for Li-batteries (Figure 4.11b).[39, 56] Overall, the full discussion of parallel screening, optical and non-optical, is well beyond the necessary scope of this thesis. The examples that were briefly discussed still represent a relatively small subset of high-throughput electrochemical techniques.[228, 268, 269, 244, 206, 89, 233]

Serial methods are another popular approach to high-throughput catalytic screening. Currently, the two most prominent methods include scanning electrochemical microscopy (SECM) and scanning droplet cells. These methods involve automated scanning of ultra-micro electrode (UME) probes across a sample surface. For SECM, the entire library is immersed in electrolyte, while the electrolyte in the droplet cell is locally contained around the electrode probes.

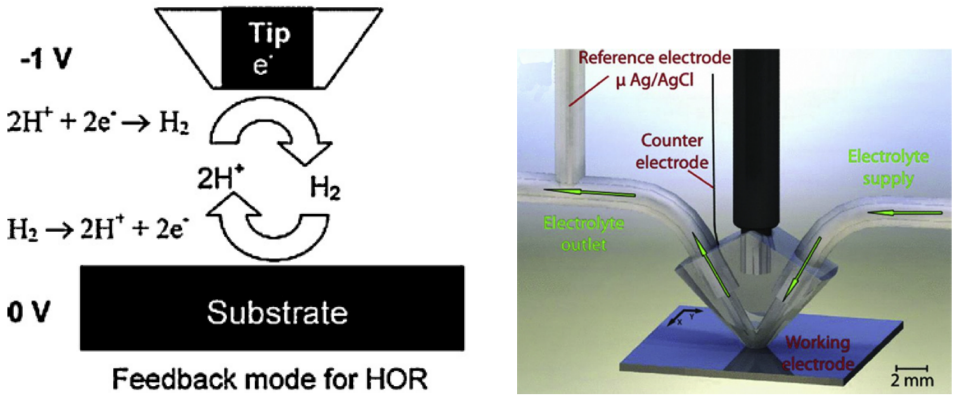

(a) (b)

Figure 2.12: SECM feedback model for hydrogen oxidation reaction (HOR).[137] (b) Three-electrode droplet cell.[134]

In SECM, electrochemical currents are locally measured using a moveable ultra-micro electrode (UME) tip that is scanned across the sample surface while the entire sample is im-

mersed in electrolyte. This method has been used in studies related to ORR[55], HOR[103], and OER[155], rendering high-resolution activity maps of the entire catalyst library. One common mechanism for SECM is the feedback mode (Figure 4.12).[137, 134] For instance, when screening hydrogen oxidation reaction (HER) catalysis, a UME tip hovers above the substrate, which is maintained at a potential of 0 V (vs. RHE), while the tip is held at a potential within the diffusion-limited regime for HER.[137] The evolved hydrogen from the UME tip diffuses toward the substrate, subsequently oxidizing into protons, which in turn diffuse back to the probe, reducing back to hydrogen. The added reduction current quantifies the HER activity of the local surface. The feedback mode is similarly used for ORR catalysis studies, where the UME probe generates oxygen, which then reduces at the substrate surface.[134] The difference in this case is that the current is directly measured at the substrate.

One of the major limitations with SECM is subjecting the entire catalyst library to analyte solution, which may chemically change the surface over time, especially if the entire test takes several hours. Thus, the droplet cell design deviates from SECM by having the electrolyte contained around the probe and locally interfaced with the measured surface (Figure 4.12. For example, a droplet cell designed may consist of a three-electrode cell within a microliter volume of electrolyte, which can be measured and refreshed at any given time.[134] When the setup is fully automated, it becomes a powerfully versatile tool for measuring catalysis across several composition libraries, discrete or continuous.

2.8 Closing Summary

This research centers on addressing the major kinetic limitations of oxygen reduction and evolution. Both reactions are major performance inhibitors, and currently employed commercial catalysts constitute a major fraction of the overall cost of fuel cells, air batteries, and electrolyzers. Active research on suitable oxygen catalysts for both acidic and alkaline systems has spawned sev-

eral studies on unique catalyst systems that either minimizes Pt and Ir-loading, or eliminate them altogether. These alternative catalysts span a wide spectrum of material classes such as non-Pt metals, composites, doped-carbon nanomaterials, and metal oxides. In this study, we focused on discovering new and unique metal oxide catalysts through the application of various high-throughput electrochemical techniques. Most notably, we extensively evaluated two unique oxide systems: a mixed Mn-Ru oxide, which exhibits remarkably strong catalytic properties, and Pb-Ir oxide, which became a suitable system for demonstrating the arsenal of modified and standard electrochemical and characterization techniques available at Cornell. Lastly, this work demonstrates the proven utility of high-throughput electrochemistry for the rapid discovery of new catalysts materials synthesized from modified deposition methods for creating composition libraries, which were then subjected to a variety of electrochemical techniques derived from well-designed parallel and/or serial test methods.

CHAPTER 3

ELECTROCHEMICAL TECHNIQUES

3.1 Introduction

A well-designed, well-controlled electrochemical system is crucial for acquiring accurate and reproducible information regarding the underlying factors that govern electrochemical behavior. While there are several different electrochemical techniques (e.g. chronoamperometry, cyclic voltammetry, rotating disk electrode, electrochemical impedance, etc.) that serve to analyze different processes, they broadly share the same basic experimental setup, which consists of a core test apparatus (electrochemical cell) connected to a potentiostat that both perturbs and measures the cell output (i.e. current, potential). Whether the test cell is operating under galvanic or electrolytic conditions, the controlled output reveals qualitative and quantitative information regarding the behavior of faradaic (e.g. redox concentration, reaction kinetic parameters, pseudo-capacitance), non-faradaic (e.g. double-layer charging, specific and non-specific adsorption, capacitance, etc.), and mass-transport (e.g. diffusion, migration, convection) processes. This chapter will therefore discuss the basic test setup for an experimental cell, along with a brief summary of the most common standard electrochemical techniques. Most importantly, this chapter will detail the custom-built test cells and modified electrochemical techniques that were developed within the van Dover laboratory by which we utilize high-throughput testing.

3.2 Experimental Electrochemical Cell

The prototypical electrochemical cell consists of two electrodes (i.e. anode, cathode) separated by ionically conductive electrolyte (See Appendix I). The thermodynamic state (Nernst equation) of an electrochemical cell is controlled by the potential difference between the two elec-

trodes. Thus, deviating from the equilibrium potential will electrochemically drive the cell to reach a new chemical state through faradaic and/or non-faradaic processes. Experimental cells are generally designed as half-cells with a designated working electrode (WE) and reference electrode (RE). During an experiment, the applied potential is measured and controlled by the WE against the fixed potential of the RE. Accordingly, electrochemical behavior is measured at the WE/electrolyte interface.

The RE functions as a fixed reference point to the WE by maintaining a fixed potential that's stable over a wide WE potential range, with little potential drift during the passage of current across the RE/electrolyte interface (ideally non-polarizable). The standard RE is known as the standard hydrogen (H_2) electrode (SHE). The SHE refers to the following hydrogen redox half-reaction:

$$2H^+(aqs) + 2e^- \rightleftharpoons H_2 \tag{3.1}$$

Although SHE has an absolute potential of 4.44 ± 0.02 V at 25 °C [7, 284], its formal potential E^0 is designated as zero to establish a practical potential scale.

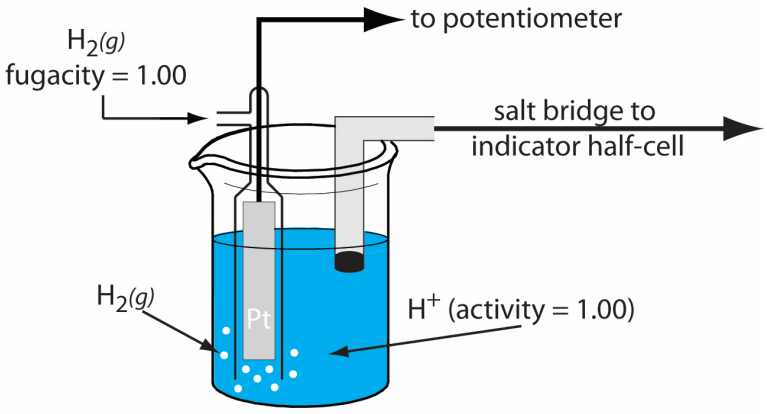

Figure 3.1: An illustration of an normal hydrogen electrode (NHE), consisting of platinum dipped in acidic solution. The concentration of H^+ and fugacity of H_2 are at their standard states ($E=E^0=0$). Taken from URL: https://chem.libretexts.org/LibreTexts/Northeastern/ on 09/27/2017.

In practice, the SHE represents a more theoretical RE rather than a phyical one. A physical setup that approaches the SHE scale is known as the normal hydrogen electrode (NHE), which

Reference	**Materials**	**Reaction**	**Potential (V vs. NHE) @ 25 °C**
Calomel (SCE)	Hg/Hg_2Cl_2, KCl (sat'd)	$Hg_2Cl_2 + 2e^- \rightleftharpoons 2Hg(liq) + 2Cl^-$	0.241
Silver/Silver Chloride	Ag/AgCl, KCl (sat'd)	$AgCl + e^- \rightleftharpoons Ag(s) + Cl^-$	0.197
Mercury/Mercury Oxide	Hg/HgO, NaOH (1M)	$HgO + H_2O + 2e^- \rightleftharpoons Hg + 2OH^-$	0.140
Silver/Silver Sulfate	Ag/Ag_2SO_4, H_2SO_4 (1M)	$Ag_2SO_4 + 2e^- \rightleftharpoons 2Ag(s) + SO_4^{2-}$	0.710
Hydrogen	H^+/H_2, Acid (1M)	$2H^+ + 2e^- \rightleftharpoons H_2(g)$	0

Table 3.1: Common reference electrodes

consists of a large area platinum metal electrode, one of the most active catalysts for H_2 reduction/oxidation, immersed in 1M acidic aqueous solution with H_2 bubbled near it; both the H_2 fugacity and H^+ ion concentration maintains standard activities, respectively (See Figure S.1). The subtle difference between SHE and NHE is related to the difference in ionic behavior within the electrolyte. More specifically, the SHE solution assumes that the H^+ does not interact with other ions, which is not tenable for concentrated systems. Another practical scale is the reversible hydrogen electrode (RHE), which is pH independent by theoretically matching the pH of the electrolyte that interfaces with the WE. The RHE scale can be quantitatively converted from the NHE scale by -59 mV/pH.

Table 8.1 shows a list of common RE materials with fixed potentials measured against the NHE. These systems are known for their stability over a wide applied potential range. One common RE that was used extensively in this work is a silver/silver chloride (Ag/AgCl), which consists of a solid Ag coated with AgCl and immersed in potassium chloride (KCl) solution. The

concentration of KCl affects the measured potential value vs. NHE, thus, most KCl solutions are saturated to remove ambiguity regarding its potential (0.197 V vs. NHE). Regardless of which RE is used during an experiment, potentials can be adjusted to a different scale. For instance, the measured potential vs. a saturated Ag/AgCl RE can be converted into the SHE scale by offsetting the measured potentials by 0.197 V (not counting any pH correction).

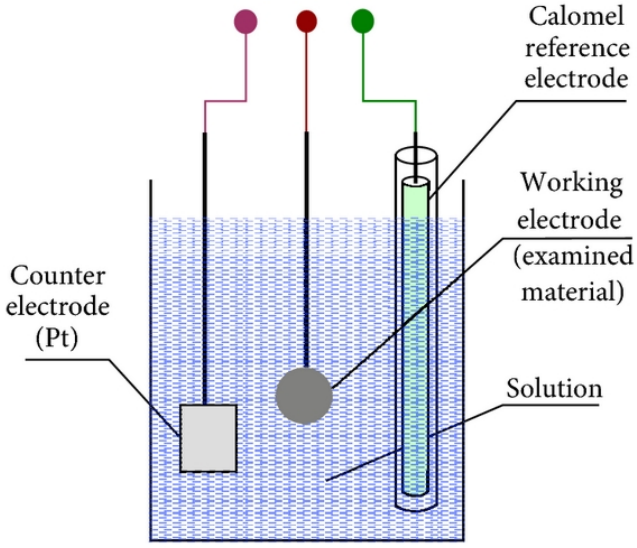

Figure 3.2: A three-electrode configured cell.[192]

3.2.1 Three-Electrode Cell

One of the major challenges with a two-electrode cell is the possible drift in the RE potential during an experiment due to the passage of high currents across the RE/electrolyte interface. This convolutes the potential measurement, negating the primary function of the RE. Moreover, the electrochemical output at the WE is limited by the kinetics of the counter-reaction at the RE. Thus, many experimental cells are equipped with an additional high surface-area auxiliary electrode, or counter electrode (CE), which is situated near the WE to function as a current collector in order to balance the output of the WE. The potential between the WE and CE varys to compensate the charge-transfer that counters the current across the WE. Consequently, the WE current is

no longer limited by the counter current across the RE since the output. Moreover, any faradaic activity across the RE is now minimized, reducing issues associated with potential drift. The three-electrode setup is often the preferred configuration for voltammetry-based measurements, where the focus is on measuring the electrode processes at the WE. However, a two-electrode setup can be sufficient if the measured current is very low (~1-10 nA or μA)[7], which is achieved with microelectrodes.

3.2.2 Uncompensated Resistance

A common challenge that must be factored into the design of an experimental cell, especially if the current outputs are high, is minimizing uncompensated resistance (UR), which represents energy loss from an unaccounted Ohmic (i.e. $E_u = iR_u$) drop across the cell. The potential drop due to UR is a linear function of both current output and the resistivity of the electrolyte ($R_u = \rho L/A$). Not only does the iR_u drop increase with current, the overall resistance across the electrolyte increases with distance between the WE and RE. If not properly corrected, UR can significantly decrease the accuracy of the measured applied potential.

$$E_{Measured} = E_{Cell} + iR_u \tag{3.2}$$

For instance, during a linear voltammetry scan in which the potential changes at a constant rate, the actual cell potential versus time can deviate from the expected linear progression as the iR_u changes with the measured current output. Additionally, high UR can also cause significant potential lag due to non-instantaneous capacitive effects from electrode charging/discharging, which has a time constant of R_uC_l. This induces greater error at faster scan speeds.

$$E_{Actual} = E_{Applied}\left(1 - e^{\frac{-t}{R_\Omega C_l}}\right) \tag{3.3}$$

While not trivial, UR can be corrected if the resistance of the electrolyte is properly measured using some form of electrochemical impedance techniques, typically in supporting electrolyte without the presence of analyte. A common way of reducing UR is by increasing the concentration of non-reactive supporting ions within the electrolyte, which effectively reduces the migration path length when the cell is perturbed. Another way to reduce UR is placing the RE close to the WE, thereby reducing the overall resistance drop across the electrolyte. Operating at low currents ($\sim$ 1-10 nA or μA) will also reduce iR_u, which is generally the case when measuring with ultra-micro electrodes (UME).

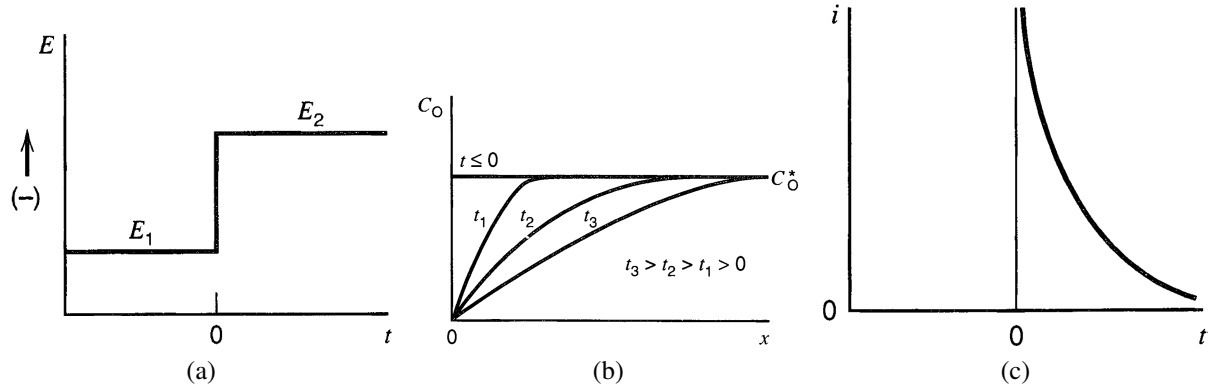

Figure 3.3: (a) The potential step curve. (b) Transient concentration, C_O, gradient over time, t. (c) Current vs. time.[7]

$$O + e^- \rightleftharpoons R \tag{3.4}$$

3.3 Chronoamperometry

The most fundamental electrochemical technique is chronoamperometry, which measures the cell current as a function of time when the perturbed to a fixed potential. Figure S.3 illustrates chronoamperometry of a simple facile redox reaction (Eq. A.4), where the output current is fully governed by diffusion. Consider the response of an initially static electrochemical system that

is instantaneously changed from an initial potential, E_1, to a more negative potential, E_2 (Figure S.3a). The cell becomes immediately perturbed, resulting in the reduction of O species to R. Consequently, the surface concentration, C_O, immediately depletes, creating a transient composition gradient relative to the bulk, C_O^*. There is an immediate spike in the reduction current, which decays as the flux of O decreases due to the change in the concentration gradient over time (Figure S.3c).

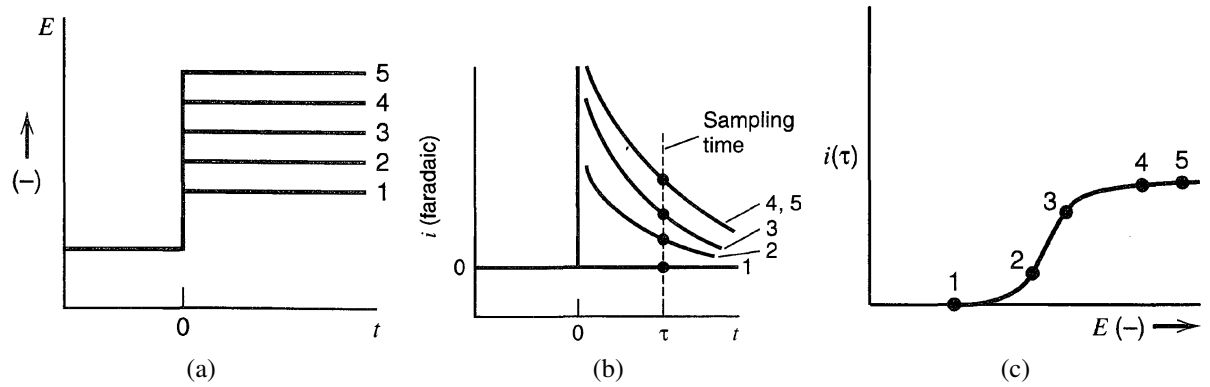

Figure 3.4: (a) Series potential steps. (b) Series current-time curves. (c) i vs. potential half-wave at time τ.[7]

3.4 Sample-Current Voltammetry

In practice, a more complete experiment involves multiple chronoamperometry measurements at multiple potentials, which are incrementally changed over a defined range. This is known as sample-current voltammetry (SCV). Consider the behavior of the cell (Figure S.4) when multiple chronoamperometry measurements are made at increasingly more negative potentials (Figure S.4a), which in this case is near the formal potential, $E^{0'}$. When the current-time curves are sampled at a set time, τ, along the current-time curves (Figure S.4b), we generate a current-potential plot that resolves a half-wave reduction curve (Figure S.4c). The measured points along the half-wave curve illustrate the different regimes corresponding to the extent of the reduction reaction. For instance, the first change in the potential, E_1, is not negative enough to drive the reaction to-

wards reduction, thus, no faradaic current is observed. Conversely, at a very negative potential, E_5, the surface concentration, C_O, fully depletes to zero, yielding a mass-transport limit on the current-time decay. Similarly, E_4 is still within the mass-transport limit regime, thus, the reduction current follows the same time-decay as E_5. At intermediate potentials, E_2 and E_3, the driving force for reduction is not enough to deplete C_O to zero at the electrode, resulting in lower outputs over time. Both still exhibit current-time decay due to the changing composition gradient transient.

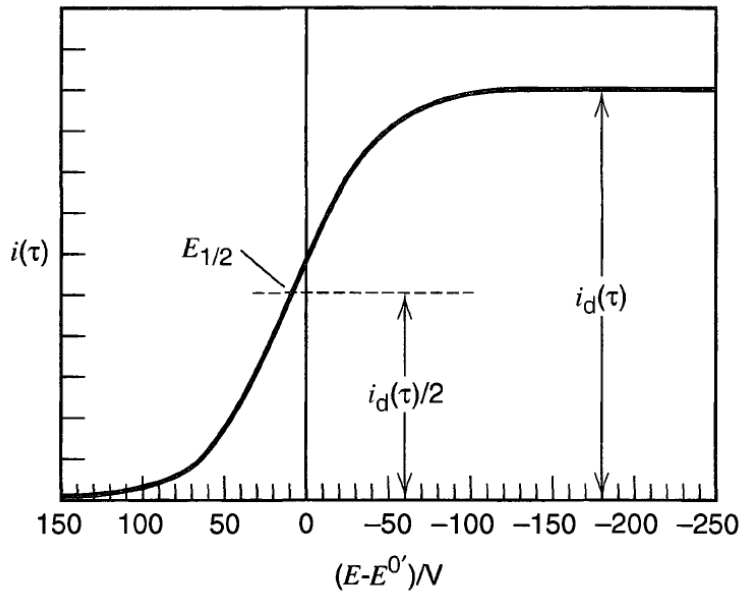

Figure 3.5: Current-potential half-wave of a Nernstian reaction.[7]

3.4.1 Current-Potential Half-Wave

The shape, position, and amplitude of the half-wave curve provides quantitative information regarding the thermodynamics, reversibility, integrated charge-transfer, mass-transport, and kinetics of the reaction. The simplest case is a Nernstian reaction (Figure S.5), which has a half-wave governed by the following equation:

$$E = E_{1/2} + \frac{RT}{nF} ln\left(\frac{i_d(\tau) - i(\tau)}{i_d(\tau)}\right) \tag{3.5}$$

The potential is dependent on the current, i, and the mass-transported limited current, i_d. The half-wave potential, $E_{1/2}$, the potential by which $i(\tau) = i_d/2$, is dependent on the mass-transport properties of the redox species.

$$E_{1/2} = E^{0'} + \frac{RT}{nF} ln\left(\frac{D_R^{1/2}}{D_O^{1/2}}\right) \tag{3.6}$$

These equations, however, do not apply to more complex systems that involve multi-step, quasireversible or irreversible reactions. Qualitatively, deviations from Nernstian behavior are most apparent by the potential shift of the half-wave curve relative to $E^{0'}$. In general, outputs that are limited by the reaction kinetics, as opposed just mass-transport, are now governed by the kinetic parameters of the reaction (Butler-Volmer equation) (See Appendix I) in conjunction with Ficks laws of diffusion.

3.4.2 Cottrell Equation

The features of the time-dependent decay in redox current also provides quantitative information regarding the kinetics (reaction, mass-transport) of the redox. Consider an expression for the mass-transport limited reduction current, i_d, as a function of time. Lets presume a simple planar electrode, which simplifies the derivation by employing a semi-infinite linear diffusion model. Recall the simple equation for Fick's second law of diffusion.

$$\frac{\partial C_O(x,t)}{\partial t} = D_O \frac{\partial^2 C_O(x,t)}{\partial x^2} \tag{3.7}$$

The boundary conditions assumes an initial bulk concentration of C_O*. As soon as the reduction potential is applied at $t > 0$ (assuming no lag in the potential response), the surface concentration, $C_O(0,t)$, immediately goes to zero.

$$
\begin{aligned}
C_O(x,t) &= C_O^* \\
\lim_{x\to\infty} C_O(x,t) &= C_O^* \\
C_O(0,t) &= O \ \ (t>0)
\end{aligned}
\tag{3.8}
$$

Using general mathematical techniques such as Laplace transformation, we determine the flux equation, which is directly proportional to the redox current.

$$
J_O(0,t) = -\frac{i(t)}{nFA} = -D_O\left[\frac{\partial C_O(x,t)}{\partial x}\right]_{x=0} \tag{3.9}
$$

Consequently, a closed-form equation for the current-time curve is represented as:

$$
i(t) = i_d(t) = \frac{nFAD_O^{1/2}C_O^*}{(\pi t)^{1/2}} \tag{3.10}
$$

This is known as the Cottrell equation, though variations of this equation exist depending on the boundary conditions. It is important to note that the Cottrell equation is derived from a reaction in which mass-transport is the rate-limiting process. However, this equation still holds for any system that is perturbed at a potential well within the mass-transport limited regime, regardless of whether the reaction is Nernstian, irreversible, or quasireversible. Thus, at intermediate potentials where $C_O(0,t)$ is non-zero ($i < i_d$) the Cottrell equation must be modified by the inclusion of the scale factor, $1/(1+\xi\theta)$.

3.5 Fundamentals of Linear Scan Voltammetry

Both chronoamperometry and sampled-current voltammetry are limited when it concerns applications that require a more systematic approach to analyzing known and unknown electrochemical systems, particularly when spanning a system over a wide potential window without any

preexisting knowledge of active redox processes. This leads to another common type of voltammetry technique by which the current output is measured over a continuously changing potential. This method is commonly known as linear sweep voltammetry (LSV), or cyclic voltammetry (CV) when the potential continuously sweeps back and forth within a set potential window. Both methods traverse a wider current-time-potential domain, providing qualitative information regarding several electrochemical behaviors, including the nature of the redox reactions and non-faradaic charging.

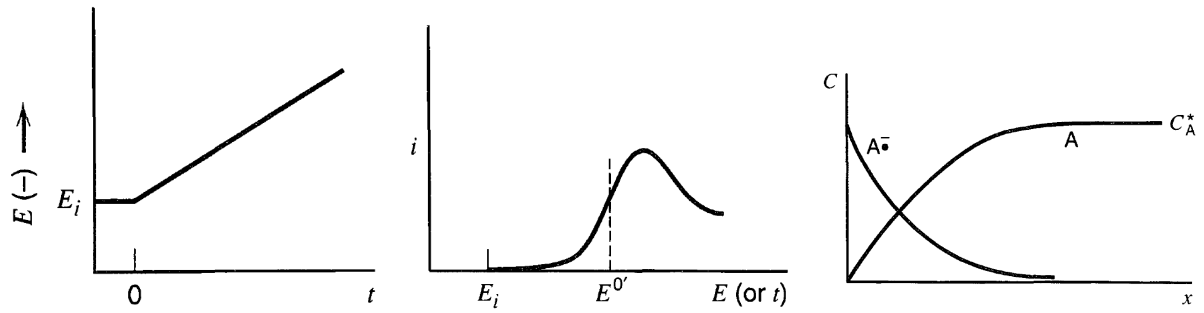

(a) (b) (c)

Figure 3.6: (a) Linear potential scan step. (b) Current vs. potential at a constant scan rate. (c) Concentration of A and A^{-}* at mass transport-limit.[7]

Consider the LSV of an electrochemical cell containing anthracene (represented as A and A^{*-}), a compound that can reversibly reduce to its negative anionic radical counterpart, as illustrated by Figure S.6. In this example, the potential is linearly negatively swept at a constant sweep rate, driving the reaction towards reduction. Near the formal potential, $E^{0'}$, the negative potential sweep resolves a cathodic peak corresponding to the increasing flux in anthracene reduction, causing the surface concentration to decrease before fully depleting. At the point of depletion, the cathodic curve reaches a peak corresponding to the mass-transport limit. Although the above figures do not showcase this behavior, many LSV and CV curves often show a flat, non-zero baseline current, which corresponds to capacitive non-faradaic charging due to the adsorption of ionic species. The superimposition of the redox peaks and the charging current is a summed effect. Thus, a well-defined baseline can be easily subtracted from the measured peak, though this is not always the case for many systems.

In contrast to the typical I-V behavior of sample-current voltammetry, deriving an expression for LSV behavior is far more complicated. Thus, going through the derivation steps involving numerical solutions is well beyond the scope of this thesis, and the reader is encouraged to read the Faulkner textbook (Chapter 6) to see the full mathematical treatment.[7] Regardless, LSV provides a wealth of qualitative information regarding double-layer effects and redox behavior. Moreover, techniques such as rotating disk electrode (RDE), which are LSV scans that operate on a well-defined, steady-state analyte flow model across the working electrode, can yield highly quantitative information (more on RDE within a later section).

3.5.1 Peak Current and Potential

Despite the absence of a closed-formed expression that generalizes LSV behavior, particularly the current output as a function of potential and time, there are explicit equations for both the redox peak current, i_p, and the double-layer current, i_c, as functions of the potential sweep rate, υ. They are of course mostly applicable to more contrived systems that exhibit Nernstian behavior governed by a semi-infinite linear diffusion model.

$$i_p = (2.69 \times 10^5) n^{3/2} A D_O^{1/2} C_O^* \upsilon^{1/2} \tag{3.11}$$

$$|i_c| = A C_d \upsilon \tag{3.12}$$

The peak current (i_p) corresponding to a Nernstian faradaic process (in this case reduction) at 25 °C is a function of the active surface area, A, diffusion coefficient, D_O, bulk concentration, C_O*, electron transfer number, n, and $^{1/2}$. The double-layer current, i_c is linearly dependent on υ, as well as the double-layer capacitance, C_d. The ratio of both equations becomes:

$$\frac{|i_c|}{i_p} = \frac{C_d \upsilon^{1/2}(10^{-}5)}{2.69 n^{3/2} D_O^{1/2} C_O^*} \tag{3.13}$$

This ratio shows how the LSV peak relative to the baseline double-layer current is affected by the scan rate υ. For instance, i_p is amplified relative to i_c when υ decreases. Conversely, by increasing υ, the rate at which i_c increases overshadows the increase in i_p, reducing the intensity of the peak realtive to the double-layer. Thus, it is common practice to perform LSV measurements at very low scan rates in order to minimize the double-layer.

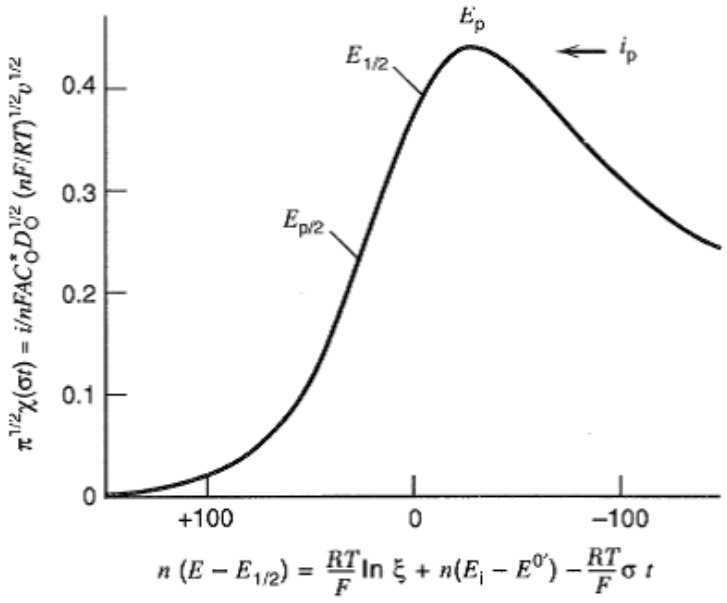

Figure 3.7: Linear scan voltammetry curve of a Nernstian reaction.[7]

The redox peak potential, E_p, for a Nernstian reaction is independent of ν. Additionally, the half-peak potential, $E_p/2$, at $i_p/2$, is a function of $E_{1/2}$ (recall Eq. A.6).

$$E_p = E_{1/2} - 1.109\frac{RT}{nF} = \frac{28.5}{n}\,mV \;\; (at\,25\,^{\circ}C) \tag{3.14}$$

$$E_{p/2} = E_{1/2} + 1.09\frac{RT}{nF} = E_{p/2} + \frac{28.0}{n}\,mV \;\; (at\,25\,^{\circ}C) \tag{3.15}$$

$$|E_p - E_{p/2}| = 2.20\frac{RT}{nF} = \frac{56.5}{n}\,mV \;\; (at\,25\,^{\circ}C) \tag{3.16}$$

We see that regardless of the peak current and scan rate, E_p-$E_p/2$ is only a function of n at a given temperature. For instance, the E_p-$E_p/2$ for a 1-electron reaction at 25 °C is 56.5 mV.

3.5.2 Irreversible and Quasireversible Reactions

Whether a reaction is reversible, quasireversible, or completely irreversible, the general relationship between i_p with υstill holds. For example, Equation A.11 for an irreversible system is modified as:

$$i_p = (2.99 \times 10^5)\alpha^{1/2} A D_O^{1/2} C_O^* \upsilon^{1/2} \tag{3.17}$$

The charge transfer coefficient, α, is a kinetic parameter that that quantifies the properties of the kinetic barrier (See Appendix I) for a given reaction. Unlike the peak potential for a Nernstian process, E_p for an irreversible or quasireversible system is now a function of υ, the intrinsic rate constant, k^0, and α.

$$E_p = E^{0'} - \frac{RT}{\alpha F}\left[0.780 + ln\left(\frac{D_O^{1/2}}{k^0}\right) + ln\left(\frac{\alpha F \upsilon}{RT}\right)^{1/2}\right] \tag{3.18}$$

Consequently, we see that for high sweep rates, coupled with sluggish reaction rates (low k^0), the peak potential shifts away from $E^{0'}$, resulting in a greater overpotential near the onset of current.

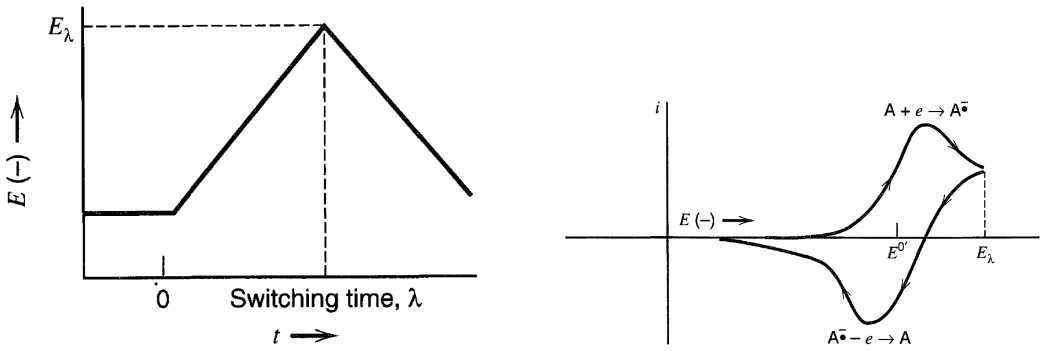

Figure 3.8: (a) Cyclic potential window. (b) Cyclic voltammogram redox couple.[7]

3.6 Cyclic Voltammetry

Consider now the response when the potential is reversed upon the reduction of anthracene, A (Figure 5.8). The accumulated anionic radical anthracene, A^{*-}, oxidizes back to A, generating a positive anodic peak. As a result, the hysteresis resolves two opposing peaks corresponding to the anthracene redox couple. This extension of LSV, where the potential is continuously cycled within a set potential window, is known as cyclic voltammetry (CV). The shape, location, and separation of the peaks provide qualitative information regarding the reversibility and kinetics of the redox couple.

Figure 4.9 shows a typical CV of a redox couple superimposed with a baseline double-layer current. In response to the sweep rate, LSV Equations A.11 and A.12 still apply with respect to the double-layer width and relative height of the redox peaks. Key characteristics of the redox couple include the ratio of the cathodic (E_{pc}) and anodic (E_{pa}) peaks (upon subtracting the baseline

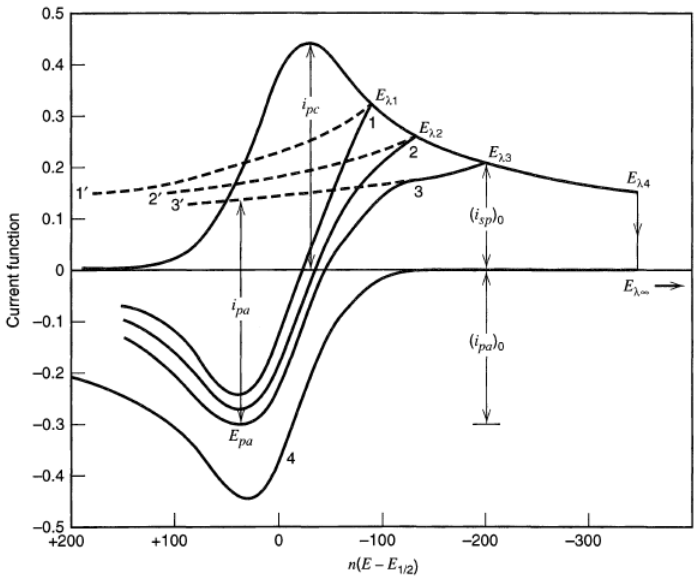

Figure 3.9: CV Redox couple in response to different window potential limits, E_λ.[7]

current); and the peak spacing (E_{pc}-E_{pa}). The CV of a Nernstian reaction shows symmetric peaks assuming that the potential window, when centered around the formal potential, $E^{0'}$, is wide enough to fully resolve the two peaks (at least 35/n mV past both redox peaks). Thus, the ratio of E_{pa}/ E_{pc} is expected to be unity, and E_{pc}-E_{pa} is constant at a given temperature (59 mV at 25 °C for 1-electron transfer).

$$\frac{|i_{pc}|}{i_{pa}} = 1 \tag{3.19}$$

$$|E_{pc} - E_{pa}| = \frac{59}{n}\, mV \;\; (at\, 25\,^{\circ}C) \tag{3.20}$$

Subtracting the double-layer current from E_{pa} and E_{pc} may be nontrivial if the baseline is not well-resolved as illustrated in (Figure 4.9). This would mostly be the case if the potential window, E_λ, is not wide enough beyond the cathodic and anodic peaks, which ultimately highlights the limits of CV as a fully quantitative tool.

For irreversible and quasi-reversible systems, the redox peaks invariably become a function of sweep rate, and the intrinsic reaction kinetic parameters (k^0, α). Moreover, the CVs for more complex chemical systems often yield multiple, overlapping peaks corresponding to consecutive electron-transfer steps, precluding significant quantitative evaluation.

Simple CV measurements on reversible redox systems such as anthracene, ferricyanide, etc., as depicted in Figures 5.8 and 4.9, are useful for evaluating the electrochemical properties of the electrode. For example, when taking multiple measurements using anthracene analyte at different sweep rates, we expect certain behaviors (Equations A.19 and A.20) of the redox couple to be held constant. Moreover, we also expect i_{pc} (or i_{pa}) to be a function of $\upsilon^{1/2}$ (Eq. A.11). Assuming that C_O* and D_O are known (n = 1 for anthracene), one can determine the active surface area. This is most useful for electrodes with rough surfaces, or surfaces composed of nanoparticles, which have a higher active surface area than the geometric area. Additionally, deviations from the expected peak features of the redox couple may provide information regarding the effects of uncompensated resistance.

Overall, CV measurements are a reliable and rapid method for understanding and discerning various electrochemical processes (e.g. reduction/oxidation charge transfer, double layer effects, desorption, adsorption etc.) over a wide potential window. Most importantly, this is the primary method used for screening oxygen reduction/evolution catalysts, which will be discussed in a later section.

3.7 Rotating Disk Electrode

Rotating disk electrode (RDE) is one of the most prolific electrochemical techniques, and a standard for measuring catalysis, providing quantitative information regarding the nature and kinetics of specific faradaic processes. This method consists of an electrode that rotates at a con-

trolled rate while immersed in analyte solution. The electrode potential is then swept (positively or negatively) at a constant rate, forming a well-defined LSV curve corresponding to a faradaic process of interest. In contrast to the previous techniques, where the stationary electrode is controlled by a fairly uncertain transient mass-transport behavior of the reactants from bulk, RDE is controlled by introducing a hydrodynamic (i.e. convective) flow field of analyte across the rotating electrode surface. Controlled hydrodynamic flow in steady state allows for high precision and reproducible measurements. More specifically, RDE isolates and amplifies the kinetics of a given reaction without any convolution from double-layer charging.

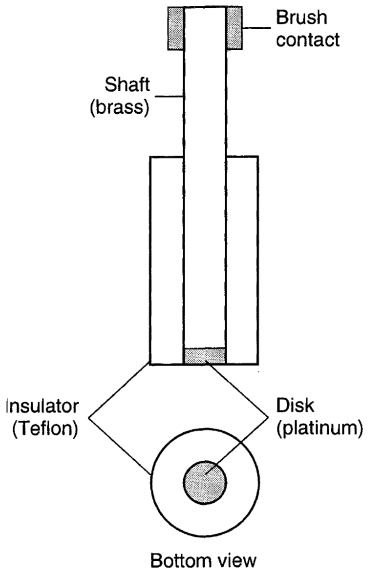

Figure 3.10: A schematic of a typical rotating disk electrode.[7]

The general setup of RDE consists of an electrode disk embedded in an insulating rod (i.e. Teflon), exposing one side of the disk face (Figure 4.10). The rod is immersed in analyte solution and rotated at a constant rate. During rotation, a steady-state flow of analyte is brought to the electrode surface. The exact steady-state behavior has been thoroughly modelled by von Karman and Cochran[7, 284], with solutions derived from a simple diffusion-convection model.

$$\frac{\partial C_j}{\partial t} = D_j \nabla^2 C_j - \vec{v} \cdot \nabla C_j$$
$$= Diffusion - Convection \tag{3.21}$$

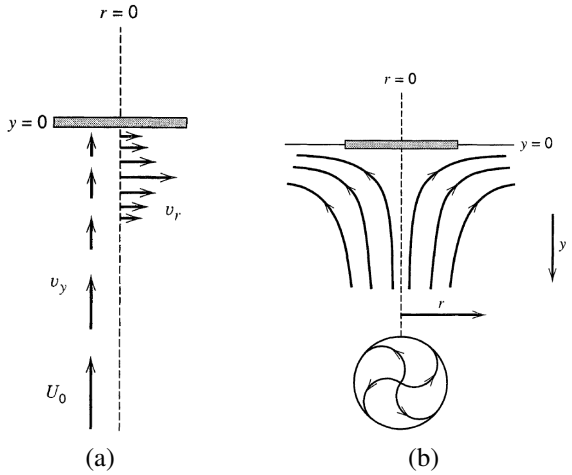

Figure 3.11: (a) Velocity profiles,υy and υ_r, of the analyte. (b) Analyte flow-field across the rotating disk.[7]

The symmetry of the electrode simplifies the flow field model corresponding to the velocity profiles of the solution, which are represented by their cylindrical coordinates (υ_χ, υ_r, υ_y). At the electrode surface, the spinning disk drags the analyte fluid at an angular velocity while the components υ_r and υ_y are zero (Figure 4.11). Away from the surface, the centrifugal force of the rotation creates a velocity profile radially, υ_r, and normal (υ_y) to the electrode surface. Towards the bulk ($y \rightarrow \infty$), both υ_χ and υ_r are zero, while υ_y is at a limiting velocity.

3.7.1 Levich and Koutecky-Levich Equation

Presenting the full mathematical derivation is well beyond the scope of this thesis (full treatment is in Faulkner[7]). In general, the known flow field coupled with the hydrodynamic properties of the analyte solution yields an explicit relationship between the flux of the analyte and the current output.

$$i = nFAD_O\left(\frac{\partial C_O}{\partial y}\right)_{y=0} \tag{3.22}$$

For the simplest case, consider the condition in which the current output has reached its mass-transport limit at a high overpotential ($C_O = 0$ at the surface). This creates a concentration gradient profile similar to the diffusion model for a stationary electrode. However, unlike stationary diffusion, the concentration profile from the electrode surface to bulk does not change with time, or $\partial C_O/dt = 0$. As a result, the limiting current is expressed as the Levich equation:

$$i_{l,c} = 0.62nFAD_O^{2/3}\omega^{1/2}\nu^{-1/6}C_O^* \tag{3.23}$$

We see that the limiting current is dependent on the rotation rate, ω, viscosity, ν, diffusion coefficient, D_O, electron-transfer number, n, and bulk concentration, C_O*.

Based on the Levich equation, we expect $i_{l,c}$ to be a linear function of $\omega^{1/2}$. Thus, information about the reaction is contained within the slope of the linear trend upon taking multiple RDE measurements at different rotation rates. The RDE behavior of sluggish reactions, such as oxygen reduction, is more complicated. A deviation from the expected linearity when trending i vs. $\omega^{1/2}$ indicates a secondary factor that's governing the current output, which in this case is the intrinsic reaction kinetics. Thus, the Levich plot is rearranged as the Koutecky-Levich (K-L) equation.

$$\frac{1}{i} = \frac{1}{i_l} + \frac{1}{i_K} = \frac{1}{0.62nFAD_O^{2/3}\omega^{1/2}\nu^{-1/6}C_O^*} + \frac{1}{i_K} \tag{3.24}$$

The i_k component is governed by the kinetic rate of reaction, $k_f(E)C_O^*$ (See appendix I).

$$i_K = FAk_fCo^* \tag{3.25}$$

Thus, the slope of the K-L plot is determined by the plot, 1/i vs. $\omega^{-1/2}$, which yields an intercept of $1/i_k$. This allows one to determine the reaction kinetic parameters, α and k^0.

3.8 High-Throughput Electrochemistry: van Dover Lab

All current electrochemical instruments within the van Dover group were custom-built, and are specifically designed for high-throughput testing for screening composition libraries in the form of thin film composition spreads (more about composition spreads in Chapter 4). Electrochemical screening is a crucial facet to high-throughput research, particularly for systematic studies on the catalytic properties of complex, multi-elemental materials, allowing the user to expedite the process of discovering and sequestering certain compositions that exhibit these unique or enhanced properties. Previous studies have utilized these experimental cells to measure and screen the electrochemical properties of several different catalyst systems, most notability for hydrogen/methanol oxidation reaction (HOR/MOR), hydrogen evolution reaction (HER), oxygen reduction reaction (ORR), and oxygen evolution reaction (OER).[182, 242, 77, 76, 193, 130, 63] This work primarily focuses on instruments that were used to analyze catalytic activity for ORR and OER.

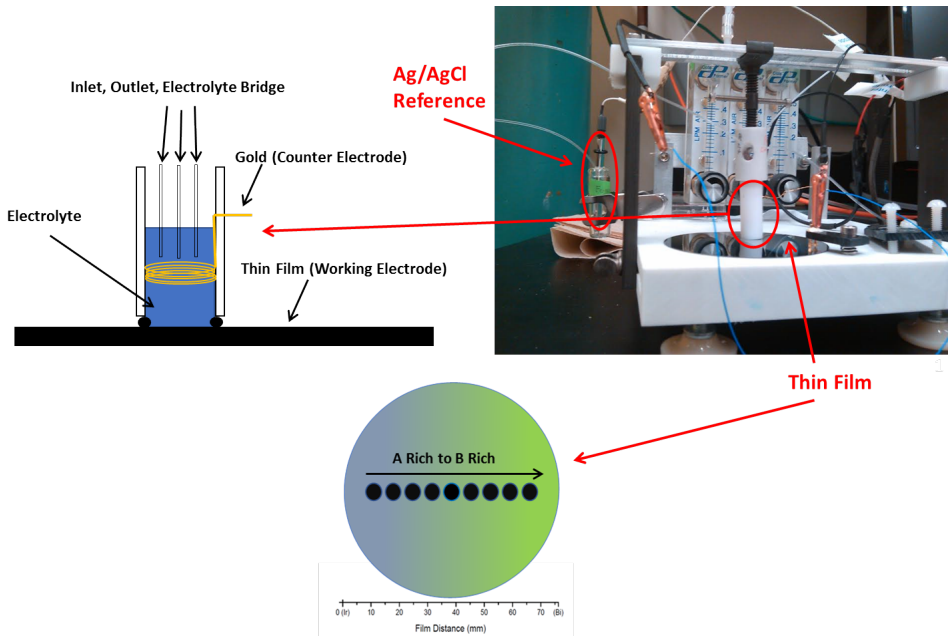

Figure 3.12: Illustrative cross-section and picture of electrochemical minicell setup.

3.8.1 Electrochemical Minicell

The Minicell is a quasi-high-throughput test cell designed to locally measure catalytic activity, specifically for ORR and OER, at the film/electrolyte interface, allowing the user to screen the entire material library by sequentially taking multiple measurements taken across the entire film. The apparatus is a custom-built three-electrode cell connected to a potentiostat controlled by a custom LabView program, where various parameters such as scan rate, voltage range, voltage gain are set and adjusted within the program. In addition to ORR/OER catalysis, the Minicell is ostensibly capable of a variety of different catalytic measurements when different test analyte solutions (e.g. NaOH, H_2SO_4, methanol, etc.) are used.

Figure 4.12 shows both an illustration of the cell cross-section and a photo of the actual setup. The base of the minicell setup is a flat platform for the composition spread thin film (faced upward). Connected to the platform are supports that hold a steel plate, which is connected to the top of the test cell by a rotatable flat head screw, allowing the cell to hover above the film and manually lower onto a given local test spot. Manual XY movement of the cell is facilitated by both

an open slit across the length of the overhead plate, and moveable supports that slide along grooves located across the sides of the platform.

The test cell is a hollow Teflon cylinder that locally interfaces with the surface of the film, which is designated as the working electrode. The test area has a diameter of 6 mm. During testing, the analyte is sealed inside the cell by a rubber O-ring that fits around the bottom lip of the cylinder. The interior wall of the cylinder is lined with a coiled gold (Au) auxiliary wire. The interior also contains three thin plastic tubes located near the bottom of the cell (close to the film surface when interfaced). The other ends of the tubes protrude from the top of the cell. Two of the three tubes function as an inlet and outlet for injecting and removing electrolyte solution, respectively, while the third tube functions as an electrolytic bridge between the film and the reference electrode. Capillary forces along the tube help maintain a continuum of analyte solution between the cell and the RE container. The reference electrode is a silver/silver chloride Ag/AgCl wire in saturated KCl (stable potential of 0.197 V vs. SHE). The reference is sealed within a glass tube, and is held within a separate container filled with the same analyte as the cell. The choice of housing the reference electrode in a separate container, as opposed to situating it near the film surface to minimize uncompensated resistance, was done to avoid chloride (Cl-) contamination of the Au counter electrode and the film surface.

Minicell Cyclic Voltammetry for Oxygen Reduction/Evolution Screening

Although the minicell is technically compatible with various electrochemical techniques (e.g. chronoamperometry, sample-current voltammetry, impedance, etc.), cyclic voltammetry (CV) was the primary test method conducive to semi-rapid screening. To illustrate what the screening analysis for ORR/OER catalytic activity entails, consider the CV of a sputtered Pt film, a common control sample. Figure 4.13 contains two superimposed CVs of the Pt film in de-oxygenated and oxygenated 0.1 M NaOH solution. At a given test spot, the Minicell is initially filled with nitrogen-bubbled 0.1 M NaOH, purging the solution of any oxygen. A baseline (or background) CV is

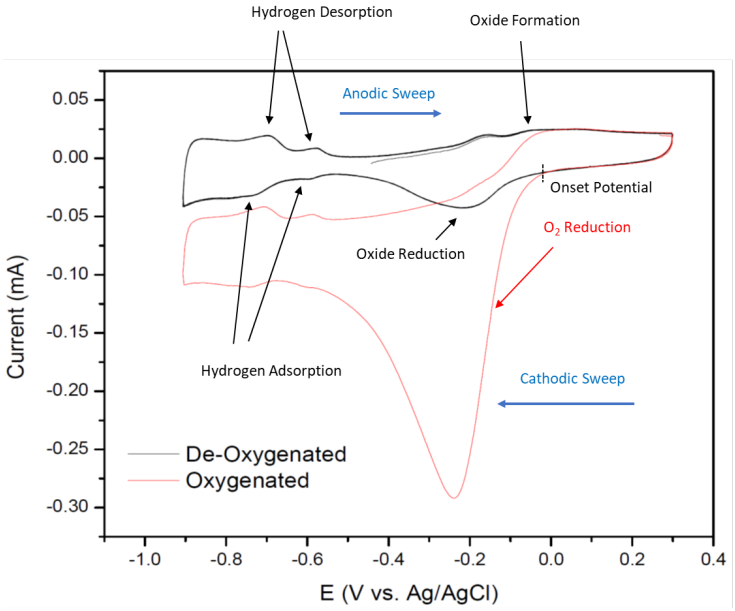

Figure 3.13: Oxygen reduction cyclic voltammogram (CV) of a sputtered platinum (Pt) film. The CV was scanned at a sweep rate of 50 mV/s.

measured, resolving various electrochemical processes that take place at the Pt surface within a potential window of -0.9 to 0.3 V vs. Ag/AgCl. During the background scan, the film undergoes multiple CV cycles in order to pretreat the surface. The pretreatment step usually ends upon reaching a steady hysteresis that doesn't change over several cycles.

The background CV of the Pt film shows multiple peaks in addition to a double-layer baseline. The set of cathodic/anodic peaks between -0.5 and -0.9 V are attributed to hydrogen adsorption/desorption, while the broader peaks between -0.3 and 0.2 V correspond to oxide formation/reduction. Now, lets consider the oxygenated CV, which now shows a steep negative ORR curve along the cathodic sweep at an onset potential of -0.05 V vs. Ag/AgCl, which is around 300 mV lower than the theoretical potential of 0.315 V (or 1.23 V vs. RHE). To ensure that no oxygen is prematurely reduced, the starting potential is set a more positive value relative to the expected onset. The general metrics for ORR catalytic activity, in this case, are both the onset potential, and the kinetic current at a certain overpotential that's within the kinetic regime beyond the onset. For instance, the onset for the Pt film was determined to around -0.05 V, while the kinetic current at -0.1 V is around -0.075 mA. These values represent qualitative benchmarks against novel materials

with unknown catalytic properties. When this approach is now extended to a series of CVs across a composition spread thin film, we can establish an ORR activity trend as a function of composition.

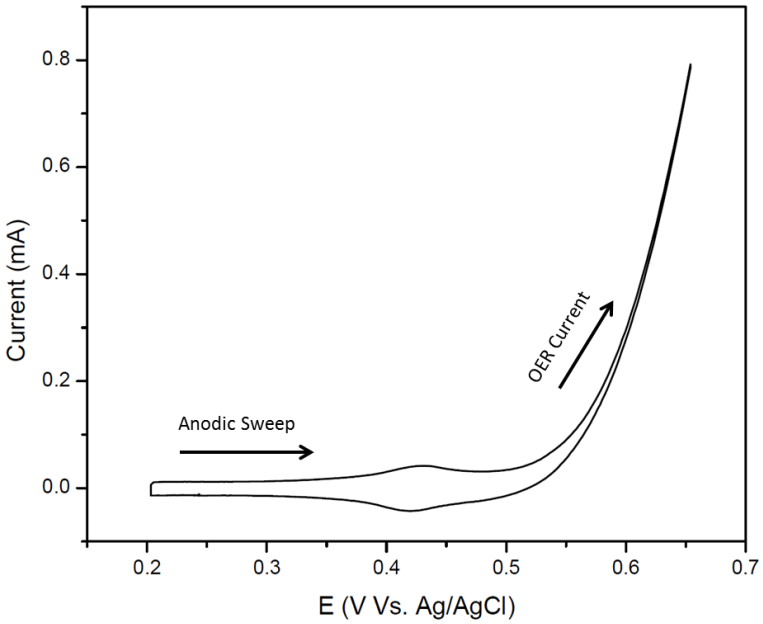

Figure 3.14: Oxygen evolutin cyclic voltammogram (CV) of a sputtered ruthenium oxide (RuO_2) film at a sweep rate of 50 mV/s.

In the previous example with Pt, the positive limit of the potential window was too low to resolve any current corresponding to oxygen evolution, which is activated along the anodic sweep typically between 0.4 and 0.7 V vs. Ag/AgCl. Similarly to ORR, OER is also kinetically sluggish overpotentials that are ~350 mV. Even in the presence of a strong OER catalyst, OER onset potentials are still round 0.55-0.6 V vs. Ag/AgCl (~1.45-1.52 V vs. RHE). Because Pt is not a particularly strong OER catalyst, the example CV shown in Figure 4.14 was measured on a ruthenium oxide (RuO_2) thin film, a material known for being catalytically active for OER.[80, 171, 177, 176] Oxygen is generated by oxidizing hydroxide (OH^-) at the film surface, yielding positive current that increases at greater overpotentials. The qualitative metrics for OER catalytic activity

are primarily the onset potential and kinetic current at a specified overpotential. In this case, the onset is approximated as ~0.515 V with a current that reaches 0.71 mA at 0.65 V. Again, these values serve as activity benchmarks for comparison, specifically against new materials. Generally, OER catalysis is performed after ORR, given that high positive potentials can cause many materials to degrade due to leaching.

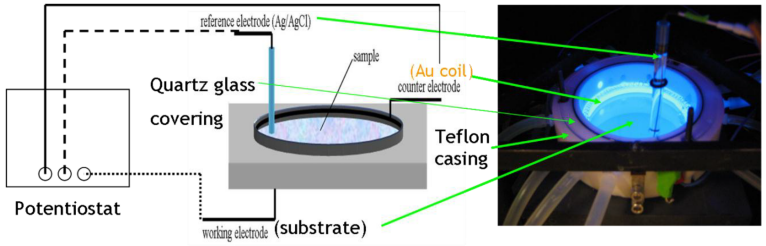

(a)

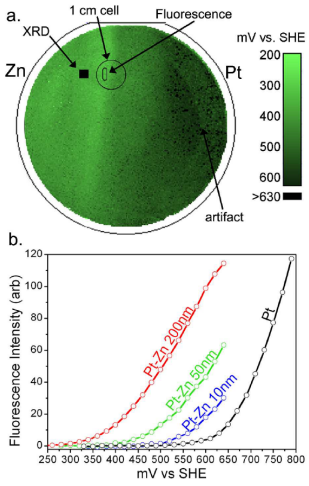

(b)

Figure 3.15: (a) Illustration and picture of fluorescence assay (FA) setup.[182] (b) Captured image of the fluorescence intensity (onset scale) across a Pt-Zn composition spread along with the intensity vs. potential.[74]

3.8.2 Fluorescence Assay

The fluorescence assay (FA) is another custom-built electrochemical cell that truly exemplifies high-throughput testing. With the entire thin film designated as the working electrode,

FA measures catalytic activity across an entire composition spread, which identifies active regions based the relative fluorescence intensity. Figure 3.15 shows an illustration along with the actual picture of the van Dover lab setup. The core operation of this experiment is based on previous work reported by Jing Jin and Mark Prochaska [188], which uses a special fluorescent dye that luminesces when activated by certain electrochemical reactions. This method was heavily utilized by previous graduate students for various catalytic processes, including hydrogen oxidation, methanol oxidation, and oxygen reduction.[242, 182, 74] For instance, previous works by Gregoire et al. used the FA to measured hydrogen oxidation in various analyte solutions (i.e. methanol, supporting solution, ethanol, etc.) mixed with a quinine dye. Quinine is an organic compound that fluoresces when illuminated with UV light upon H^+ protonation. The intensity of quinine, which has a center emission of around 460 nm, increases when the pH decreases. Thus, catalytically active regions for hydrogen oxidation locally decreases the pH due to rapid H^+ generation, causing the Quinine to fluoresce at a higher intensity relative to the surrounding regions.

The van Dover FA electrochemical cell consists of a 3 diameter open Teflon cylinder. The cylinder contains a coiled gold wire that lines the inner wall, held in place by black wax. The composition spread thin film is tightly held in place by the creases on the sides and back of the sample stage. The height of the stage is manually adjustable, allowing the film to tightly interface with the bottom lip of the Teflon cell. A special lip at the bottom is fitted with a rubber O-ring, forming a tight seal with the film. Also below the cell are three conductive probes that contact the outer periphery of the composition spread; all three are connected in parallel to the working electrode input of the potentiostat. The top of the Teflon cell is covered by removable quartz window, allowing the user to observe the fluorescence activity. A quartz window contains a small hole to embed the reference electrode within the cell, which hovers above the film surface. The Teflon cell contains several inlets and outlets along the side, each connected to a network of plastic tubes. Each inlet is connected to a dedicated container for a specific electrolyte test solution, which is pumped in and out of the Teflon cell using a peristaltic pump. For example, one container may contain 0.1 M sulfuric acid mixed with methanol and quinine for methanol

oxidation catalysis measurements. Before introducing the methanol solution, another container may house a calibration solution to capture background fluorescence, or another fill with distilled water for rinsing and cleaning between experiments. To ensure that fluorescence is not polluted from outside light sources, the stage and the cell are housed within a custom-built frame equipped with black cloth to veil the entire cell. The top of the frame supports a circular UV light source to uniformly illuminate the film, as well as a CCTV camera to capture fluorescence during the experiment. Lastly, the entire experiment is run through LabVIEW, allowing the user to control the pumping/draining of a chosen electrolyte, as well as operate the potentiostat.

With respect to nature of this work, one would consider this setup to be an ideal high-throughput screening method for ORR catalysis. Although Quinine is limited to only hydrogen oxidation, another compound called Umbelliferone has been previously used as an indicator for ORR.[182] This compound operates within a pH range of around 6 to 8.5. Active regions for ORR rapidly consume H^+ (See Chapter 2 for reaction) during the reaction, locally increasing the pH. Thus, the intensity of Umbelliferone fluorescence increases at higher pH. However, Umbelliferone is ineffective as an indicator under highly alkaline conditions (pH >> 7), and a working pH between 6 and 8.5 is not practical for most devices, which either operates under acidic or alkaline conditions. Although practical pH conditions are not always necessary for testing, the catalytic activities, particularly for ORR, may be dependent on pH due to changes in reaction mechanisms and double-layer coverage under certain operating potentials. Thus, a material or region that is active for ORR at a certain pH may not necessarily be active over the full pH range. Consequently, ORR and OER screening was soley achieved using the minicell. However, in retrospect, it would have been beneficial for a more thorough investigation on making FA more compatible with alkaline ORR catalysis.

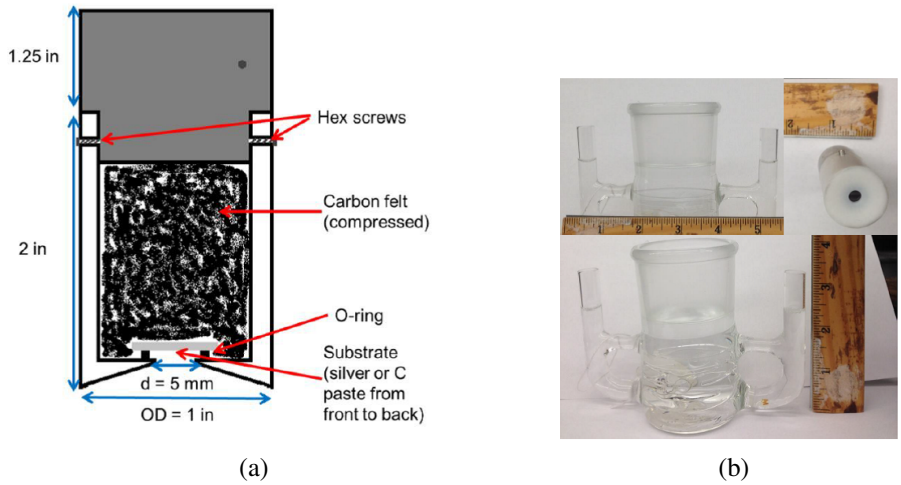

(a) (b)

Figure 3.16: (a) Illustrative cross-section of RDE rod, including film, carbon felt, and steel backing. (b) Picture of RDE glass basket.[260]

3.8.3 Thin Film Rotating Disk Electrode

The methodology for high-throughput analysis of thin film catalysts necessitates techniques that can validate the screening data, and provide additional information regarding the basic catalytic properties of the materials being studied. The early stages of high-throughput testing identify catalytically active regions, which, when coupled with several characterization techniques (i.e. XRD, XRF, XANEs, SEM, AFM, etc.), provides greater insight on how certain catalytic processes or enhancements are governed by the intrinsic features of the new material. Ideally, the culmination of high-throughput testing is the transfer of active materials to more practical and scalable forms.

As previously discussed, RDE is one of the most prolific electrochemical techniques, most notably for catalysis studies. However, conventional RDE methods are generally limited to powdered systems, or coated carbon disks. Partitioning the composition spread and performing RDE on the most active regions requires some type of modified setup. The utility of a modified RDE system represents the next step towards validating the screening data, as well as provide additional information regarding particular catalytic processes that are taking place at the film

surface.

The modified thin film RDE setup shown in Figure 3.16 was designed by Ryo Wakabayashi. The setup consists of a 1" diameter hollow Teflon cylinder that can hold a 10 x 10 mm thin film (cleaved from the composition spread). A 5 mm diameter surface area of the sample film is exposed at the bottom end of the cylinder, which slightly recesses from the outer periphery towards the planar film surface. The lip of the opening has a 0.25" O-ring, forming a tight seal with the film. Before placing the cleaved film inside the Teflon cylinder, the sides and back of the film are coated with silver paste and heated slightly to remove the solvent. This ensures contact with the carbon backing. Once the film is placed inside, the rest of the cylinder is filled with carbon felt (Alfa Aesar) and capped with a custom-made, stainless-steel current collector, which is tightened using a vice, and held together with hex screws.

The RDE cylinder was tested within a three-compartment cell (Figure 3.16b). The main chamber is 2" wide with an inner glass basket to prevent cavitation (whirlpool). The three compartments are connected at the bottom with glass frits, and at the top with simple glass tubing (to equalize the pressure in the three compartments). A graphite rod (Sigma Aldrich) was used as the counter electrode and a home-made saturated silver/silver chloride electrode (Ag/AgCl) was used as the reference. No platinum (or any noble metals) was used in the cell to ensure that there was no contamination from trace Pt from previous experiments. After any tests involving Pt and Au films, the cell is typically soaked in aqua regia for several hours to remove any residual noble metals.

RDE Analysis for ORR

Assuming that the screening results yield catalytically active regions, we invariably narrow the focus of subsequent electrochemical experiments on the optimal regions using thin film RDE. To demonstrate the analysis of a given spot, consider the ORR kinetic current density at different rotation speeds (Figure 3.17a) of a sputtered Pt film in 0.1 M NaOH. The series of mass-

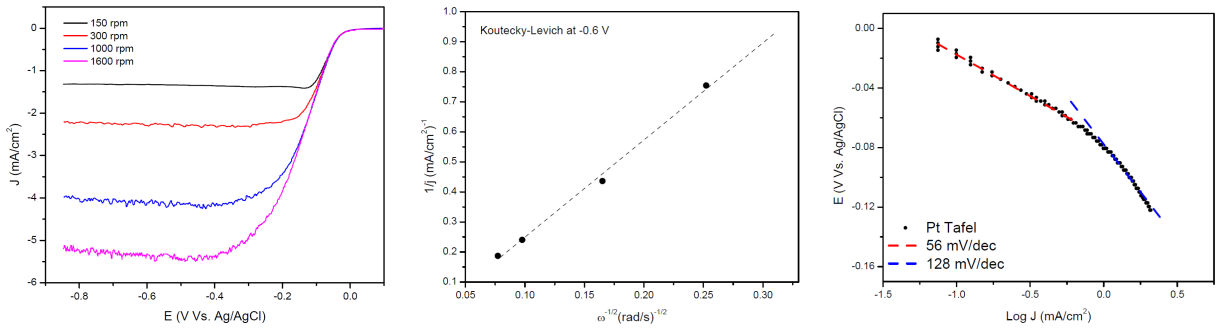

(a) (b) (c)

Figure 3.17: Platinum RDE (a) LSV Curves at different rotation speeds. (b) Koutecky-levich plot. (c) Tafel plot at 1600 rpm.

transport limited current, i_d, regimes is expected to increase with the rotation speed based on the Koutecky-levich equation (Equation A.24). Despite some issues with flow turbulence at higher rotation speeds, which places the set limit to around 1600 rpm, the RDE LSV confirms the high ORR activity of Pt based on the measured onset potential and kinetic current. Moreover, the LSV curves are reproducible and consistent with expected behavior for Pt.[62, 71, 227, 282, 251]

The most basic RDE analysis is extrapolating the slope from the linear fit ($1\imath_d \propto \omega^{-1/2}$) based on the Koutecky-levich relationship (Figure 3.17b). Assuming that the diffusion coefficient, D_O, oxygen bulk concentration, C_O, and geometric area, A, are known, the K-L slope can be used to calculate the electron transfer number, n, which measures the efficiency of the reaction. In the case of the Pt film at a potential of -0.6 V, n is around 3, suggesting a combination of 4-electron and 2-electron transfer pathways that yield fully reduced oxygen hydroxide (OH^-) and hydrogen peroxide (H_2O_2), respectively. Additionally, the intercept of the K-L plot is the inverse of the reaction kinetic current, i_k (Eq A.25). Thus, i_k with respect to the overpotential along the LSV curve, allows one to calculate the intrinsic reaction kinetic parameters, α and k^0. The features of the RDE LSV curves also provide information regarding the rate-limiting reaction mechanisms. These features are amplified when the LSV is represented as a Tafel plot (Figure 3.17c). At low overpotentials, the Tafel slope is typically within the range of 60 mV/dec before increasing to 120 mV/dec at greater overpotentials.[227, 217] These Tafel slopes are indicative of certain rate-limiting steps within the

entire oxygen reduction reaction (discussed in Chapter 2). Near the onset, the two Tafel slopes (Figure 3.17c) are around 56 mV/dec and 128 mV/dec, well within the expected values.

Often, many use a modified form of RDE, known as rotating ring disk electrode (RRDE), which follows the same setup as a traditional RDE, except now theres a second working electrode in the form of a ring concentrically separated from the disk by an insulating layer. During testing, the ring (at fixed potential) reacts with the product species that form upon reacting at the the disk. In the case of ORR catalysis, RRDE is most important for detecting hydrogen peroxide (H_2O_2) when oxidized by the ring. The current output, which is proportional to incoming flux, quantifies the amount of hydrogen peroxide that forms, which is a hazard for applications such as fuel cells. Additionally, the formation of H_2O_2 represents a 2-electron transfer reaction per oxygen molecule, which is ideally should undergo a full 4-electron reaction for maximum efficiency. Although this setup would have been invaluable to this research, no RRDE measurements were ever taken for this work.

3.9 Closing Summary

Electrochemical testing is a core part of this research, warranting a full chapter that delves into the key principles of various techniques. Most importantly, we discussed and demonstrated some of the main electrochemical test cells that were developed by past and present individuals within the van Dover and Abruña lab. This work represents an important facet to catalyst research, one that takes a systematic approach to identifying new alternative catalysts. Overall, these techniques are built on the confluence of systematic catalyst research, and high-precision electrochemical characterization.

CHAPTER 4

SPUTTERING AND THIN FILM CHARACTERIZATION TECHNIQUES

4.1 Introduction

Thin films are broadly defined as a thin layer of material that ranges from several micrometers to a single monolayer in thickness. The scientific importance of thin film technology and processing is underscored by their ubiquity in several applications, most notably microelectronics, solar cells, protective, and optical coatings. Given the design of our high-throughput approach to screening thin film catalysts and membranes in the form of composition spreads, thin film fabrication is a crucial component to this research. In addition to thin film processing and electrochemical screening, several characterization techniques were instrumental in qualitatively and quantitatively correlating and reconciling the structural and chemical properties of several new material systems with their measured electrochemical behavior. Nearly all of the characterization instruments are available here at the Cornell Center for Materials Research (CCMR) and the Cornell High Energy Synchrotron Source (CHESS) facilities. Because both sputtering and thin film characterization were critical to the work reported in chapters 5, 6, and 7, this chapter will briefly summarize some of the key sputtering systems and characterization instruments that were used throughout this research.

4.2 Sputtering

Thin film processing for commercial and/or research purposes includes several different deposition methods: evaporation, sputtering, pulsed laser deposition, chemical vapor deposition, and molecular beam epitaxy.[172, 223] Whether its thin film synthesis and/or etching, sputtering is one of the more common physical deposition techniques capable of depositing a wide array of

materials including metallics, oxides, sulfides, carbides, and nitrides.

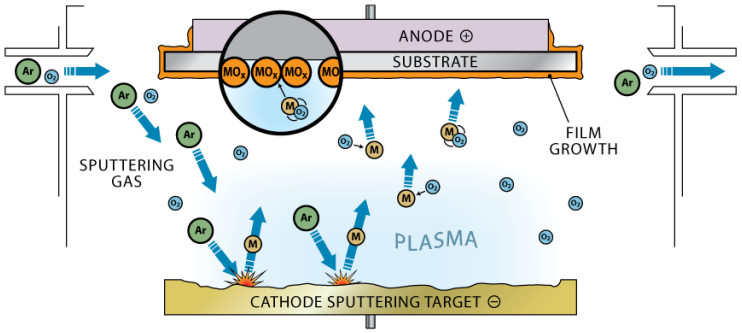

Figure 4.1: Illustration of reactive sputtering under DC bias. Image was taken from *http* : *//clearmetalsinc.com/technology/* on 01/08/2018.

4.2.1 Basics of Sputtering

The typical sputter setup is illustrated in Figure S.1. The target material, designated as the cathode, is connected to the negative terminal of the power supply (negatively biased) while the substrate (anode) is typically grounded or positively biased. Prior to sputtering, the chamber is filled with an inert noble gas (i.e. He, Ar, Ne, Kr, Xe) at a fairly low partial pressure (ranging from a few to hundreds of mTorr). When a potential is applied, the noble gas breaks down, creating a plasma discharge composed of noble gas ions (e.g. Kr^+, Ne^+, Ar^+) that accelerate and bombard the target surface, causing the target atoms to eject through the transfer of momentum. The ejected target atoms traverse through the low pressure ambient, atomistically depositing onto the substrate anode. The most striking visual feature of sputtering is the plasma glow near the target surface, signifying radiation emission induced by the cascade of gas ionization and recombination within the plasma discharge.

The cascade mechanism for creating and sustaining a steady plasma discharge for continuous sputtering is called the Townsend discharge. This involves an avalanche effect whereby the flux of electrons and gas ions multiply exponentially upon the onset of sputtering. During

the initial stages, stray electrons from the target accelerate through the electric field between the target and substrate. A fraction of the stray electrons collide and subsequently ionize the noble gas, initiating a multiplicity effect where several more secondary electrons are generated from the impact ionization, which in turn increases multiplies the number of positive ions for further target bombardment.

$$e^- + A \rightarrow 2e^- + A^+ \tag{4.1}$$

Upon reaching the full multiplicity effect, there is a complete breakdown (discharge) of the noble gas near the target surface (analogous to a dielectric breakdown in insulating solids), which initiates a self-sustaining plasma glow.

Properties of the Townsend Discharge are dependent on the chamber pressure and distance between the cathode (target) and anode (substrate). Unsurprisingly, there is an optimal pressure and substrate-target distance at which the breakdown voltage is at a minimum. For instance, if the pressure is too low, initiating the self-sustaining discharge will become increasingly difficult due to the lack of ionization collisions between the noble gas ions and secondary electrons. Conversely, if the pressure is too high, then the secondary electrons experience a smaller mean free path, precluding the ability to gain the kinetic energy needed for impact ionization.

4.2.2 Magnetron Sputtering

For most existing sputtering systems, magnets are typically incorporated underneath the target material inside the sputter gun. Known as magnetron sputtering, the use of magnets facilitates greater sputter yield and current at lower breakdown voltages. Illustrated in figure S.2a, the combination of electrostatic forces from the applied electric field and Lorentz forces from the magnetic field redirects the electron trajectory to stay near the target surface, increasing the impact ionization frequency. More specifically, the combined forces of the electric and magnetic fields influence the secondary electron trajectory to undergo a cycloidal hopping motion along the

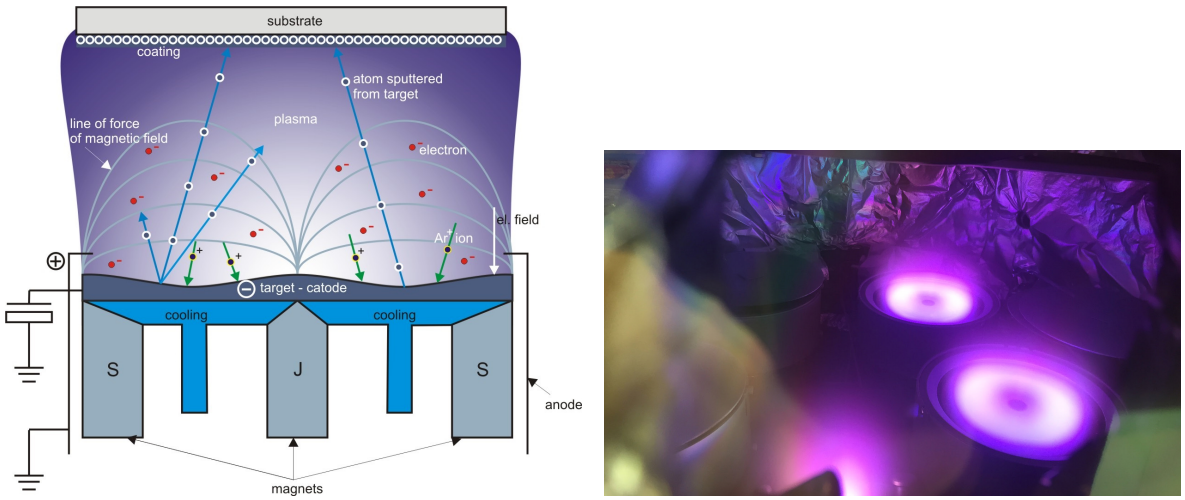

(a) (b)

Figure 4.2: (a) An illustration of magnetron sputtering. From *http* : *//www.umms.sav.sk/*6493 – *en/physical* – *vapor* – *deposition/*(b) The concentrated plasma glow along the target racetrack. From *https* : *//lightmachinery.com/optics/custom* – *optics/thin* – *film* – *coating/* on 01/18/2018

"racetrack" of the target surface within the plasma cloud, forming an intense luminescent ring above the racetrack (Figure S.2b). This concentrated glow signifies the highest degree of sputtering. Consequently, an erosion pit will eventually form around the surface of the target.

4.2.3 RF Sputtering

The sputter systems depicted in the previous examples and illustrations operate under a direct current (DC) bias as a means to more easily convey the basic principles of sputtering. However, there is a second operating mode known as radio frequency (RF) sputtering. In contrast to DC sputtering, RF introduces an AC voltage to the target, inducing a harmonic response from the secondary electrons and ions within the plasma discharge. Typically, AC sputtering requires a high-frequency signal that exceeds ~1MHz, with practical RF frequencies ranging from 5 to 30 MHz. However, a frequency of 13.56 MHz, which has been reserved for plasma processing by the Federal Communications Commission (FCC), is the most widely used. Within this frequency range, a sustainable discharge forms by rapidly oscillating electrons back and forth between the sheath

(dark region between the plasma glow and target surface) and the glow region, acquiring enough kinetic energy for repeated impact ionization. RF sputtering incidentally partitions more energy to oscillating electrons, resulting in lower ion bombardment energies, which generally reduces residual stress within the deposited film. The biggest advantage of RF sputtering is the ability to sputter insulating (high resistivity) target materials such as oxides and semiconductors, which are nearly impossible to sputter under a DC bias. This is achieved by exploiting the reduced impedance of dielectrics at higher AC frequencies, allowing current to pass through.

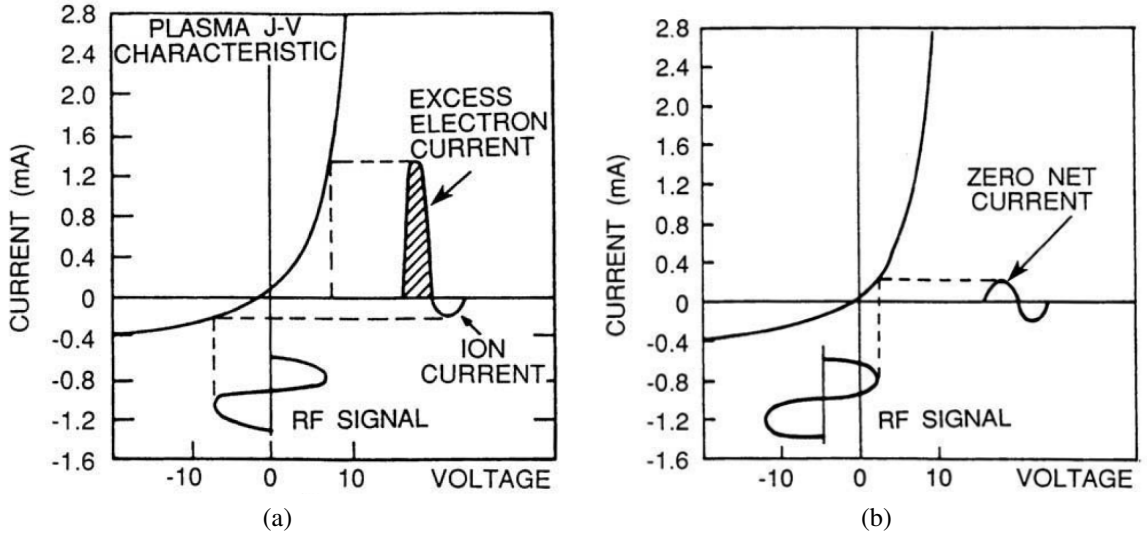

Figure 4.3: The formation of negative self-bias. (a) Net current under no negative self-bias. (b) Net zero current under negative self-bias.[172]

One notable consequence of RF sputtering is that the target negatively self-biases due to the higher mobility of electrons relative to ions. Figure S.3a illustrates the target AC signal when there is no self-bias, which draws more electron current during the first half-cycle than the positive ion current during the negative half-cycle, constituting non-zero net current despite the absence of any charge transfer through the target. Thus, a maintaing a zero net current signal results in a negative bias (Figure S.3b). Additionally, the plasma discharge for an insulating target has capacitive and well as resistive characteristics, thus, efficient coupling of the RF power supply to the target requires an impedance-matching network. This network, which consists of some combination of variable and fixed capacitors and inductors, is needed to match the load impedance

with the source impedance, thus maximizing power delivery to the target.

4.2.4 Reactive Sputtering

For more complex systems, such as metal oxides, the introduction of a reactive gas (i.e. oxygen) is needed to initiate reactive sputtering. Depending on which reactive gas is introduced during sputtering, several different types of compound thiln flms (e.g. oxides, nitrides, carbides, etc.) can be readily made. Compound thin film properties such as doping content, oxidation state(s), structure, vacancy concentration, etc., are largely dependent on the sputtering conditions (e.g. partial pressure, gas flow rate, and reactive gas/noble gas flow ratio).

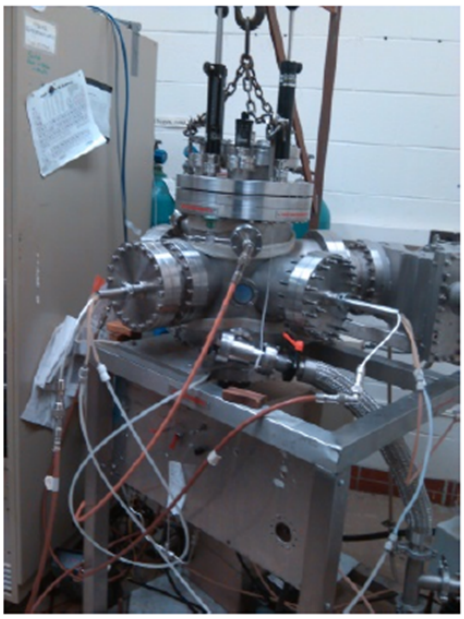

(a)

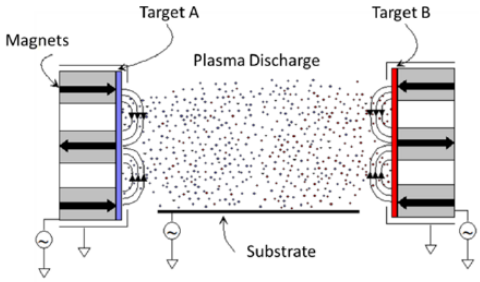

(b)

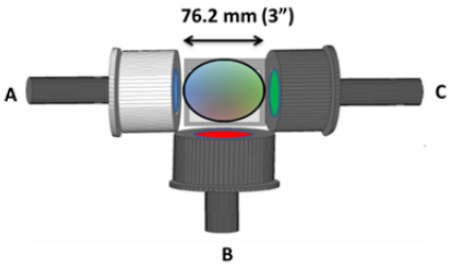

(c)

Figure 4.4: (a) A picture of Fenris RF sputterer. (b) A schematic of off-axis reactive sputtering to form composition spread thin films. (c) A top view of co-sputtering 3 different targets on a 3" diameter substrate.

4.3 Laboratory Sputter Systems

4.3.1 Fenris RF Sputterer

One of our flagship sputter systems is an RF-sputter system located within the van Dover lab. Uniquely given the name ”Fenris” (Figure S.4a), this instrument is an off-axis sputter system capable of reactively co-sputtering as many as three targets simultaneously. While connected to dedicated Ar, O_2 and N_2 tanks, this system is capable of sputtering complex compound films using conductive and non-conductive target materials (i.e. oxides, semiconductors, etc.). The setup, illustrated in Figure S.4b-c, consists of three independent magnetron sputter guns oriented orthogonal to one another and off-axis from the substrate that rests on top of a removable flat stage mounted at the center of the chamber. The off-axis configuration is specifically designed for non-uniform co-sputtering, facilitating the formation of continuous composition spreads. This configuration also reduces direct bombardment of ionized oxygen, which is known to induce pinholes and other defects.

The chamber is evacuated to semi-high vacuum ($\sim 10^{-6}$ Torr) using a turbo pump. The gate valve between the turbo pump and chamber is finely controlled using a wheel valve, allowing the user to partially close the gate valve to establish steady gas flow to reach intermediate partial pressures. Both the turbo pump and the chamber are connected to a mechanical pump used to initially evacuate the chamber to intermediate pressures (~50-100 mTorr) prior to opening the gate valve to the turbo pump. The top of the chamber contains spring-loaded shutters that can be lowered to cover the magnetron sputter guns in order to sequester the substrate during pre-sputtering. Whether for reactive or non-reactive sputtering, the operating partial pressure was typically set to around 30 mTorr. During deposition, the Ar/O_2 flow rates are generally set between 40/10 and 15/10 SCCM, depending the material being sputtered and the desired properties of the compound films.

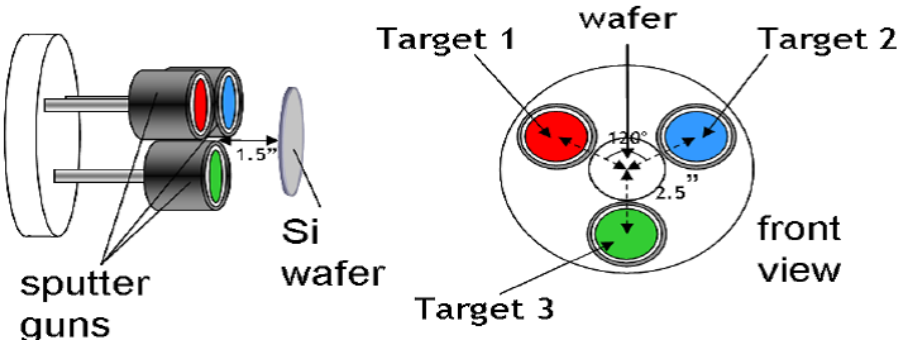

Figure 4.5: An illustration of on-axis sputtering in Gilamesh.[182]

4.3.2 Gilgamesh DC Sputterer

Another combinatorial sputter instrument owned by the van Dover lab is "Gilgamesh", a DC co-sputter system containing five magnetron sputter guns, three of which are arranged 120 °C apart (Figure S.5). The three-gun cluster has an on-axis configuration with a vertically mounted substrate. Up to three samples can be loaded into the chamber at a time, which are mounted on a rotatable post. In addition to the three-gun cluster, there is a secondary magnetron sputter gun and an S-gun for more uniform sputtering.

The chamber is connected to a high vacuum cryopump, which evacuates the chamber through the condensation of gas and vapor using condensed helium to chill the cryo-wall. Typical chamber pressures reached around ~2 x 10^{-6} at cryo-temperatures of around 14.5-15 Kelvin. As a standard for most vacuum systems, the chamber is also connected to a mechanical pump to reach intermediate pressures prior to transitioning into high vacuum. Unlike Fenris, the gate valves for Gilgamesh are controlled electronically by switches. The chamber also contains a valve that partially opens to allow gas flow to reach a suitable sputter pressure.

Partial pressures of Ar were typically set to 10 mTorr during sputtering. One of the advantages of Gilgamesh relative to Fenris is the built-in quartz crystal monitor for deposition rate measurements, making calibration far less tedious and time-consuming. Although Gilgamesh, like Fenris, was designed specifically for co-sputtering, and has previously been utilized by other grad-

uate students, it was generally relegated as a secondary system, since this research was heavily focused on oxide thin films. Consequently, Gilgamesh was limited to DC-sputtering conductive under layer films, which were subsequently loaded into Fenris.

4.4 Characterization Techniques

4.4.1 X-Ray Diffraction

X-ray diffraction is one of the most prolific and powerful techniques for obtaining key quantitative information regarding the atomic structure of a material. Interactions between X-rays and matter leave a scattered footprint corresponding to the periodic atomic structure and morphology of a given material, whether perfectly crystalline, polycrystalline, strained, or amorphous. The basic principles of X-ray diffraction (Braggs Law, reciprocal space, structure factor, etc.) are the foundation for any materials scientist and crystallographer.[38] There are several standard XRD methods (i.e. powder, Laue, rotating-crystal, etc.) for measuring the various structural properties (e.g. crystal structure, crystallinity, lattice constant(s), texture, grain size, etc.) of a given sample material. State-of-the-art XRD equipment here at Cornell (CCMR and CHESS) constituted a major analytical component to this research. The subsequent sections will briefly discuss some of these instruments.

GADDS XRD

Although it was the least sophisticated amongst the available CCMR XRD equipment, the Bruker AXS general area detector diffraction system (GADDS) was one of the major instruments used during the early stages of this research. This system is an area diffractometer that uses a collimated Cu-kα (λ = 1.54059 nm) X-ray source. The Hi-STAR area detector detects diffraction

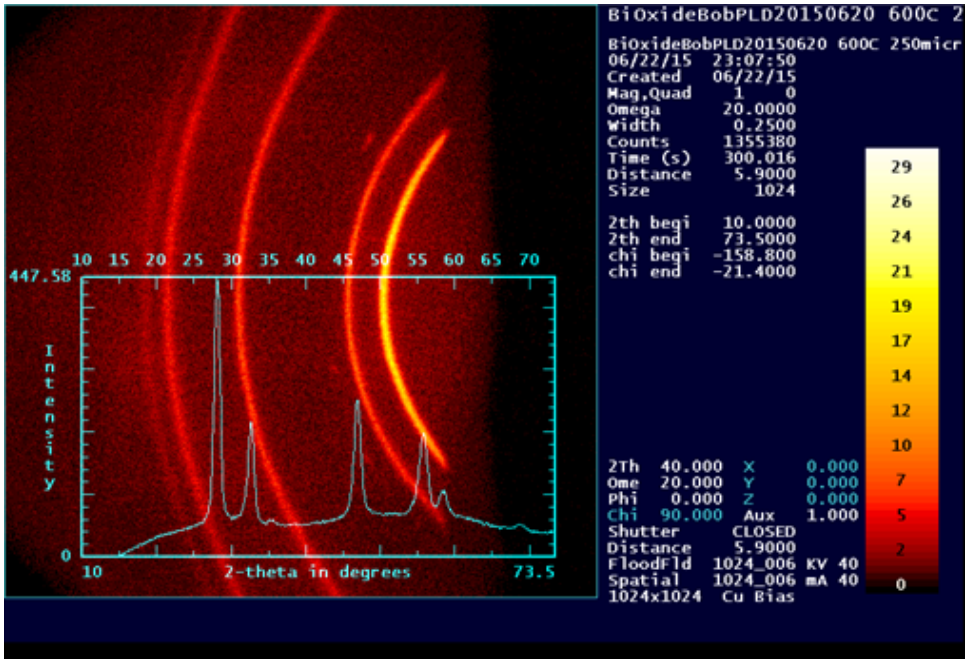

Figure 4.6: Measured diffraction rings of delta-phase bismuth oxide from GADDS.

spanning the azimuthal space, rapidly identifying crystallographic texture based on the measured intensities along the diffraction arcs (Figure S.6). Different sample holders can be mounted for a given sample form (e.g. film, powder, bulk), which includes a flat platform for 3" wafers. Most of the mounted stages also have adjustable tilt (χ) and rotation (ϕ). Multiple XRD measurements were taken at increments along the composition gradient, though the procedure required manual adjustment of the XY stage. For most of my experiments, the area detector was oriented to 2θ = 40°. Before each experiment, the sample-to-detector distance had to be calibrated using a piece of iron (Fe) foil as the calibration sample. Over time, this instrument was used less and less frequently given its relative antiquity and limited functionality in comparison to the Rigaku. However, a new GADDS was recently installed. Unfortunately, the complete installation of this system was after completing most of my experimental work.

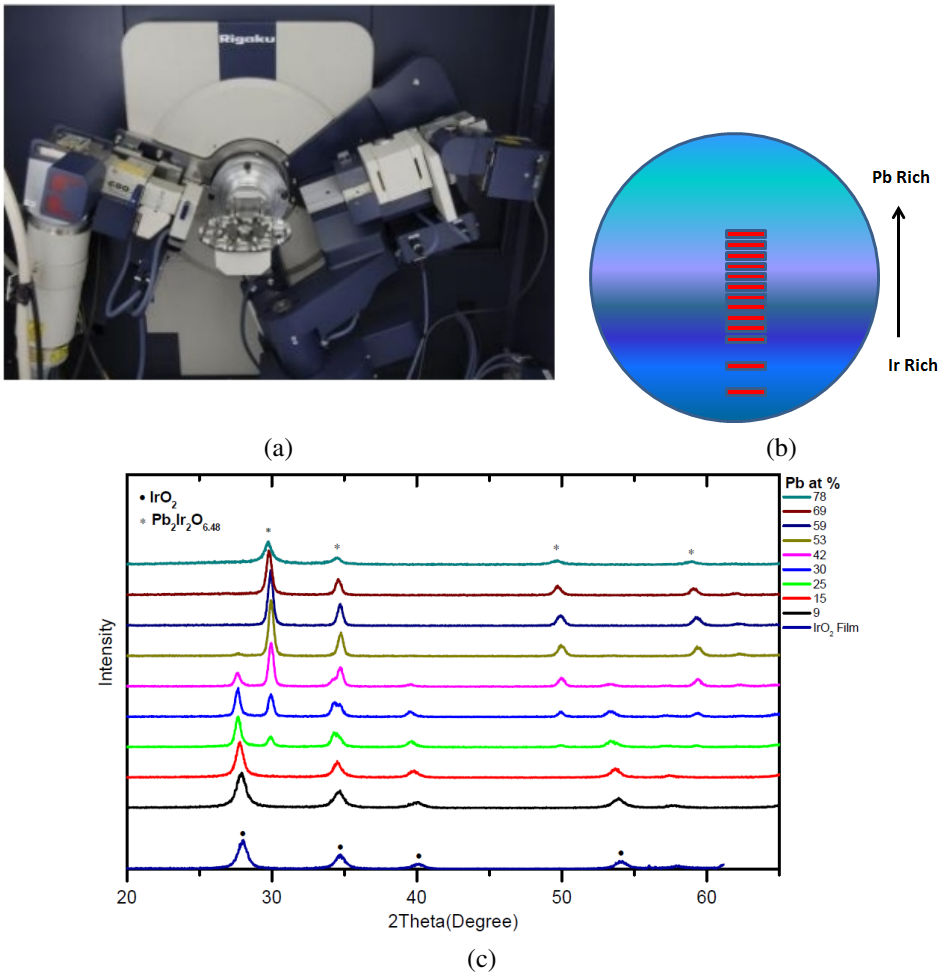

Figure 4.7: (a) Picture of Rigaku XRD setup. (b) Measured XRD spots across a Pb-Ir oxide composition spread. (c) Stacked 1-D XRD patterns.

Rigaku

The Rigaku (Figure S.7a) is a theta-theta XRD instrument that is generally the most widely used diffractometer amongst CCMR users due to its versatility. The system is equipped with several interchangeable optical components and sample stages. Several custom sample stages are also available, many of which have adjustable Chi (tilt) and Phi (rotation) axes for rocking curve, pole, and reflectivity measurements for texture, roughness and film thickness analysis. The Rigaku is also equipped with a moveable XY sample stage that can support 3”-4” wafers for high-throughput measurements. An automated routine can be programmed into the Smartlab software,

allowing for multiple measurements to be taken across the composition spread to resolve the localized crystal structures as a function of composition. Figure S.7c shows the stack of Rigaku patterns taken across the composition gradient of a Pb-Ir oxide composition spread (Figure S.7b). This approach becomes somewhat more difficult for ternary systems given the large divergence of the incident beam size at low incident angles, which changes as the 2θ changes during the experiment.

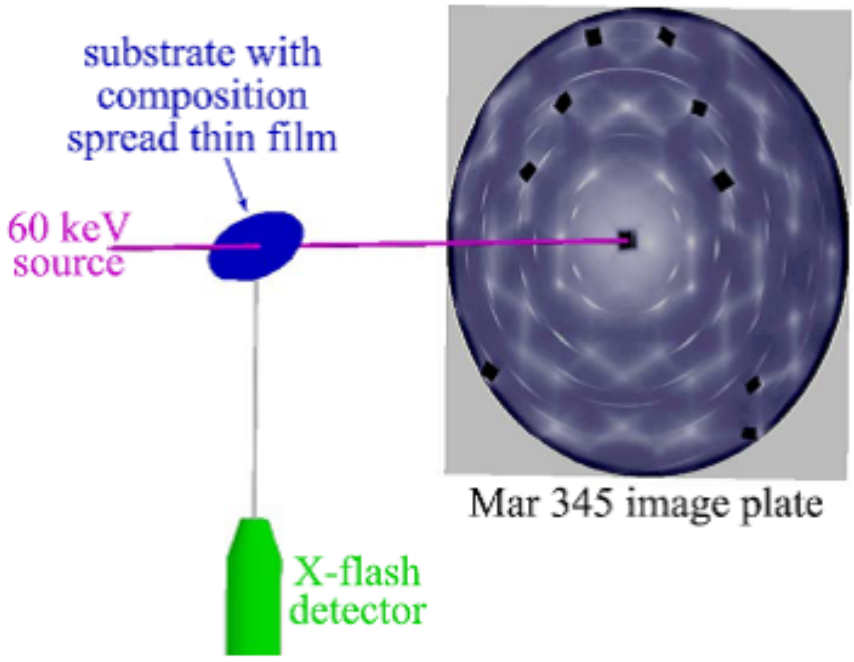

Figure 4.8: Schematic of XRD/XRF setup in the CHESS A2 hutch.[75]

Synchrotron-Sourced XRD

During a 1-2 week (24/7) period annually, our group performs high-throughput XRD and XRF experiments at CHESS. These experiments were are critical part in our effort to de-convolute XRD patterns of complex ternary spread systems, which allows us to fully resolve structural and compositional maps of our entire composition libraries. The use of high energy X-rays (~30 keV) generates XRD patterns that resolve higher order peaks, providing additional information on the local structure(s) of our films, as well as quantify thin film morphological characteristics such as

texture, strain and crystallite size. Over the years, we've explored several different configurations to circumvent some of the pervasive issues that have precluded a more streamlined analysis of the massive cache of data.

One of our earlier setups involved XRD in transmission mode (Figure 5.8) using a Mar 345 area detector downstream from the sample.[73, 75] For this setup, the composition spread was mounted (taped) onto a flat sample stage connected to a moveable XY stepper motor, and moved incrementally between each scan, whether in a straight line for a binary spread, or grid-like for a ternary spread. However, the detected diffraction rings collected downstream are convoluted by air-scattering, and high intensity spots corresponding to thermal diffuse scattering (TDS) from the silicon wafer. This was problematic due to the difficulty of developing a systematic algorithm (in collaboration with the Gomes group in the Computer Science department) that reliably and systematically removes the TDS background. This challenges is largely attributed to back ground drift due to slight changes in the orientation of the Si wafer, forcing the user to remove the background manually during analysis.

One major modification made for the transmission XRD setup involved the development of a periodic array of etched silicon, leaving thin silicon nitride (SiN) membranes. These membranes leave a faint amorphous background as opposed to the strong TDS signal, significantly simplifying the analysis. However, this approach was also met with additional challenges associated with additional processing and difficult handling. Aside from the time consumption of etching these Si nitride windows, which was done at the Cornell nanofabrication facility (CNF), the membranes were mechanically brittle, resulting in several broken membranes for a single substrate.

Another configuration, which constituted a major fraction of the characterization results reported in Chapters 5 and 7, used a fixed-angle reflection setup (Figure 4.9a). This setup was derived from a grazing-angle setup designed by Peter Beaucage from the Weisner group, which involves an X-ray beam that is incident at a low angle, though the incident angle for this setup was set between 5-7° relative to the plane of the film. The scattered X-rays are then measured by

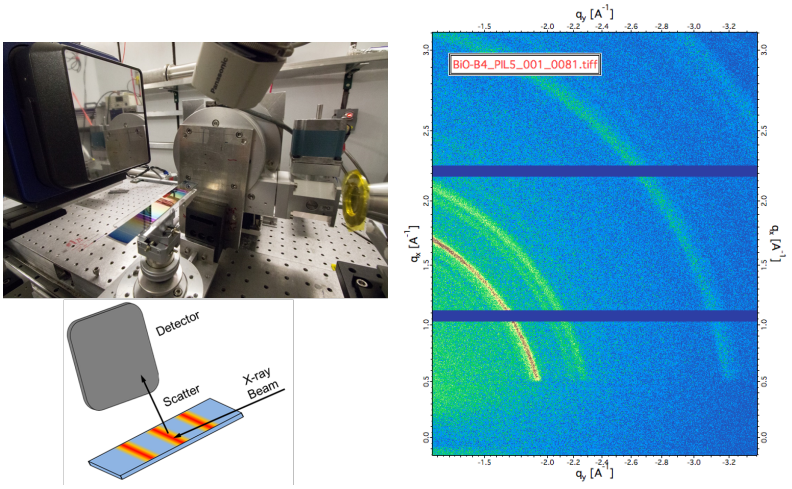

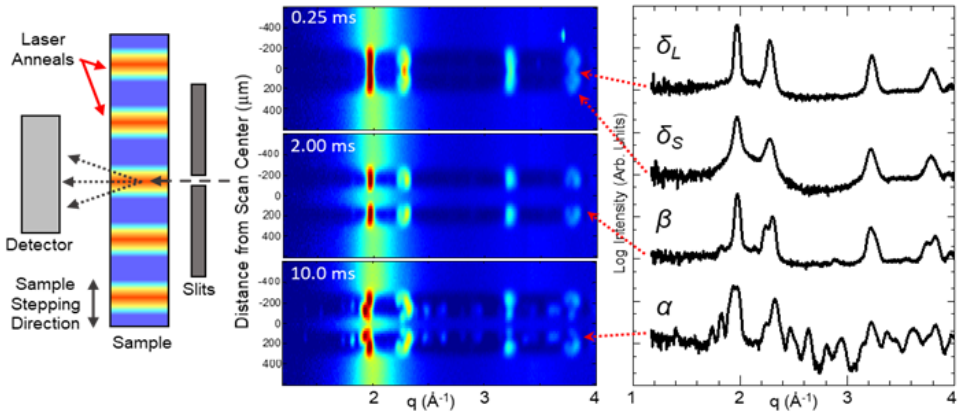

Figure 4.9: (a) Picture and illustration of the CHESS XRD reflection setup. (b) Area diffraction pattern of delta-phase bismuth oxide. (c) Top view of bismuth oxide film with different laser anneal lines, and corresponding phase map across each anneal line.

a Pilatus3-300K pixel array detector setup down-stream. This approach was somewhat limited to binary composition spread systems due to the divergence of the incident beam. By taking measurements in reflection mode as opposed to transmission mode, this configuration greatly reduces the intensity of the TDS background signal, though the signal is unfortunately still present. Efforts to further reduce the intensity of the TDS background included a custom-built sample stage that cools the sample using liquid nitrogen, since TDS signal is governed by the phononic activity of the Si atoms. This setup was instrumental in mapping the phase structures of bismuth oxide as a function

of annealing temperature and dwell time (Figure 4.9b-c), which resolve phase regions across several different anneal lines corresponding to specific annealing conditions (i.e. peak temperature, anneal time) - See chapter 7 for the full manuscript.

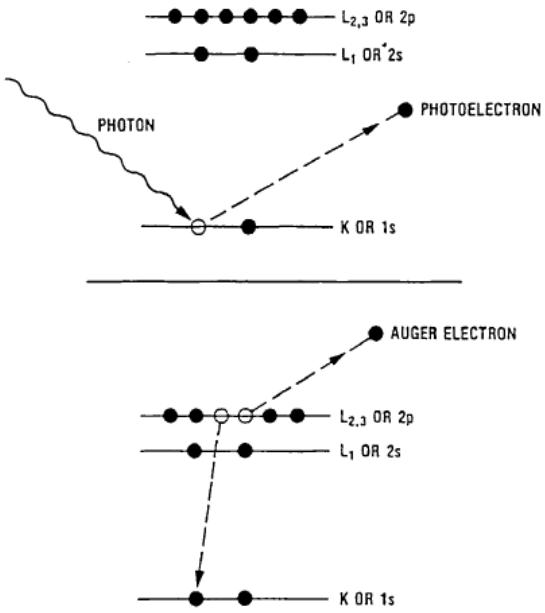

Figure 4.10: Illustraton of photoelectron emission (top) and Auger electron emission (bottom).[161]

4.4.2 X-Ray Photoelectron Spectroscopy

X-ray photoelectron spectroscopy (XPS), also known as electron spectroscopy for chemical analysis (ESCA), is a popular surface characterization technique for composition analysis. XPS works by irradiating the sample surface with X-rays, producing photoelectrons that are ejected at a kinetic energy characteristic of the ionized material electron shell structure.[161, 259] X-ray adsorption also causes outer-shell Auger electrons to eject in response to ion relaxation upon photoemission (Figure 4.10). Typical X-rays sources for XPS use Mg-K_α (1253.6 eV) or Al-K_α (1486.6 eV) emission. Although X-rays can penetrate a given sample material at a depth between 1-10 μm, the depth for detectable photoemission is only tens of angstroms. Photoelectrons deeper within the sample lose energy from scattering, and are subsequently detected as background.

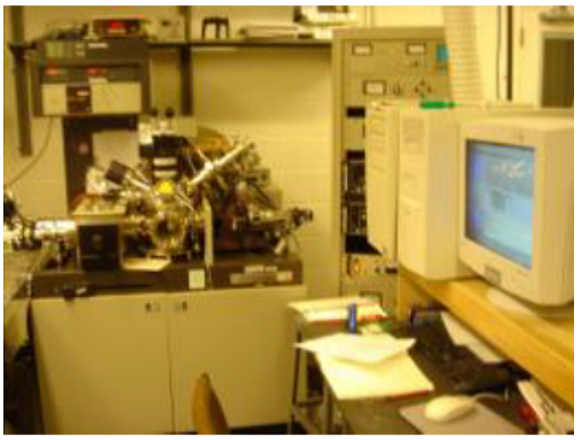

(a)

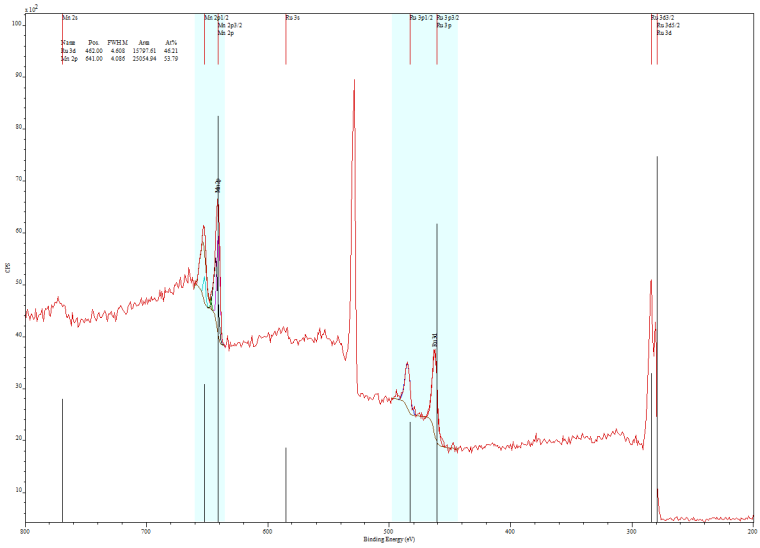

(b)

Figure 4.11: (a) Picture of XPS setup in Clark Hall. (b) XPS spectrum of a Mn-Ru oxide composition spread with highlighted Mn 2p and Ru3d peaks.

XPS was the primary tool for thin film surface composition analysis. The XPS system within CCMR uses an Al anode as the X-ray source (Figure 4.11a). In addition to reduce photoelectron scattering, XPS experiments must be done in ultra-high vacuum (UHV) at around $\sim 10^{-9}$ torr in order to remove adsorbed gases and other contaminants from the sample surface. The detector operates as a channel photoelectron multiplier, in which an incoming electron moves through a biased channel. As the incoming photoelectron bombards the channel wall, it produces secondary electrons, triggering a cascade effect of multiplied secondary electron emission upon each bombardment while collectively moving down the channel. Consequently, what started as a single

photoelectron turned into an amplified pulse signal.

The typical XPS spectrum shows various peaks at a particular binding energy corresponding to the electron shell structure of the irradiated material (Figure 4.11b). Quantifying the composition is achieved by integrating select peaks corresponding to the elements of the sample. This was done using a fairly simple Casa XPS program, which quantifies the intensity of the peaks while accounting for factors such as electron population, the Scofield cross-section, and the relative sensitivity factor (RSF). Many insulating samples may experience sample-charging in which the ionized surface is not charge-compensated, causing a secondary electrostatic effect on the emitted electrons. This results in a systematic shift in the spectra due to the reduction in kinetic photoelectron energies. This is most problematic when trying to de-convolute overlapping peaks corresponding to different oxidation states. To circumvent this problem, a secondary probe is used to charge-compensate the measured surface. Moreover, post-analysis can use a reference peak to manually correct the shift. For instance, the carbon C1s peak, which is typically fixed at a binding energy of 284 eV, is one of the more common reference peaks.

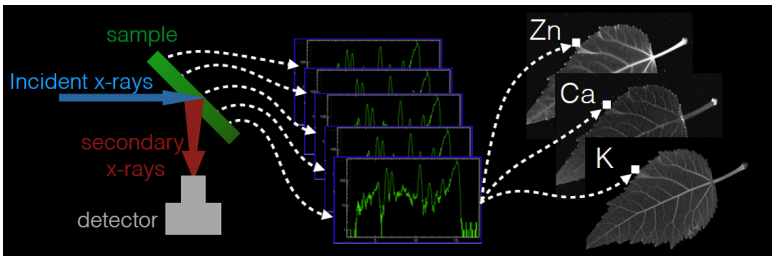

(a)

Figure 4.12: Illustration of XRF.

4.4.3 Synchrotron-Sourced X-ray Fluorescence

In contrast to XPS, X-ray fluorescence (XRF) measures the excitation-induced fluorescent signal emitted from the sample thats irradiated from an X-ray source (Figure 4.12). The fluorescence energies correspond to the electron shell structure unique to the sample material. Unfortu-

nately, there were no existing CCMR instruments capable of XRF. However, high-resolution XRF measurements were performed at CHESS using their synchrotron-sourced high-energy X-rays and state-of-the-art detectors.

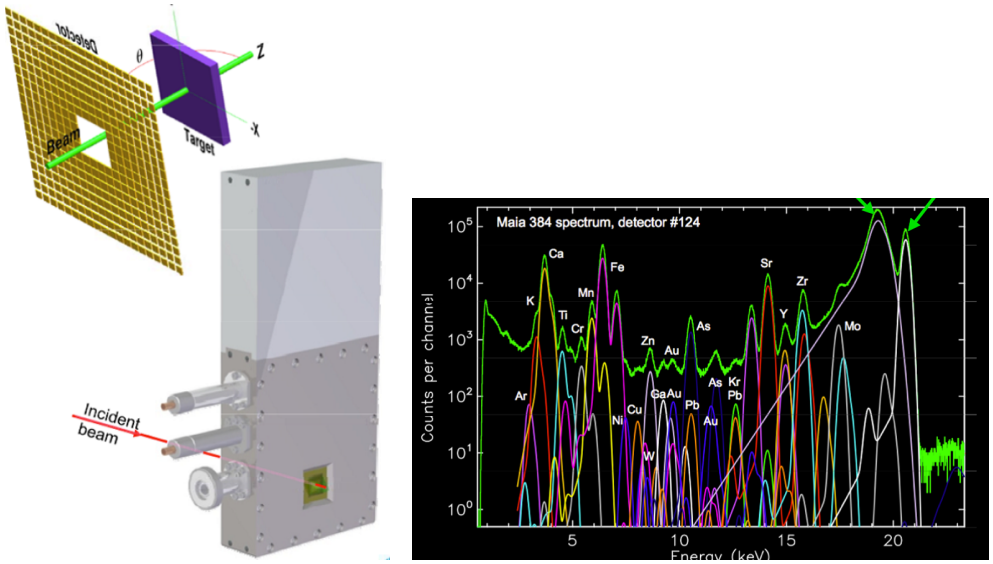

(a) (b)

Figure 4.13: (a) Schematic of the Maia detector and XRF setup. (b) De-convolution of XRF spectra using dynamic analysis.[204, 220]

We used a state-of-the-art high-resolution area Maia detector[204, 220] to rapidly retrieve XRF signals, generating high-resolution composition maps of our films (Figure 4.13a). A high-energy X-ray source (31.9 KeV) was incident perpendicular to the film, and spatially scanned across the entire area in step increments of 200 μm. Composition analysis was performed using the software, Geopixe, capable of dynamic analysis for real time fitting and de-convolution of the fluorescent spectra (Figure 4.13b).[203, 199, 202, 201, 200] In our previous CHESS runs, XRF measurements were taken in parallel with synchrotron-sourced XRD experiments using a conventional solid-state (SS) detector. The Maia detector, which regrettably was only used a handful of times throughout this research, is a detector array consisting of 384 solid-state detectors, allowing the user to capture intricate compositional details of complex materials, chiefly minerals and biological systems. Using a large array of SS detectors mitigates the limitations of conventional single detectors, which suffer from signal saturation due to photon pileup.

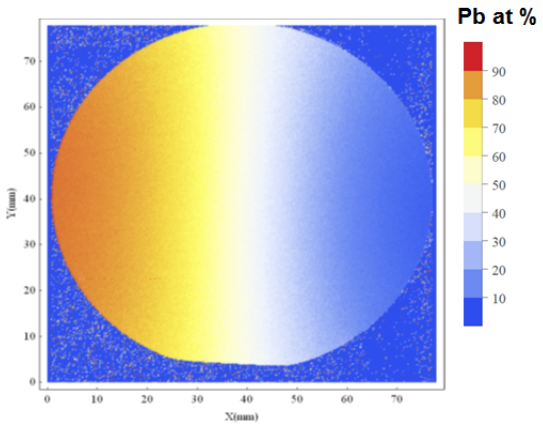

(a)

Figure 4.14: Composition mapped Pb-Ir oxide composition spread.

The Maia detector has an annular ”backscattering” geometry where the beam passes through an opening embedded within the surrounding detector array. With the sample upstream from the detector, this configuration increases fluorescent yield, and imposes far less restrictions on sample size and scale of scanning. When coupled to the Geopixe software, rapid collection of data is immediately processed (real-time processing). As mentioned earlier, rapid spectral deconvolution is done through dynamic analysis, while circumventing common artifacts attributed to pile-up, elastic and Compton peaks, escape peaks, and peak tails from incomplete charge collection. The utility of the Maia detector is exemplified by figure 4.14, which shows a highly resolved composition image of the entire Pb-Ir oxide thin film.

4.5 Closing Summary

In this chapter, we summarized the basic operation of sputtering, and elaborated on key sputtering instruments available within the van Dover lab. These systems are a core part of our high-throughput combinatorial approach to fabricating new complex material libraries for any application. Additionally, this chapter summarized some of the key characterization methods (i.e. XRD, XPS, XRF) that were used throughout my time as a graduate student. Secondary instru-

ments such as filmetrics, ellipsometry, and profilometry were also used, but their infrequent use or overly simplistic design didn't warrant their own summary. Other characterization methods that I feel would have bolstered some of the results presented in this thesis include SEM and AFM. Both would have added some additional information regarding surface roughness and film morphology, which does affect catalytic activity.

CHAPTER 5

MANUSCRIPT - HIGH THROUGHPUT OXYGEN REDUCTION/EVOLUTION CATALYST STUDIES ON MANGANESE-RUTHENIUM OXIDE

5.1 Abstract

Considerable progress in the design and optimization of alkaline electrolytes in low temperature fuel cells, metal-air batteries, and electrolyzers has become the impetus for expanding the search for inexpensive alternative bifunctional oxygen reduction/evolution reaction catalysts. Manganese-based oxides are one of the central bifunctional catalysts of interest, exhibiting activities comparable to platinum-based materials, though far more abundant and less expensive. In this study, co-sputtered manganese ruthenium oxide composition spread thin films were screened using cyclic voltammetry, mapping ORR and OER catalytic activities as a function of composition. Structural information from synchrotron-source X-ray diffraction reveals the most active regions of the film to be single-phase $Mn_xRu_{1-x}O_{2-y}$ ($0.07 < x < 0.45$), a mixed cation rutile structure not been previously reported. Rotating disk electrode measurements of the most active composition range (12-20 at. % Mn) not only validates the high-throughput screening results, but the catalytic activity was comparable to Pt for ORR, and RuO2 for OER. While the synergistic effects that govern the enhanced bifunctional activity of $Mn_xRu_{1-x}O_{2-y}$ is speculative, this new oxide material represents a new and promising alternative catalyst.

5.2 Introduction

Research and development of low temperature fuel cells, metal-air batteries, electrolyzers for fuel regeneration, and unitized regenerative fuel cells (URFC) has played a crucial role in integrating clean energy technologies into our current energy infrastructure. However, electro-

chemical performance is still limited by sluggish oxygen reduction/evolution reaction (ORR/OER) rates, necessitating the incorporation of active electrode electrocatalysts in order to reach viable performance standards. Commercial electrolytes such as proton-exchange membranes (PEM) are highly corrosive to most materials, restricting candidate ORR/OER catalysts to rare and expensive precious metals, most notably Pt and Pt-alloys for ORR[61, 71], and (Ir,Ru)-based materials for OER.[119] Serving as viable alternatives to PEMs, anion exchange membranes (AEM) have recently spiked in interest due to major improvements on OH- ion transport kinetics and chemical stability.[253, 91, 254] Moreover, AEMs impose a far less oxidizing environment, enabling a more expansive search for alternative non Pt-based electrocatalysts.

Amongst the vast library of potential catalysts chemically compatible with alkaline electrolytes, manganese (Mn)-containing oxides are promising alternative non-precious metal bifunctional catalysts.[127, 22, 29, 68, 174, 234, 221, 163, 110, 276, 45, 275, 28, 21, 92, 50] Demonstrating fair catalytic activity for ORR and OER, Mn-oxide is attractive for its high abundance, low toxicity, and low cost. Previous studies have looked extensively at the catalytic properties of Mn-oxide, reporting widely disparate activity results due to the existence of various forms of Mn-oxide that are differentiated by their valence state, phase structure, polymorphic structure, composition, and morphology.[45, 149] For instance, α-Mn_2O_3, MnOOH, Mn_3O_4, and certain polymorphs of MnO_2 have been identified as active ORR catalysts while MnO is comparatively inactive.[127, 146, 128] Interests in Mn-based catalysts have also extended towards mixed oxide systems[16, 113] such as ternary Mn-metal oxides (spinel, perovskites)[131, 106, 122, 27, 238], Mn-oxide/metal composites[179, 50, 49], and Mn-doped carbon nanomaterials.[131, 250] These mixed-cation and composite systems have been reported as strong bifunctional oxygen electrocatalysts with evidence of synergistic enhancements attributed to combinations of dual active sites of the constituent materials, improved electron transfer, and electronic coupling effects.[238]

Ruthenium oxide is well-known oxygen evolution catalyst, exhibiting one of the highest known activities for OER[119], and therefore a component material of interest for hosting mixed

oxides, including Ni, Co, Fe, and Zn-doped RuO2.[183, 184] However, there have been few studies on Mn-Ru oxide as candidate bifunctional electrocatalysts.[158, 157, 79, 102] Although RuO_2 is not highly abundant in the Earths crust, it is significantly less expensive than theprecious metals used ascatalysts (Pt, Pd, Ir, and Au). Beyond some theoretical work on using Mn to stabilized a high-pressure cubic fluorite polymorph of RuO_2[98], there is currently no known phase database or reports of an atomically-mixed Mn-oxide and RuO_2 system ($Mn_xRu_{1-x}O_{2-y}$). Jang et al. synthesized and evaluated a physically separated mixture of α-MnO_2 and RuO_2 as evidenced by the distinct set of XRD patterns corresponding to the aforementioned phases.[102] Guo et al. also describes an oxide catalyst system containing γ-$MnO_2$and RuO_2 which was also phase separated with no evidence of Mn-substitution.[79]

In this study, co-sputtered Mn-Ru oxide thin films, which form a continuous composition gradient across a single film, were evaluated as bifunctional oxygen electrocatlaysts using high-throughput electrochemical and characterization techniques. Upon screening ORR/OER catalytic activities combined with an XRD map taken across the composition gradient, the most catalytically active regions were identified to be single-phase Mn-doped RuO_2, or $Mn_xRu_{1-x}O_{2-y}$ ($0.07 < x < 0.45$), a previously unreported ternary oxide system.

5.3 Experimental Procedure

5.3.1 Reactive Co-sputtering of Mn-Ru Oxide

Non-uniform (150-400 nm thick) binary manganese-ruthenium oxide (Mn-Ru-O) composition spread thin films were deposited onto76.2 mm (3") diameter silicon (100) wafers using off-axis reactive RF co-sputtering. The sputter system used has been previously described.[46] The film was co-sputtered from Mn and Ru metal targets for 20 minutes on a substrate holder heated to ~350 °C. Films that were used for electrochemical testing were first coated with a 60 nm Ru metal

layer using DC sputtering in 10 mTorr Ar; the Ru underlayer is a conductive backing required for electrochemical testing in order to minimize the resistance drop across the area of the composition spread film. Each film was then placed in the vacuum chamber until a base pressure of ~2 x 10^{-6} Torr was reached. Subsequently, a steady flow of 40 sccm Ar and 10 sccm O2 gas (20% O2) was introduced to obtain a partial pressure of 30 mTorr. To clean the target surfaces and develop a steady sputter rate, both targets were pre-sputtered for 10-15 minutes prior to co-sputtering.

5.3.2 Characterization

Multiple X-ray photoelectron spectroscopy (XPS) measurements were obtained in order to calculate and fit the surface composition gradient across the Mn-Ru oxide spread. The XPS system itself consisted of an Al-anode X-ray source and a chamber that evacuates to UHV (~10^{-9} Torr). Each scan was taken incrementally across the composition gradient of the film. Composition analysis involved peak integration of the Mn 2p and the Ru 3d peaks.

High-energy fixed-angle area detector synchrotron source XRD measurements were taken across the Mn-Ru oxide composition spreads at the Cornell High Energy Synchrotron Source (CHESS). A 19.6582 keV beam that was reduced to a 25x200 μm rectanglular spot size using knife-edge slits, and incident at a fixed angle ranging from 7-5° relative to the film plane. The scattered x-rays were detected using a Pilatus 2k area detector. The sample was placed on top of a moveable stage, and 143 XRD measurements were taken across the composition gradient of the film in 500 μm step increments. The long dimension of the beam spot was oriented perpendicular to the composition gradient to minimize the composition range across the beam spot. The Ru metal under-layer acted as a calibration standard to accurately infer the sample-to-detector distance during post-experiment analysis.

5.3.3 CV Measurements

Oxygen reduction and oxygen evolution activity screening was performed across the surface of the Mn-Ru oxide composition spread using a three-electrode test cell connected to a model BAS CV-27 potentiostat. The custom-built electrochemical cell consists of a 6 mm inner diameter cylindrical Teflon container that locally seals and interfaces the electrolyte solution with the film surface that acts as the working electrode. The geometric surface area measured at any location has a diameter of 6 mm. The interior of the cell features a long coiled gold auxiliary electrode that lines the interior of the Teflon tube, and is fitted with three plastic tubes with one end protruding from the top of the cell and the other end near the film surface. Two of the three tubes act as an inlet and outlet for electrolyte solution to be injected and removed, while the third tube functions as an electrolyte bridge that connects the cell to a separate container holding the Ag/AgCl reference electrode. The choice of housing the reference electrode in a separate container, as opposed to situating it near the film surface to minimize uncompensated resistance, was done to avoid chloride (Cl^-) contamination of the Au counter electrode and the film surface.

A series of cyclic voltammetry measurements were taken across the composition spread to screen the ORR and OER catalytic activities of the film. Each measurement was taken at room temperature in 0.1 M NaOH alkaline solution. Each spot was initially cycled at 50 mV/s in N_2 saturated solution for 15-30 minutes to determine the background CV hysteresis. No reduction pretreatment step was taken prior to testing in order to avoid the risk of irreversibly reducing the oxide surface. The potential range in which each surface was cycled was typically within a range that did not expand beyond the -0.8 to 0.2 V window. The N_2 saturated solution was subsequently removed from the cell, and replaced with an O_2-saturated solution. Beginning the scan at a potential above the onset of oxygen reduction, a cathodic sweep was performed to determine the ORR current. Because the oxygen near the film surface quickly depletes during reduction, the solution is removed and replaced with fresh oxygenated after the first cycle. First cycle oxygenated CV measurements were then repeated 5-6 times to establish consistency, as well as quantify variations

in our activity results. The potential window for OER was between 0.3-0.7 V, and the film was cycled at a reduced scan rate of 20 mV/s to reduce the risk of forming oxygen bubbles. After the first CV cycle, the new solution was introduced, and the measurement was repeated. Similar to ORR, 5-6 first-cycle measurements were taken to ensure consistent outputs.

5.3.4 Rotating Disk Electrode

CV measurements, while valuable for first level electrochemical screening and rapid analysis carries well-known uncertainties associated with oxygen mass-transport and the formation of an oxygen-depletion layer after the first CV cycle, precluding quantitative analysis of the catalytic nature of the film surface. Thus, RDE was modified for testing thin films, particularly the active areas of the Mn-Ru oxide composition spread. The main chamber of the custom-built three-compartment cell is 2 inches wide, and has an inner glass basket to prevent cavitation (whirlpool). The three compartments are connected at the bottom with glass frits, and at the top with simple glass tubing to equalize the pressure in the three compartments. A large graphite rod (Sigma Aldrich) was used as the counter electrode and a saturated silver/silver chloride electrode (Ag/AgCl) was used as the reference electrode.

After screening the Mn-Ru oxide composition spread, the most active region of the film was cleaved into a 9x9 mm and placed in the RDE test cell. The back of the cleaved film was coated with a thin layer of silver paint a good electrical contact with the carbon backing. The film was then placed in a 1" diameter Teflon holder machined to fit an electrode with a 10x10 mm surface area, with a 5 mm diameter opening to expose the test electrode to the electrolyte is located at the test end of the Teflon rod. A recess was made to place an O-ring (0.25 in), in order to prevent liquid leakage into the sample holder. After placing the back-contacted sample inside, the Teflon holder was packed with carbon felt (Alfa Aesar) and capped with a custom-made, stainless-steel current collector (that could be connected to a Pine rotator) by screwing the stainless steel piece to

the Teflon piece using small hex screws. This process was carried out using a vise to ensure that the carbon felt was well-packed in order to ensure good electrical conductivity. The RDE was then mounted onto a PINE rotator connected to a potentiostat and immersed into a beaker full of 0.1 M NaOH aqueous solution.

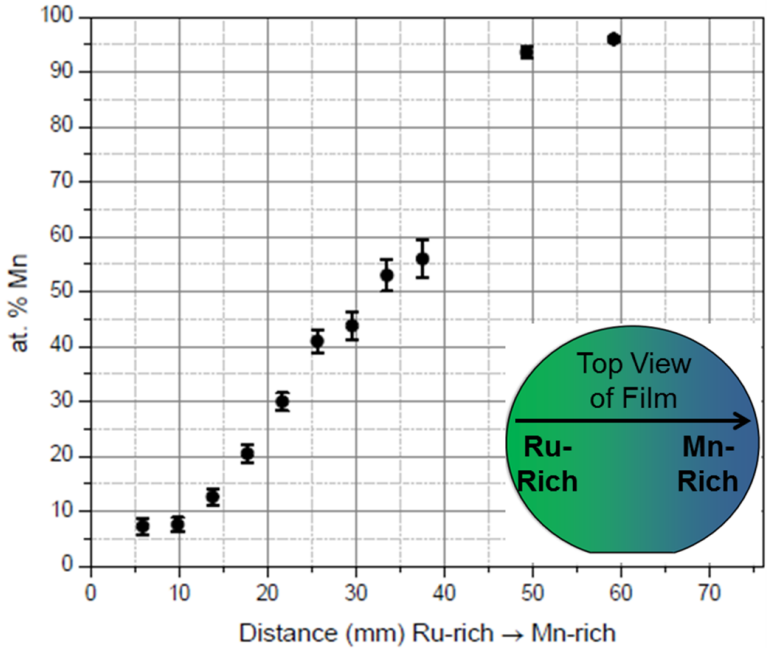

Figure 5.1: Surface composition of Mn across the Mn-Ru oxide composition spread inferred from XPS.

5.4 Results and Discussion

5.4.1 X-Ray Diffraction

Figure S.1 shows the plot of the surface composition obtained from the integrated peaks of a series of XPS survey scans measured across the Mn-Ru oxide composition spread, which had a continuous gradient ranging from 7 to 96 at.% Mn. Figure S.2a displays a 2D intensity map of the integrated area XRD pattern, which were measured across the composition gradient that bisects the film (same measured path as XPS). The vertical lines correspond to specific crystalline peaks,

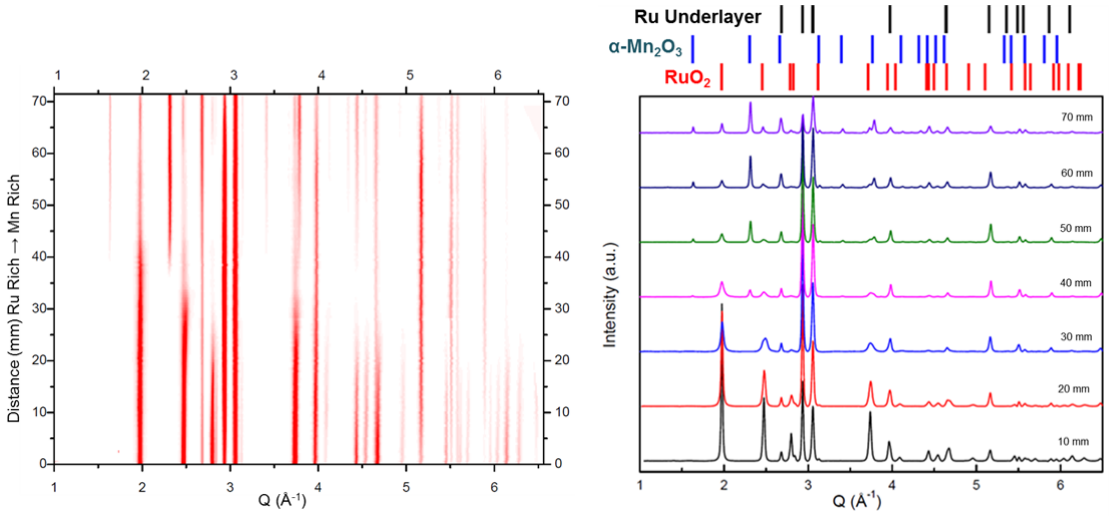

(a) (b)

Figure 5.2: (a) Synchrotron-source area detector XRD scans were integrated along the azimuthal direction (see supplementary). The collection of scans, which are taken along the Mn-Ru oxide composition spread, are spatially stacked and projected as a color map. The color map is comprised of 143 scans taken across the film at 0.5 mm increments. (b) Sample integrated area-detector XRD scans taken in increments of 10 mm across the film. The lines above the figure correspond to theoretical peaks for Ru (black), RuO_2 (red), and Mn_2O_3 (blue).

showcasing structural transitions based on the changing line width and intensity when moving through the composition gradient. Figure S.2b shows select integrated 1D scans corresponding to specific positions indicated on Figure S.2a in increments of 10 mm. Starting from the Ru-rich region (bottom of Figure S.2a), the film maintains a single RuO_2-like rutile structure that extends to ~32 mm,[119] with evidence of lattice strain induced by Mn-doping, forming an atomically mixed cation phase, $Mn_xRu_{1-x}O_{2-y}$. Beyond ~32 mm towards the Mn-rich region, the film appears to contain both Mn-doped RuO_2 and cubic bixbyite $\alpha\alpha$-Mn_2O_3. However, there was no discernable peak shift for α-Mn_2O_3 across the composition gradient, showing no evidence of Ru^{4+} doping the α-Mn_2O_3 lattice frame. The most intense peaks, which appear uniform in intensity across the phase map, corresponds to metallic Ru. However, no metallic Ru peaks were detected from the XRD results on a RuO_2 film and a second Mn-Ru oxide composition spread that were deposited

onto bare silicon, Confirming that the 60 nm Ru underlayer is the source of metallic Ru diffraction.

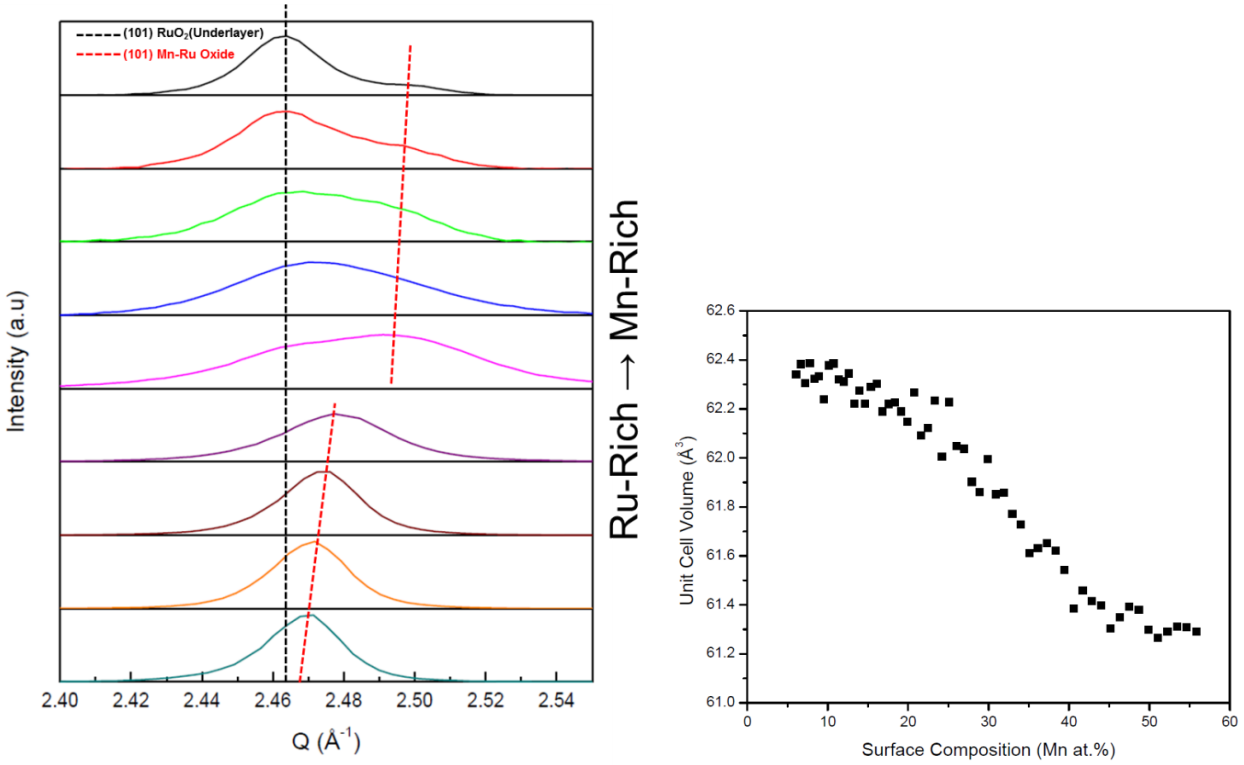

(a) (b)

Figure 5.3: (a) A stacked plot XRD overlay of the RuO_2 (101) peaks of the Mn-Ru oxide composition spread and the RuO_2/Ru underlayer. (b) A plot of the unit cell volume calculated from the a and c constants, inferred from the (110) and (101) RuO_2 peaks, as function of Mn-content.

Evidence of Mn-doping is exemplified by the stacked of (101) RuO_2 peaks shown in Figure S.3a, which clearly to shift to higher Q as the Mn-content increases. The positive shift signifies lattice contraction due to Ru^{4+} (r = 0.62 Å)[181] site substitution of smaller Mn ions, most notably Mn^{3+} (r = 0.58 Å)[181] and/or Mn^{4+} (r = 0.53 Å)[181], though the Mn oxidation states within the film is currently unknown. However, the detection of the single secondary phase, α-Mn_2O_3, may suggest that Mn^{3+} is a possible dopant incorporated into the RuO_2 lattice, which must be charge compensated by the formation of oxygen vacancies. Moreover, similarly doped RuO_2 systems ($Co_xRu_{1-x}O_{2-y}$ and $Ni_xRu_{1-x}O_{2-y}$) showed that the Ru^{4+} sites of RuO_2 can be occupied by lower valence Co^{3+} and Ni^{3+} (oxidation state of Ni changed with composition).[183]

Peak doublets are also observed when the (101) diffraction intensity decreases when ap-

proaching higher Mn compositions (diffraction intensities of each stacked plot are not at the same scale). The lower Q peak of the doublet matches the theoretical $Q_{(101)}$ value of pure RuO_2 (2.456 $Å^{-1}$)[119]. Thus, the doublet may be an overlap of (101) $Mn_xRu_{1-x}O_{2-y}$ and (101) RuO_2 from a partially oxidized Ru underlayer, which likely formed when the sample was heated during reactive sputtering. Figure 3b displays a plot of the rutile $Mn_xRu_{1-x}O_{2-y}$ unit cell volume across the composition gradient. Beginning at the edge of the film within the Ru-rich region, the unit cell volume decreases as the Mn-content increase until reaching a plateau at ~45 at.% Mn (~32 mm), which coincides with the point in which α-Mn_2O_3 begins to form.

The XRD results combined with XPS estimates a composition range for single phase $Mn_xRu_{1-x}O_{2-y}$ ($0.07 < x < 0.45$). However, as previously inferred, the morphology of the Mn-Ru oxide composition spread is not well understood. The possibility of nano-sized or amorphous phase segregated Mn-oxide domains may inflate the composition of Mn, including the saturation point of $Mn_xRu_{1-x}O_{2-y}$. Furthermore, XPS is limited to surface composition, which is problematic if there are large disparities between surface and bulk compositions. Surprisingly, single phase $Mn_xRu_{1-x}O_{2-y}$ has not been reported in literature, suggesting that MnOx and RuO_2 are largely immiscible.[158, 157, 79, 102] Thus, $Mn_xRu_{1-x}O_{2-y}$, may be metastable, which is not uncommon for sputtered systems.[53] Reactive sputtering, coupled with a relatively low deposition temperature of ~350 °C may have imposed kinetic restrictions on phase separation, locking in the intermixed crystal structure.

Figure S.4b,c,d compares cyclic voltammetry (CV) plots taken of representative regions within the film: the Ru-rich region (single phase $Mn_xRu_{1-x}O_{2-y}$), Mn-rich region (where α-Mn_2O_3 is the predominant phase), and the center region (both $Mn_xRu_{1-x}O_{2-y}$ and α-Mn_2O_3 phases present). Each plot contains CVs in nitrogen-bubbled solution, and oxygen-bubbled 0.1 M NaOH solution. Additionally, CVs of RuO_2 (Figure S.4c) and Mn-oxide thin films (Figure S.4e) provide baseline comparisons.

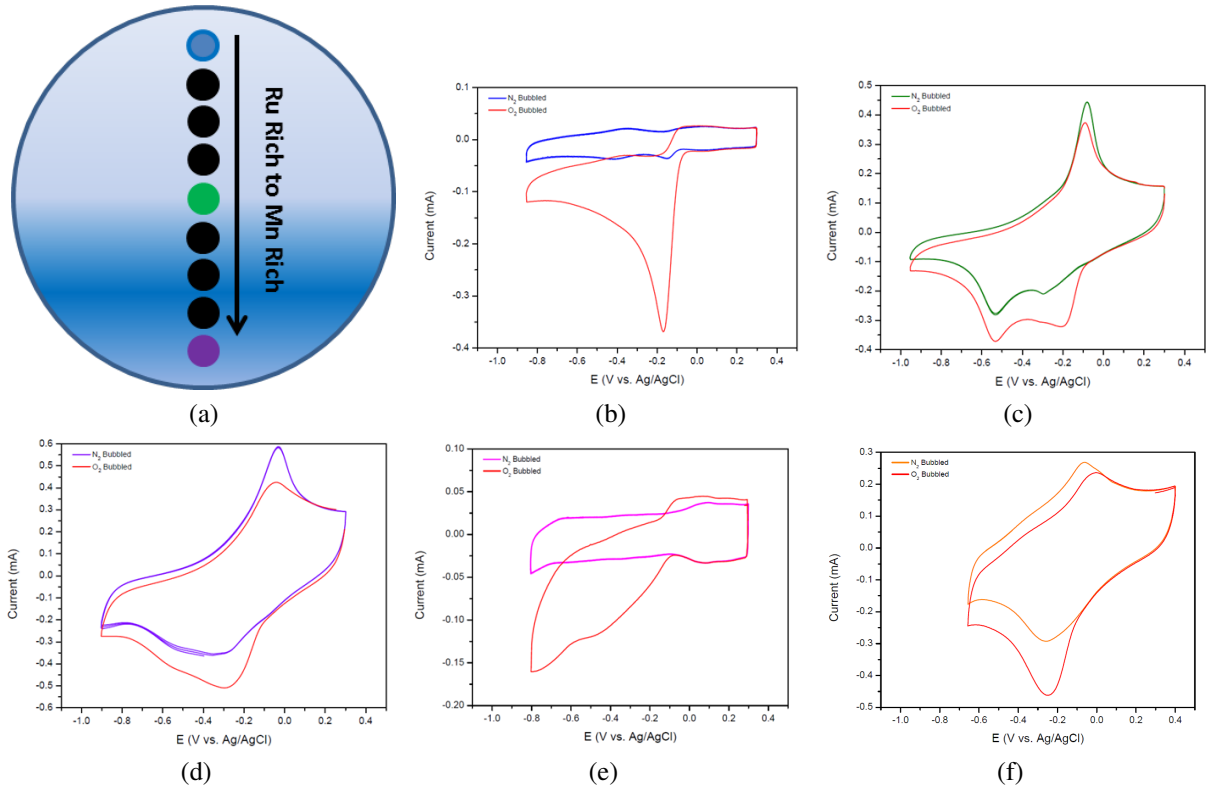

Figure 5.4: Cyclic voltammograms at 50 mV/s in oxygen-bubbled and nitrogen-bubbled 0.1 M NaOH for the ORR catalytic screening (b) Ru-rich, (c) Center, (d) Mn-Rich of the Mn-Ru oxide composition spread. The results were compared to (e) RuO_2 thin film, and a (f) Mn-Oxide thin film.

5.4.2 Oxygen Reduction Catalysis

The background CV of $Mn_xRu_{1-x}O_{2-y}$ within the Ru-rich region shows a mixture of broad peaks corresponding to the surface redox transitions of RuO_2 and Mn-oxide. The cathodic/anodic peaks between 0 and 0.2 V are characteristic of the Ru(IV)/Ru(V) transitions.[80, 25] Moreover, the CV contains additional peaks that are absent from the RuO_2 film; the redox couples between -0.05 and -0.2 V and 0.3 and -0.5 V likely correspond to the Mn(IV)/Mn(III), and Mn(III)/Mn(II) transitions, respectively.[127, 68, 146, 128, 195, 145] The CV features of the center and Mn-rich region matches closely with the Mn-oxide film, identified as α-Mn_2O_3.[69] However, the difference between the center and Mn-Rich region is underscored by the increase in double-layer capacitance and integrated charge of the redox peak between -0.2 and 0 V as the phase composition of α-Mn_2O_3

increases. In general, this behavior is consistent with many Mn-oxides, which are known for their high capacitance and pseudo-capacitance.[104, 266]

Superimposed on the background CVs, the oxygen-saturated CVs (all shown in red) show the onsets of oxygen reduction current. Among the CVs shown, the single phase $Mn_xRu_{1-x}O_{2-y}$ shows the strongest ORR activity as evidenced by the more positive onset potential and strong reduction current within the kinetic regime upon correcting for double-layer current. As expected, RuO_2 is a relatively poor ORR catalyst[25], while the activity of the Mn-oxide film is comparatively better and consistent with previous studies that have noted α-Mn_2O_3 catalysts.[145] However, the Mn-oxide film, based on onset and corrected kinetic current, appears less active than $Mn_xRu_{1-x}O_{2-y}$, suggesting catalytic enhancement thats predicated on the atomic mixing of both RuO_2 and MnOx. The oxygenated CVs of the center and Mn-rich regions are also less catalytic active than $Mn_xRu_{1-x}O_{2-y}$, with the Mn-rich region closely matching the CV of the Mn-oxide film. Therefore, the decrease in activity may be attributed to an increase in phase-segregated α-Mn_2O_3. However, the composition of Mn in $Mn_xRu_{1-x}O_{2-y}$ may also affect the overall ORR activity.

Qualitative ORR activity screening across the entire composition spread is presented in figure 5 along with the activity results obtained on sputtered Pt and RuO_2 for comparison. The region for single phase $Mn_xRu_{1-x}O_{2-y}$ ($0.07 < x < 0.45$) is highlighted within the Ru-rich region in Figure S.5a, as well as the region corresponding to phase segregated $Mn_xRu_{1-x}O_{2-y}$ and α-Mn_2O_3. The most active region of the composition spread, notably contained within the Ru-rich (highlighted by the (*) symbol), is single-phase $Mn_xRu_{1-x}O_{2-y}$ with a surface composition roughly between 12 and 20 at.% Mn; this region has the highest measured E_{Onset} of -55 ± 2 mV, an $E_{1/2}$ of -106 ± 2 mV, and the highest current value (at -100 mV) of -110 ± 3 mA. Furthermore, the most active spot has an activity comparable to that of sputtered Pt; the Eonset and $E_{1/2}$ of Pt are higher by only around 30 and 25 mV, respectively. Beyond the most active spot towards the Mn-rich region, the activity diminishes as demonstrated by the progressive decrease in E1/2 and sharp decrease in kinetic current. This suggests that ORR activity diminishes when the doping composition of Mn

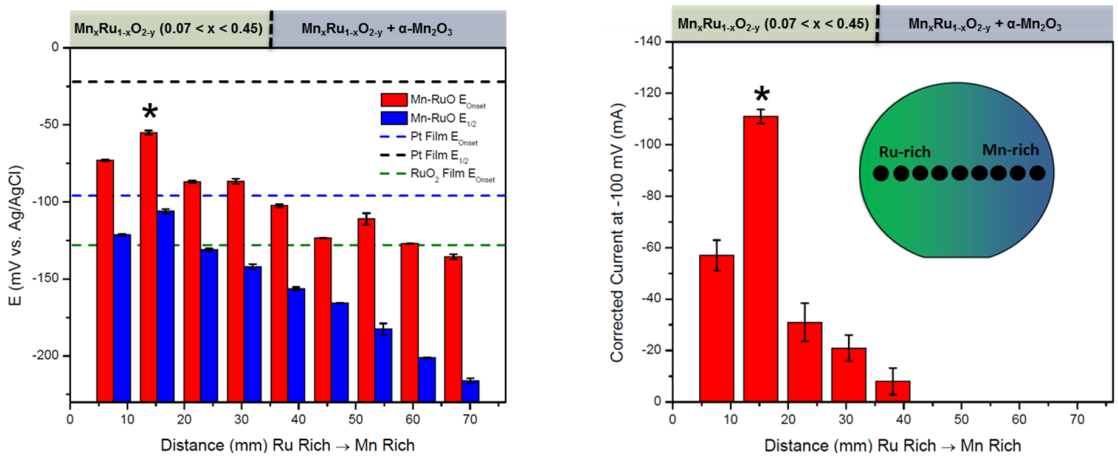

Figure 5.5: Qualitative ORR activity screening across the Mn-Ru-O composition spread along with comparative results from Pt and RuO_2. (a) Onset potential (E_{Onset}) and the half-wave potential ($E_{1/2}$) bar graph along the composition gradient. E_{Onset} is defined at -10 μA relative to the baseline (double-layer) current of the CV. $E_{1/2}$, is defined as the potential half-way between the onset potential and the potential where the peak reduction current is observed. (b) The kinetic reduction current at -100 mV vs. Ag/AgCl along the composition gradient. The was corrected for the doublelayer current.

in $Mn_xRu_{1-x}O_{2-y}$ increases beyond 20 at. % Mn, and when the phase composition of α-Mn_2O_3 increases.

5.4.3 Oxygen Evolution Catalysis

Each spot measured for OER catalysis was cycled between 0.3 to 0.7 V. Figure S.6 displays the OER CVs of the Ru-rich, Mn-rich, and center regions (same regions previously discussed for ORR). Although pure Mn-oxide is not a remarkably active material for OER15, many have sought to utilize manganese as a major constituent in alternative OER catalysts. The notable activity of Mn is seen in CaMn4Ox clusters, which are active water oxidation centers with high turnover frequencies for the naturally ubiquitous photosystem II (PSII)[221, 163], and ternary Mn-based oxides such as Mn-Co spinels and Mn-La perovskites.[106, 123] Additionally, RuO_2 is among the most active materials for OER. As expected, $Mn_xRu_{1-x}O_{2-y}$ is very active for OER

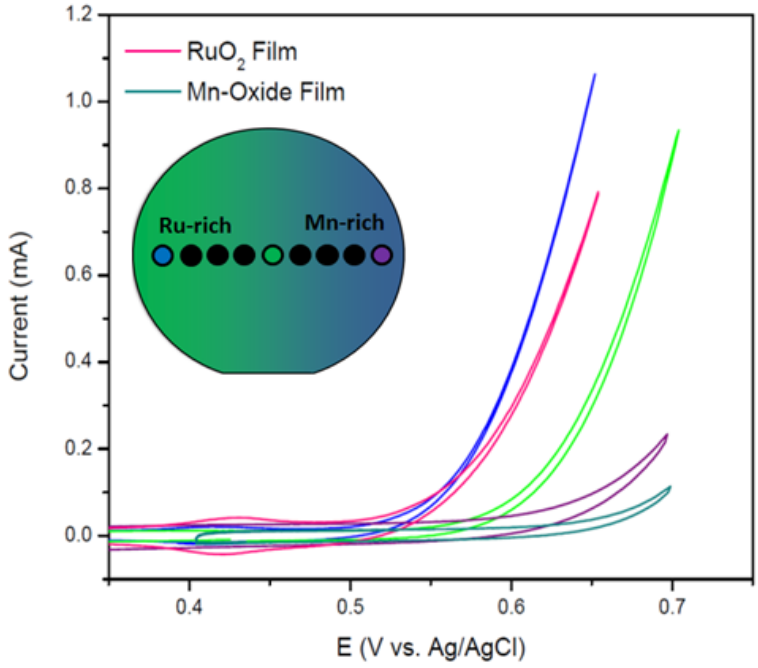

Figure 5.6: Cyclic voltammograms at 20 mV/s in oxygen-saturated and nitrogen-saturated 0.1 M NaOH for the OER catalytic screening between Ru-rich, center, Mn-rich, RuO_2 film, and Mn-oxide film.

catalysis, even slightly better than pure RuO_2, though the difference is too small to discern any perceived enhancement due to Mn-mixing.

Figure S.7 presents the OER screening results across the Mn-Ru-O composition spread. The OER onset potentials (Figure S.7a) were measured at 10 μA relative to the baseline current. The OER current is presented in Figure S.7b, which was obtained at 600 mV upon subtracting the double layer current. The first two spots (tagged by the symbol *) within the Ru-rich region, which contains single-phase $Mn_xRu_{1-x}O_{2-y}$ with compositions ranging from 7 to 20 at.% Mn, are clearly the most active, even showing slightly higher activity than the RuO_2 film. Toward the Mn-rich region, the OER onsets increase and the kinetic current sharply drops, suggesting that the incorporation of Mn beyond ~20 at.% Mn diminishes the OER activity, which is further reduced in regions that contain α-Mn_2O_3. The screening results could not resolve a lower limit on Mn-content to maximize OER activity, suggesting that even trace mixing of Mn may enhance OER activity, though the discrepancy between the active regions and RuO_2 film are too small to conclude that

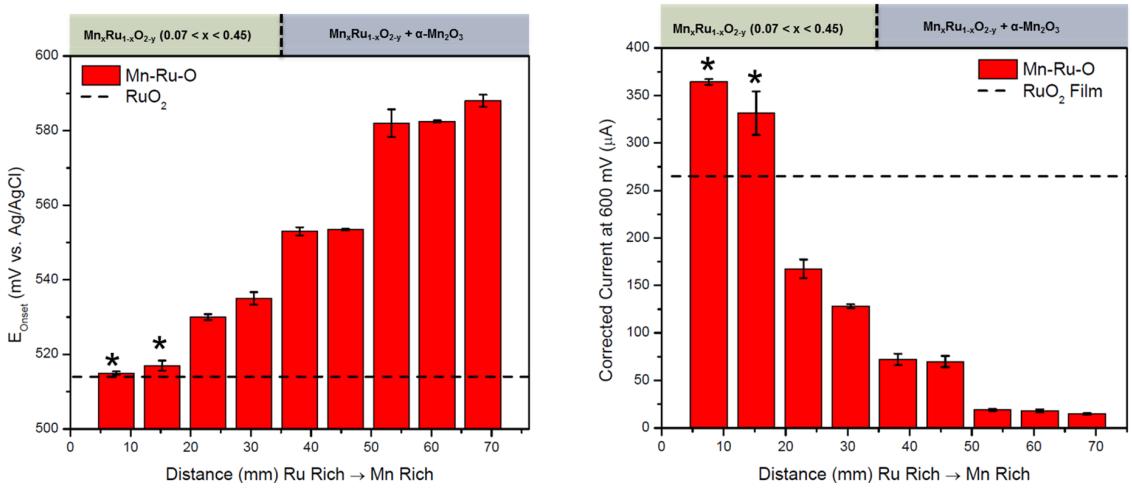

Figure 5.7: Qualitative OER activity screening results compared to RuO_2. (a) Onset potential (E_{Onset}), defined at 10 μA relative to the baseline (double-layer) current of the CV. (b) The kinetic OER current at 600 mV vs. Ag/AgCl corrected for the doublelayer current. The dashed line corresponds to RuO_2 for comparison.

$Mn_xRu_{1-x}O_{2-y}$ is a superior OER catalyst to pure RuO_2.

5.4.4 Rotating Disk Electrode for ORR and OER

As previously shown, the most active region (between 12 and 18 mm in figure S.5 a,b) throughout the Mn-Ru oxide composition spread, has a surface composition ranging from 12-20 at. % Mn, and exhibits the best overall "bifunctional" activity. The optimal region was cleaved into a 9x9 mm piece for thin film RDE testing.

Figure 5.8a shows the ORR sweep of the MnRuO-12/20 sample. The results match well with the CV results obtained by the screening technique, though the RDE sweep curve does show a slight negative potential shift (15-20 mV) compared to the CV result. More importantly, the activity of MnRuO-12/20 is comparable to Pt, separated by only ~50 mV. The OER behavior is also very strong for MnRuO-12/20 as evidenced by figure 8d. In comparison to a sputtered IrO_2 film, the active region of the composition spread is significantly better, although the OER

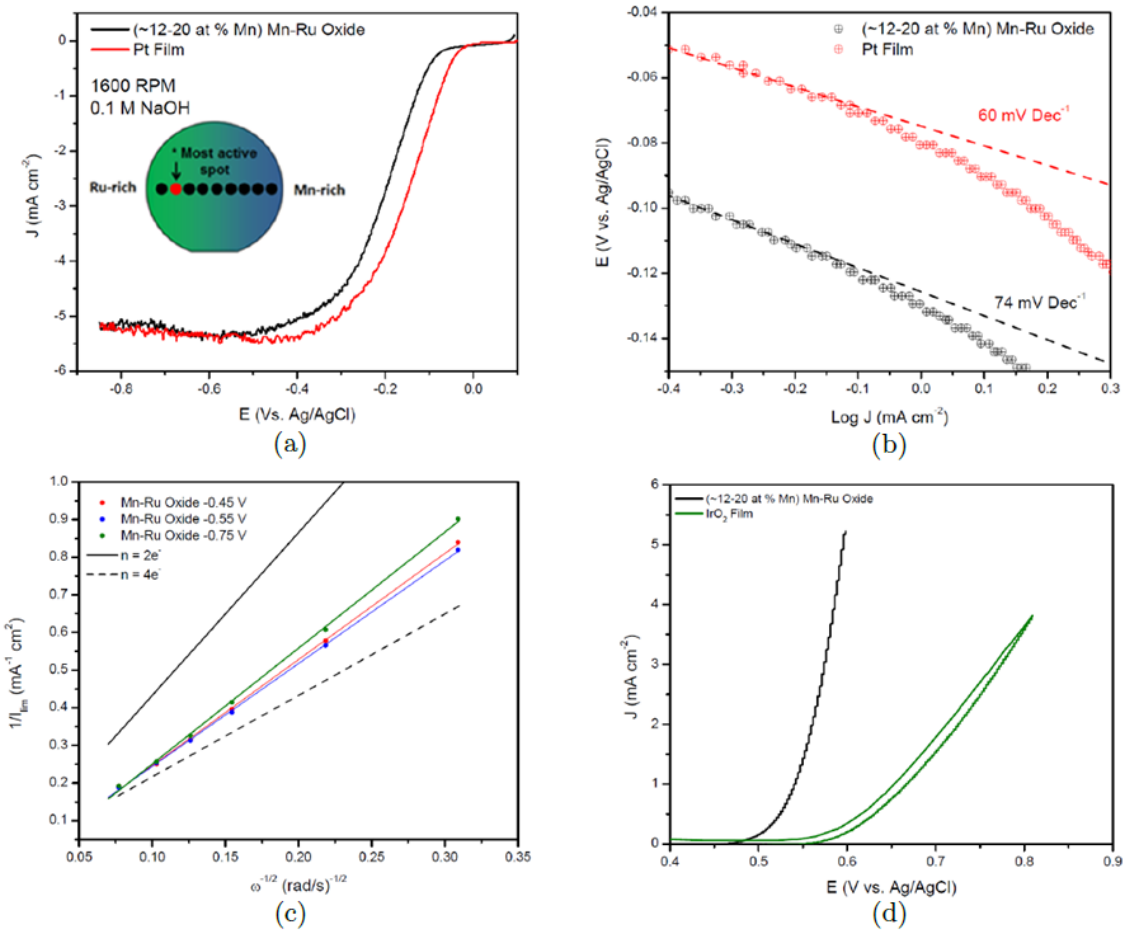

Figure 5.8: (a) ORR RDE 1600 rpm linear sweep voltammetry, (b) ORR Tafel, and (c) Koutecky-Levich plots of 12-20 at.% Mn of Mn-Ru Oxide and a Pt film. (e) OER RDE linear sweep voltammetry 12-20 at.% Mn of Mn-Ru Oxide and Ir_2film.

activity of IrO_2 film is somewhat worse than what has been reported for optimized IrO_2 and RuO_2 catalysts[119, 110], which may be attributed to a lower active surface area for the IrO_2 film. Figure 8b shows the Tafel slopes for MnRuO-12/20 and Pt films obtained at low overpotentials. The Tafel slope for MnRuO-12/20 appears slightly higher at 74 mV/dec compared to the Pt film (60 mV/dec); The slope for Pt is consistent with previous studies of Pt surfaces in acidic and alkaline media.[225] The electron count from the Koutecky-Levich (K-L) plot shown in Figure 5.8c ranges from 2.9 to 3.2 within the mass-transport limited current regime (-0.3 to -0.8 V), similar to the Pt film (2.8 to 3.0). These electron counts indicate a mixture of a two-electron and an indirect four-electron pathway in which peroxide (HO_2^-) intermediates form.

Inferences on the ORR reaction mechanisms on MnRuO-12/20 are highly speculative, though it is apparent from the screening data that Mn plays a significant role in ORR catalysis. Previous studies on Mn-based oxide catalysts have generally agreed that Mn-oxide goes through an indirect reaction pathway, involving a partial reduction of oxygen to form HO_2^- intermediates, which can either form hydrogen peroxide or be further decomposed into OH- through a disproportionation step with neighboring HO_2^- intermediates.[127, 22] Because of the variations between different Mn-oxide types, the electron transfer efficiency varies widely, ranging from pure peroxide formation (n=2) to complete decomposition to OH^- (n = 4). Moreover, some studies have emphasized the role that the Mn(IV)O2/Mn(III)OOH redox couple plays in the ORR activity by acting as an acceptor/mediator for electron transfer as supported by in-situ XANES.[22, 195] In the case of RuO_2 in alkaline solution, the reduction reaction primarily prefers the two-electron pathway to form H_2O_2 due to the strong binding energy of oxygen on Ru sites.[281]

Regardless of the exact catalytic nature of $Mn_xRu_{1-x}O_{2-y}$, it is clear that the combination of Mn-oxide and RuO_2 facilitates a certain type of synergistic enhancement for ORR activity. This effect may be due to improved electronic conductivity and/or a greater tunneling pathway as a result of well-dispersed reactive Mn-centers within a RuO_2 lattice frame, similar to the coupling behavior observed in Mn-oxide dispersed on precious metal, graphene or carbon nanotubes (CNT) supports.[149, 179] Also, based on the extensive DFT studies on Pt-alloy systems and perovskite oxides[94], one may also consider the electronic coupling effects of RuO_2 when doped with Mn, or specifically the effects of Mn doping on the d-band centers of RuO_2, descriptors for the balance between the oxygen binding and oxygen bond-breaking energies that govern ORR catalysis.[238]

5.5 Conclusion

We evaluated a wide range of Mn-Ru oxides in the form of composition spread thin films. By employing synchroton-source XRD mapping and electrochemical screening for ORR and OER,

we discovered a highly active composition range that forms a unique mixed cation rutile oxide structure, $Mn_xRu_{1-x}O_{2-y}$ ($0.07 < x < 0.45$). The most active composition range was found between 12 to 20 at. % Mn. Through thin film RDE, the catalytic activity of the optimal composition region of Mn-Ru oxide was confirmed to be comparable to Pt for ORR, and RuO_2/IrO_2 for OER. RDE analysis yielded an electron transfer number ranging from 2.9 to 3.2, indicating a mixed two-electron and partial four-electron pathway. It is clear that mixing Mn and Ru oxide enhances ORR activity while maintaining good active OER activity, and thus a promising alternative bifunctional catalyst.

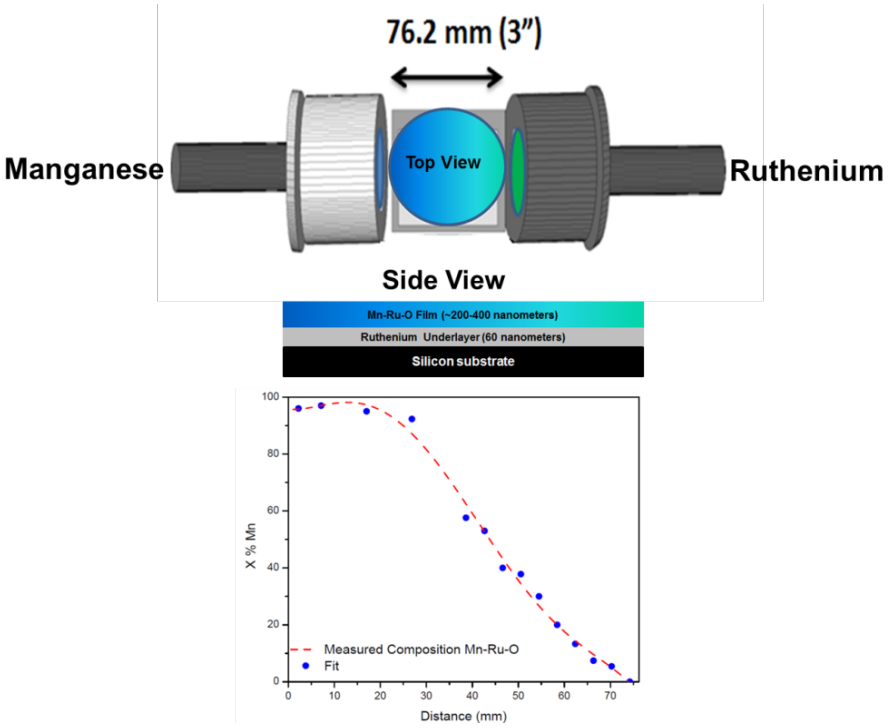

Figure S.1: Illustration of off-axis co-sputtering and cross section of Mn-Ru oxide composition spread.

5.6 Supplementary

Non-uniform (150-400 nm thick) binary manganese-ruthenium oxide (Mn-Ru-O) composition spread thin films were deposited onto 76.2 mm (3") diameter silicon (100) wafers using

an off-axis reactive radio frequency (RF) co-sputtering system. Figure S.1 illustrates the off-axis co-sputtering configuration for fabricating binary Mn-Ru oxide composition spreads. The film was co-sputtered for 20 minutes on a heated (~350 °C) substrate holder. Films that were used for electrochemical testing were first coated with a 60 nm Ru metal layer using direct current (DC) sputtering in 10 mTorr Ar; the Ru underlayer is a conductive backing required for electrochemical testing in order to minimize the resistance drop across the area of the composition spread film. Each film was then placed in the vacuum chamber until a base pressure of ~2 x 10^{-6} Torr was reached. Subsequently, a steady flow of 40 sccm Ar and 10 sccm O2 gas (20% O_2) was introduced to obtain a partial pressure of 30 mTorr. Prior to co-sputtering, a 10-15 minute pre-sputter step was taken to clean the target surfaces as well as develop a steady sputter rate.

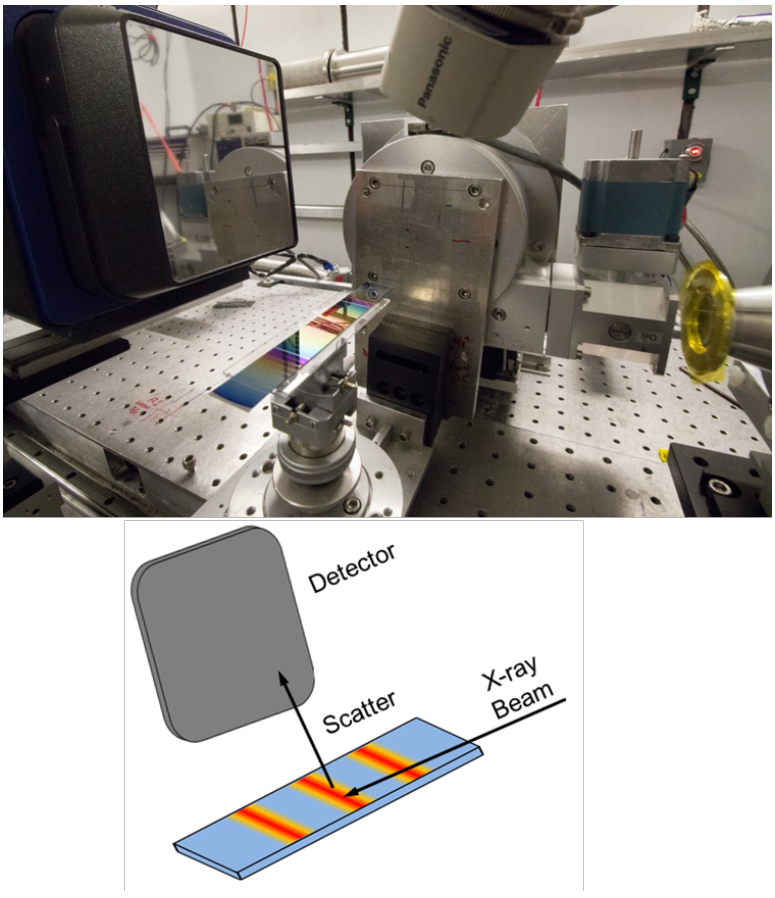

Figure S.2: Picture and illustration of the CHESS XRD reflection setup.

5.6.1 Characterization

High-energy fixed-angle area detector synchrotron source XRD measurements were taken across the Mn-Ru oxide composition spreads at the Cornell High Energy Synchrotron Source (CHESS). A 19.6582 keV beam that was reduced to a 25x200 μm rectangular spot size using knife-edge slits, and incident at a fixed angle ranging from 7-5° relative to the film plane (Figure S.3). The scattered X-rays were detected using a Pilatus 2k area detector. The sample was placed on top of a moveable stage, and 143 XRD measurements were taken across the composition gradient of the film in 500 μm step increments. The long dimension of the beam spot was oriented perpendicular to the composition gradient to minimize the composition range under the beam spot. The Ru metal under-layer acted as a suitable calibration standard to accurately infer the sample-to-detector distance during post-experiment analysis.

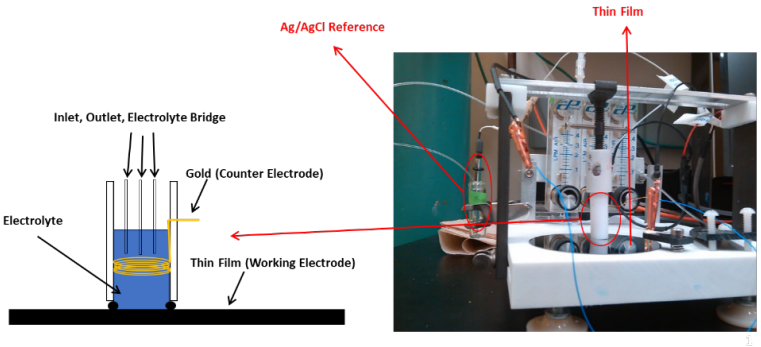

Figure S.3: Illustrative cross-section and picture of electrochemical minicell setup.

5.6.2 CV Measurements

The ”Minicell” is a quasi-high-throughput test cell designed to locally measure the catalytic activity of ORR and OER at the film/electrolyte interface, allowing the user to screen the entire material library across the film. The apparatus is a custom-built three-electrode cell connected to a potentiostat controlled by a custom LabView program by which the scan rate, voltage range, voltage gain are set and adjusted. Figure S.3 shows both an illustration of the cell cross-

section and a photo of the actual setup. The composition spread thin film rests on top of a flat platform, the base of the minicell setup. Connected to the platform are two supports for a flat steel plate with a built-in slit, which is connected to the top of the test cell by a rotatable flat head screw. The cell can move laterally above the film and manually lower onto a chosen test spot. Manual XY movement of the cell is facilitated by sliding the screw that is connected to the cell along the slit embedded into the overhead plate, and moveable supports that slide along grooves along the sides of the platform.

The test cell is a hollow Teflon cylinder that locally interfaces with the surface of the film, which is designated as the working electrode. The test area has a diameter of 6 mm. During testing, the analyte is sealed inside the cell by a rubber O-ring that fits around the bottom lip of the cylinder. The interior wall of the cylinder is lined with a coiled gold (Au) auxiliary wire. The interior also contains three thin plastic tubes located near the bottom of the cell (close to the film surface when interfaced). The other ends of the tubes protrude from the top of the cell. Two of the three tubes function as an inlet and outlet for injecting and removing electrolyte solution, respectively, while the third tube functions as an electrolyte bridge between the film and the reference electrode. Capillary forces along the tube help maintain a continuum of analyte solution between the cell and the RE container. The reference electrode is a silver/silver chloride Ag/AgCl wire in saturated KCl (stable potential of 0.197 V vs. SHE). The reference is sealed within a glass tube, and is held within a separate container filled with the same analyte as the cell. The choice of housing the reference electrode in a separate container, as opposed to situating it near the film surface to minimize uncompensated resistance, was done to avoid chloride (Cl^-) contamination of the Au counter electrode and the film surface.

A series of cyclic voltammetry measurements were taken across the composition spread to screen the ORR and OER catalytic activities of the film. Each measurement was taken at room temperature in 0.1 M NaOH alkaline solution. Each spot was initially cycled at 50 mV/s in N_2 saturated solution for 15-30 minutes to determine the background CV hysteresis. No reduction

pretreatment step was taken prior to testing in order to avoid the risk of irreversibly reducing the oxide surface. The potential range in which each surface was cycled was typically within a range that did not expand beyond the -0.8 to 0.2 V window. The N_2 saturated solution was subsequently removed from the cell, and replaced with an O_2-saturated solution. Beginning the scan at a potential above the onset of oxygen reduction, a cathodic sweep was performed to determine the ORR current. Because the oxygen near the film surface quickly depletes during reduction, the solution is removed and replaced with fresh oxygenated solution after the first cycle and repeated 5-6 times to establish consistency, as well as quantify variations in our activity results. The potential window for OER was between around 0.3-0.7 V, and cycled at a reduced scan rate of 20 mV/s to reduce the risk of forming oxygen bubbles. After the first CV cycle, the new solution was introduced, and the measurement was repeated. Similar to ORR, 5-6 first-cycle measurements were taken to ensure consistent outputs. The primary metrics used to qualitatively measure ORR activity was our defined onset potential, half-wave potential, and kinetic current at a potential of -100 mV vs. Ag/AgCl (within the kinetic regime). Our defined onset potential was the potential at -10 μA relative to the capacitive baseline current. Our defined half-wave potential, which slightly deviates from technical definition, was defined as the half-way between our defined onset potential and our peak current potential. For OER, the onset was defined as the potential at which the current is at 10 μA relative to the baseline.

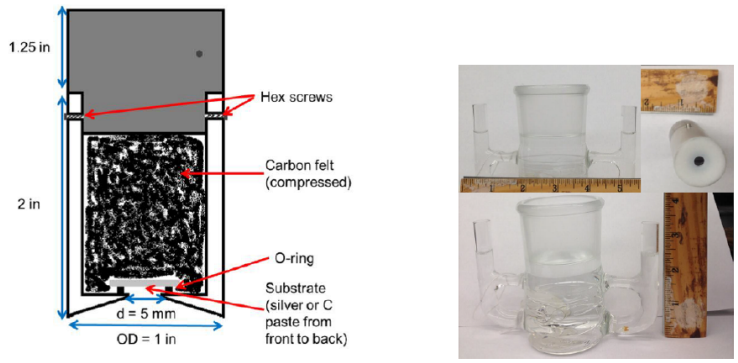

Figure S.4: Illustrative cross-section of RDE rod, including film, carbon felt, and steel backing. Picture of RDE glass basket.

5.6.3 Rotating Disk Electrode Measurements

The modified thin film RDE setup shown in Figure S4 shows an illustration of the cross section of the 1 inch diameter hollow Teflon cylinder used to hold a 10 x 10 mm thin film (cleaved from the composition spread). A 5 mm diameter surface area of the sample film is exposed at the bottom end of the cylinder, which slightly recesses from the outer periphery towards the planar film surface. The lip of the opening has a 0.25" O-ring, forming a tight seal with the film. Before placing the cleaved film inside the Teflon cylinder, the sides and back of the film are coated with silver paste and heated slightly to remove the solvent. This ensures contact with the carbon backing. Once the film is placed inside, the rest of the cylinder is filled with carbon felt (Alfa Aesar) and capped with a custom-made, stainless-steel current collector, which is tightened using a vice, and held together with hex screws.

The RDE cylinder was tested within a three-compartment cell (Figure S.3). The main chamber is 2" wide with an inner glass basket to prevent cavitation (whirlpool). The three compartments are connected at the bottom with glass frits, and at the top with simple glass tubing (to equalize the pressure in the three compartments). A graphite rod (Sigma Aldrich) was used as the counter electrode and a home-made saturated silver/silver chloride electrode (Ag/AgCl) was used as the reference. No platinum (or any noble metals) was used in the cell to ensure that there was no contamination from trace Pt from previous experiments. After any tests involving Pt and Au films, the cell is typically soaked in aqua regia for several hours to remove any residual noble metals.

5.6.4 XPS Surveys

Multiple XPS survey scans were taken across the composition spread and analyzed using CasaXPS software. The Mn2p and Ru3d peaks were integrated to calculate the surface composition. Although the Ru 3d electrons between 250 and 300 eV registered the strongest signal, the

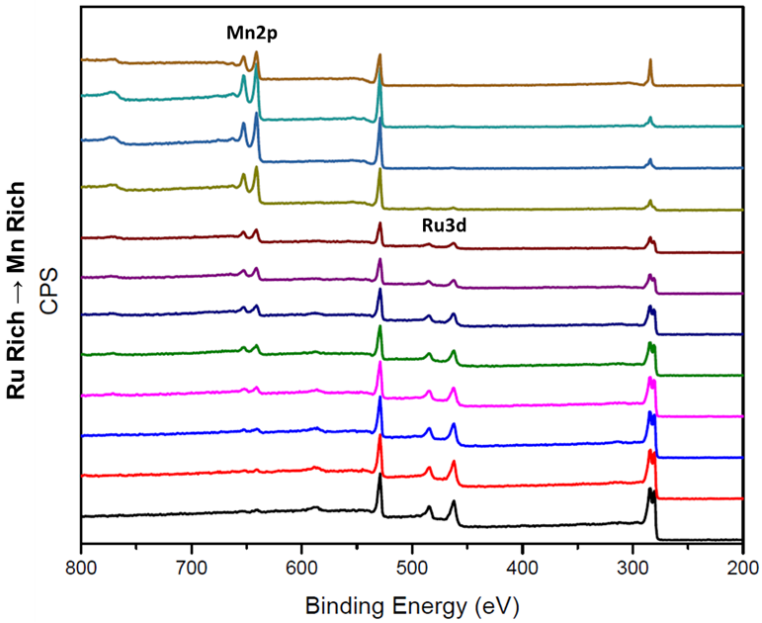

Figure S.5: Stacks of XPS survey scans of Mn-Ru oxide composition spread between 200 and 800 eV.

peaks were convoluted by an overlap with the C1s peak at 284 eV.

5.6.5 CV Results

Nine local CV measurements were taken across the Mn-Ru oxide spread using the method detailed earlier. The CVs shown in Figure S.6 are for measuring ORR activity. Figure S.7 shows the 9 CVs to measure OER activity within a potential window of 0.3 to 0.7 V vs. Ag/AgCl (spot C was swept to 0.75 V and spot D was swept to 0.25 V)

5.6.6 XRD Results

High energy area XRD was performed at CHESS to generate 143 separate images taken at 500 m steps across the composition spread. Figure S.8 shows some of the representative area scans. The bright spots and broad streaks correspond to thermal diffuse scattering (TDS) from the

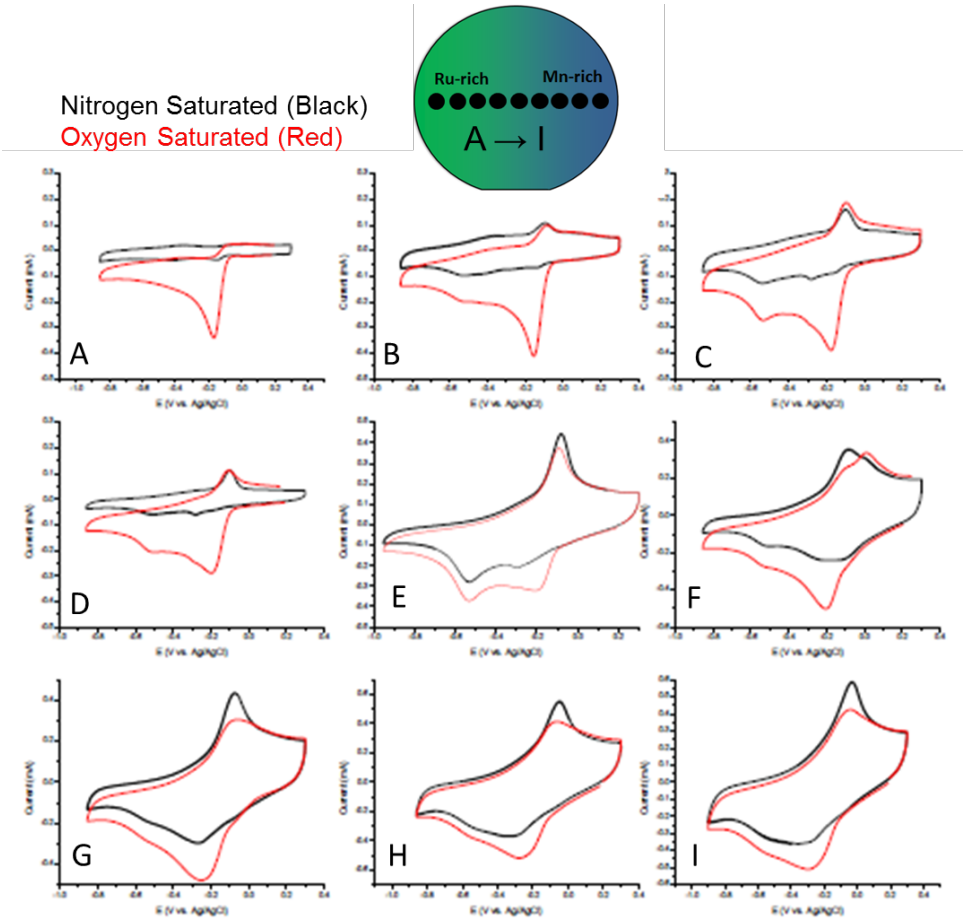

Figure S.6: Minicell ORR CVs across the entire Mn-Ru oxide composition spread.

silicon substrate. The films also show some variations in ring intensities, indicating some degree of film texture. For each image using an XRD analysis program called Igor, the background signal was reduced by masking the TDS. The Q space was then calibrated based on the peak placement of the Ru underalyer. Selected areas were then integrated to generate the 1D patterns. The residual background signal in each pattern was subtracted piecewise using a very basic Python fitting routine.

One of the major observations reported in the heat map (Figure S.2a) was the presence of strong peaks corresponding to metallic Ru. We were able to confirm that the Ru footprint came from the Ru underlayer measuring the XRD patterns of an RuO2 film, which was sputtered under the same conditions as Mn-Ru oxide in the absence of co-sputtering, and a single spot within the

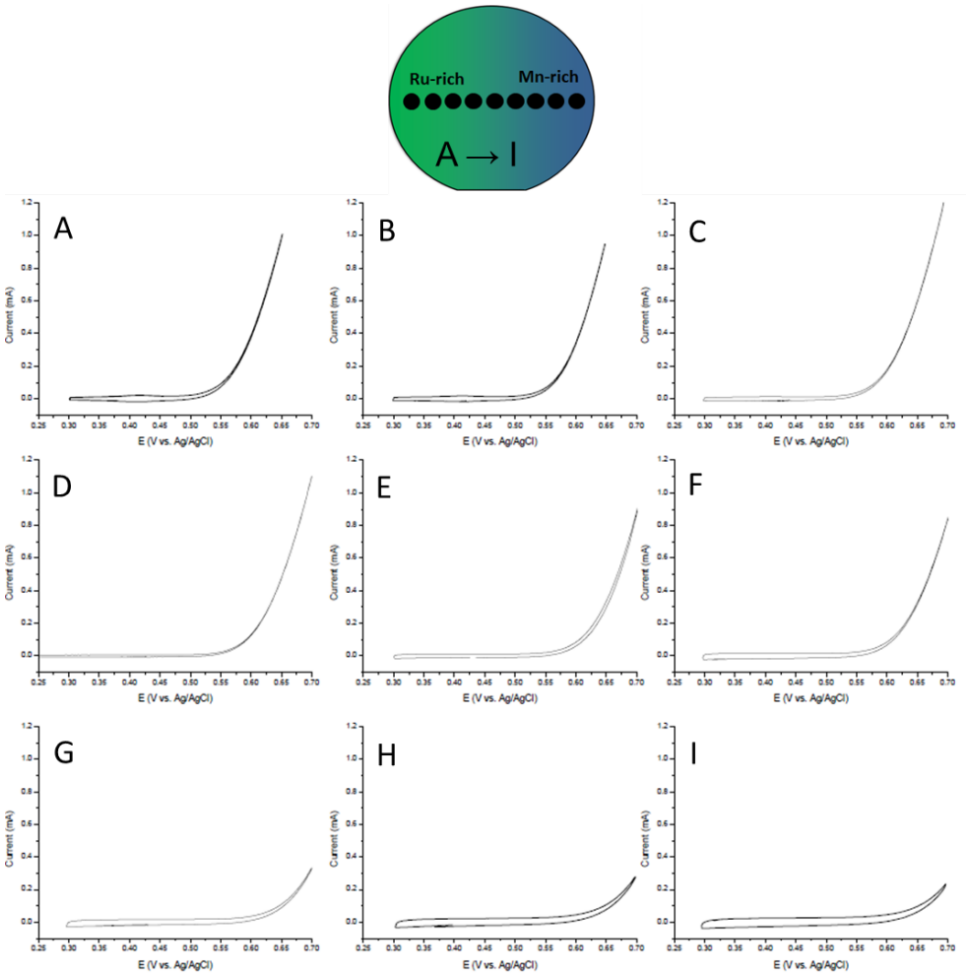

Figure S.7: Minicell OER CVs across the entire Mn-Ru oxide composition spread.

Ru-rich region on the MnRuO composition spread on bare silicon. Figure S.9 shows the integrated patterns for both films, which show no peaks corresponding to metallic Ru, particularly the (110) and (101) peaks, which are most prominently observed at 1.974 and 2.45 $Å^{-1}$. It should be noted that the RuO2 film was not measured at CHESS, but at the Cornell Center for Materials Research (CCMR) using the Bruker AXS general area detector diffraction system (GADDS). Another important note is that the pattern for the Mn-Ru oxide was not calibrated, meaning the peak placement is not accurate. Regardless, the absence of strong Ru peaks is sufficient evidence.

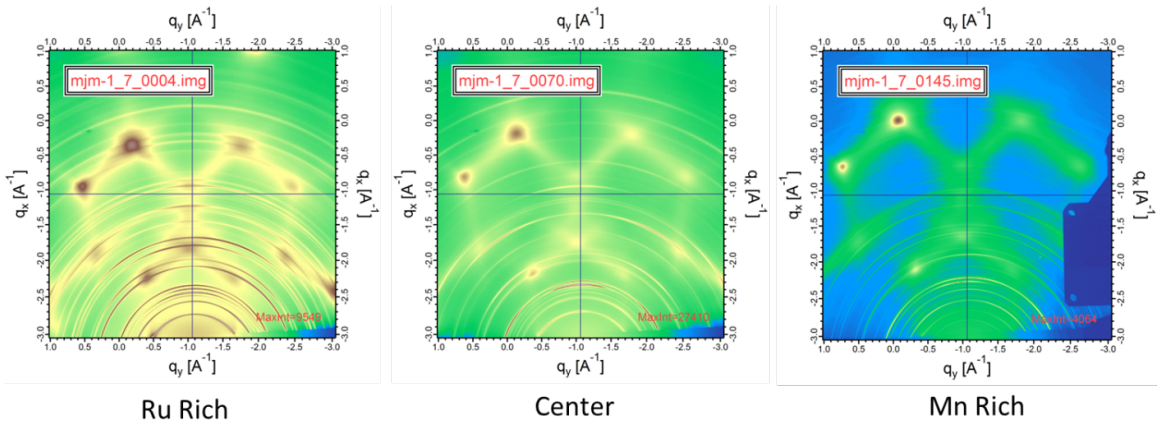

Figure S.8: Representative CHESS XRD area images of the Ru-rich , center and Mn-rich regions.

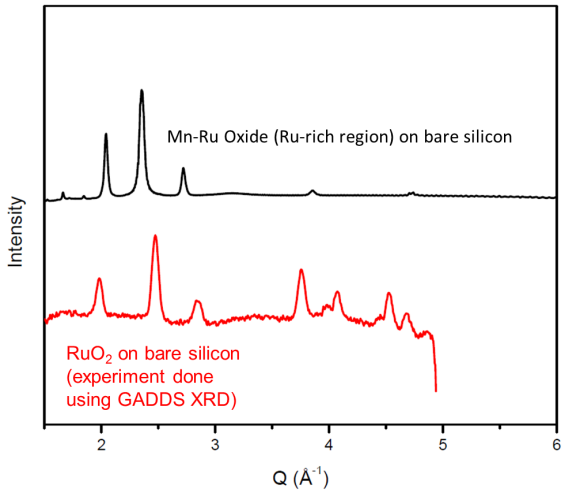

Figure S.9: Integrated XRD patterns of Mn-Ru oxide (black) composition spread and RuO2 (red) on bare silicon.

CHAPTER 6

MANUSCRIPT - COMBINATORIAL HIGH THROUGHPUT OXYGEN REDUCTION STUDIES ON LEAD-IRIDIUM OXIDE

6.1 Abstract

Renewed interests in low temperature alkaline fuel cells have spurred active research on alternative non-Pt oxygen reduction catalysts, most notably metal oxides, given the expansive library of alkaline-stable materials. Exploring the massive class of metal oxide catalysts, especially when comprised of two or more constituents, fully necessitates combinatorial high-throughput synthesis and electrochemical approaches to facilitate rapid ORR activity screening. In this study, we demonstrate high-throughput ORR catalysis screening on a lead-iridium oxide composition spread (5-92 at.% Pb) thin film using electrochemical test cells designed to locally measure ORR activity sequentially across the composition gradient. Active regions were then identified and tested using a modified thin-film rotating disk electrode setup. Two phases were or notable interest for ORR catalysis: non-stoichiometric solid solution $Pb_2[Pb_xIr_{2-x}]O_{7-y}$ pyrochlore, and Pb-doped rutile IrO2 ($Pb_xIr_{1-x}O_{2-y}$). While $Pb_2[Pb_xIr_{2-x}]O_{7-y}$ is known to exhibit strong bifunctional activity, the Pb-doped rutile $Pb_xIr_{1-x}O_{2-y}$ phase has not been previously evaluated as an oxygen catalysts, though the thin film compound showed similar catalytic ORR activity to the pyrochlore phase.

6.2 Introduction

Widespread commercial integration of low temperature fuel cells has long been a stated goal amongst several invested in building a robust clean energy landscape as part of the global initiative to reduce our carbon footprint. However, poor oxygen reduction reaction (ORR) kinetics at the cathode continues to be a major performance inhibitor, compounded by the heavy commercial

dependence on platinum-based catalysts. Over the years, there have been concerted efforts in advancing alternative electrocatalysts comprised of more abundant and less expensive materials that can exhibit comparable ORR activities to Pt. Although the acidic environment found in proton-exchange membrane fuel cells (PEMFCs) significantly limits the library of compatible alternative electrocatalysts, the transition to anion exchange electrolytes for alkaline fuel cells (AFCs) facilitates a far greater selection of stable and ORR active cathode materials; this includes metal and nitrogen-doped nanostructured carbon[263, 125, 66, 189, 17], transition metals[141, 93] and complex metal oxides.[110, 238, 174]

In particular, metal oxides represent an intriguing class of potential ORR catalysts, exhibiting wide ranging and tunable properties due to their high degree of structural tolerance for lattice distortion, oxygen vacancy formation, and cationic substitution. More specifically, several unique oxides have demonstrated strong catalytic activity for ORR, including perovskites[246, 81, 107, 283, 238], spinels[122, 27, 131, 126, 237], manganese oxide-based systems[113, 127, 146, 49, 145, 150, 29, 22], and pyrochlores.[95, 97, 4, 48, 236]

Select compounds within the pyrochlore ($A_2[A_xB_{2-x}O_6O']$ (A = Bi, Pb; B = Ir, Ru)) family have previously been reported as strong ORR catalysts with metallic conductivity and high surface areas, thereby functioning as viable stand-alone cathode catalysts.[97, 95, 96, 15, 186] Subsequent studies extensively evaluated the effects of pH[186, 67], oxygen vacancy concentration[60] and B-site substituted composition[96] on the mechanisms that govern the overall ORR activities. In this study, we electrochemically screen and evaluate active regions for ORR of co-sputtered lead-iridium (Pb-Ir) oxide composition spreads, which notably contains two composition-varying phase regions: solid-solution pyrochlore ($Pb_2[Pb_xIr_{2-x}]O_6O'$) and Pb-doped rutile IrO2 ($Pb_xIr_{1-x}O_{2-y}$).

Consequently, systematic navigation through the massive library of complex oxides comprised of two or several distinct elements with efficacy and expedition demands a combinatorial high-throughput approach to facilitate rapid electrochemical screening.[162, 152] Many of these high-throughput electrochemical approaches have been thoroughly demonstrated optically[152,

182], and sequentially[55, 134] on a number of different material combinations, and catalytic processes. Oxygen reduction screening coupled with modified characterization methods provides a broad range of information regarding catalytic and structural trends for Pb-Ir oxide.

6.3 Experimental Section

6.3.1 RF Reactive Co-Sputtering

Lead-iridium (Pb-Ir) oxide composition spread thin films were deposited using an off-axis reactive RF magnetron co-sputtering (summarized in a previous study)[46]) on 76.2 mm diameter Si substrates (See Supplementary for system description and configuration). Each substrate contained a thin SiO_2 buffer layer act as a diffusion barrier. Prior to deposition, the SiO2/Si substrate was loaded into the chamber and evacuated to a base pressure of $\sim$ 2 x 10^{-6} Torr. Two inch diameter metal Pb and Ir targets were then co-sputtered in a 15/10 sccm Ar/O_2 reactive gas mixture maintained at an intermediate partial pressure of 30 mTorr. Both targets were pre-sputtered for 15 minutes prior to a 30 minute co-sputter step, producing a highly intermixed film with a continuous composition gradient across diameter of the substrate. The applied power to Pb and Ir were calibrated to 20 to 25 W in order to approximately set a 1:1 composition ratio at the center of the film with a thickness range of 150-400 nm. Upon deposition, the Pb-Ir oxide composition spreads were annealed in an air furnace for 1 hour at 600 °C. Although the Pb-rich region was non-conductive, the pyrochlore and Ir-rich regions of the composition spread were conductive enough for electrochemical screening without any substantial Ohmic losses through the film.

6.3.2 X-ray Diffraction

Theta/2Theta X-ray diffraction was performed on multiple spots across the Pb-Ir oxide spread using a Rigaku Smartlab system equipped with a Cu-kα X-ray (λ = 1.54059 nm) source to identify the local oxide phase(s), and the structural transitions as a function of composition.

6.3.3 Synchrotron-Source X-ray Fluorescence

Synchrotron X-ray fluorescence (SXRF) measurements were taken at the Cornell High Energy Synchrotron Source (CHESS) using a state-of-the-art solid-state detector array that facilitates high-resolution composition imaging.[220, 204] A high energy synchrotron-sourced X-ray (31.9 KeV) was incident perpendicular and scanned across the entirety of the film in increments of 200 μm, rendering a detailed composition image. Measurements were intermittently calibrated using the measured XRF spectra of a nickel foil. The compositions corresponding to each imaged pixel was fully quantified using real-time dynamic analysis of the XRF spectra during measuring, particularly the L-edge peaks of Ir (9.174 keV) and Pb (10.550 keV). The analytical XRF software used for dynamic analysis was Geopixe, developed by the Commonwealth Scientific and Industrial Research Organization (CSIRO) in Australia.[204] Dynamic analysis consisted of least-squares fitting followed by rapid deconvolution into linear combinations of the elemental signatures, which were expressed as inverse matrices, and subsequently transformed into an area mass concentrations of Pb and Ir. The mass concentrations were then normalized as a Pb/Ir composition map.

6.3.4 Electrochemical Screening-Cyclic Voltammetry

Screening the ORR activity across the Pb-Ir oxide composition spread was performed using a custom-built three-electrode cell apparatus that locally interfaces with the film surface (desig-

nated as the working electrode). The electrochemical cell consists of a cylindrical Teflon container that locally seals the electrolyte solution with the film, yielding a 6 mm diameter geometric surface area. The film was electrolytically driven by a BAS CV-27 potentiostat against a KCl-saturated Ag/AgCl reference electrode. The cell contains a high surface area counter-electrode in the form of a long Au wire coiled along the Teflon cell wall interior. A series of cyclic voltammetry (CV) measurements were taken across the composition spread at room temperature in 0.1 M NaOH alkaline solution. Each spot was initially cycled at 50 mV/s in N_2-saturated solution for 15-30 minutes to measure the background CV hysteresis within a -0.7 to 0.2 V window. The N_2-saturated solution was subsequently removed from the cell, and replaced with an O_2-bubbled solution, and cathodically scanned at a starting potential well above the expected onset. Because the oxygen near the film surface quickly depletes during reduction, the electrolyte was removed and replaced with freshly oxygenated solution after the first cycle. First cycle oxygenated CV measurements were then repeated 3-4 times to establish consistency.

6.3.5 Thin Film Rotating Disk Electrode

Active regions that were identified after ORR screening were cleaved from a newly deposited Pb-Ir oxide composition spread into 9x9 mm pieces, and placed in a specialized one inch diameter Teflon cylinder designed for thin film RDE testing. The test end of the RDE holder exposes a 5 mm diameter geometric area of the cleaved film (See Supplementary for RDE holder design). The back of the cleaved film was coated with a thin layer of silver paint as a conductive contact with tightly packed carbon felt (Alfa Aesar), which was capped with a custom-made, stainless-steel current collector. The RDE holder was then mounted onto a PINE rotator connected to a potentiostat and immersed in 0.1 M NaOH aqueous solution.

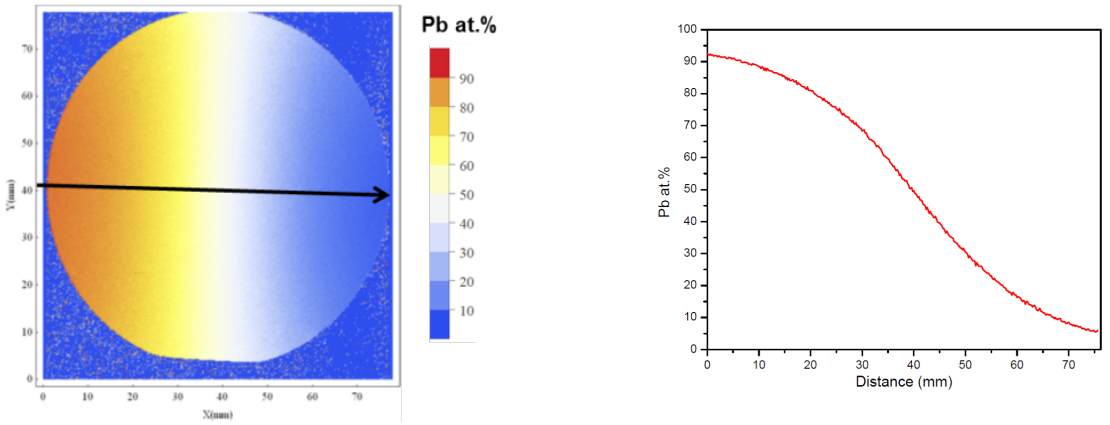

(a) (b)

Figure S.1: (a) Pb composition map from XRF imaging. (b) Pb composition profile across the center of the Pb-Ir oxide composition spread.

6.4 Results and Discussion

Figure S.1a shows the rendered image of the Pb composition distribution for the entire Pb-Ir oxide film. The imaged pixels were calculated from SXRF spectral fitting and dynamic analysis (DA) of the Ir and Pb L-edge peaks. The DA matrix was then transformed into area mass densities, and subsequently normalized to their atomic compositions. Figure S.1b trends the composition of Pb along the cross-section of the film through the center, showing a range of 5 to 92 at.% Pb with an approximate 1:1 Pb/Ir atomic ratio at the center. The contours perpendicular to the sampled cross-section show vertical composition uniformity orthogonal to the lateral gradient, only showing slight curvature near the left and right edges of the film.

The as-deposited Pb-Ir oxide film was initially amorphous, and the majority of the film fully crystallized upon annealing in air at 600 °C. Despite the high temperature anneal, the Pb-rich region (> 76 at.% Pb) showed no discernable diffraction peaks corresponding to any form of PbO_2 other than a broad low angle amorphous peak. Although the absence of crystallinity is confounding, Pauleau et al. did report wide variations in the resulting phase structures and morphology of lead-oxide films as a function of oxygen content, including amorphous Pb-oxide

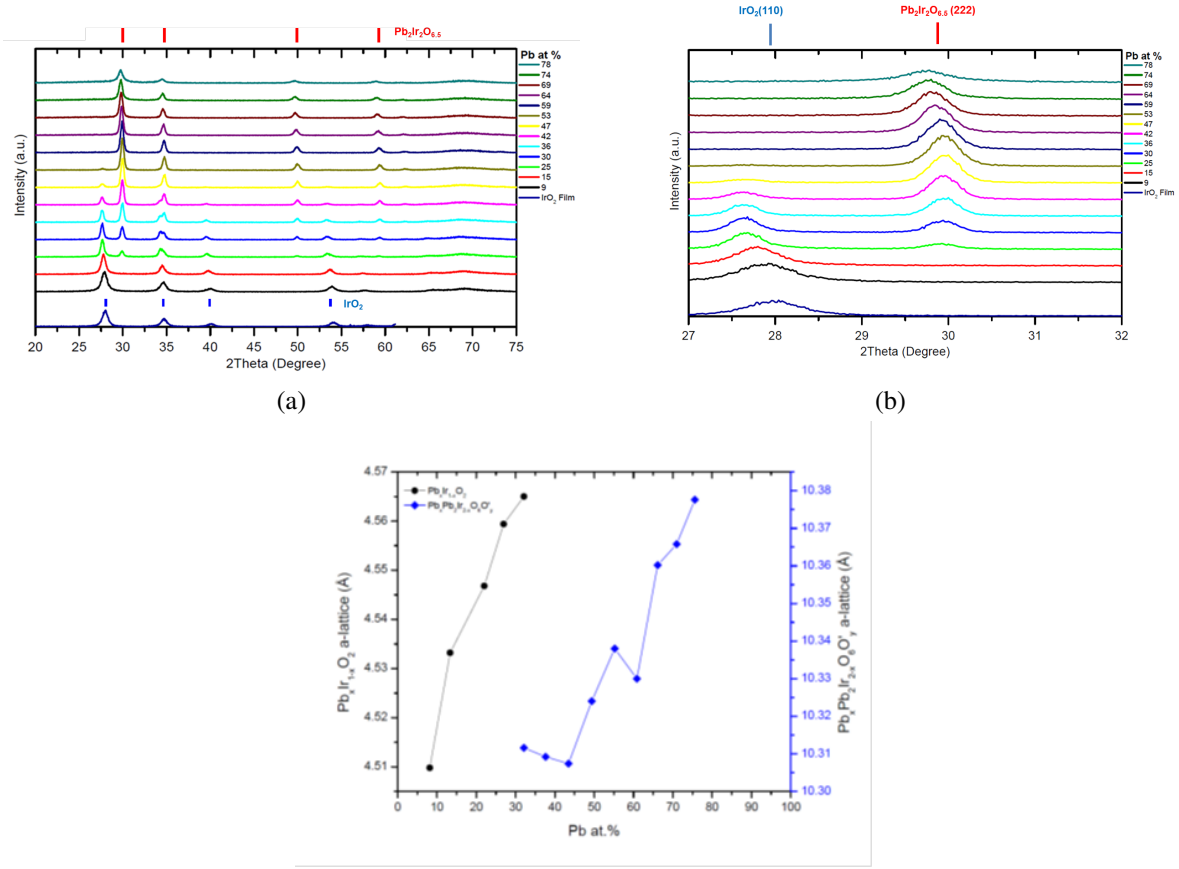

Figure S.2: (a) Stacked XRD patterns across the Pb-Ir oxide composition spread. (b) Magnified peaks with respect to IrO_2 (110) and $Pb_2Ir_2O_{6.5}$ (222) at different Pb compositions. (c) Lattice parameters for $Pb_xIr_{1-x}O_{2-y}$ (only a-lattice shown) and $Pb_2[Pb_xIr_{2-x}]O_{7-y}$, calculated from Rietveld Refinement.

at oxygen contents above 6% within the discharge.[180] However, his films did not undergo a post-deposition annealing step, though its possible that the morphological pre-structure prior to annealing may have inhibited crystallization, or significant crystalline growth

The film regions that did crystallize formed two distinct phases: a solid solution $Pb_2[Pb_xIr_{2-x}]O_{7-y}$ pyrochlore, and Pb-doped rutile IrO_2 ($Pb_xIr_{1-x}O_{2-y}$) (Figure S.2a). Variations in the Pb composition of both phases are evident by the notable systematic peaks shifts to lower 2θ, as highlighted by the $Pb_2[Pb_xIr_{2-x}]O_{7-y}$ (222) and $Pb_xIr_{1-x}O_{2-y}$ (110) peaks, across the composition gradient (Figure S.2b), clearly indicating lattice expansion. Between ~5 and 15 at.% Pb, the Ir-

rich film region, within the detection limit of the Rigaku instrument, shows single phase Pb-doped $Pb_xIr_{1-x}O_{2-y}$ prior to the onset of a solid-solution $Pb_2[Pb_xIr_{2-x}]O_{7-y}$ based on the emergence of the $Pb_2[Pb_xIr_{2-x}]O_{7-y}$ (222) peak between 15-25 at.% Pb. Signature peaks corresponding to $Pb_xIr_{1-x}O_{2-y}$ disappear above ~47 at.% Pb, leaving only a single-phase $Pb_2[Pb_xIr_{2-x}]O_{7-y}$. Figure S.2c trends the lattice parameters (calculated using Rietveld refinement) for $Pb_xIr_{1-x}O_{2-y}$ and $Pb_2[Pb_xIr_{2-x}]O_{7-y}$ as a function of Pb composition; although not presented in the figure, the c-lattice of $Pb_xIr_{1-x}O_{2-y}$ (rutile lattice is tetragonal) similarly expands with increasing Pb composition. Variations in composition are well documented for $Pb_2[Pb_xM_{2-x}]O_{7-y}$ (M=Ir, Ru), most notably in the form of B-site substitution of the Pb^{4+}.[96, 15] Surprisingly, there have been no reports on rutile $Pb_xIr_{1-x}O_{2-y}$ beyond a computational study[224]. The presence of Pb^{4+} has been detected by hi-res XPS measurements of Pb4f peaks (See Supplementary) for both phases. While this suggests that a mixture of Pb^{2+}/Pb^{4+} may be incorporated into the IrO_2 lattice, its possible that the secondary peaks may correspond to excess Pb-oxide at the surface.

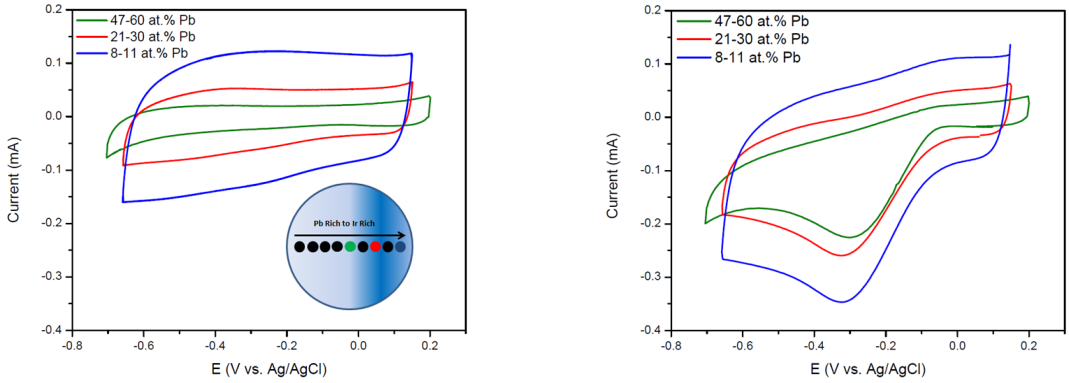

Figure S.3: (a) Background (nitrogen-bubbled) and (b) oxygen-bubbled CVs of key regions across the Pb-Ir oxide composition spread. Each spot was cycled at 50 mV/s in 0.1 M NaOH electrolyte at room temperature.

Figure S.3a,b shows the cyclic voltammograms of 8-11 at.% $Pb_xIr_{1-x}O_{2-y}$, 21-30 at.% Pb intermediate mixed phase $Pb_2[Pb_xIr_{2-x}]O_{7-y}$/ $Pb_xIr_{1-x}O_{2-y}$ (predominantly $Pb_xIr_{1-x}O_{2-y}$), and single-phase (some regions may be mixed with amorphous phase) 47-60 at.% $Pb_2[Pb_xIr_{2-x}]O_{7-y}$ regions of

the Pb-Ir oxide spread in 0.1M NaOH solution. Although the film has no conductive underlayer, the active regions containing $Pb_2[Pb_xIr_{2-x}]O_{7-y}$ and $Pb_xIr_{1-x}O_{2-y}$ were electronically conductive enough to electrochemically measure without any significant iR drop to distort the CV. However, the CVs were not corrected for uncompensated resistance (UR) of the electrolyte, though the effects of UR are the same between each spot, which still validates the screening method as a qualitative comparative measurement. The background CVs (figure S.3a) of all representative regions were largely featureless, similar to previous reported results for $Pb_2Ir_2O_{7-y}$[111], while some were able to resolve the redox transitions of Pb^{2+}/Pb^{4+}, Ir^{3+}/Ir^{4+}, or Ir^{4+}/Ir^{5+} under alkaline conditions.[67, 115]. Additionally, the CVs show a clear increase in double-layer charging when moving from the center towards the Ir-rich region. Within the amorphous Pb-rich region, the CVs are warped within the set potential window (See Supplementary) due to the regions high resistivity. When oxygen is introduced into the analyte, the CVs (Figure S.3b) show the onset of oxygen reduction during the cathodic sweep. When corrected for the double-layer base-line, the activity between the center, intermediate, and Ir-rich regions are to comparable one another.

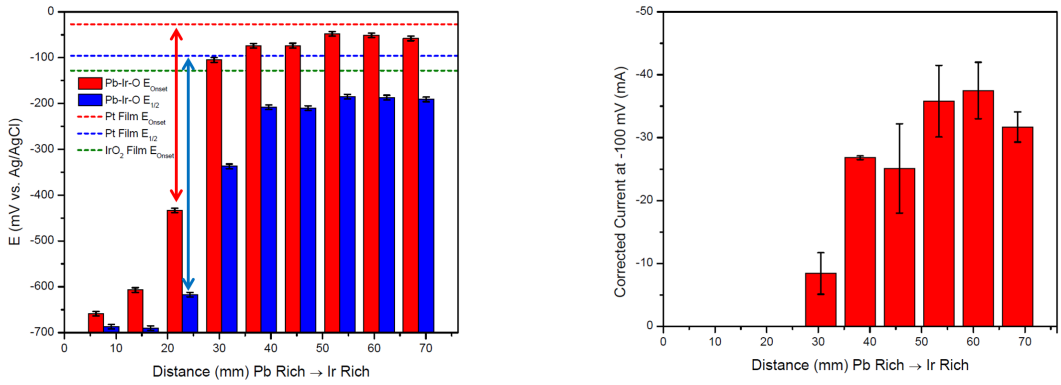

(a) (b)

Figure S.4: (a) The mapping of E_{Onset} and $E_{1/2}$ of the ORR curves extracted from the measured CVs that were locally measured across the composition spread with respect to the position on the film. (b) Measured current (corrected for double layer) of the oxygenated CVs at -100 mV vs. Ag/AgCl.

The ORR activity was characterized by the defined onset potential, E_{Onset} (potential at -0.01 mA after correcting for the double layer), half-wave potential, $E_{1/2}$ (potential halfway be-

tween the onset and peak potential), and current (corrected for the double-layer) at -100 mV. These activity metrics were plotted and compared across the composition spread (Figure S.4a,b), as well as to sputtered Pt and IrO_2 films. Between the center and Ir-rich spots, the ORR activity does not appear to change until approaching 76 at.% Pb by which the activity dramatically decreases due to a sharp increase in film resistivity from the amorphous PbO_x. In comparison to the Pt film, the active regions of Pb-Ir oxide show fairly close onsets with only about ~25-50 mV negative shifts. However, the lagging ORR kinetics at higher overpotentials is evident by the relatively high $E_{1/2}$ gap compared to Pt, which approximates to around 80-100 mV. Surprisingly, the activities of the Ir-rich and center regions are comparable, suggesting that the activity of $Pb_xIr_{1-x}O_{2-y}$ and $Pb_2[Pb_xIr_{2-x}]O_{7-y}$ are similar, and more active than pure IrO_2, regardless of composition.

Figure S.5a,b,c shows the ORR RDE polarization curves for the single-phase 47-60 at.% $Pb_2[Pb_xIr_{2-x}]O_{7-y}$, 21-30 at. % Pb intermediate mixed phase $Pb_2[Pb_xIr_{2-x}]O_{7-y}$/ PbxIr1-xOy (predominantly PbxIr1-xOy) region, and 8-11 at. % PbxIr1-xOy. Although the onset potentials only have a ~40 mV negative shift away from the Pt film, the half-wave shows a significant negative shift at more negative overpotentials (Figure S.5d). The CV screening results show comparatively better ORR kinetics at more negative overpotentials relative to the RDE polarization curves, underscoring some discrepancy between the activity results under stationary versus hydrodynamic flow conditions, which may be amplified when the film has a rough surface morphology, and/or if the surface is changing during testing. The mass-transport limited current for all Pb-Ir oxide regions is higher than expected. The expected maximum is close to 6 mA cm^{-2} (calculated from the Levich equation for a 0.196 cm^2 geometric area). The high limiting current, most notable seen in the 8-11 at.% Pb Ir-rich region, suggests that the surface coverage of the steady-state analyte flow exceeds the geometric area, possibly due to a higher surface roughness and/or changing surface morphology. The high surface roughness of certain films regions, as clearly indicated by SEM images within the Ir-rich region, also appears to affect the catalytic results as further supported by the comparatively stronger redox peaks compared to the sputtered Pt film (See Supplementary for images and CVs) when cycling in 0.1 NaOH mixed with 10mM of ferricyanide. Ultimately, the

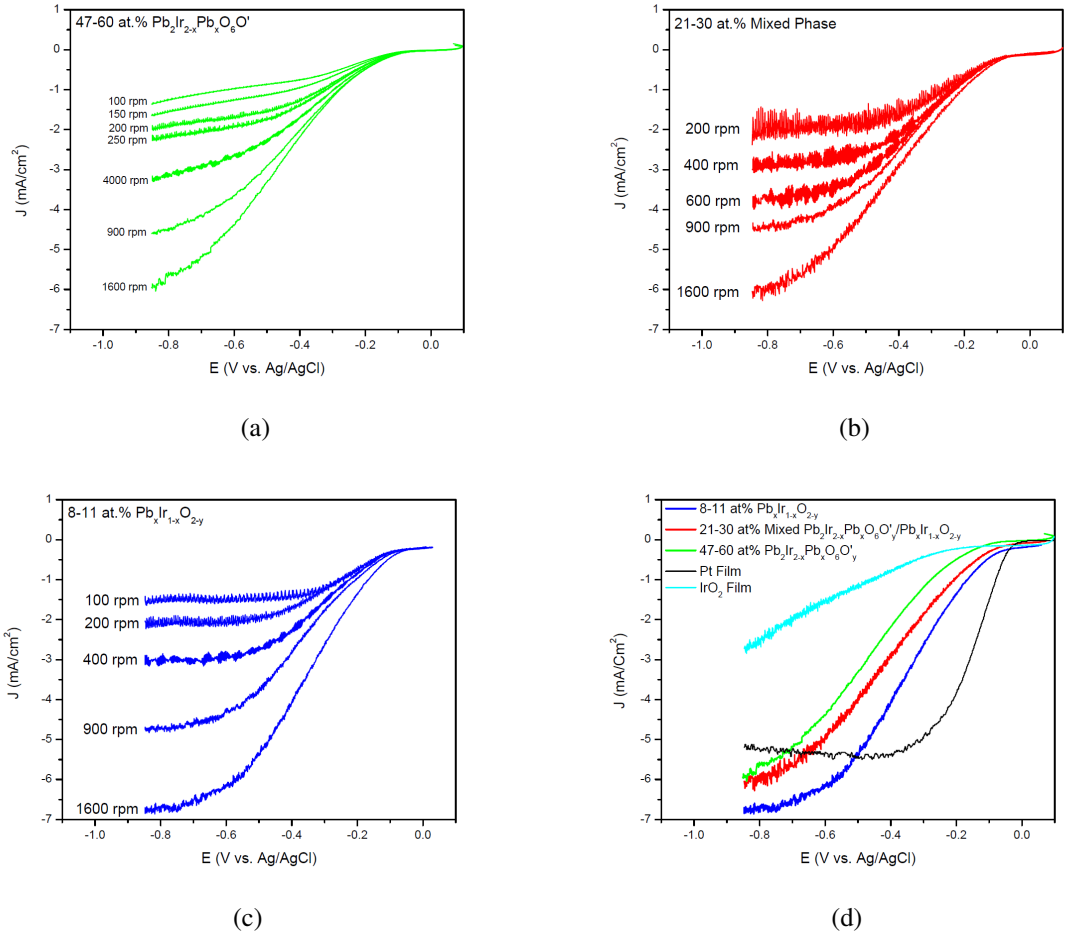

Figure S.5: RDE polarization curves of the (a) single-phase 47-60 at.% $Pb_2[Pb_xIr_{2-x}]O_{7-y}$, (b) 21-30 at.% Pb intermediate mixed phase $Pb_2[Pb_xIr_{2-x}]O_{7-y}$/ $Pb_xIr_{1-x}O_{2-y}$ (predominantly $Pb_xIr_{1-x}O_{2-y}$) region, and (c) 8-11 at.% $Pb_xIr_{1-x}O_{2-y}$. (d) Comparison of all film regions against Pt and IrO_2 at 1600 rpm.

uncertainty in active surface area precludes a reasonable Koutecky-Levich fit, further evidenced by the non-linearity of some of the K-L plots (See Supplementary).

Figure S.6 shows multiple Tafel plots taken from the 1600 rpm polarization curves in the previous figures. The Tafel slopes for the Pt film were determined to be 61 and 121 mV/dec at the lower and higher overpotential regimes, respectively.[217, 214] The Tafel slopes for 47-60 at.% $Pb_2[Pb_xIr_{2-x}]O_{7-y}$ was determined to be around 99 and 121 mV/dec. The measured slope at low overpotentials was a notable larger compared to previous reports showing slopes of around 55 mV/dec.[111, 219] However, the measured spot has a fairly wide composition range, while

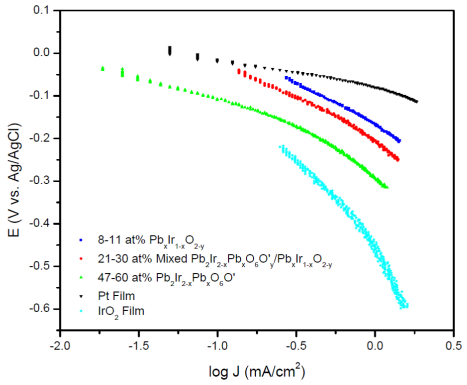

Figure S.6: Tafel plots of single-phase 47-60 at.% $Pb_2[Pb_xIr_{2-x}]O_{7-y}$, 21-30 at.% Pb intermediate mixed phase $Pb_2[Pb_xIr_{2-x}]O_{7-y}/Pb_xIr_{1-x}O_{2-y}$ (predominantly $Pb_xIr_{1-x}O_{2-y}$) region, 8-11 at.% $Pb_xIr_{1-x}O_{2-y}$, Pt film, and IrO_2 film.

the reported Pb-Ir pyrochlores were stoichiometrically fixed. Both the 21-30 and 8-11 at.% Pb regions showed significantly larger Tafel slopes of 165 and 178 mV/dec, respectively, within the lower overpotential regime, while 240 and 235 mV/dec, respectively, at higher overpotentials. In the case of $Pb_2[Pb_xIr_{2-x}]O_{7-y}$ and similar pyrochlore systems such as lead-ruthenates, many have modeled the ORR pathway via displacement of OH^- ions by O_{2ads}^- at the O′ sites upon an initial electron transfer step[186], which was inferred by the measured surface-charge density versus pH[67, 186] and the effects of O vacancies[60], though the exact role of the Pb and Ru sites is still not well understood. The higher Tafel slopes for $Pb_xIr_{1-x}O_{2-y}$ indicate a different a pathway for ORR, unsurprisingly due to the differences in the Ir-O framework compared to the pyrochlore structure, as well as a decreasing role in the Pb-sites. Regardless, without any in-situ probing techniques, elucidating the mechanistic nature for both phases based on the present RDE data cannot be examined beyond speculation.

6.5 Conclusion

In this study, Pb-Ir oxide composition spreads thin films were evaluated as ORR catalysts by employing electrochemical screening combined with high-throughput XRD and composition mapping. Active phase regions consisted of solid-solution rutile $Pb_xIr_{1-x}O_{2-y}$ and pyrochlore $Pb_2[Pb_xIr_{2-x}]O_{7-y}$. Through thin film RDE, the catalytic activities of the optimal and representative composition were measured. Although the activities are not comparable to the current standards, they represent a series of viable metal oxide catalysts, as well as highlight the utility of combinatorial high-throughput approaches to rapidly navigate and screen new ORR catalysts.

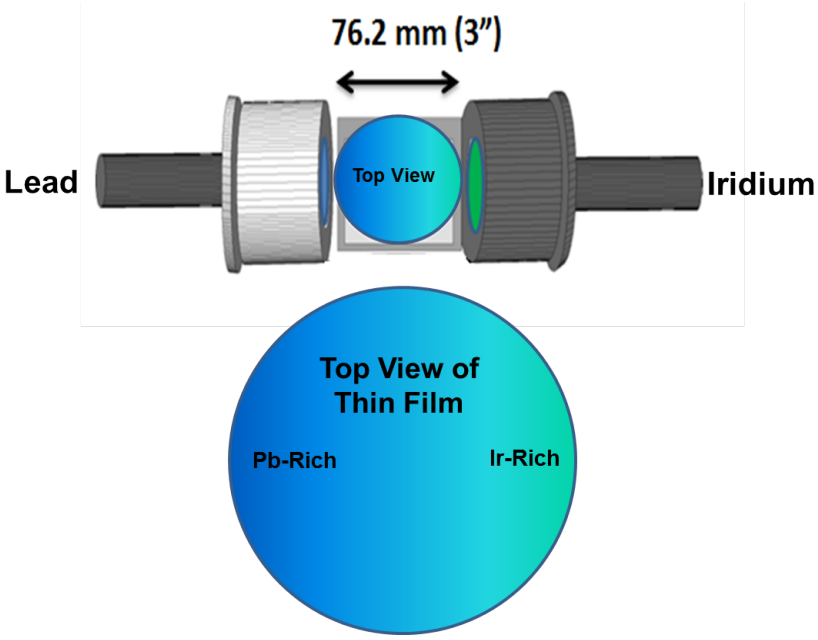

Figure S.1: Illustration of off-axis co-sputtering and cross section of Pb-Ir oxide composition spread.

6.6 Supplementary

6.6.1 Co-Sputtering

Non-uniform (150-400 nm thick) binary lead-iridium oxide (Pb-Ir-O) composition spread thin films were deposited onto 76.2 mm (3") diameter silicon (100) wafers using an off-axis reactive radio frequency (RF) co-sputtering system. Figure S.1 illustrates the off-axis co-sputtering configuration for fabricating binary Pb-Ir oxide composition spreads. The film was co-sputtered for 30 minutes in a 10/15 O_2/Ar sccm gas mixture at 30 mTorr. Prior to co-sputtering, a 10-15 minute pre-sputter step was taken to clean the target surfaces as well as develop a steady sputter rate.

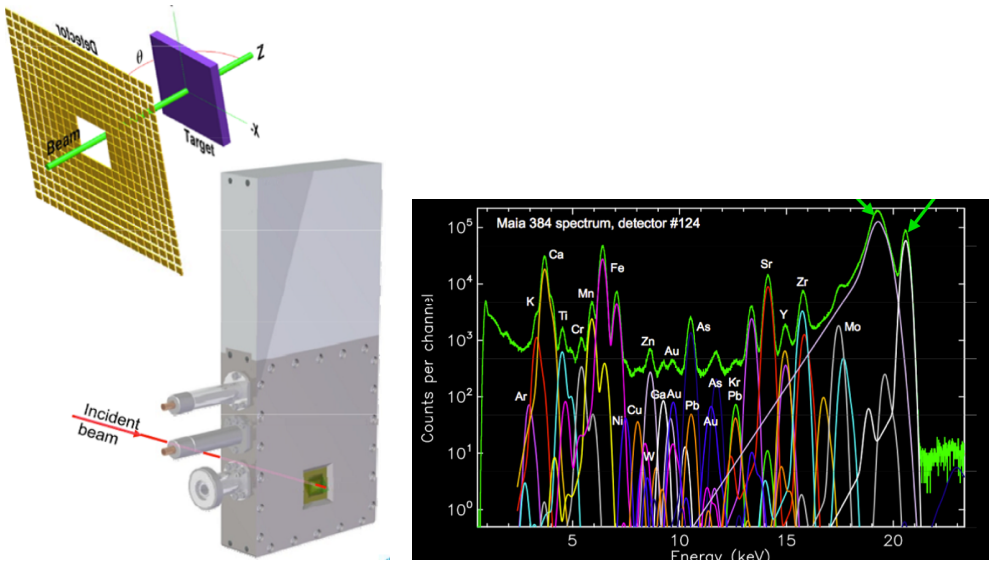

(a) (b)

Figure S.2: (a) Schematic of the Maia detector and XRF setup. (b) De-convolution of XRF spectra using dynamic analysis.[204, 220]

6.6.2 Synchrotron-Sourced X-ray Fluorescence

High-resolution XRF measurements were performed at CHESS using their synchrotron-sourced high-energy X-rays. We used a state-of-the-art high-resolution area Maia detector[204, 220](Figure S.2) to rapidly retrieve the XRF signal, generating high-resolution composition maps of our films. A high-energy X-ray source (31.9 KeV) was incident perpendicular to the film, and spatially scanned across the entire area in step increments of 200 μm. Composition analysis was performed using the software, Geopixe, capable of dynamic analysis for real time fitting and deconvolution of the fluorescent spectra (Figure S.2b).[203, 199, 202, 201, 200] Using a large array of SS detectors mitigates the limitations of conventional single detectors, which suffer from signal saturation due to photon pileup.

The Maia detector has an annular "backscattering" geometry by which the beam passes through an opening embedded within the surrounding detector array. With the sample upstream from the detector, this configuration increases fluorescent yield, and imposes far less restrictions on sample size and scale of scanning. When coupled to the Geopixe software, rapid collection of data is immediately processed (real-time processing). As mentioned earlier, rapid spectral deconvolution is done through dynamic analysis, while circumventing common artifacts attributed to pile-up, elastic and Compton peaks, escape peaks, and peak tails from incomplete charge collection.

6.6.3 Cyclic Voltammetry

The "Minicell" is a quasi-high-throughput test cell designed to locally measure the catalytic activity of ORR and OER at the film/electrolyte interface, allowing the user to screen the entire material library across the film. The apparatus is a custom-built three-electrode cell connected to a potentiostat controlled by a custom LabView program by which the scan rate, voltage

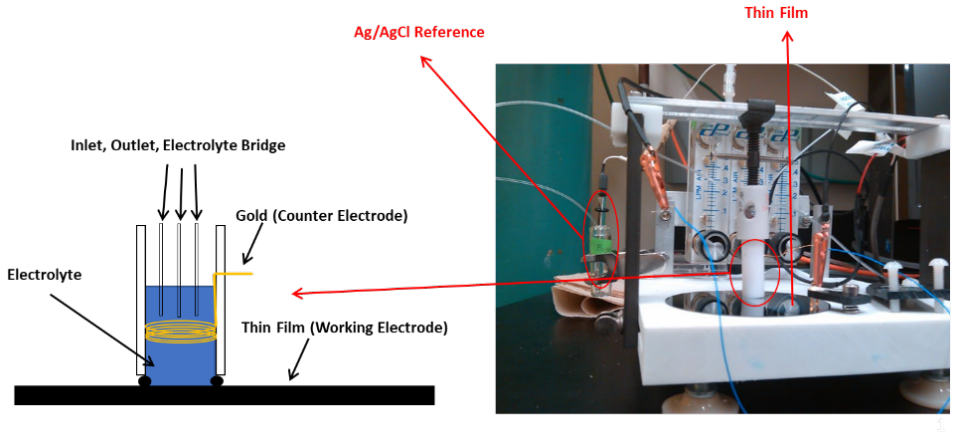

Figure S.3: Illustrative cross-section and picture of electrochemical minicell setup.

range, voltage gain are set and adjusted. Figure S.3 shows both an illustration of the cell cross-section and a photo of the actual setup. The composition spread thin film rests on top of a flat platform, the base of the minicell setup. Connected to the platform are two supports for a flat steel plate with a built-in slit, which is connected to the top of the test cell by a rotatable flat head screw. The cell can move laterally above the film and manually lower onto a chosen test spot. Manual XY movement of the cell is facilitated by sliding the screw that is connected to the cell along the slit embedded into the overhead plate, and moveable supports that slide along grooves along the sides of the platform.

The test cell is a hollow Teflon cylinder that locally interfaces with the surface of the film, which is designated as the working electrode. The test area has a diameter of 6 mm. During testing, the analyte is sealed inside the cell by a rubber O-ring that fits around the bottom lip of the cylinder. The interior wall of the cylinder is lined with a coiled gold (Au) auxiliary wire. The interior also contains three thin plastic tubes located near the bottom of the cell (close to the film surface when interfaced). The other ends of the tubes protrude from the top of the cell. Two of the three tubes function as an inlet and outlet for injecting and removing electrolyte solution, respectively, while the third tube functions as an electrolyte bridge between the film and the reference electrode. Capillary forces along the tube help maintain a continuum of analyte solution between the cell and the RE container. The reference electrode is a silver/silver chloride Ag/AgCl wire in saturated

KCl (stable potential of 0.197 V vs. SHE). The reference is sealed within a glass tube, and is held within a separate container filled with the same analyte as the cell. The choice of housing the reference electrode in a separate container, as opposed to situating it near the film surface to minimize uncompensated resistance, was done to avoid chloride (Cl^-) contamination of the Au counter electrode and the film surface.

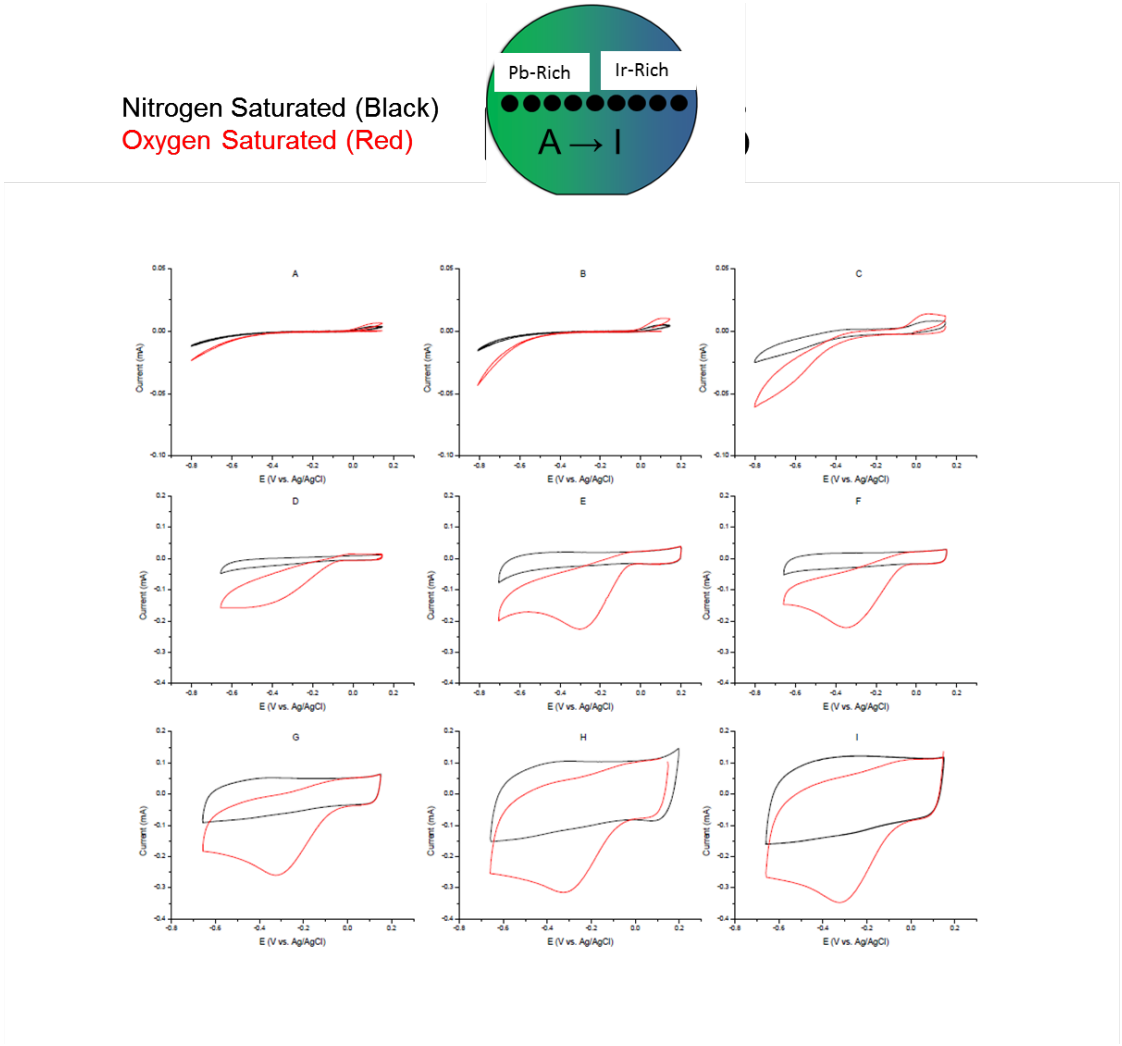

Figure S.4: Minicell ORR CVs across the entire Pb-Ir oxide composition spread.

6.6.4 Minicell CVs

Nine local CV measurements were taken across the Pb-Ir oxide spread using the method detailed earlier. The CVs shown in Figure S.4 are for measuring ORR activity.

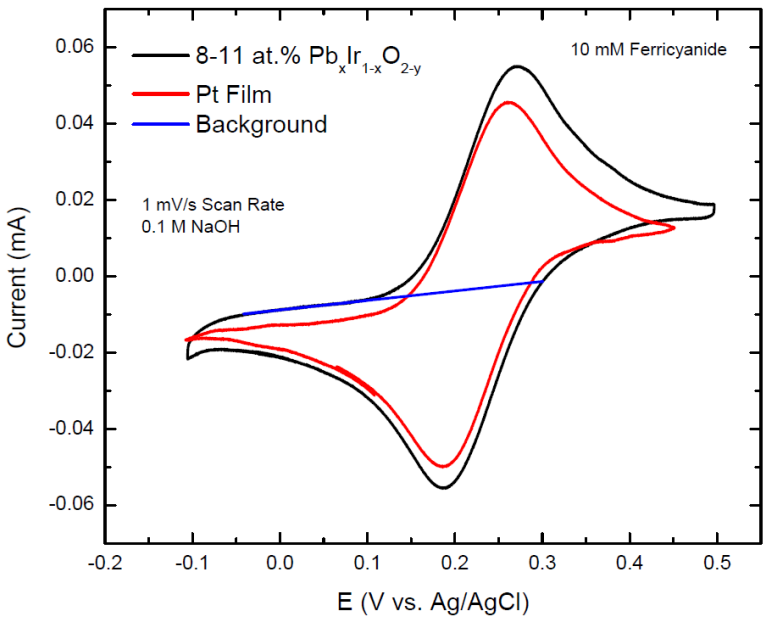

Figure S.5: Cyclic voltammetry of 8-11 at.% Pb spot compared to sputtered Pt. The films were cycled in 10mM ferricyanide

CV measurements of the active spot within the Ir-rich region (8-11 at.% Pb), and a uniformly sputtered Pt film, were cycled between -0.1-0.5 V at a scan rate of 1mV/s in 0.1 M NaOH solution with 1 mM of ferricyanide using the same test cell that was used for ORR screening. The active areas were approximated from the redox peak currents using the Randles-Sevcik equation.

Rotating Disk Electrode Measurements

The modified thin film RDE setup shown in Figure S.6 shows an illustration of the cross section of the 1 inch diameter hollow Teflon cylinder used to hold a 10 x 10 mm thin film (cleaved

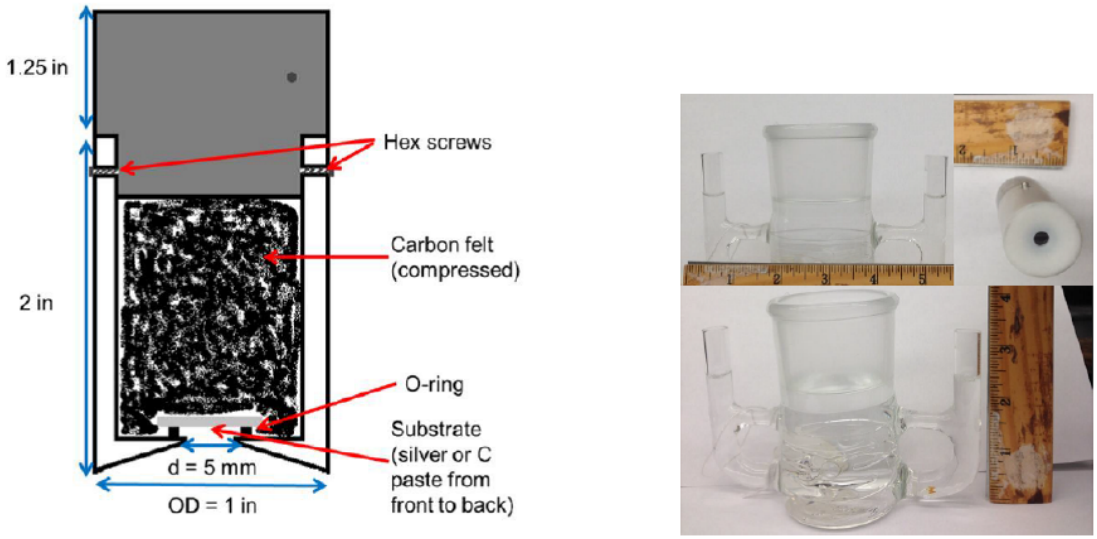

Figure S.6: Illustrative cross-section of RDE rod, including film, carbon felt, and steel backing. Picture of RDE glass basket.

from the composition spread). A 5 mm diameter surface area of the sample film is exposed at the bottom end of the cylinder, which slightly recesses from the outer periphery towards the planar film surface. The lip of the opening has a 0.25" O-ring, forming a tight seal with the film. Before placing the cleaved film inside the Teflon cylinder, the sides and back of the film are coated with silver paste and heated slightly to remove the solvent. This ensures contact with the carbon backing. Once the film is placed inside, the rest of the cylinder is filled with carbon felt (Alfa Aesar) and capped with a custom-made, stainless-steel current collector, which is tightened using a vice, and held together with hex screws.

The RDE cylinder was tested within a three-compartment cell (Figure S.6). The main chamber is 2" wide with an inner glass basket to prevent cavitation (whirlpool). The three compartments are connected at the bottom with glass frits, and at the top with simple glass tubing (to equalize the pressure in the three compartments). A graphite rod (Sigma Aldrich) was used as the counter electrode and a home-made saturated silver/silver chloride electrode (Ag/AgCl) was used as the reference. No platinum (or any noble metals) was used in the cell to ensure that there was no contamination from trace Pt from previous experiments. After any tests involving Pt and Au films,

the cell is typically soaked in aqua regia for several hours to remove any residual noble metals.

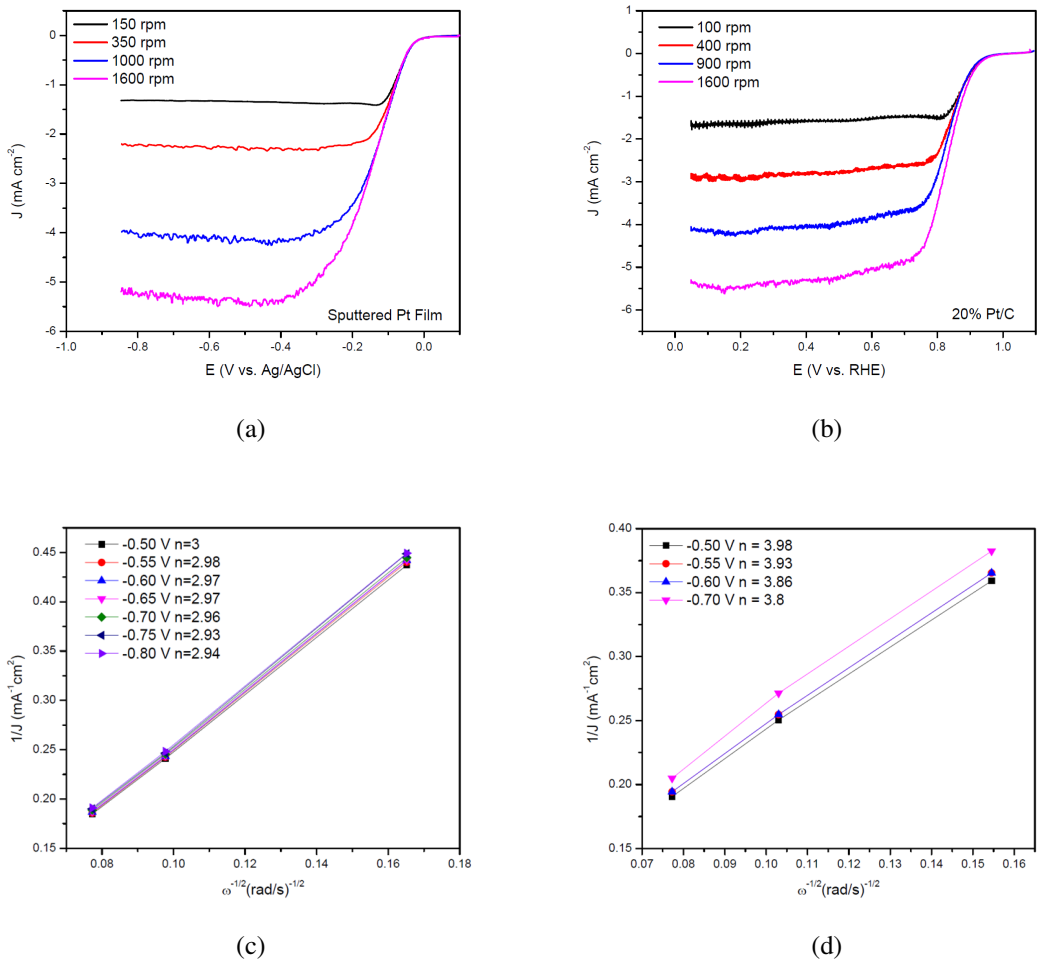

Figure S.7: adfadsfadsf

The thin film RDE setup used a sputtered Pt film as a control sample. Figure S.7a,c shows the ORR polarization and Koutecky-Levich plots. It should be noted that the polarization curves at low rotation speeds were too noisy to incorporate into the K-L fit. Regardless, the n values across the mass-transport limited regime are around 3, suggesting a mixed reduction pathway. This contrasts other studies that reported a full 4-electron reduction pathway, which was experimentally confirmed from in-lab RDE data on a 20% Pt/C mixture (Figure S.7b,d). While the thin film RDE results could accurate behavior intrinsic to polycrystalline Pt films, it's also possible that the thin film RDE setup requires a correction factor, which was not used on any of the Pb-Ir oxide results.

This will ultimately require additional tests, particularly RRDE experiments to quantify the amount of peroxide produced, if any. If peroxide production is too low to yield a mixed reduction pathway, then this strongly suggests that the setup needs a small correction factor to yield more accurate results.

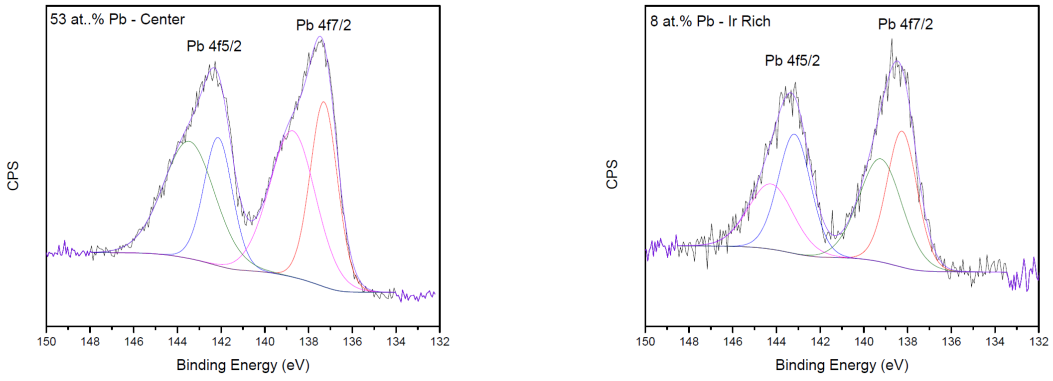

(a) (b)

Figure S.8: hi-res XPS Pb4f peaks of the center (53 at.% Pb) and Ir-rich (8 at.% Pb)

6.6.5 XPS

Survey and hi-res XPS measurements were taken across the composition spread (Figure S.8a,b). The spectra showed assymetric Pb4f peaks corresponding to mixed oxidation states of Pb^{2+}/Pb^{4+}. There was some shifting of the XPS spectra due to charge buildup, but corrections using the C1s peak (284 eV) as a reference. The presence of mixed oxidation states within the Ir-rich region may suggest that multi-valent Pb can be incoporated into the IrO_2 lattice, or the additional set of peaks may correspond to native Pb-oxide. The higher BE sets of peaks may also be $PbCO_3$.

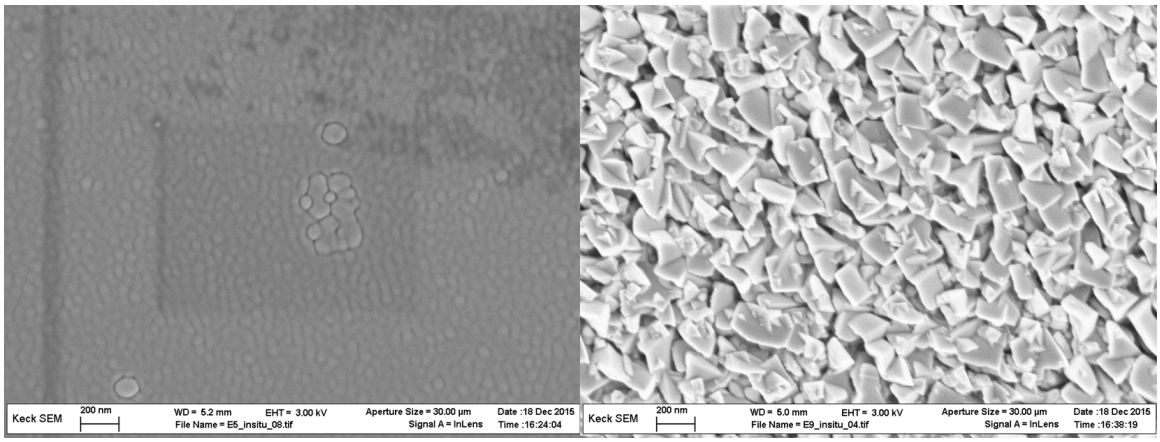

(a) (b)

Figure S.9: SEM images of the (a) center (53 at.% Pb) and (b) Ir-rich (8 at.% Pb) regions.

6.6.6 SEM

The SEM images (Figure S.9a,b) of the center (53 at.% Pb) and Ir-rich (8 at.% Pb) regions prior to electrochemical testing highlights differences in the surface morphology, which may have affect the polarization results.

CHAPTER 7

MANUSCRIPT - SYSTEMATIC EXPLORATION OF RAPID QUENCH YIELDS ROOM TEMPERATURE δ-BI_2O_3

Department of Materials Science and Engineering, Cornell University, Ithaca, NY 14853

*These authors contributed equally to this work

#Corresponding authors. E-mail: MOT (mot1@cornell.edu), RBVD (vandover@cornell.edu)

7.1 Background

7.1.1 Introduction

This research, as reported up to this point, has primarily been centered on oxide catalysts for oxygen reduction/evolution catalysis. However, during the last 2.5 years, I was involved in a number of secondary projects corresponding to novel metastable structure materials, most notably solid oxides used in applications related to oxygen ion conductive membranes and piezoelectrics. What began as an early attempt to lock in and expand the solubility of existing oxide structures became a full-fledged collaborative effort to systematically evaluate novel metastable oxides that are formed under a wide range of extreme annealing conditions using a modified laser spike annealing method.

This research project was built on locking in known and unknown metastable structures of solid oxide thin films using Dr. Robert Bells lateral gradient laser spike annealing (lgLSA) technique.[13] lgLSA facilitates extremely rapid thermal heating/quenching conditions, imposing kinetically driven crystallization pathways for metastable structure nucleation and growth. The combination of lgLSA with a variety of characterization tools capable of high-throughput exper-

imentation spawned an efficient and accurate methodology for generating comprehensive phase maps of a given oxide system annealed under a wide range of conditions defined by temperature and heating/cooling rates. Most importantly, this high-throughput approach has proven to be an effective approach to discovering new structures with potentially unique properties, ultimately adding another dimension to the materials discovery initiative.

Our biggest deliverable for this project was a comprehensive study on metastable bismuth oxide (Bi_2O_3). Within a narrow band of heating/quenching conditions, we were able to form delta-phase bismuth oxide (δ-Bi_2O_3), a polymorphic structure with incredible application value for fuel cell and sensor applications. Although our manuscript and supplementary presented later in this chapter provides a fairly thorough background on our methods and results, this preceding section will provide a brief summary on the motivation behind δ-Bi_2O_3 and Dr. Bell's lgLSA method.

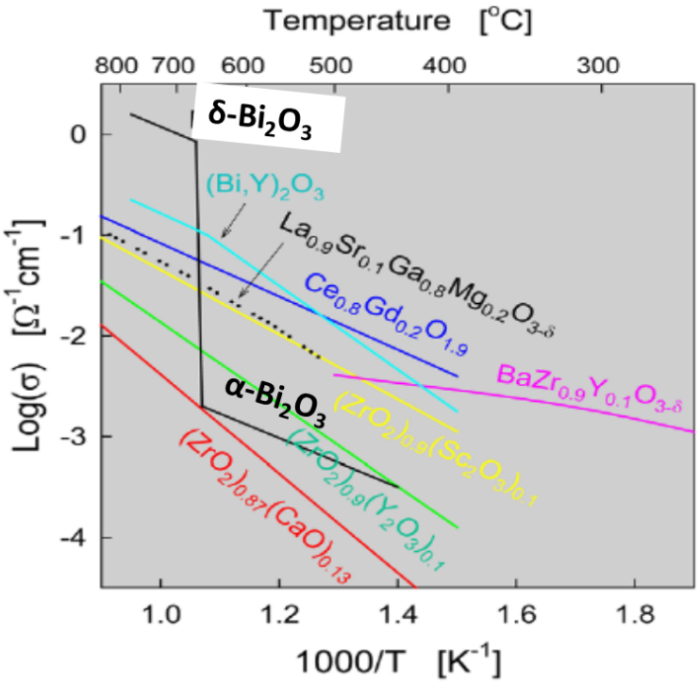

Figure S.1: Ionic conductivity versus temperature for various known solid oxide electrolytes.[83]

7.1.2 Motivation: Solid Oxide Membranes

Solid oxides are ceramic materials characterized as inorganic compounds containing oxygen. They represent a massive and indispensable class of materials as evident by their widespread use in a number of applications, including semiconductors, building infrastructure, aviation, medicine, superconductors, insulation, and clean energy. Among the wide range of properties that solid oxides possess, there is a subclass of oxides that are oxygen-ion conductive. Consequently, these ionically conductive solid oxide membranes (SOMs) are used as solid electrolytes in solid oxide fuel cells (SOFCs) and oxygen sensors. As shown in Figure S.1, we compare the ionic conductivities of several prominent SOM materials as a function of temperature, showing that most commercial SOMs, such as yttrium-doped zirconia (YSZ), can only reach suitably high oxygen-ion (O^{2-}) conductivities at extremely high temperatures. Because SOFC performance in terms of power output and efficiency is significantly governed by the oxygen-ion conductivity, practical outputs can only be sustained at temperatures ranging from 700 to 1100 °C, severely limiting their application to stationary power systems.

7.1.3 Delta-Phase Bismuth Oxide

In the subsequent manuscript, we characterize and map the polymorphic structure(s) of bismuth oxide (Bi_2O_3) over a wide range of annealing conditions using lgLSA. Most notably, we identify a set of unique annealing conditions that can crystallize and stabilize delta-phase bismuth oxide (δ-Bi_2O_3), a high temperature (730-825 °C) polymorphic structure, at room temperature. Arranged as a cubic fluorite with high oxygen-ion mobility coupled with a large fraction (25% of the sublattice) of oxygen vacancies, δ-Bi_2O_3 exhibits one of the highest known oxygen-ionic conductivities (~1 Scm^{-1}). [207, 218] Many studies have actively focused on δ-Bi_2O_3 as a potential oxygen ion transport membrane for solid oxide fuel cells (SOFCs), gas sensors, and oxygen separators.[87, 85, 245] However, δ-Bi_2O_3 cannot be maintained at temperatures below 730 C,

which transforms into a monoclinic α-Bi_2O_3 or a tetragonal beta-phase structure β-Bi_2O_3, depending on the cooling rate. Consequently, the ionic conductivity drops by as much as 3 orders of magnitude upon phase transformation to either polymorph.[207, 218] Furthermore, the commercial application of δ-Bi_2O_3 is limited due to poor chemical stability at high temperatures. This has led to concerted efforts throughout the years to phase-stabilize δ-Bi_2O_3 to between ranging from room to intermediate temperatures while still maintaining its extrapolated conductive properties.

Phase stabilizing δ-Bi_2O_3 to lower temperatures has traditionally been achieved through lanthanide and rare earth doping, though the major tradeoff is a reduction in the ionic conductivity (below the extrapolated value) as a result of oxygen sublattice ordering.[101, 255, 258, 19, 20, 109, 9, 10, 8, 105, 241] However, Switzer et al. was able to stabilize pure δ-Bi_2O_3 at room temperature by electrodepositing in-plane and out-of-plane textured δ-Bi_2O_3 films epitaxially grown on single crystal Au 111, 100, and 110 oriented substrates.[241, 118, 222] Since then, other researchers have had some success growing pure, and highly textured δ-Bi_2O_3 through chemical vapor deposition, sol gel synthesis, and magnetron sputtering.[222, 138, 54, 52, 248, 247, 267, 65] However, most studies that report the delta-phase are mostly based on fairly serendipitous findings, as opposed to a systematic effort in understanding the phase behavior of bismuth oxide. Despite the outpour of studies on phase-stabilized pure δ-Bi_2O_3, there have been no reported results on their ionic conductive properties. One major speculation is that the film quality in terms of film density, defects (grain boundaries, pinholes, crystallinity, etc.) concentration may have been too poor to yield any meaningful intrinsic measurements. Fortunately, this missing piece turned out to be one of our major deliverables in this work.

7.1.4 Lateral Gradient Laser Spike Annealing

Recently, Bell et al. demonstrated a high-throughput thermal annealing method derived from laser spike annealing (LSA). Known as lateral gradient laser spike annealing (lgLSA)[13],

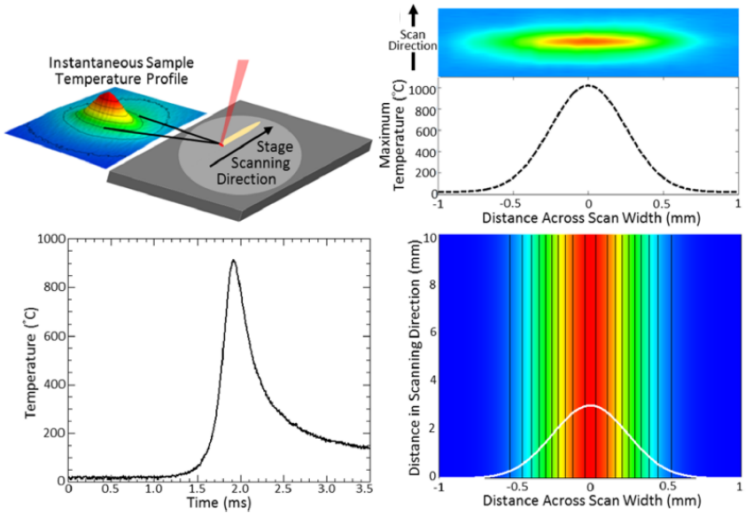

Figure S.2: (a) Schematic of the lgLSA setup scanning across an moveable XY stage. (b) Intesnity profile of the focused beam. (c) Temporal temperature profile for a 150 μs anneal with a peak temperature of 900 °. (d) Shematic contour temperature map of laser line.[13]

this method uses a high-powered laser source that is focused and scanned across the thin film oxide sample, where heat is absorbed and dissipated locally by the temperature-calibrated silicon substrate (Figure S.2). The source is a CO_2 (λ=10.6 μm, 120 W) line-focused continuous wave (CW) laser with a Gaussian temperature profile, which has a FWHM of 580 μm laterally and 90 μm along the scan direction.

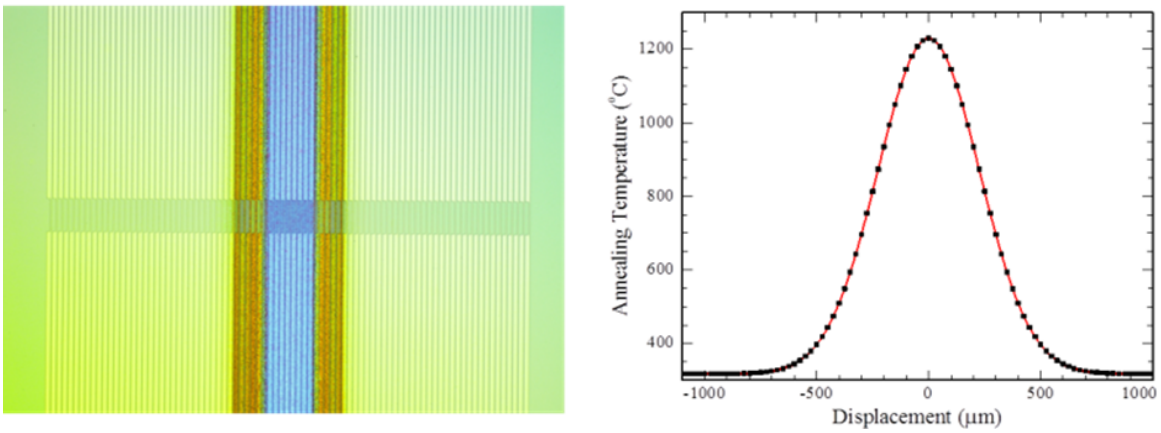

(a) (b)

Figure S.3: (a) Optical image of lgLSA anneal line with Au contact pads. (b) Temperature-distance profile laterally across the laser line

A single laser scan leaves a well-defined streak across the sample. Figure S.3a clearly

shows the well-defined optical contrast laterally across the laser scan, which coincides with the Gaussian temperature profile (Figure S.3b of the laser spot. Depending on the laser scan speed and power setting, the laser profile is defined by the peak temperature and dwell time. The dwell time is an indirect measure of annealing time, and is the ratio of the FWHM of the temperature profile divided by the laser scan speed. Limited only by the laser intensity profile, sample adsorption properties, substrate thermal conductivity, and laser scan velocity, the lgLSA system used in our study can produce temperature gradients up to 5 °C/μm with peak temperatures as high as 1400 °C, and heating/cooling rates ranging from 10^4-10^7K/s. These rates substantially exceed the typical heating/cooling rates for more conventional annealing methods, vastly expanding the scope of materials exploration, which now encompasses metastable oxides.

Localized annealing coupled with the Gaussian lgLSA profile is instrumental to the design of our high-throughput approach to generating and evaluating the different phase structures. For a single laser scan, defined by peak temperature and dwell time, the phase-temperature distribution is resolved when multiple XRD measurements are taken across the width of the annealed film region coinciding with the Gaussian temperature profile. This was achieved using high-energy XRD at CHESS, which produced a focused spot size of 25 x 200 μm (See manuscript). The approach, when expanded to several laser lines across a 4 ” diameter thin film, provides a fully systematic process that generates a detailed phase map as a function of temperature and dwell time. Our most complete demonstration of this approach is discussed in the subsequent manuscript.

7.2 Manuscript

7.2.1 Abstract

Devices using oxygen-ion conductors (OICs), including oxygen-ion batteries, solid oxide fuel cells, and oxide-based oxygen sensors, are typically limited to temperatures above 300°C

due to low conductivities. One OIC, the δ-phase of Bi_2O_3, has exceptionally high oxygen-ion conductivities above 650°C. Its predicted outstanding room temperature conductivity has never been realized due to phase transformations that occur during conventional temperature quenches. Utilizing a high throughput laser annealing technique to map quench rates 5-8 orders of magnitude faster than previously possible, here we have successfully quenched δ-Bi_2O_3 to room temperature resulting in films with few structural defects, and device conductivities several orders of magnitude higher than from previous best-in-class materials. The high-resolution/throughput phase mapping and OIC material described here hold substantial fundamental as well as technological promise.

7.2.2 Introduction

The absence of materials with high oxygen ion conductivity at room temperature has limited the application of rechargeable oxide batteries, solid oxide fuel cells, oxygen pumping devices, and oxide oxygen sensors to temperatures above ~300°C[14, 257, 139, 208, 124, 117, 232, 47]. The δ-phase of Bi_2O_3 has high oxygen ion conductivity when stable above 729°C, but transforms during conventional cooling into polymorphs with substantially lower ionic conductivities[11, 87]. Even best-in-class oxygen ion conductors[257, 208, 124, 18] extrapolated to room temperature have conductivities orders of magnitude lower than expected for δ-Bi_2O_3[257, 208, 124, 18, 86, 118]. Here we quenched δ-Bi_2O_3 to room temperature using laser annealing with rates 5–8 orders of magnitude faster than furnace quenching. A lateral gradient laser spike annealing (lgLSA)[13] method coupled with synchrotron diffraction enabled high-throughput screening of anneals on amorphous Bi_2O_3, with durations of 0.15–10 ms, temperatures up to 900°C, and cooling rates of 10^4–10^6 °C s^{-1}. δ-Bi_2O_3 formed in two annealing regimes: via solid state transformation $\leq$ 5 ms and melt quench $\leq$ 1 ms. Pinhole free δ-Bi_2O_3 showed conductivities of ~10^{-5} S cm^{-1} at room temperature, several orders of magnitude higher than any previously reported room temperature oxygen ion conductors. This work not only presents high throughput anneal mapping that has the capability to revolutionize material screening in fields where rapid laser annealing

is[270, 194, 175, 272, 249, 5] or can be applied, it also presents an exceptional room temperature oxygen ion conductor that greatly expands the application space for oxygen ion based devices.

A range of approaches have been have attempted to preserve or duplicate the high oxygen ion conductivity of δ-phase Bi_2O_3, stable only above 729°C, at low temperatures. Direct quenching of the δ-phase from high temperatures has been attempted at quench rates up to 10°C min^{-1}[87, 212], but always resulted in transformation below 600°C to either the low temperature stable α-phase or metastable β or γ-phases, all with substantially lower conductivities[47, 11, 87, 212], leading many to declare thermal quench of δ-Bi_2O_3 to room temperature impossible[34, 265]. Stabilization of the δ-phase by alloying with heavy metals has been demonstrated[208, 47, 18], but results in dramatically reduced low temperature oxygen-ion conductivities compared to pure δ-Bi_2O_3. Direct low-temperature synthesis of δ-Bi_2O_3 has been reported using a variety of synthesis techniques[208, 118, 241, 247], but none has included conductivity measurements of δ-Bi_2O_3 below 350°C[118], likely due to poor film quality or phase purity in the resulting materials. We speculate that such issues have also prevented the application of room temperature δ-Bi_2O_3 in devices. We report the nucleation and quenching of δ-Bi_2O_3 to room temperature using lateral gradient laser spike annealing (lgLSA)[13], which accesses heating and quenching rates 5 to 8 orders of magnitude faster than conventional techniques[47, 87, 13, 212] and microseconds to milliseconds annealing durations. The unique capabilities of laser annealing have been applied for decades in the semiconductor industry to activate dopants[270, 194] and contemporaneously to control phase changes[175, 272] and nano-confined crystal growth[249, 5]. However, rapid screening of laser annealing time and temperature conditions has recently been made feasible by the development of the lgLSA technique[13] which combines spatial gradients of peak temperature across single laser scans (Fig. 1a) with variable dwell time, enabling the creation of broad arrays of peak temperature and time annealing conditions. We combined lgLSA-prepared samples with spatially resolved synchrotron X-ray diffraction measurements to enable the systematic high-throughput exploration of phase behavior as a function of annealing temperatures between room temperature and 900°C (above the Bi_2O_3 equilibrium melting point at 830°C) and dwell times between 0.15–10 ms (peak

quench rates between 104 and 106 °C s^{-1}, Fig. 1b,c), a regime well beyond that previously explored for Bi_2O_3 by any other method. By starting with amorphous Bi_2O_3, which has the extremely high free energy of a frozen liquid, the driving force for nucleation of an initial crystalline phase is much larger than the driving force for subsequent crystal-crystal transformations, allowing the limited kinetics of a short anneal to capture even the first nucleated phases. Finally, exceeding the melting point during anneals erases as-deposited film defects (Fig. 1d), creating pinhole-free films ideal for device applications and providing a great deal of flexibility for post-processing of differently deposited materials.

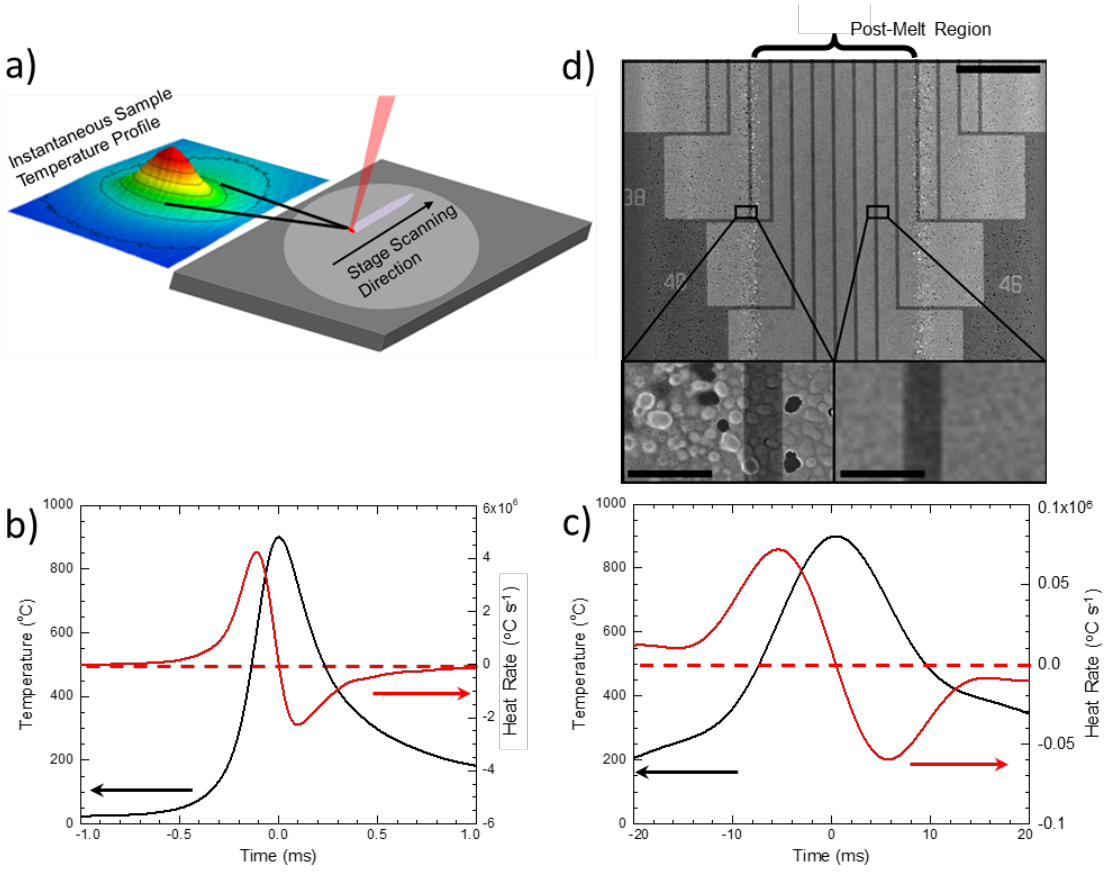

Figure S.4: Laser annealing of Bi_2O_3. a) Illustration of lgLSA scan over a sample and instantaneous temperature profile. b,c) Time, temperature, and heating rate profiles for a 0.15 ms (b) and 2 ms (c) dwell anneal with peak temperatures of 900°C and peak quench rates of ~2x106 °C s^{-1} (b) and ~7x10^4 °C s^{-1} (b). d) SEM of electric contacts patterned on top of 1 ms dwell annealed Bi_2O_3 film showing the pinhole-free post-melt region in the center bounded by regions with peak temperature below the melt on either side of the center (scalebar 100 μm). Insets are magnified views of both post-melt and sub-melt regions (scalebars 10 μm).

7.2.3 Mapping Phase Formation

Phase development across lgLSA temperature gradients was determined after annealing using spatially resolved X-ray diffraction measurements (Fig. 2a). Spatial maps (Fig. 2b) of diffraction patterns for dwells of 0.25, 2, and 10 ms show the transition from amorphous at low peak temperatures (edges) to crystalline at higher temperatures (centers). Splitting of peaks at 2, 2.3, and 3.8 $^{-1}$ shows formation of multiple phases as a function of the peak temperature and dwell. In the case of 2 ms and 10 ms anneals, damage is observed at the highest peak temperatures (Characteristic diffraction patterns for α, β, and δ (shown for two regions, δ_S) and δ_L) are given in Figure 2c. The signal from each phase was determined spatially across the laser scans (Fig. 2d), and subsequently converted from spatial to temperature dependence (Fig. 2e).

By identifying the dominant phase for each peak temperature and seven dwells between 0.15 and 10 ms, a temperature-dwell-transformation (TDT) diagram was constructed (Fig. 3a). Processing regimes resulting in the same dominant phase are identified. The film remains amorphous for temperatures below 350–400°C for all dwells investigated. At temperatures above the amorphous transition, the fractional intensity of each phase was mapped (Fig. 3b-d). Two δ-phase forming regimes are identified, one in a solid-state transformation (δ textsubscriptS) in a shrinking temperature window ranging from just above the amorphous transition to 750°C at 150 μs and 500°C at $\leq$ 5 ms, and the other by melt mediated transformation (δ_L) for temperatures above ~750°C and dwells below 2 ms. A β-rich region is found between high and low temperature δ-phase regions and extends to 10 ms, and an -rich region appears at the longest dwells and highest temperatures.

We believe the low temperature δ_S regime is the result of a direct amorphous to δ transformation due to a remnant phase fraction of amorphous Bi_2O_3 (evident in the broad amorphous peak near 2 Å^{-1} for δ_S shown in Fig. 2c), and that the high temperature δ_L-region has a lower temperature bound depressed from the 830°C equilibrium melting point to closer to 750°C due to

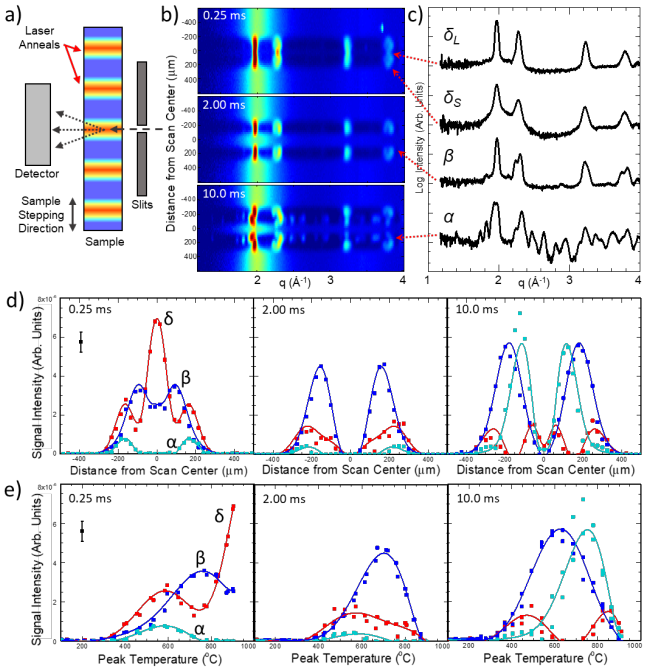

Figure S.5: Mapping spatial and temperature dependent phase formation for different annealing dwell times. a) Schematic showing X-ray micro-beam mapping of laser annealed sample. The incident X-ray beam (dashed, 25 μm wide after slits) is parallel to the laser annealed regions. Diffraction patterns are taken as the sample is stepped perpendicular to the micro-beam, measuring the structure of the sample across different peak temperature and dwell annealing conditions. b) Heat maps of diffraction intensity, I(q), as a function of spatial location across lgLSA scans of Bi_2O_3 after anneals with dwells of 0.25, 2.00, and 10.0 ms and peak temperatures in the scan centers of 900°C. c) Diffraction patterns for resultant δ (cubic) nucleated by liquid→solid, δ_L, and solid→solid, δ_S, transformations, β (tetragonal), and α (monoclinic) phases with arrows marking their origin in part (b). d) Relative diffraction intensities for δ (red), β (blue), and α (teal) phases across each lgLSA scan in (b). A typical least-squares fitting error bar is shown in black in the 0.25 ms figure. Solid lines are symmetric fits. e) Intensities from (d) converted from location to peak temperature using lgLSA calibrations.

a glass to liquid transition of the amorphous precursor. For the δ_L-region, a combination of faster liquid kinetics and nucleation-limited growth, where grain growth is much faster than nucleation, explain the absence of a remnant amorphous peak, high phase purity, and large domains (>100 nm indicated by Scherrer analysis).

The data maps from this high-throughput study suggest that initial nucleation and growth of the δ-phase occurs under all transformations measured herein, with subsequent solid-phase transformations from δ to β and α phases in specific time/temperature regimes. The presence of an

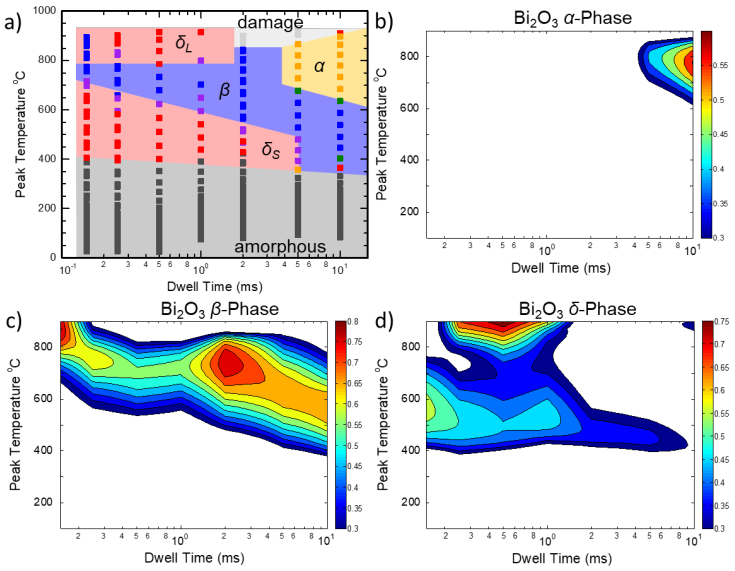

Figure S.6: Annealing temperature and dwell time maps of Bi_2O_3 phases. a) Temperature-dwell-transformation (TDT) diagram displaying the predominant room temperature phase as a function of dwell time and peak temperature: δ red, β blue, α yellow, mixed α/β green, mixed δ/β purple, amorphous dark grey, and damage light grey. Each square is a measured condition and colored regions indicate the extrapolated processing regimes expected to result in each phase. b-d) Weighted phase fractions of room temperature stable α-phase (b), β-phase (c), and δ-phase (d).

amorphous signal in short dwell δ_S strongly suggests that δ-phase nucleates first in solid state transformations. The β rich region between δ_S and δ_L largely overlaps the temperature region where δ is the equilibrium phase and δ nucleation is expected to be increasingly preferred. While direct β -phase nucleation is impossible to rule out with ex-situ measurements, this β-rich region is likely the product of an amorphous$\rightarrow\delta\rightarrow\beta$ transformation pathway, as the rapid transformation of $\delta\rightarrow\beta$ at 650°C has been widely reported in furnace quenches[87] and the δ-phase fraction appears to exchange directly with the β -phase at higher temperatures and dwell times (Fig. 3c,d). In fact, the continued presence of δ to longer dwells at lower temperatures suggest that the $\delta\rightarrow\beta$ nucleation rate maximum is at some temperature between 550°C and 650°C. The presence of a local maximum in β -composition at the shortest dwells and highest temperatures is not fully explained by this model and suggests another factor may influence nucleation under the most extreme conditions. The lack of the very distinct α signal until long times and high temperatures suggests that, despite being the stable phase at temperatures below 730°C, α does not directly nucleate from the amorphous

and is instead produced by an amorphous→δ→β→α transformation pathway. This mirrors the transformation pathway during furnace quenching from high temperature stable δ-phase of δ→β →α[47, 87]. The disappearance of both δ regimes by 10 ms dwells, with greater than 10^4 °C s^{-1} quench rates, explains why the quench of the δ-phase has not been previously reported by studies using much lower quench rates.

The δ-phase is preserved in melt processed films for dwells up to 1 ms, despite nucleation of β at sub-melt temperatures for dwells as short as 0.15 ms. These results suggest that melt processing substantially lowers the concentration of defects in the Bi_2O_3 film, reducing the number of heterogeneous nucleation sites and subsequently depresses δ→β nucleation rates compared to exclusively solid state processing. This also suggests that the melt produced δ-films may have increased low-temperature stability compared to δ-films with higher defect concentrations produced by other methods.

7.2.4 Ionic Conductivity Measurements

Annealing conditions of 850°C with 0.25 ms dwell were chosen to create phase-pure, large domain, pinhole free δ-Bi_2O_3 devices (Fig. 4a) that enable measurement of the room temperature conductivity. Impedance spectroscopy was used to determine the frequency dependence of the real and imaginary impedance of δ-Bi_2O_3 devices (Fig. 4b-d). The conductivity of the δ-Bi_2O_3 layer was determined by fitting a circuit model (red lines in Fig. 4 b-d), yielding a room temperature conductivity of $10^{-5.05 \pm 0.03}$ S cm^{-1}. This is over 6 orders of magnitude greater than the conductivity of the room temperature stable α-phase ($10^{-11.9}$ S cm^{-1})[212]. The DC resistance of the device was greater than the instrumental limit of 1 MΩ, and is likely much higher, strongly suggesting the conduction of the device was mediated by δ-Bi_2O_3 rather than pinholes.

This ~10^{-5} S cm^{-1} conductivity measured for δ-Bi_2O_3 is orders of magnitude higher than extrapolations to room temperature of any reported solid oxide oxygen-ion conducting material

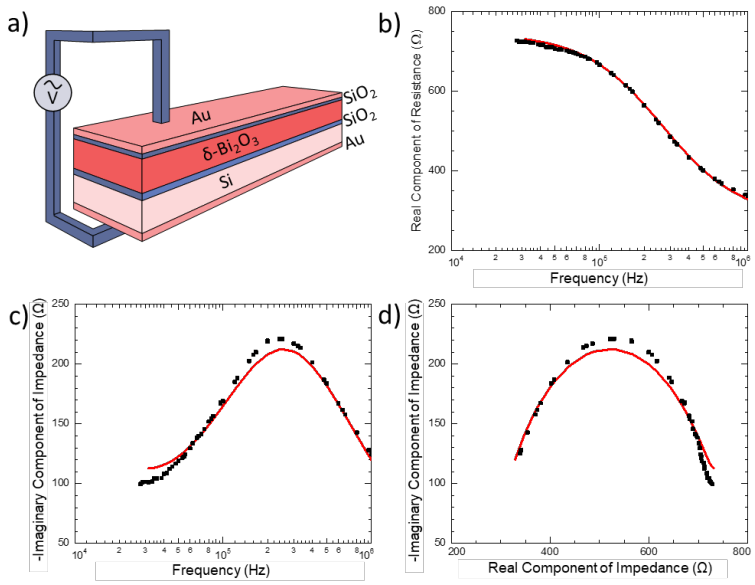

Figure S.7: Electrical measurements of δ-phase Bi_2O_3. a) Schematic of δ-Bi_2O_3 devices tested via impedance spectroscopy. b,c) Real (b) and imaginary (c) components of impedance as a function of frequency. d) Real vs. imaginary impedance showing a semicircle shape typical of ionic conductors. Squares are raw data and red lines are derived from modeling the circuit in a).

reported to date, including YSZ (10^{-13} S cm^{-1})[118], $Na_{0.5}Bi_{0.5}TiO_3$ (10^{-10}S cm^{-1})[124], Pb and Y stabilized δ-Bi_2O_3 (10^{-8} S cm^{-1})[18], and Er stabilized δ-Bi_2O_3 (10^{-8}) S cm^{-1})[208] 4. Extrapolations of pure δ-phase Bi_2O_3 from high temperatures suggest a room temperature conductivity near $10^{-3.6}$S cm^{-1} 12,13, significantly higher than our experimental value. This discrepancy may be due to ordering of the oxygen sublattice, an effect observed to decrease conductivity by ~2 orders of magnitude at temperatures below 600-800°C for dopant stabilized δ-Bi_2O_3[208, 19]4,26. Reports of δ-Bi_2O_3 at 350°C show no deviations from high temperature extrapolations13, suggesting that the ordering temperature of pure δ-Bi_2O_3 occurs below 350°C. Measurements of Pb and Y stabilized δ-Bi_2O_3 continue to show oxygen ion conduction rather than electron conduction after oxygen ordering11; we expect the same to be true for pure δ-Bi_2O_3. Our results represent the highest reported room temperature oxygen ion conductivity, by several orders of magnitude, and would enable a substantial expansion of the operable temperature range of many oxygen-ion based devices.

7.2.5 Methods

Deposition

Sample films of Bi_2O_3 were sputtered from a metallic Bi target (>99.99 %) using an active plasma of argon and oxygen onto silicon wafers (p type, 0.01 Ω-cm, WRS Materials) with a thermal SiO_2 buffer layer. The substrate was unheated during sputtering, and the Bi_2O_3 was amorphous as deposited (Extended Data Fig. 1). The thermal SiO_2 buffer layer between the silicon wafer and Bi_2O_3 was used to prevent melt alloying with the silicon wafer in the center of the laser scans where temperatures exceed the 830°C Bi_2O_3 melting temperature. Melt alloying of Bi_2O_3 and SiO2 is known to precipitate a stable body centered cubic bismuth silicate phase with a melting point near 900°C at low silicon concentrations[87, 121]; this phase was not observed for melt anneals in this study. On these time scales, the SiO_2 buffer layer appears to successfully prevent alloying of the Bi_2O_3 films even during melt. Samples used for structural analysis had a 100 nm thermal SiO_2 buffer, while samples used for electrical conductivity measurements had a thinner, 5 nm SiO_2 buffer layer. Production of phase pure δ-Bi_2O_3 in the devices used for electrical measurements was verified by XRD (Extended Data Fig. 2). After laser annealing and X-ray analysis, and prior to device patterning, an additional 5 nm of SiO2 was deposited using electron beam evaporation from an SiO_2 target as a capping layer on top of the Bi_2O_3 film; this protected films from solvents during photolithography, enabling the patterning of electrical contacts. Thermal evaporation was used to deposit adhesion layers (1 nm Cr) and gold top and bottom contacts (30 nm).

Laser Annealing

Laser annealing was performed by scanning a continuous 10.6 μm wavelength line-focused CO_2 laser (as described previously[13]) across the sample, as shown in Figure 1a. Dwell time is defined as the full width at half maximum (FWHM) of the laser intensity profile in the scan-

ning direction divided by the scanning speed. Anneals were performed in air. Temperature evolution as a function of time across the entire scan width was measured as described previously[13]. The peak temperature experienced across the laser scan width is approximately Gaussian with a maximum slope of 2°C m^{-1} and FWHM of 680 m. The Bi_2O_3 thickness dependent perturbation to surface temperature was calibrated by Bi_2O_3 and Au dot melts[13]. Laser scans create a line of annealed material where annealing conditions are invariant along the scan length but vary across the scan width. This allows the use of high aspect ratio rectangular areas for both X-ray diffraction and ion conduction measurements, with large areas of comparable annealing conditions despite the steep temperature gradient across the scan width. A characteristic annealing time, referred to as the dwell, is defined as the FWHM of the line-focused laser in the scanning direction divided by the scanning speed. On the same sample, multiple separated scans were made with dwells of 0.15 – 10 ms and peak temperatures in the scan centers ~900°C and center-center separations of 3 mm. This allowed high throughput measurements of annealing times and temperature conditions on a single sample using spatially resolved measurements.

Phase Identification

X-ray diffraction measurements were conducted at station G1 of the Cornell High Energy Synchrotron Source (CHESS). The X-ray beam was reduced to a 25x200 μm rectangle using a standard three-slit setup. The sample was mounted in a near-grazing-incidence configuration (ω=3°) and aligned such that the temperature gradient across the laser scans was orthogonal to the incident beam, allowing diffraction measurements to be spatially indexed to precise temperature (averaging over a 0-50°C temperature range) and dwell annealing conditions. Diffracted X-rays were collected on a Pilatus 3-300K pixel array detector (Dectris, Inc.). The incident beam energy was 9.81 keV and a typical sample-detector distance was 20 cm; the precise sample-detector distance was calibrated using copper tape adhered to each end of each sample measured to ensure precision. Radial integration was performed using the Nika package for Igor Pro[99]. The fraction

of polymorphs present in each diffraction pattern was determined by multi-peak fitting and scaled relative to phase-pure patterns. For Figure 3a, if a single phase has more than 25 % higher signal than all other phases it is defined as dominant, if two phases have intensities within 25 % then it is mixed phase. Fits in Figure 2d were developed using even polynomials which forced symmetry of the fit for equivalent annealing conditions on either side of the laser scan, and were transformed into temperature for Figure 2e using lgLSA calibrations. 3D surfaces used to create contour plots in Figure 3b,c,d were developed using fitting shown in Figure 2e. The reported limit on coherent scattering domain size was determined by the Debye-Scherrer equation assuming zero instrumental broadening and, as such, represents a lower limit on domain size. Prolonged anneals above the equilibrium melt resulted in damage in the form of an amorphous structure with a shifted amorphous peak compared to the as-deposited amorphous film, likely due to the well reported instability of Bi_2O_3 in low oxygen partial pressure environments at high temperatures[208].

Scanning Electron Microscopy

The morphology of the annealed areas was examined using a Tescan Mira3 scanning electron microscope (SEM) using an in-lens detector and an accelerating voltage of 15 kV. Figure 1d gives an SEM image of a 1 ms dwell 900°C peak temperature laser scan.

Electrical Measurements and Devices

Devices had a Bi_2O_3 contact area of 0.328 mm^2 were constructed on areas of 160 nm thick δ-Bi_2O_3 generated by anneal to a peak temperature of 850°C with a 0.25 ms dwell (Fig. 4a). Conductivity was measured using impedance spectroscopy using a 4284A LCR meter (Hewlett-Packard Inc) at frequencies from 25 kHz to 1 MHz at room temperature. The impedance of the Bi_2O_3 layer was extracted by fitting the measured curves using a model consisting of parallel resistor and constant phase element (Bi_2O_3 film) in series with a parallel resistance and capacitance

circuit (SiO2 buffer layers) and series resistor (substrate). Conductivity measurement error was calculated from errors of fit and device dimensions. DC measurements were conducted using handheld multimeters and confirmed by 10 Hz measurements with the 4284A LCR meter.

7.2.6 Data Availability

The datasets generated and analyzed in this study are available from the corresponding authors on reasonable request.

7.2.7 Acknowledgements

This work made use of the Cornell Center for Materials Research Shared Facilities which are supported through the NSF MRSEC program (DMR-1719875), the Cornell High Energy Synchrotron Source (CHESS) which is supported by the NSF (DMR-1332208), and the Cornell NanoScale Facility, a member of the National Nanotechnology Coordinated Infrastructure (NNCI), which is supported by the NSF (ECCS-1542081). R.T.B. was supported by the NSF GK12 fellowship program (DGE-1045513) and Kionix fellowship. P.A.B. was supported by the NSF Graduate Research Fellowship Program (DGE-1650441). U.W. thanks the U.S. Department of Energy Office of Science, Basic Energy Sciences, under Award No. DE-SC0010560 for support. We thank A. Woll and H. Joress for generous assistance with equipment for synchrotron diffraction.

7.2.8 Author Contributions

RTB (Dr. Robert Bell) and MJM (Dr. Marc Murphy) proposed the study. MJM and RTB designed deposition. MJM deposited samples. RTB designed and ran laser annealing. PAB and RTB designed and ran X-ray experiments. RTB, MOT, and PAB analyzed X-ray data. RTB, MOT,

RBVD, PAB, and MJM designed ionic conductivity experiment and equipment. RTB fabricated electrical devices. RTB and MJM measured electrical devices. PAB measured and UW supervised SEM experiments. RTB, MJM, and PAB wrote the manuscript with input from all authors.

CHAPTER 8

FUTURE OUTLOOK AND CHALLENGES

8.1 Introduction

For all PhD students and researchers in general, especially in the early stages of a project, obtianing the relevant data that is subsequently published often constitutes a fairly small fraction of data that is actually acquired. As expected, research is met with a litany of challenges that require extensive trial-and-error testing, technical troubleshooting, and desciphering confounding and sometimes contradictory results. However, combinatorial high-throughput research by design facilitates open-ended materials research, affording greater flexibility for a "shot-in-the-dark" approach to materials selection and discovery, which can lead to some interesting, even remarkable discoveries amongst a sea of nothing. Sometimes, many promising projects fall short due to time and funding constraints, or perhaps the payoff is not worth the time and effort it will take to complete. Regardless, it is worth mentioning some of these projects, as well as summarizing some of the pervasive challenges that have plagued this research.

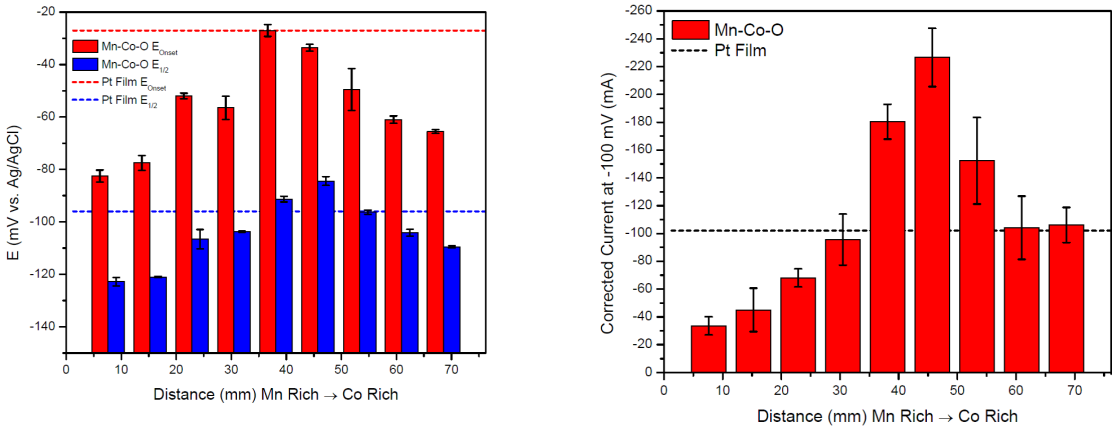

(a) (b)

Figure S.1: Minicell ORR screening results of (a) E_{Onset} adn $E_{1/2}$ and (b) Kinetic current at -100 mV vs. Ag/AgCl.

8.2 Other Work

8.2.1 Mn-M (M= Co, Ni, Fe) Oxide

The latest project of interest, and one that I believe is a potential publication, is a combinatorial high-throughput study on Mn-M (M=Co, Ni, Fe) bimetallic oxide thin film catalysts. This project is another major collaboration with the Abruña group, and centric to the concerted interests in transition metal, Mn-based oxide catalysts, particularly Mn-Co spinels.[237, 126, 122, 27] Previous studies by Liang and Li et al. demonstrated stoichiometric $MnCo_2O_4$, and tunable cubic and tetragonal $Co_{3-x}Mn_xO_4$ ($1 \leq x \leq 2$) spinel oxides as highly active bifunctional catalysts under alkaline conditions.[126, 122] Both Mn and Co are inexpensive materials in comparison to all precious metals, making them ideal commercial catalysts for alkaline fuel cells and electrolyzers.

Preliminary results on the ORR activity of co-sputtered Mn-Co oxide composition spread, shown in Figure S.1a,b, were obtained using the minicell. The most active regions are near the center of the film, though the composition was not measured prior to finishing this thesis. According to Cheng et al., the optimal composition is ostensibly near the 2:1 Mn:Co molar ratio.[27] While the active regions appear to be slightly off-centered towards the Co-rich region, XPS measurements of subsequent Mn-Co samples showed a severe Co deficiency due to changes in the Mn sputter rate.

Because Mn-Co oxide are poorly conductive, the composition spread cannot be properly screened without a conductive underlayer. In the first iterative stage, a thin film of RuO_2 was sputtered onto a heated substrate (~530 °C) prior to co-sputtering Mn-Co oxide. Unfortunately, the RuO_2 underlayer does introduce the risk of surface contamination as a consequence of high-temperature inter-diffusion and/or incomplete Mn-Co oxide film coverage. If there was evidence of contamination, this would preclude rendering the activity results as incontrovertibly tied to the intrinsic catalytic activity of the Mn-Co oxide. Although preliminary XPS analysis showed no Ru footprint, even traces amounts of Ru at the surface would unequivocally affect the catalytic

results for OER. Consequently, this work has prompted a different approach involving a series of glassy carbon (GC) rods (5 mm diameter) placed along the projected composition gradient. In the same manner as depositing onto a silicon wafer, Mn-Co oxide is co-sputtered onto the series of GC rods. Each coated GC will then be electrochemically measured using RDE. Glassy carbon has the advantage of being fairly catalytically inactive, and chemically inert with the coated Mn-Co film. Currently, this work is still undergoing the calibration stages. Moreover, other Mn-M oxide systems (Mn-Fe oxide, Mn-Ni oxide) are also being explored.

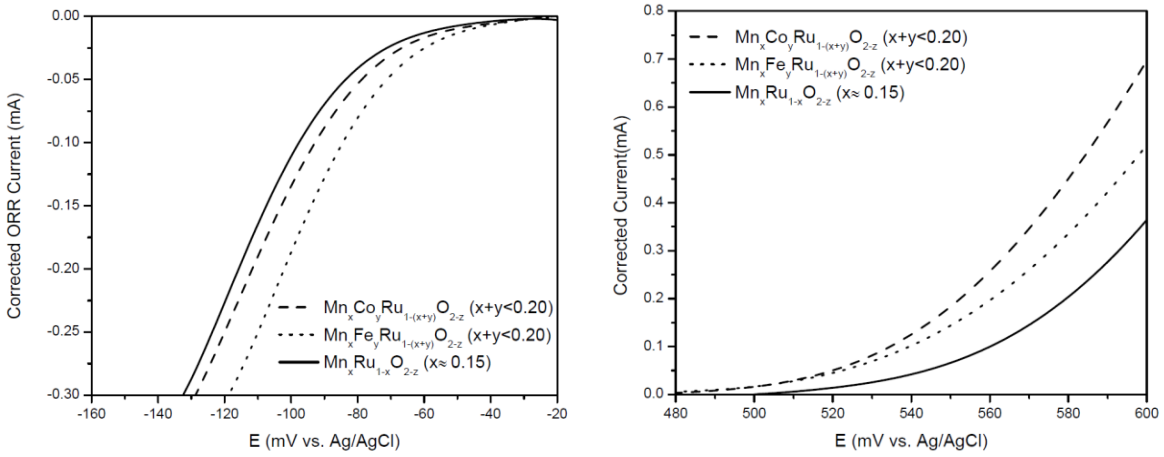

(a) (b)

Figure S.2: (a) adskfjdakadskfladsjf. (b) alkdsfjdafjakllasjdlk;kldfl

8.2.2 Ternary Spreads

Ternary (technically quaternary oxides) composition spreads were explored on a preliminary basis, but the results were too fragmented to justify a publication. These systems included Pb-Ir-Ru and Mn-M-Ru (M = Ni, Fe, Co) oxide systems. In particular, the Mn-M-Ru oxides were the most promising as viable bifunctional oxygen catalysts, showing slightly better activity than the most active composition range of the binary Mn-Ru oxide system (FigureS.2a,b), suggesting that the incorporation of Fe and Co does slightly enhances the ORR and OER activity. Moreover, the active regions are still ostensibly within the $Mn_xM_yRu_{1-x-y}O_{2-z}$ (M=Fe, Co) single phase region,

which have not been previously reported by anyone.

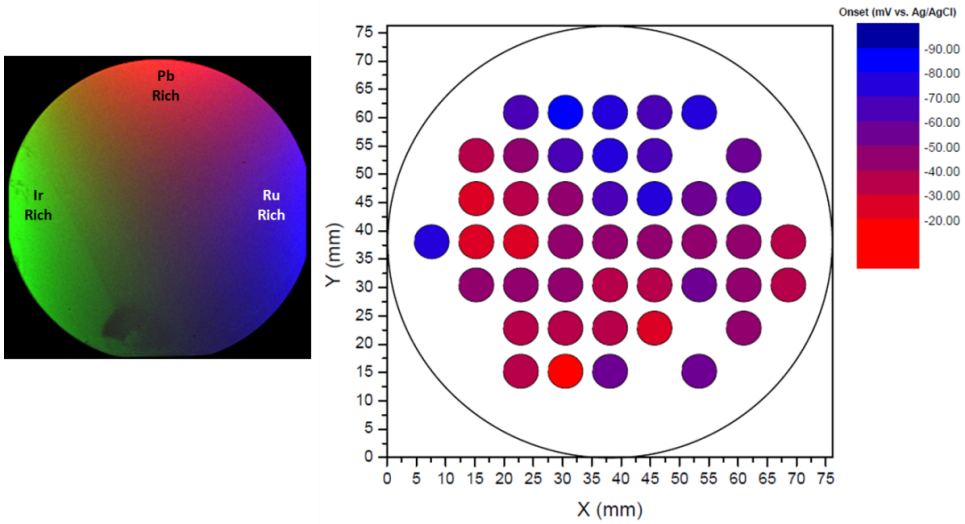

Figure S.3: (a) adskfjdakadskfladsjf. (b) alkdsfjdafjakllasjdlk;kldfl

For the Pb-Ir-Ru oxide, we were able to fully map the composition distribution using XRF at CHESS, as well as map the ORR activity, which shows the projected onset potentials (Figure S.3) across the entire film. The incorporation of Ru does enhance activity as indicated by the regions showing higher onsets than the most active regions of the Pb-Ir oxide binary spread. However, the project lost traction due to the fact that the catalytic enhancements from Ru were too marginal to yield activities comparable to precious metal catalysts.

8.2.3 Other Binary Pyrochlores

Other pyrochlore oxide systems of interest included binary Pb-Ru-O, Bi-Ru-O, and Bi-Ir-O. Unfortunately, none were active enough to warrant further study. The most ideal pyrochlore system based on several previous studies was the Pb-Ru pyrochlore, which has consistently demonstrated the highest ORR catalytic activity amongst all other prominent pyrochlore catalysts of interest.[185, 48, 191, 186] However, there were confounding difficulties when attempting to co-sputter Ru and Pb, which repeatedly resulted in a severe Ru deficiency. It was found that Ru

inexplicably re-sputters to a high degree when co-sputtering with Pb. Despite efforts adjusting the sputter conditions and even attempting PLD, I was never able to make a working sample.

8.2.4 Metastable Oxides

Our work on metastable oxides (Chapter 7) has culminated into an impactful research project despite being fairly secondary to my primary research focus (i.e. oxygen catalysts). As reported in Chapter 7, we were able to fully demonstrate a high-throughput methodology for forming and mapping metastable bismuth oxide (Bi_2O_3) over extremely rapid annealing conditions using Robert Bell's lateral gradient laser spike annealing (lgLSA) method.[13] While interests in Bi_2O_3 were driven by the application value of the delta-phase cubic polymorph (δ-Bi_2O_3) due the structure's incredibly high ionic conductivity, the broad utility of lgLSA studies expanded the scope to a broader systematic study on unknown or predicted metastable structures. Additional solid oxide systems were studied using this high-throughput lgLSA method, which included metastable $BaTiO_3$, $MnFeTiO_3$ (varying composition), $LiMnO_2$, Na_6PbO_5, Li_4WO_5, Li_2MnWO_6, and $MnTiO_3$. These oxide materials were selected from a computational study performed by Jong et al., who computed the piezoelectric tensors of almost a thousand distinct inorganic compounds with various crystallographic symmetries, many of which were metastable and only computationally predicted, using a density functional perturbation theory model as a first-principle calculation.[44]

Each oxide system was synthesized using a simple ball-mill mixing method (this wasn't done for all mixtures) and subsequently pressed into 1" diameter disks. Each target was placed in a tube furnace, undergoing solid-state sintering between 1000-1100 °C for 24 hours. Because there was a significant time constraint when synthesizing each of these targets prior to our CHESS run, there was not much time devoted to researching specific synthesis routes for each mixed oxides system, and consequently each oxide powder mixture underwent the same mixing and sintering

procedure. This was concerning because the chosen synthesis route may not be well-tailored to every oxide sample due to varying factors associated with powder morphology regarding particle size, wettability, thermal expansion, vapor pressure, etc. This was notably concerning for $LiMnO_2$, Li_4WO_5, and Li_2MnWO_6, which contain light-weight Li alkali metal, rendering these mixtures susceptible to Li-loss during sintering. It's not known how much Li is lost during the high temperature sintering step, but I did compensate by adding an additional 5 wt% to the mixture. Overall, the target compositions or compositional uniformities are not truly known. Thus, the quality of each film is predicated on the assumption that the oxide powders were well-mixed and sintered uniformly.

Each target was deposited onto 4" lgLSA calibrated silicon wafers using pulsed laser deposition (PLD). Each film then underwent a series of lgLSA scans, each corresponding to specific annealing condition based on peak temperature and anneal time. A series of XRD measurements were then taken laterally across the width of each laser scan using the fixed angle area XRD method at CHESS (See Chapter 4 and 7 for details on the XRD setup). We came across several interesting XRD patterns, some of which didn't match any reported polymorphic structures. However, the difficulty of de-convoluting the measured diffraction peaks were compounded by systems with predicted low symmetry metastable structures, or systems comprised of multiple phases. This has prompted close collaborations with crystallographers and computer scientists to streamline XRD data processing based on computationally predicted structures.

$MnTiO_3$

Among the previously listed piezoelectric materials that were measured, prelminary results for $MnTiO_3$ were the most interesting. Over time, Dr. Robert Bell gained greater ownership of this project.[12] Thus, his thesis provides a much more detailed summary on metastable $MnTiO_3$. To quickly summarize, $MnTiO_3$ has three reported phases (See Table 8.1). $MnTiO_3$-I is the stable atmospheric phase while the $MnTiO_3$-II is a stable high pressure (~6 GPa) phase.[114, 197] Both are trigonal structures differentiated only by the stacking orders of Mn and Ti along the c-axis.

Name	Symmetry	Point Group	Mineral Terms	Space Group	Space Group Name
$MnTiO_3$-I	Trigonal	-3	Ilmenite $FeTiO_3$ Type	148	R-3
$MnTiO_3$-II	Trigonal	3m	$LiNbO_3$ Type	161	R3c
$MnTiO_3$-III	Orthorhombic	mmm	Perovskite $GdFeO_3$	62	Pbnm

Table 8.1: Polymorphs of $MnTiO_3$.

$MnTiO_3$-III is a metastable orthorhombic phase.

In the same manner in which we measured metastable bismuth oxide (Chapter 7), we obtained multiple XRD images across the lateral lgLSA profile of several laser scans. The XRD images were then integrated and stacked to generate a diffraction map versus Q-space (Figure S.4a). Each subfigure corresponds to the full XRD map across the width of the laser scane at a specific dwell time, all of which have peak temperatures of 1000 °C. These peaks were then de-convoluted in order to generate the phase map as a function of temperature and dwell time (Figure S.4b). At 5ms, there is a primary peak that matches the peaks corresponding to the trigonal $MnTiO_3$-I and II, which are only differentiated by their relative peak intensities. For dwell times below 5 ms, the pattern shows a primary peak near 2.3 $Å^{-1}$ and a secondary peak near 2.6 $Å^{-1}$, none of which are matched with any known phase of $MnTiO_3$. Moreover, we were able to confirm that the 2.4 $Å^{-1}$ peaks were not missing due to texturing as evidenced by the uniform diffraction ring intensities. Currently, we were not able to determine the base structure of this ostensibly $MnTiO_3$ phase, which we labeled as $MnTiO_3$-IV. Below 1000 °C at every measured dwell time, the film appeared to remain amorphous. At higher temperatures of around 1250 °C with longer dwell times, the films formed a mixture of $MnTiO_3$-I and II, which we distinguished by the measured peak intensity ratios, though distinguishing the two is muddied when there is a mixture of both phases.

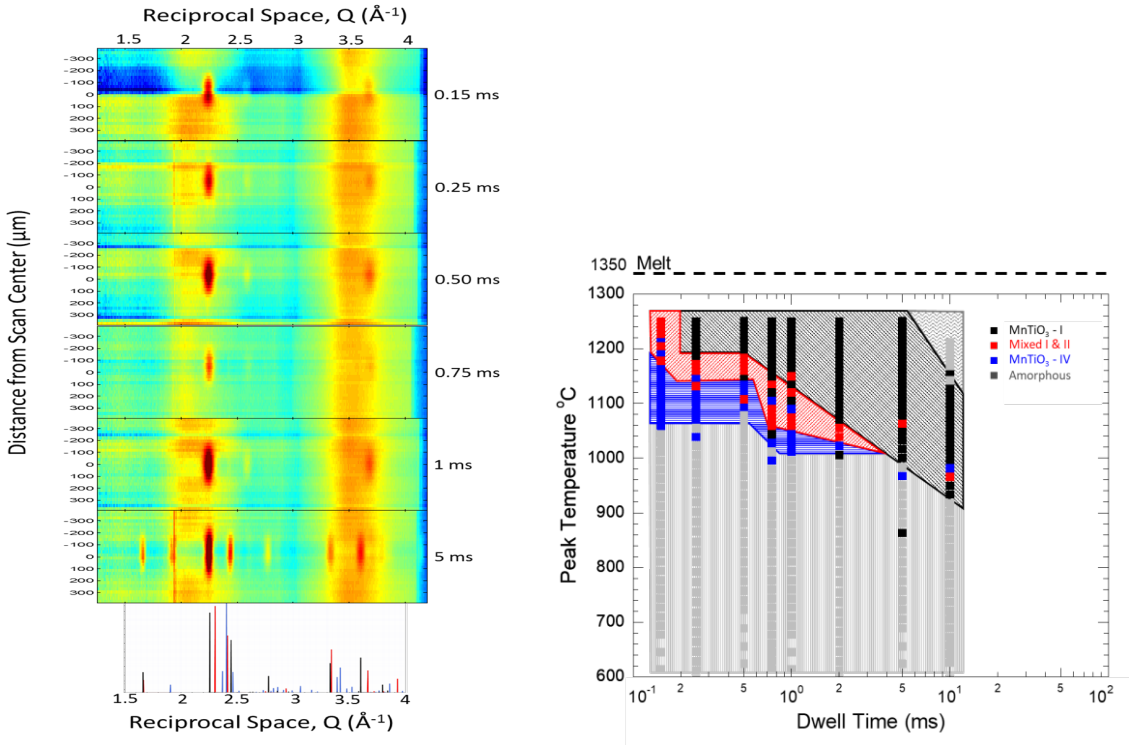

(a) (b)

Figure S.4: (a) Diffraction measures across multiple laser scans with peak temperatures of 1000 °C as a function of distance from each scans center, reciprocal vector, and logarithmic intensity (color). The dwell time for each laser scan is listed on the right. At the bottom are diffraction patterns from the ICSD database for MnTiO3-I (black)[114], $MnTiO_3$-II (red)[114], and $MnTiO_3$-III (blue)[197]. All three previously reported phases have a large peak at ~2.4 $Å^{-1}$ which does not appear in our results until 5 ms, even for patterns that show an additional peak near 2.6 $Å^{-1}$. The peak near 1.8$Å^{-1}$ is convoluted with a silicon peak known to appear at long dwells and high temperatures. (b) Temperature dwell transformation (TDT) diagram of predominant phase at different conditions. Each square is a discrete annealing condition measured. Filled backgrounds are used to denote regions with the same phases.[12]

This is currently an ongoing study, leaving open the prospect of a newly discovered $MnTiO_3$-IV phase.

8.3 Research Challenges

Although our high-throughput approach to research facilitates a substantial output of sample films, my actual sample output was fairly compared to previous graduate students; this was

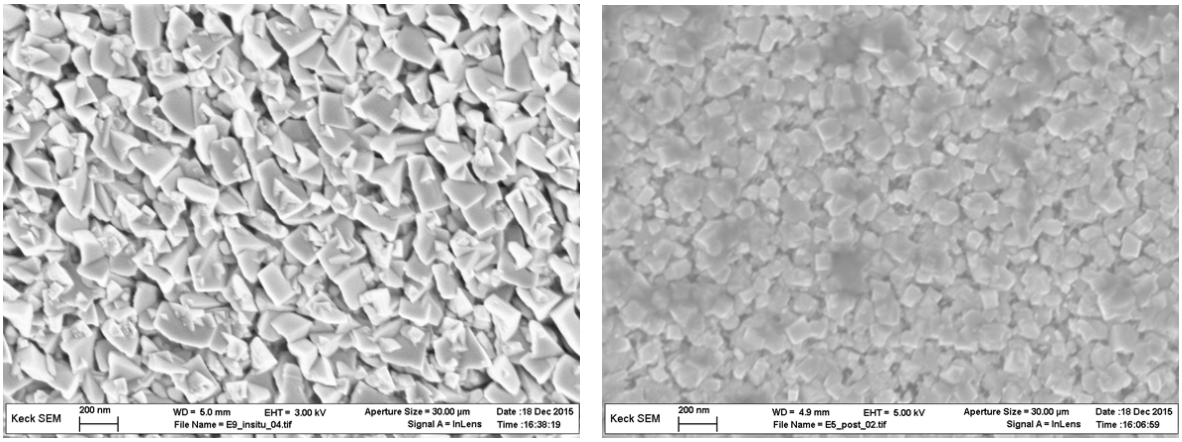

(a) (b)

Figure S.5: (a) Pb-doped IrO_2 (Ir-rich) region. (b) Pyrochlore region.

mostly attributed to the confounding complexities and challenges associated with oxide thin films. Even from the reported work on Mn-Ru oxide, Bi_2O_3, and Pb-Ir oxide, there were additional tests that could have been taken to potentially provide more insight on some of the underlying results. Overall, I sought to practice a good balance of high-throughput experimentation and more meticulous testing. For instance, I confirmed that the roughness of certain oxide catalyst thin films did indeed affect the electrochemical results, which is clearly demonstrated by the RDE curves for Pb-Ir oxide (Chapter 6). We saw that that mass-transport limited current was unrealistically high when normalized to the assumed geometric area (5 mm diameter). Both cyclic voltammetry using ferrocyanide using the minicell and SEM imaging, which was performed by Ryo Wakabayashi, did confirm a generally rough surface (Figure S.5). Because of this additional challenge, it would have been beneficial to measure the local surface roughness of the film across the composition gradient using common probing techniques such as SEM or AFM, thereby obtaining a more accurate active surface area to normalize the activity results.

Another major challenge for many films was the need to introduce a conductive underlayer. Most of the oxide catalyst films were not conductive enough to measure electrochemically with the exception of materials containing IrO_2 and RuO_2, which are among the few existing conductive oxides. For a stacked film that must undergo a 500-750 °C anneal, there is the high risk of

complications associated with thermally activated inter-diffusion and oxidation of the conductive underlayer. For instance, one cannot simply use a common transition metal underlayer such as Ti or Cu; not only can they diffuse to the film surface, thus contaminating the film, they will invariably oxidize upon annealing in a standard air furnace, destroying their conductive properties. The only metals that are resistant to oxidation at high temperatures are noble metals, including Pt, Pd, Au, Ag, Ru, and Ir, all of which happen to be active catalysts for ORR and OER.

In previous runs, I tried making Ti nitride films, which function as strong diffusion barriers.[166, 196] Predictably, the TiN films quickly oxidized during the annealing step, destroying their conductivity. Another route that I regrettable abandoned was using fluorine doped titanium oxide (FTO) coated glass substrates of indium tin oxide (ITO). Both possess conductive properties suitable for electrochemical testing. This was confirmed when testing a binary Pb-Ir oxide composition spread that was deposited onto FTO. However, most commercial FTO substrates had a high surface roughness, which was clearly observed in the preliminary minicell screening measurements. While the surface roughness would have been a major challenge, which would have likely prompted AFM or SEM testing, it may still have been a feasible route, though it would compromise the notion of high-throughput testing. Lastly, as already summarized, the use of glassy carbon would have fully addressed the issue, though much of the electrectrochemical testing would have been delegated to someone in the Abruña lab. Overall, a chemically inert conductive support would have substantially circumvented the challenge of maintaining intact non-contaminated oxide films upon annealing to high temperatures.

APPENDIX A

APPENDIX I: ELECTROCHEMISTRY

A.1 Introduction

In the established paradigm of cutting-edge research that cultivates new and existing technologies, building a robust intellectual foundation on the fundamental principles of nature is the nexus between critically approaching existing scientific challenges, and creatively navigating beyond our current technological zenith. Electrocatalysts for oxygen reduction/oxidation are pivotal to this research; hence, developing a strong grasp of basic electrochemistry is a necessity. This appendix is an abridged discussion on some of the key principles (thermodynamics, kinetics, and mass transport) of electrochemistry. It is in the best interest of the reader to explore these concepts in greater depth from established literature.[7, 284]

A.2 Definition of Electrochemistry and the Electrochemical Cell

Electrochemistry is a fundamental study of chemical processes that facilitate the transfer of electrons from one reactant to another. This electron exchange is defined by a coupled oxidation/reduction (redox) process. During redox, oxidation reactants lose electrons, and positively ionize to higher oxidation states, while reduction reactants receive electrons, lowering their oxidation states in the process. Redox reactions are ubiquitous in nature; one common example is the oxidation of iron when exposed to moist environments over a certain period, forming a brittle iron-oxide layer (i.e. rust) upon reacting with oxygen. However, the practical value of electrochemistry is the inextricable link between a chemical reaction and electricity, which is the operating basis for several indispensible technologies, including fuel cells, batteries, super capacitors, water-splitting electrolyzers, and catalytic converters. These technologies are instrumental to several established

and emerging applications related to materials processing, filtration, energy conversion, energy storage, fuel electrolysis, and solar-to-fuel generation.

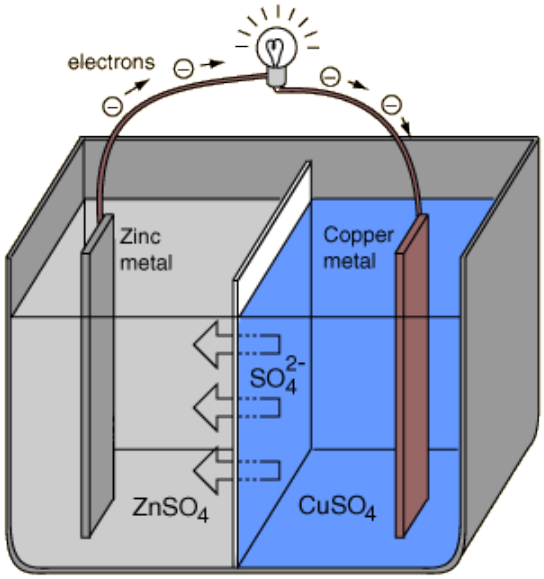

Figure S.1: An illustration of classic electrochemical cell. Zinc (Zn) and copper (Cu) plates are separated by aqueous electrolyte and a selective ion membrane to facilitate the ionic transport of SO_4^{2-} ions from the cathode (Cu) to the anode (Zn). Image taken from *http://hyperphysics.phy-astr.gsu.edu/hbase/Chemical/electrochem.html*

An electrochemical cell, as depicted by Figure S.1, is a device that operates on the exchange between chemical reactions and charge-transfer. A typical cell consists of two electrodes, an anode and a cathode; both electrodes are separated by an ionically conductive electrolyte consisting of reactive and/or non-reactive ions. When an electrochemical cell is connected to an external circuit, whether it's electrically driving (galvanic) the circuit or being driven by the circuit (electrolysis), active species at the anode/electrolyte interface are oxidized, generating electrons that subsequently transfer through the external circuit to the cathode, where active species are reduced. In general, the full redox reaction of the cell is characterized by the half-reactions (i.e. oxidation/reduction) designated to anode and cathode.

Consider the illustrated electrochemical cell (Figure S.1) comprised of a copper (Cu) cathode and a zinc (Zn) anode. Both are immersed in a pool of aqueous electrolyte containing sulfate ions (SO_4^{2-}). Assuming that there is a chemical potential gradient between the Cu cathode

and Zn anode across the electrolyte, there is thermodynamic driving force for spontaneous redox to occur, which is quantified by the voltage (or cell potential) difference between the two plates. When the Zn-Cu cell is connected to a resistive external circuit, it spontaneously discharges, causing the Zn anode to oxidize and dissociate to form Zn^{2+} ions.

$$\begin{aligned} &Zn \rightarrow Zn^{2+} + 2e^{-} \\ &or \\ &Zn \rightarrow ZnSO_4 + 2e^{-} \end{aligned} \tag{A.1}$$

The oxidation-generated electrons flow through the external circuit, generating electrical current, towards the Cu cathode, reducing the Cu^{2+} ions near the electrode surface to electroplate metallic Cu.

$$\begin{aligned} &Cu^{2+} + 2e^{-} \rightarrow Cu \\ &or \\ &CuSO_4 + 2e^{-} \rightarrow Cu \end{aligned} \tag{A.2}$$

The negative transfer of charge from the anode to the cathode is balanced by the transport of selective ionic species within the electrolyte solution. In the case of Zn-Cu cell, non-electroactive sulfate (SO_4^{2-}) ions migrate and diffuse towards the anode. To minimize crossover of Cu^{2+} or Zn^{2+}, this cell contains a selective ion membrane for the exclusive permeation of SO_4^{2-}.

Though there are many other electrochemical applications beyond the previous example, the principle operation that details the relationship between redox behavior and electricity is the same. For instance, fuel cells generate electricity by oxidizing hydrogen (H_2) near the anode to form protons, or H^+, while the cathode reduces oxygen (O_2) to its anionic form (O^{2-}). Both ions combine to form H_2O. Although the reactants are different, fuel cells still operate on the principle mechanism of redox-facilited charge transfer.

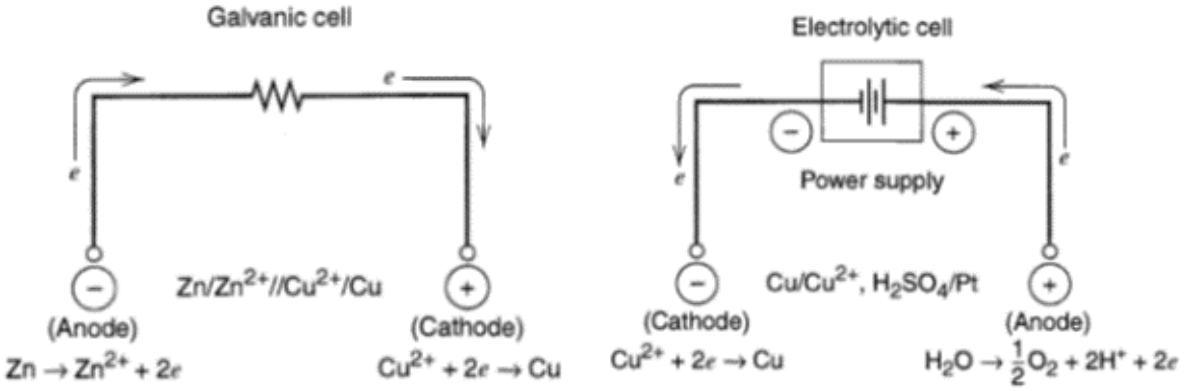

Figure S.2: A illustration of two electrochemical cells under (a) galvanic operation and (b) electrolytic operation.[7]

A.2.1 Galvanic and Electrolytic Cell

It was mentioned earlier that an electrochemical cell can either operate galvanically or electrolytically. Figure S.2 differentiates cells under galvanic and electrolytic operation. Under galvanic operation, electricity is generated from the spontaneous redox reaction taking place within the cell. Conversely, electrolysis reverses the direction of electrical current when a cell is driven by an opposing external power source, thus, reversing the direction of electron flow and redox reaction. However, in order for electrolysis to occur, the direct-current (DC) voltage of the opposing external power source must exceed the open-circuit potential (OCP) of the electrochemical cell. Common examples of galvanic cells include energy conversion and storage devices such as fuel cells and discharging batteries. Electrolytic cells include water-splitting for hydrogen generation, charging batteries. Although synthesis of specific chemicals, electro-refining to treat metals, and electroplating to form coatings of high purity metals (e.g gold and silver) is mostly achieved through electrolytic operation for greater control, these processes can technically be achieved under galvanic operation if the conditions of the cell can drive these processes to occur spontaneously. One important caveat is that the designation of the cathode and anode is strictly based on the specific half-reaction taking place as opposed to the electrode material. The designated cathode electrode always receives electrons (reduction) while the anode always loses electrons (oxidation).

Thus, if the operation of the cell is reversed, the cathode becomes the anode and vice versa.

A.2.2 Faradaic vs. Non-Faradaic Current

There are two processes in which an electrochemical cell responds to a perturbation: faradaic and non-faradaic current. The passage of faradaic current comes directly from the redox reaction, which entails full electron-transfer across the electrode/electrolyte interface. Analogous to a capacitor, non-faradaic current is a transient process generated by charging current that creates charge separation between the two electrodes. As a result, there is an accumulation layer of specifically and non-specifically adsorbed charged species and/or dipole molecules, forming an electrical double layer. Pure non-faradic behavior is exhibited by an ideal polarized electrode (IPE). Although no true IPE exists, real systems such as mercury electrodes in potassium chloride (KCl) can closely approach IPE behavior within a fairly wide potential window (~2V). However, unlike a true capacitor, the capacitance of an electrochemical cell is dependent on the cell potential due to the transient effects of the double layer. Consequently, non-faradaic charge, or a combination of non-faradaic and facile faradaic (pseudo capacitive) currents, have significant application value as alternative energy storage devices (supercapacitors) due to their fast charge/discharge times.

A.3 Thermodynamic Electrochemistry

Thermodynamics is a scientific branch that describes the relationship between heat and all forms of energy. Thermodynamics represents a core template to just about every single scientific discipline. For an electrochemical cell that is outside of equilibrium, the difference in free energy drives the redox reaction. Thus, there is a quantitative link between the free energy as dictated by the properties of the cell (temperature, concentration-activities of the active redox species), and the cell potential, a measurable quantity.

A.3.1 Nernst Equation

Consider an electrochemical cell with an infinite impedance voltmeter connected across the cathode and anode; the voltmeter measures and displays the cell potential - also known as the open circuit potential (OCP). Most importantly, the cell potential, E_{rxn}, is directly proportional to the change in the redox free energy, ΔG.

$$\Delta G = -nFE_{rxn} \tag{A.3}$$

Furthermore, the redox process in standard state is shown as:

$$\Delta G^0 = -nFE^0 \tag{A.4}$$

Equations A.3 and A.4 show that E_{rxn} is proportional to ΔG by a pre-factor n, which is the number of electrons that transfer per unit (mol, atom) for a given reaction, and Faradays constant, F (charge per unit mol of 96,500 C/mol).

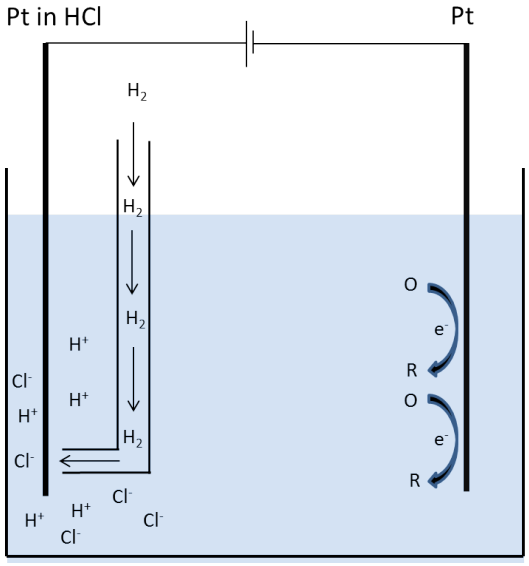

Figure S.3: An inert working electrode (Pt) against a NHE reference. The working electrode is being driven by an external source towards reduction.

We can derive an explicit relationship between the thermodynamic states of the redox species and the cell potential using the illustration shown in Figure S.3. Two wires, a platinum

(Pt) wire and an inert metal wire (also Pt), are both immersed in an aqueous electrolyte solution of hydrochloric acid (HCl). The solution also contains a small concentration of reversible redox couples, such as ferrocene, an organometallic compound, and its oxidized cation counterpart (ferrocenium). Because the base chemical structure of the ferrocene/ferrocenium couple are essentially the same, the redox reaction is facile and reversible. For simplicity, the reactants will be designated as reduced ferrocene (R = ferrocene) and oxidized ferrocenium (O = ferrocenium). In the above illustration, the entire reaction of the cell is written as shown:

$$H_2 + 2O \rightarrow 2R + 2H^+ \tag{A.5}$$

When the reaction is broken up into their half-reactions at the cathode and anode, we see that the NHE (anode) oxidizes H_2 into H^+ protons.

$$H_2 \rightleftarrows 2H^+ + 2e^- \tag{A.6}$$

At the cathode, O is reduced to R.

$$O + e^- \rightleftarrows R \tag{A.7}$$

The spontaneity of the reaction in Equation A.5 is governed by the partial molar change in Gibbs free energy, ΔG. Under constant temperature and pressure, we express ΔG as the chemical potential, μ_{i}, difference between the reactants and products. If we rewrite Reaction A.5 in its broadest form, we get:

$$aH_2 + bO \rightarrow cR + dH^+ \tag{A.8}$$

Thus, the chemical potential of each active specie is:

$$\Delta G = d\mu_{H^+} + c\mu_R - b\mu_O - a\mu_{H_2} \tag{A.9}$$

The standard state free energy, ΔG^0, is similarly written as:

$$\Delta G^0 = d\mu^0_{H^+} + c\mu^0_R - b\mu^0_O - a\mu^0_{H_2} \tag{A.10}$$

We then write ΔG as a function of activity:

$$\Delta G = \Delta G^0 + RT ln\left(\frac{a^d_{H^+} a^c_R}{a^a_{H_2} a^b_O}\right) \tag{A.11}$$

Assuming that the partial pressure of H_2 and activity of H^+ is fixed to their standard states (a_{H_2}, $a_{H^+} = 1$), which is the set condition for an NHE reference, Equation A.11 is simplified to:

$$\Delta G = \Delta G^0 + RT ln\left(\frac{a_R^c}{a_O^b}\right) \tag{A.12}$$

Because the NHE potential is zero, Equation A.12 shows that ΔG depends soley on the cathode half-reaction. Since the cell potential (E_{rxn}) is proportional to ΔG, Equation A.12 can be re-written as:

$$\Delta E_{rxn} = \Delta E^0 + \frac{RT}{nF} ln\left(\frac{a_O^b}{a_R^c}\right) \tag{A.13}$$

This relationship is known as the Nernst Equation, which explicitly represents E_{rxn} as a function of the chemical states of the redox species. The Nernst equation is most often represented as a function of redox concentration (ex. mol/cm^3).

$$\Delta E_{rxn} = \Delta E^{0'} + \frac{RT}{nF} ln\left(\frac{C_O^b}{C_R^c}\right) \tag{A.14}$$

Equation A.14 now incoporates the term containing the activity coefficients, γ, with E^0, rewritten as the formal potential, $E^{0'}$.

$$\Delta E^{0'} = \Delta E^0 + \frac{RT}{nF} ln\left(\frac{\gamma_O^b}{\gamma_R^c}\right) \tag{A.15}$$

To balance Reaction A.7, the powers b and c are both equal to 1, with n = 1. Therefore, the final equation for E_{rxn} is:

$$\Delta E_{rxn} = \Delta E^{0'} + \frac{RT}{F} ln\left(\frac{C_O}{C_R}\right) \tag{A.16}$$

Sign Conventions

The designated sign convention of the cell potential in relation to the free energy can often be a source of confusion. Many define the cell potential as a directionless quantity, whereby an infinitesimal change in the overall value dictates the direction of the redox reaction. This contrasts the definition of the Gibbs free energy, a directional quantity by which the sign corresponds to the direction of the reaction. Consequently, separate definitions now exist in order to reconcile the

direct relationship between the free energy and cell potential. For instance, E_{rxn} is also known as the electromotive force (emf), which is designated as a directional quantity tied to the cell reaction as opposed to the physical cell. For example, if we consider a convention of assigning the reduction half-reaction spontaneously taking place at the right electrode with respect to the oxidation half-reaction taking place at the left electrode, E_{rxn} becomes:

$$E_{rxn} = E_{Right} - E_{Left} \tag{A.17}$$

If the left electrode (oxidation) is at a lower potential than the right electrode (reduction), the reaction will spontaneously reduce, resulting in a positive emf quantity. Conversely, if the cell reaction reverses, the potential difference is now between the left electrode (reduction) and the right electrode (oxidation), resulting in a negative emf. This facilitates consistency in quantitatively connecting E_{rxn} to ΔG (Equation A.3), which are opposite in sign since a positive emf and negative ΔG defines a spontaneous reaction.

Reversibility

Reversibility is an important descriptor for characterizing the nature of various electrochemical processes. In practice, however, there are different degrees of reversibility in electrochemistry. Thermodynamic reversibility represents the absolute limit in which a system is always at equilibrium - the path from one state to another is changed infinitesimally, incurring no net change in entropy. Consequently, reals systems are not perfectly reversible in nature, but they can exhibit behavior that closely aligns with thermodynamic reversibility. In the context of electrochemistry, a system can be characterized as being chemically and/or practically reversible. Chemical reversibility is defined by a chemical reaction that can proceed forwards or backwards. Many practical systems show chemical reversibility; one example is the following redox reaction of a silver/silverchloride (Ag/AgCl) (eq. 2.xx) is an example a chemically reversible reaction:

$$AgCl + e^- \rightleftharpoons Ag(s) + Cl^- \tag{A.18}$$

In forward direction, AgCl is reduced, dissociating to form metallic Ag. If the reaction is reversed, that same metallic Ag will re-oxidize to form AgCl. For irreversible reactions, the product, R, may decompose into a different byproduct in the presence of another reactant. Thus, the direction of the reaction can no longer be reversed.

$$O + ne^- \rightarrow R \rightarrow T \tag{A.19}$$

If a reaction is thermodynamically reversible, then it is by extension chemically reversible, though a chemically reversible reaction may not always be thermodynamically reversible. Common examples include reactions that are extremely limited kinetically, resulting in a significant perturbation threshold to activate the reaction. Facile reactions that are close to thermodynamically reversible are often defined as practically reversible, or "Nernstian", which is notably found in simple reactions that exhibit rapid reaction kinetics within short time domains.

A.4 Reaction Kinetics

The Nernst equation, a relationship derived from the redox free energy, provides a quantifiable link between the cell potential and the chemical states (i.e. concentration, activities) of the redox species. However, a thermodynamic model is limited in scope when it comes to quantitatively explicating the mechanistic and dynamic behavior of an electrochemical cell. To demonstrate, consider a generalized reversible redox reaction shown below:

$$O + ne^- \underset{k_a}{\overset{k_c}{\rightleftharpoons}} R \tag{A.20}$$

Up to this point, the behavior of a redox reaction was quantified by the thermodynamic driving force (Nernst equation) while ignoring the rate at which O reduces to R (or vice versa). For this reaction, we define two opposing reaction rates corresponding to the reduction of O to R, and oxidation of R to O. The rate constants, k_c and k_a, are proportionality coefficients that relate the

rate of reaction, υ, to the concentration of the redox species, O and R.

$$\upsilon_a = k_a C_R \tag{A.21}$$

$$\upsilon_c = k_c C_O \tag{A.22}$$

The subscripts c and a correspond to the cathodic (reduction) and anodic (oxidation) current, respectively. For an electrochemical cell, most redox reactions are heterogeneous - electron-charge transfer during redox occurs across two phases (electrolyte/electrode). Thus, the heterogeneous rate of reaction, υ, has a flux unit of mol/cm^{2}s across the surface area of the electrode/electrolyte interface while k has a unit of cm/s. If both half-reactions are combined, the net rate of reaction becomes:

$$\upsilon_{net} = k_c C_O - k_a C_R \tag{A.23}$$

At equilibrium, υ_{net} is zero, and the ratio of k_c and k_a equals the equilibrium constant K.

$$K = \frac{k_c}{k_a} = \frac{C_R}{C_O} \tag{A.24}$$

Outside of equilibrium $\upsilon_{net} = 0$ ($\upsilon_{net} \neq 0$), we see that υ_{net} is directly proportional to the redox current by the electron-transfer number, n, Farday's constant, F, and the electrode surface area, A.

$$\upsilon_{net} = \frac{i}{nFA} \tag{A.25}$$

$$i = nFA[k_c C_O - k_a C_R] \tag{A.26}$$

Because the reaction is heterogeneous, the redox current is dependent on the surface concentrations $C_O(0,t)$ and $C_R(0,t)$.

$$i = nFA[k_c C_O(0,t) - k_a C_R(0,t)] \tag{A.27}$$

The connection between the rate of reaction and the free energy of the redox species, whether in equilibrium or perturbed, is illustrated using the transition state theory (TST) model (Figure S.4). The free energy diagram, which is a function of the reaction coordinate, describes the transition of reactants into products and vice versa. Between the two energy levels, there is a high

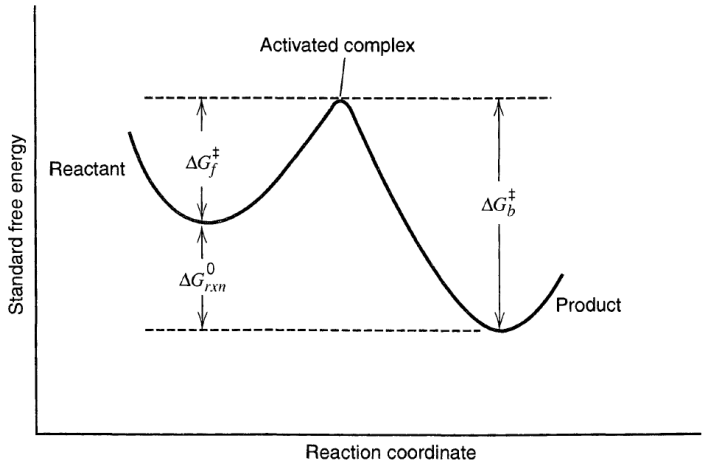

Figure S.4: Free energy changes during a reaction. The transition states represents the maximum free energy.[7]

energy barrier known as the transition state, which represents the energy transition to an activated complex. Although the reaction shown is spontaneous, the rate of the reaction is highly dependent on the activation potential, $\Delta G^{\ddagger}$, of the transition state.

The first step is recognizing that the rate constant, k, follows an Arrhenius relationship with respect to $\Delta G^{\ddagger}$ and temperature. The forward and backward rate constants are written as follows:

$$k_c = A_c e^{-\Delta G_c^{\ddagger}/RT} \tag{A.28}$$

$$k_a = A_a e^{-\Delta G_a^{\ddagger}/RT} \tag{A.29}$$

The pre-factor, A, is a phenomenological value that quantifies the change in entropy, molecular and statistical mechancial behavior of the redox species. The transition state complex is designated as a quasi-equilibrium state by which its concentration can be written in terms of the reactant/product concentration. Figure S.5 contrasts changes to the standard free energy diagram when the redox reaction is at equilibrium, or driven towards reduction/oxidation. At equilibrium, the free energy levels of the redox species are equal, thus, the forward and backward rates of reaction are equally opposed, yielding a net rate of zero. At a negative potential relative to $E^{0'}$, the free energy of R is shifted downward, driving the reaction towards reduction. Conversely, a positive potential shifts

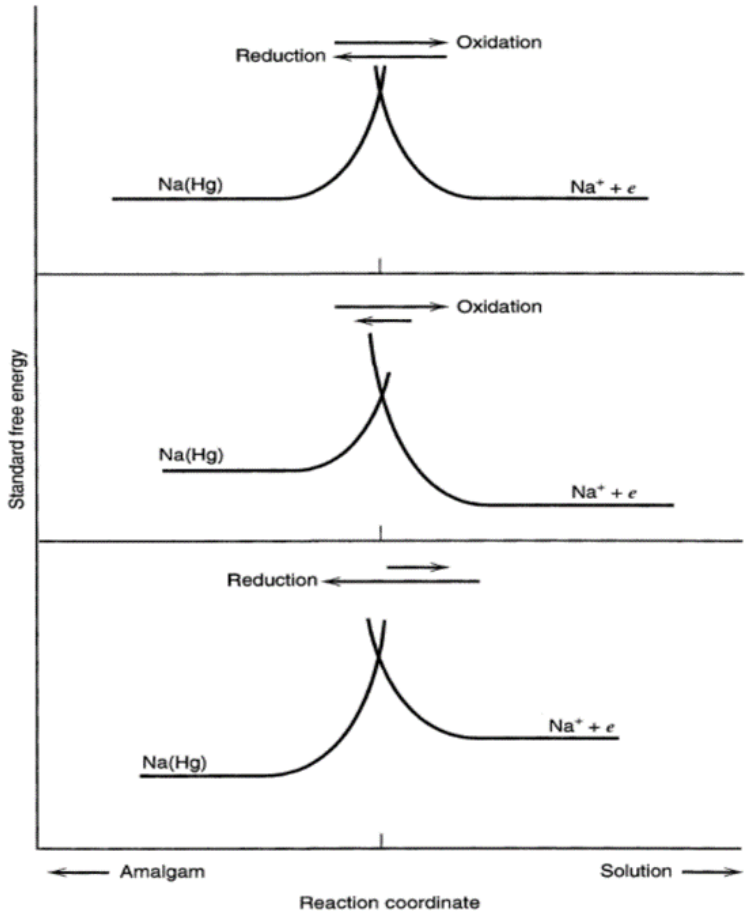

Figure S.5: Standard free energy changes at the equilibrium potential (Top), a more postive potential relative to equilibrium (Middle), and more negative potential relative to equilibrium (Bottom).[7]

the free energy of O downward, driving the reaction towards oxidation.

A.4.1 Standard Rate Constant

Under equilibrium, the free energy barriers, $\Delta G_c^{\ddagger}$ and $\Delta G_a^{\ddagger}$ for O and R are equal. Thus, the forward and backward rate constants are equal ($k_f = k_b$), assuming that the concentrations of O and R are the same ($C_O = C_R$). Based on the stated criteria, both k_f and k_b are redefined as the

standard rate constant, k^0.

$$k_c = k_a = k^0 = Ae^{-\Delta G^{\ddagger}/RT} \tag{A.30}$$

The standard rate constant is an intrinsic kinetic quantity of the redox reaction. Typical k^0 values for very rapid and facile 1-electron transfer reactions range from 1 to 10 cm/s. Common examples of high k^0 reactions include the transitions of aromatic species such as anthracenes, pyrene, and perleyne into their radical counterparts. In contrast, complex n-electron multi-step reactions with large rate-limiting free energy barriers typically have significantly lower k^0 values. Oxygen reduction and oxygen evolution are prime examples of low k^0 reactions.

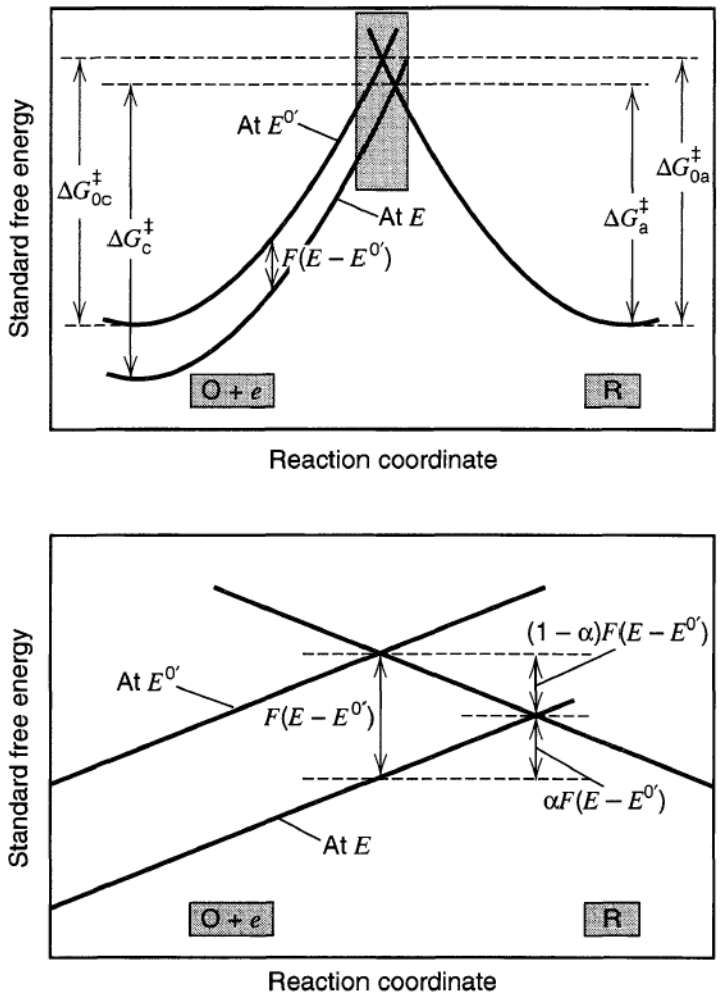

Figure S.6: Wide (Top) and magnified (Bottom) effects of a potential change on the standard free energy of activation.[7]

A.4.2 Butler-Volmer Equation

Using the example shown in Figure S.6, the extent at which the free energy of O + e- is shifted when a positive potential is applied relative to $E^{0'}$. Under the assumption that the free energy profile is linear near the transition state , the free energy barriers for oxidation ($\Delta G_a^{\ddagger}$) and reduction ($\Delta G_c^{\ddagger}$) are shifted proportionally by the difference between the cell potential, E, and the formal potential $E^{0'}$.

$$\Delta G_c^{\ddagger} = \Delta G_{0c}^{\ddagger} + \alpha nF(E - E^{0'}) \tag{A.31}$$

$$\Delta G_a^{\ddagger} = \Delta G_{0a}^{\ddagger} - (1 - \alpha)nF(E - E^{0'}) \tag{A.32}$$

The transfer coefficient, α, is a unitless parameter normalized between 0 and 1, and described as the fraction by which the free energy changes when shifted. Thus, the value of α is dependent on the shape and symmetry of the free energy profile and transition state. Although α is technically not a constant, but a function of potential, the change is generally negligible within a small potential window, especially for a facile reaction.

By substituting Equations A.31 and A.32 into the Arrhenius Equations A.28 and A.29 for k_c and k_a, respectively, we now have an explicit relationship between the rate constant and the change in cell potential.

$$k_c = A_c e^{-\Delta G_{0c}^{\ddagger}/RT} \times e^{-\alpha nF(E-E^{0'})/RT} \tag{A.33}$$

$$k_a = A_a e^{-\Delta G_{0a}^{\ddagger}/RT} \times e^{(1-\alpha)nF(E-E^{0'})/RT} \tag{A.34}$$

Equations A.33 and A.34 can be simplified further by expressing the relationship in terms of the standard rate constant, k^0.

$$k_a = k^0 e^{(1-\alpha)nF(E-E^{0'})/RT} \tag{A.35}$$

$$k_c = k^0 e^{-\alpha nF(E-E^{0'})/RT} \tag{A.36}$$

By revisiting equation A.27, we can now express the current, i, as a function of E.

$$i = i_c - i_a = nFAk^0\left[C_O(0,t)e^{-\alpha nF(E-E^{0'})/RT} - C_R(0,t)e^{(1-\alpha)nF(E-E^{0'})/RT}\right] \tag{A.37}$$

This expression is famously known as the Butler-Volmer (BV) equation, an explicit relationship between the redox current and the cell potential.

Exchange Current

We see that the key parameters of the BV equation is k^0 and α. Consider the behavior of a system under equilibrium conditions, where $\upsilon_{net} = 0$ when the cell potential is at E_{eq}. Consequently, the anodic and cathodic currents are equal ($i_a = i_c$).

$$C_O(0,t)e^{-\alpha nF(E_{eq}-E^{0\prime})/RT} = C_R(0,t)e^{(1-\alpha)nF(E_{eq}-E^{0\prime})/RT} \tag{A.38}$$

Assuming that the surface and bulk compositions are equal at equilibrium, we see that Equation A.38 simplifies to the Nernst equation:

$$\frac{C_O^*}{C_R^*} = e^{nF(E_{eq}-E^{0\prime})/RT} \tag{A.39}$$

$$E_{eq} = E^{0\prime} + \frac{RT}{nF} ln\left(\frac{C_O^*}{C_R^*}\right) \tag{A.40}$$

The magnitude of i_a and i_c at equilibrium becomes known as the exchange current, i_0.

$$i_0 = i_c = i_a = nFAk^0 C_O^* e^{-\alpha nF(E_{eq}-E^{0\prime})/RT} \tag{A.41}$$

By substituting Equation A.39, the exchange current is rearranged as a function of C_O^* and C_R^*.

$$i_0 = nFAk^0 C_O^{*(1-\alpha)} C_R^{*\alpha} \tag{A.42}$$

In the specific case where $C_O = C_R$, the Equation A.42 simplifies to:

$$i_0 = nFAk^0 C_O \tag{A.43}$$

Current-Overpotential

For real systems, its more practical to represent the BV equation as a function of the overpotential ($\eta = E - E_{eq}$), and exchange current, i_0. If we take the BV equation (Equation A.37)

and divide it by i_0 (Equation A.41), the relationship becomes:

$$\frac{i}{i_0} = \left[\frac{C_O(0,t)e^{-\alpha nF(E_{eq}-E^{0\prime})/RT}}{C_O^* e^{-\alpha nF(E_{eq}-E^{0\prime})/RT}} - \frac{C_R(0,t)e^{(1-\alpha)nF(E_{eq}-E^{0\prime})/RT}}{C_R^* e^{(1-\alpha)nF(E_{eq}-E^{0\prime})/RT}}\right] \tag{A.44}$$

Using simple mathematical manipulation, the formal potential terms cancel out, and the BV equation becomes:

$$i = i_0\left[\frac{C_O(0,t)}{C_O^*}e^{-\alpha nF\eta/RT} - \frac{C_R(0,t)}{C_R^*}e^{(1-\alpha)nF\eta/RT}\right] \tag{A.45}$$

If mass transport is not a factor, which is the case for a well-stirred solution at low faradaic currents, the surface and bulk concentrations are equal, and the BV equation can be rewritten as:

$$\frac{i}{i_0} = \left[e^{-\alpha nF\eta/RT} - e^{(1-\alpha)nF\eta/RT}\right] \tag{A.46}$$

At greater overpotentials, whether cathodic or anodic, the back-reaction term becomes negligible. For instance, BV equation for a system at high reduction overpotentials is approximated as:

$$i = i_0 e^{-\alpha nF\eta/RT} \tag{A.47}$$

Relationship between BV and the Nernst Equation

The relationship between the BV equation and the Nernst equation becomes evident when looking at a Nernstian redox reaction. Consider a facile n-electron reaction, where the reaction kinetics exceeds the minimum limit within the measureable time scale. Consequently, the exchange current i_0, or the standard reaction coefficient, k^0 is very large. In the limiting case where the $i_0 \rightarrow \infty$.

$$\lim_{i_0\to\infty} \frac{i}{i_0} = 0 \tag{A.48}$$

The ratio i/i_0 converges to zero, thus, Equation A.45 becomes:

$$0 = \left[\frac{C_O(0,t)}{C_O^*}e^{-\alpha nF\eta/RT} - \frac{C_R(0,t)}{C_R^*}e^{(1-\alpha)nF\eta/RT}\right] \tag{A.49}$$

$$\frac{C_O(0,t)}{C_R(0,t)} = \frac{C_O^*}{C_R^*}e^{-nF(E-E_{eq})/RT} \tag{A.50}$$

The ratio, C_O^*/C_R^*, is substituted by Equation A.39, yielding:

$$\frac{C_O(0,t)}{C_R(0,t)} = e^{-nF(E_{eq}-E^{0\prime})/RT} e^{-nF(E-E_{eq})/RT} \tag{A.51}$$

Finally, the E_{eq} terms cancel out, and the equation reduces to the Nernst equation:

$$\frac{C_O(0,t)}{C_R(0,t)} = e^{-nF(E-E^{0\prime})/RT} \tag{A.52}$$

A.4.3 Tafel Plot

As previously summarized, the BV equation can be approximated by a single exponential term corresponding to the forward reaction at high overpotentials, showing a linear trend when plotted logarithmically. This is known as a Tafel plot. Consider a well-stirred system under a high cathodic overpotential (negative potential).

$$i = i_0 e^{-\alpha nF\eta/RT} \tag{A.53}$$

Within this regime, that the anodic back reaction term is negligible, and the logarithmic equation becomes:

$$\eta = \frac{RT}{\alpha F} log\ i_0 - \frac{RT}{\alpha F} log\ i \tag{A.54}$$

If we plot the η versus log i, we get a linear Tafel plot. The slope, a, and intercept b, are:

$$\begin{aligned} a &= \frac{RT}{\alpha F} log\ i_0 \\ b &= -\frac{RT}{\alpha F} \end{aligned} \tag{A.55}$$

Figure S.7 shows a typical Tafel plot. Deviations at lower overpotentials are due to the non-negligible back reaction term. Typically the Tafel behavior is valid if the back reaction contributes less than 1% of the forward reaction, which translates to an overpotential of around 120 mV. It should be noted that the Tafel plot is also applicable to systems limited by mass transport.

$$\eta = \frac{RT}{\alpha F} log \frac{i_0}{i_{l,c}} - \frac{RT}{\alpha F} log \frac{(i_{l,c} - i)}{i} \tag{A.56}$$

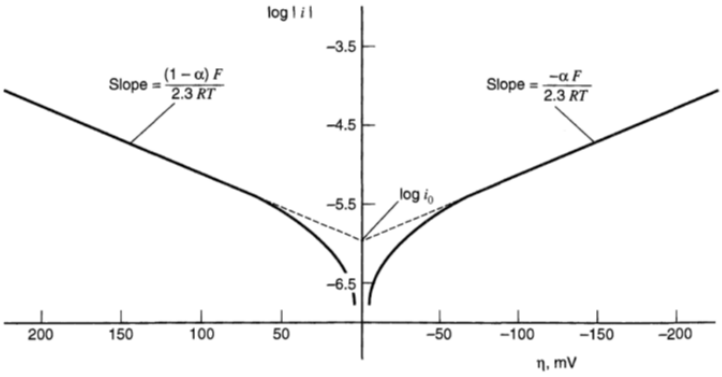

Figure S.7: Tafel plots under cathodic and anodic loads. Deviations from linearity at low overpotentials are due to non-neglible contributions from the back-reaction terms.[7]

This approach is especially useful when analyzing the kinetic behavior of sluggish reactions such as oxygen reduction, where overpotentials are typically around 300 mV.

A.4.4 Multi-electron Reactions

One important caveat is that real systems more complex, requiring multiple steps to complete a full redox reaction. An explicit relationship between the faradaic current and overpotential for a multi-step reaction is obfuscated by the number of unknown parameters that are specific to each reaction step, including the concentrations of the all of the intermediate species involved in the full reaction. Regardless, the rate of reaction for a multi-step process is only limited to the rate-determining step (RDS). In this case, the same approach outlined in the previous sections is still applicable to the RDS reaction. However, the BV equation now depends on the concentration of the intermediate species involved in the RDS, which is not always easily measured or controlled. Consider a multi-step reaction shown as follows:

$$\begin{aligned} O + n'e &\rightleftarrows O' \quad Step\ that\ precedes\ RDS \\ O' &\underset{k_a}{\overset{k_c}{\rightleftarrows}} R' \quad RDS \\ R' + n'' &\rightleftarrows R \quad Step\ following\ RDS \end{aligned} \tag{A.57}$$

Using the same mathematical treatment as previously shown, we see that the BV equation in terms of the RDS reaction step invariably involves the intermediate species, O′ and R′.

$$i = nFAk^0_{rds}\left[C_{O'}(0,t)e^{-\alpha F(E-E^{0'}_{rds})/RT} - C_{R'}(0,t)e^{(1-\alpha)F(E-E^{0'}_{rds})/RT}\right] \tag{A.58}$$

A.4.5 Microscopic Theory and Energy Distributions

Up to now, the BV equation has been treated as a phenomenological relationship without considering how the k^0 and α are influenced by the structural and chemical properties of the redox species. During the 20th century, several studies by key chemists, such as Marcus, Hush, Levich, and Dogonadze, formulated various microscopic theories that reconciled observed kinetic behavior with the microscopic behavior of the reactive species. More specifically, they fundamentally characterized the atomic behavior of the redox species, electrode surface, and solvent molecules in relation to the free energy distribution, nuclear coordinate, bond vibration, solvent motion, electron tunneling, inner sphere and outer sphere adsorption interactions.

For example, Marcus theory provides a qualitative and quantitative basis that links the structure of the chemical species to k^0, as well as the potential dependence of α. For extremely facile reactions, we see that the reactants and products require very little structural reorganization upon reaction, meaning the nuclear coordinate dictated by changes in reactant bond length and bond angles during the reaction are marginal; thus, k^0 and by extension the exchange rate, i_0, is extremely large. Conversely, sluggish reactions typically involve transitions that entail significant structural changes between reactant and product, and/or when there are strong adsorption interactions with the electrode or solvent (solvation) molecules. Other explanations include kinetic models based on the overlapping interactions between the energy states of the electrode and the energy states of the reactants within the solution. Unfortunately, this section is incredibly sparse in detail, since it's hardly pertinent to this research. I recommend reading sections 3.6.1 to 3.6.4 in the Faulkner text book to learn more about these theories.[7]

A.5 Effects of Mass Transport

In addition to the kinetic facility of a chemical system, we also have to consider another limiting factor, namely mass transport. During a faradaic reaction, the reactive species are consumed at the electrode/electrolyte interface at a given rate while the product species are created and accumlating at that same interface. When the reaction is being driven, the reactant concentration will start to deplete at the electrode surface, creating a concentration gradient between the surface and the bulk. In addition to the kinetic limitations of the reaction, the current output is also governed by the mass transport kinetics of the reactive species from bulk to the electrode surface. For Nernstian reactions, the current outptut is limited soley by mass transport. For quasireversible and irreversible systems, both processes can limit the current depending on the overpotential. Low overpotentials will predominantely be affect by kinetic properties of the reaction while high overpotentials will be limited by mass transport.

There are three types of mass transport: diffusion, migration, and convection. Both diffusion and migration are thermodynamically driven by the electrochemical potential gradient $\nabla\bar{\mu}$ (not to be confused with E) of both charged and uncharged species. The gradient arises from differences in concentration (or activity) and/or a potential gradient. Convection is characterized as a bulk flow of matter from an imbalance of forces. We can quantify these mechanisms as an area flow rate of chemical species, or flux (mol/cm^{2}s). The flux for a given specie, J_j, is proportional to the concentration C_j, the diffusion coefficient D_j, chemical potential gradient (diffusion and migration) and the velocity vector v (convection):

$$J_j = -\left(\frac{C_j D_j}{RT}\right)\nabla\bar{\mu}_j + C_j\vec{v} \tag{A.59}$$

The first term is the Nernst-Planck equation, and is expanded to terms corresponding to diffusion and migration. Thus, we now have a flux equation with respect to all three forms of mass transport is shown below:

$$J_j = -D_j\nabla C_j - \frac{z_j F}{RT}D_j C_j\nabla\phi + C_j\vec{v} \tag{A.60}$$

For a simple 1-D case, the flux equation becomes:

$$J_j(x) = -D_j \frac{\partial C_j(x)}{\partial x} - \frac{z_j F}{RT} D_j C_j \frac{\partial \phi(x)}{\partial x} + C_j v(x) \tag{A.61}$$

The first term is the diffusion flux derived from Fick's first law, the second term is the migration equation, and the third term is convection. In most cases, it is practical to simplify the effect of mass transport by controlling the electrochemical experiment in such a way that one or more the transport mechanisms no longer become a factor. For instance, let's assume that the measured system is under quiescent conditions where there is no convection - electrolyte solution is unstirred. The relative contributions of diffusion and migration to the overall flux are dependent on the time of response to a perturbation, and the distance away from the electrode. Near the electrode surface, both processes play a significant role. We can quantify the fraction of current corresponding to either diffusion or migration based on some knowledge of the conductance, diffusion coefficient, and transference of the reactive species. However, if the system has an excess of supporting electrolyte composed of non-electroactive ionic species, the contribution of migration is nearly zero, and the overall flux, or current is governed solely by diffusion.

$$J_j(x) = -D_j \frac{\partial C_j(x)}{\partial x} \tag{A.62}$$

$$i_j = -j_j z_j FA = z_j D_j FA \frac{\partial C_j(x)}{\partial x} \tag{A.63}$$

For multiple reactive species, the current equation turns into a summation.

$$i = \sum_j i_j = FA \sum_j z_j D_j \frac{\partial C_j}{\partial x} \tag{A.64}$$

BIBLIOGRAPHY

[1] Hamzah Abuadmah. Fuel Cells Versus Heat Engines: A Perspective of Thermodynamic and Production Efficiencies. 2012.

[2] S.B. Adler. Mechanism and kinetics of oxygen reduction on porous La1xSrxCoO3δ electrodes. *Solid State Ionics*, 111(1-2):125–134, 1998.

[3] Eugene Aleshin and Roy Rustum. Crystal Chemistry of Pyrochlore. *Journal of the American Ceramic Society*, 45(1):18–25, 1962.

[4] E B Anderson, E J Taylor, and G A Moniz. Lead-Ruthenium Pyrochlores as Oxygen Electrocatalysts. pages 125–130, 1999.

[5] Hitesh Arora, Phong Du, Kwan W. Tan, Jerome K. Hyun, John Grazul, Huolin L. Xin, David A. Muller, Michael O. Thompson, and Ulrich Wiesner. Block Copolymer Self-Assembly Directed Single-Crystal Homo- and Heteroepitaxial Nanostructures. *Science*, 330(October):214–330, 2010.

[6] Thomas Audichon, Eric Mayousse, Sophie Morisset, Cláudia Morais, Clément Comminges, Teko W. Napporn, and K. Boniface Kokoh. Electroactivity of RuO2-IrO2 mixed nanocatalysts toward the oxygen evolution reaction in a water electrolyzer supplied by a solar profile. *International Journal of Hydrogen Energy*, 39(30):16785–16796, 2014.

[7] Allen J Bard and Larry R. Faulkner. *Fundamentals and Fundamentals and Applications*, volume 8. 2001.

[8] P D Battle, C R a Catlow, a V Chadwick, P Cox, G N Greaves, and L. M. Moroney. Structural and Dynamical Studies of d-Bi2O3 Oxide Ion Conductors. IV. An EXAFS Investigation of (Bi2O3)1-x(M2O3)x for M=Y, Er, and Yb. *J. Solid State Chem.*, 69:230–239, 1987.

[9] P. D. Battle, C. R. a. Catlow, and L. M. Moroney. Structural and Dynamical Studies of delta-Bi2O3 Oxide-Ion Conductors. II. A Structural Comparison of (Bi2O3)1-x(M2O3) for M=Y, Er, Yb. *J. Solid State Chem.*, 67:42–50, 1987.

[10] P. D. Battle, G. Hu, L. M. Moroney, and D. C. Munro. Structural and Dynamical Studies of d-Bi203 Oxide Ion Conductors III. Phase Relationships in the System (Bi2O3)1-x(M2O3)x as a function of pressure and temperature (M=Y, Er, or Yb). *J. Solid State Chem.*, 69:30–35, 1987.

[11] Ryan D. Bayliss, Stuart N. Cook, Sakis Kotsantonis, Richard J. Chater, and John A. Kilner.

Oxygen ion diffusion and surface exchange properties of the α- And δ-phases of Bi2O3. *Advanced Energy Materials*, 4(10):2–7, 2014.

[12] Robert T. Bell. *High Throughput Screening of Structural Effects of Millisecond Time Scale Thermal Annealing*. PhD thesis, Cornell University, 2017.

[13] Robert T. Bell, Alan G. Jacobs, Victorial C. Sorg, Byungki Jung, Megan O. Hill, Benjamin E. Treml, and Michael O. Thompson. Lateral Temperature-Gradient Method for High-Throughput Characterization of Material Processing by Millisecond Laser Annealing. *ACS Combinatorial Science*, 18(9), 2016.

[14] Cornelius M. Berger, Abdelfattah Mahmoud, Raphaël P. Hermann, Waldemar Braun, Elena Yazhenskikh, Yoo Jung Sohn, Norbert H. Menzler, Olivier Guillon, and Martin Bram. Calcium-Iron Oxide as Energy Storage Medium in Rechargeable Oxide Batteries. *Journal of the American Ceramic Society*, 99(12):4083–4092, 2016.

[15] R. A. Beyerlein, H.S. Horowitz, and J M Longo. The Electrical Properties of A2[Ru2-xAx]O7-y (A = Pb or Bi) Pyrochlores as a Function of Composition and Temperature. *Journal of Solid State Chemistry*, 13:2–13, 1988.

[16] Petr Bezdicka, Tomas Grygar, Bretislav Klapste, and Jiri Vondrak. MnOx/C composites as electrode materials. I. Synthesis, XRD and cyclic voltammetric investigation. *Electrochimica Acta*, 45(6):913–920, 1999.

[17] Cicero W B Bezerra, Lei Zhang, Kunchan Lee, Hansan Liu, Aldaléa L B Marques, Edmar P. Marques, Haijiang Wang, and Jiujun Zhang. A review of Fe-N/C and Co-N/C catalysts for the oxygen reduction reaction. *Electrochimica Acta*, 53(15):4937–4951, 2008.

[18] a. Borowska-Centkowska, X. Liu, M. Holdynski, M. Malys, S. Hull, F. Krok, W. Wrobel, and I. Abrahams. Conductivity in lead substituted bismuth yttrate fluorites. *Solid State Ionics*, 254:59–64, jan 2014.

[19] Sai Boyapati, Eric D. Wachsman, and Bryan C. Chakoumakos. Neutron diffraction study of occupancy and positional order of oxygen ions in phase stabilized cubic bismuth oxides. *Solid State Ionics*, 138(3-4):293–304, 2001.

[20] Sai Boyapati, Eric D. Wachsman, and Naixiong Jiang. Effect of oxygen sublattice ordering on interstitial transport mechanism and conductivity activation energies in phase-stabilized cubic bismuth oxides. *Solid State Ionics*, 140(1-2):149–160, 2001.

[21] M. L. Calegaro, F. H B Lima, and E. A. Ticianelli. Oxygen reduction reaction on nanosized manganese oxide particles dispersed on carbon in alkaline solutions. *Journal of Power Sources*, 158(1):735–739, 2006.

[22] Y. L. Cao, H. X. Yang, X. P. Ai, and L. F. Xiao. The mechanism of oxygen reduction on MnO2-catalyzed air cathode in alkaline solution. *Journal of Electroanalytical Chemistry*, 557:127–134, 2003.

[23] Marcelo Carmo, David L. Fritz, Jürgen Mergel, and Detlef Stolten. A comprehensive review on PEM water electrolysis. *International Journal of Hydrogen Energy*, 38(12):4901–4934, 2013.

[24] Linda Carrette, K Andreas Friedrich, and Ulrich Stimming. Fuel cells : principles and applications. *ChemPhysChem*, 1:162–193, 2000.

[25] C Chang and T Wen. Kinetics of oxygen reduction at \cf{RuO2}-coated titanium electrode in alkaline solution. *Journal of Applied Electrochemistry*, 27:355–363, 1997.

[26] Fangyi Cheng and Jun Chen. Metalair batteries: from oxygen reduction electrochemistry to cathode catalysts. *Chemical Society Reviews*, 41(6):2172, 2012.

[27] Fangyi Cheng, Jian Shen, Bo Peng, Yuede Pan, Zhanliang Tao, and Jun Chen. Rapid room-temperature synthesis of nanocrystalline spinels as oxygen reduction and evolution electrocatalysts. *Nature chemistry*, 3(1):79–84, 2011.

[28] Fangyi Cheng, Yi Su, Jing Liang, Zhanliang Tao, and Jun Chen. MnO2-Based Nanostructures as Catalysts for Electrochemical Oxygen Reduction in Alkaline Media. *Chemistry of Materials*, 22(3):898–905, feb 2010.

[29] Fangyi Cheng, Tianran Zhang, Yi Zhang, Jing Du, Xiaopeng Han, and Jun Chen. Enhancing electrocatalytic oxygen reduction on MnO2 with vacancies. *Angewandte Chemie - International Edition*, 52(9):2474–2477, 2013.

[30] Serhiy Cherevko, Simon Geiger, Olga Kasian, Nadiia Kulyk, Jan Philipp Grote, Alan Savan, Buddha Ratna Shrestha, Sergiy Merzlikin, Benjamin Breitbach, Alfred Ludwig, and Karl J.J. Mayrhofer. Oxygen and hydrogen evolution reactions on Ru, RuO2, Ir, and IrO2 thin film electrodes in acidic and alkaline electrolytes: A comparative study on activity and stability. *Catalysis Today*, 262:170–180, 2016.

[31] Serhiy Cherevko, Simon Geiger, Olga Kasian, Andrea Mingers, and Karl J.J. Mayrhofer. Oxygen evolution activity and stability of iridium in acidic media. Part 2. - Electrochemically grown hydrous iridium oxide. *Journal of Electroanalytical Chemistry*, 774:102–110, 2016.

[32] Serhiy Cherevko, Tobias Reier, Aleksandar R. Zeradjanin, Zarina Pawolek, Peter Strasser, and Karl J.J. Mayrhofer. Stability of nanostructured iridium oxide electrocatalysts during

oxygen evolution reaction in acidic environment. *Electrochemistry Communications*, 48:81–85, 2014.

[33] P a Christensen, A Hamnett, and D Linares-Moya. Oxygen reduction and fuel oxidation in alkaline solution. *Physical chemistry chemical physics : PCCP*, 13(12):5206–14, 2011.

[34] Pierre Conflant, C Follet-Houttemane, and Michel Drache. The Bi2O3Sm2O3 system: phase diagram and electrical properties. *J. Mater. Chem.*, 1(4):649–653, 1991.

[35] James S. Cooper and Paul J. McGinn. Combinatorial screening of thin film electrocatalysts for a direct methanol fuel cell anode. *Journal of Power Sources*, 163(1 SPEC. ISS.):330–338, 2006.

[36] James S. Cooper and Paul J. McGinn. Combinatorial screening of fuel cell cathode catalyst compositions. *Applied Surface Science*, 254(3):662–668, nov 2007.

[37] Guillaume Couture, Ali Alaaeddine, Frédéric Boschet, and Bruno Ameduri. Polymeric materials as anion-exchange membranes for alkaline fuel cells. *Progress in Polymer Science (Oxford)*, 36(11):1521–1557, 2011.

[38] B. D. Cullity and S. R. Stock. *Elements of X-ray Diffraction*. Prentice Hall, third edition, 2001.

[39] Vivien K. Cumyn, M. D. Fleischauer, T. D. Hatchard, and J. R. Dahn. Design and Testing of a Low-Cost Multichannel Pseudopotentiostat for Quantitative Combinatorial Electrochemical Measurements on Large Electrode Arrays. *Electrochemical and Solid-State Letters*, 6(6):E15, 2003.

[40] S Curtin and J Gangi. Fuel Cell Technologies Market Report 2015. Technical report, U.S Department of Energy, 2015.

[41] Sandra Curtin and Jennifer Gangi. Fuel Cell Technologies Market Report 2014. Technical report, 2014.

[42] Gabriel C. da Silva, Nickson Perini, and Edson A. Ticianelli. Effect of temperature on the activities and stabilities of hydrothermally prepared IrOx nanocatalyst layers for the oxygen evolution reaction. *Applied Catalysis B: Environmental*, 218:287–297, 2017.

[43] Holger Dau, Christian Limberg, Tobias Reier, Marcel Risch, Stefan Roggan, and Peter Strasser. The Mechanism of Water Oxidation: From Electrolysis via Homogeneous to Biological Catalysis. *ChemCatChem*, 2(7):724–761, 2010.

[44] Maarten de Jong, Wei Chen, Henry Geerlings, Mark Asta, and Kristin Aslaug Persson. A database to enable discovery and design of piezoelectric materials. *Scientific Data*, 2:150053, 2015.

[45] Luisa Delmondo, Gian Paolo Salvador, José Alejandro Muñoz-Tabares, Adriano Sacco, Nadia Garino, Micaela Castellino, Matteo Gerosa, Giulia Massaglia, Angelica Chiodoni, and Marzia Quaglio. Nanostructured MnxOy for oxygen reduction reaction (ORR) catalysts. *Applied Surface Science*, 2016.

[46] R B Van Dover, L F Schneemeyer, and R M Fleming. Discovery of a useful thin-film dielectric using a composition-spread approach. *Nature*, 2655(March):2653–2655, 1998.

[47] Michel Drache, Pascal Roussel, and Jean Pierre Wignacourt. Structures and oxide mobility in Bi-Ln-O materials: Heritage of Bi2O3. *Chemical Reviews*, 107(1):80–96, 2007.

[48] Russell G. Egdell, John B. Goodenough, Andrew Hamnett, and Christopher C. Naish. Electrochemistry of Ruthenates. *Journal Chemical Society*, pages 893–912, 1983.

[49] Mohamed S. El-Deab and Takeo Ohsaka. Manganese oxide nanoparticles electrodeposited on platinum are superior to platinum for oxygen reduction. *Angewandte Chemie - International Edition*, 45(36):5963–5966, 2006.

[50] Mohamed S. El-Deab and Takeo Ohsaka. Electrocatalysis by design: Effect of the loading level of Au nanoparticles-MnOx nanoparticles binary catalysts on the electrochemical reduction of molecular oxygen. *Electrochimica Acta*, 52(5):2166–2174, 2007.

[51] Vincenzo Esposito, Enrico Traversa, and Eric D. Wachsman. Pb[sub 2]Ru[sub 2]O[sub 6.5] as a Low-Temperature Cathode for Bismuth Oxide Electrolytes. *Journal of The Electrochemical Society*, 152(12):A2300, 2005.

[52] H T Fan, S S Pan, X M Teng, C Ye, and G H Li. Structure and thermal stability of delta-Bi2O3 thin films deposited by reactive sputtering. *Journal of Physics D: Applied Physics*, 39(9):1939–1943, 2006.

[53] H T Fan, X M Teng, S S Pan, C Ye, G H Li, and L D Zhang. Optical properties of delta-Bi2O3 thin films grown by reactive sputtering. *Applied Physics Letters*, 87(23):3–5, 2005.

[54] H.T. Fan, S.S. Pan, X.M. Teng, C. Ye, G.H. Li, and L.D. Zhang. δ-Bi2O3 thin films prepared by reactive sputtering: Fabrication and characterization. *Thin Solid Films*, 513(1-2):142–147, 2006.

[55] José L. Fernández, Darren A. Walsh, and Allen J. Bard. Thermodynamic guidelines for the design of bimetallic catalysts for oxygen electroreduction and rapid screening by scanning

electrochemical microscopy. M-Co (M: Pd, Ag, Au). *Journal of the American Chemical Society*, 127(1):357–365, 2005.

[56] M. D. Fleischauer, T. D. Hatchard, G. P. Rockwell, J. M. Topple, S. Trussler, S. K. Jericho, M. H. Jericho, and J. R. Dahn. Design and Testing of a 64-Channel Combinatorial Electrochemical Cell. *Journal of The Electrochemical Society*, 150(11):A1465, 2003.

[57] Stephen E. Fosdick, Sean P. Berglund, C. Buddie Mullins, and Richard M. Crooks. Parallel screening of electrocatalyst candidates using bipolar electrochemistry. *Analytical Chemistry*, 85(4):2493–2499, 2013.

[58] Stephen E. Fosdick and Richard M. Crooks. Bipolar electrodes for rapid screening of electrocatalysts. *Journal of the American Chemical Society*, 134(2):863–866, 2012.

[59] E.J. Frazer and R. Woods. The oxygen evolution reaction on cycled iridium electrodes. *Journal of Electroanalytical Chemistry and Interfacial Electrochemistry*, 102(1):127–130, 1979.

[60] K. Fujii, Y. Sato, S. Takase, and Y. Shimizu. Effects of Oxygen Vacancies and Reaction Conditions on Oxygen Reduction Reaction on Pyrochlore-Type Lead-Ruthenium Oxide. *Journal of the Electrochemical Society*, 162(1):F129–F135, 2014.

[61] Hubert A. Gasteiger, Shyam S. Kocha, Bhaskar Sompalli, and Frederick T. Wagner. Activity benchmarks and requirements for Pt, Pt-alloy, and non-Pt oxygen reduction catalysts for PEMFCs. *Applied Catalysis B: Environmental*, 56(1-2 SPEC. ISS.):9–35, 2005.

[62] Hubert A. Gasteiger, Shyam S. Kocha, Bhaskar Sompalli, and Frederick T. Wagner. Activity benchmarks and requirements for Pt, Pt-alloy, and non-Pt oxygen reduction catalysts for PEMFCs. *Applied Catalysis B: Environmental*, 56(1-2 SPEC. ISS.):9–35, 2005.

[63] James B. Gerken, Jamie Y.C. Chen, Robert C. Massé, Adam B. Powell, and Shannon S. Stahl. Development of an O 2-sensitive fluorescence-quenching assay for the combinatorial discovery of electrocatalysts for water oxidation. *Angewandte Chemie - International Edition*, 51(27):6676–6680, 2012.

[64] James B. Gerken, Sarah E. Shaner, Robert C. Massé, Nicholas J. Porubsky, and Shannon S. Stahl. A survey of diverse earth abundant oxygen evolution electrocatalysts showing enhanced activity from NiFe oxides containing a third metal. *Energy Environ. Sci.*, 7(7):2376–2382, 2014.

[65] Celia L. Gomez, Osmary Depablos-Rivera, Juan C. Medina, Phaedra Silva-Bermudez, Stephen Muhl, Andreas Zeinert, and Sandra E. Rodil. Stabilization of the delta-phase in Bi2O3 thin films. *Solid State Ionics*, 255:147–152, 2014.

[66] Kuanping Gong, Feng Du, Zhenhai Xia, Michael Durstock, and Liming Dai. Nitrogen-Doped Carbon Nanotube Arrays with High Electrocatalytic Activity for Oxygen Reduction. *Science*, 323(5915):760–764, 2016.

[67] J. B. Goodenough, R. Manoharan, and M. Paranthaman. Surface Protonation and Electrochemical Activity of Oxides in Aqueous Solution. *Journal of the American Chemical Society*, 112(6):2076–2082, 1990.

[68] Yelena Gorlin and Thomas F Jaramillo. A Bifunctional Nonprecious Metal Catalyst for Oxygen Reduction and Water Oxidation. *Journal of American Chemistry Society*, 132:13612–13614, 2010.

[69] Yelena Gorlin and Thomas F. Jaramillo. Investigation of Surface Oxidation Processes on Manganese Oxide Electrocatalysts Using Electrochemical Methods and Ex Situ X-ray Photoelectron Spectroscopy. *Journal of the Electrochemical Society*, 159(10):H782–H786, 2012.

[70] J. Greeley, I. E. L. Stephens, A. S. Bondarenko, T. P. Johansson, H. A. Hansen, T. F. Jaramillo, J. Rossmeisl, I. Chorkendorff, and J. K. Nørskov. Alloys of platinum and early transition metals as oxygen reduction electrocatalysts. *Nature Chemistry*, 1(7):552–556, 2009.

[71] J Greeley, I E L Stephens, a S Bondarenko, T P Johansson, H a Hansen, T F Jaramillo, J Rossmeisl, I Chorkendorff, and J K Nørskov. Alloys of platinum and early transition metals as oxygen reduction electrocatalysts. *Nature chemistry*, 1(7):552–556, 2009.

[72] Jeff Greeley, Thomas F. Jaramillo, Jacob Bonde, Ib Chorkendorff, and Jens K. Nørskov. Computational high-throughput screening of electrocatalytic materials for hydrogen evolution. *Nature Materials*, 5(11):909–913, 2006.

[73] J. M. Gregoire and R. B. van Dover. C-16 High Energy Xrd/Xrf for High-Throughput Analysis of Composition Spread Thin Films. *Powder Diffraction*, 24(2):164, 2009.

[74] JM Gregoire. *High Throughput Material Science for Discovery of Energy-Related Materials*. PhD thesis, 2010.

[75] John M. Gregoire, Darren Dale, Alexander Kazimirov, Francis J. Disalvo, and R. Bruce Van Dover. High energy x-ray diffraction/x-ray fluorescence spectroscopy for high-throughput analysis of composition spread thin films. *Review of Scientific Instruments*, 80(12), 2009.

[76] John M. Gregoire, Maxim Kostylev, Michele E. Tague, Paul F. Mutolo, R. Bruce van Dover, Francis J. DiSalvo, H. D Abruna, and Hector D. Abruna. High-Throughput Evaluation of

Dealloyed Pt-Zn Composition-Spread Thin Film for Methanol-Oxidation Catalysis. *Journal of the Electrochemical Society*, 156(1):B160–B166, 2009.

[77] John M. Gregoire, Michele E. Tague, Sophie Cahen, Sahr Khan, Hector D. Abruna, Francis J. DiSalvo, and R. Bruce van Dover. Improved Fuel Cell Oxidation Catalysis in Pt1 xTa x. *Chemistry of Materials*, 22(3):1080–1087, feb 2010.

[78] E. Gülzow and M. Schulze. Long-term operation of AFC electrodes with CO2 containing gases. *Journal of Power Sources*, 127(1-2):243–251, 2004.

[79] Kun Guo, Yuan Li, Juan Yang, Zhiqing Zou, Xinzhong Xue, Xuemei Li, and Hui Yang. Nanosized MnRu binary oxides as effective bifunctional cathode electrocatalysts for rechargeable LiO2 batteries. *Journal of Materials Chemistry A*, 2(5):1509, 2014.

[80] Ziyang Guo, Chao Li, Wangyu Li, Hua Guo, Xiuli Su, Ping He, Yonggang Wang, and Yong-Yao Xia. Ruthenium Oxide Coated Ordered Mesoporous Carbon Nanofiber Arrays: A Highly Bifunctional Oxygen Electrocatalyst for Rechargeable Znair Batteries. *J. Mater. Chem. A*, 2016.

[81] Shiva Gupta, William Kellogg, Hui Xu, Xien Liu, Jaephil Cho, and Gang Wu. Bifunctional Perovskite Oxide Catalysts for Oxygen Reduction and Evolution in Alkaline Media. *Chemistry - An Asian Journal*, 11(1):10–21, 2016.

[82] Sossina M. Haile. Fuel cell materials and components. *Acta Materialia*, 51(19):5981–6000, 2003.

[83] Sossina M. Haile. Fuel cell materials and components. *Acta Materialia*, 51(19):5981–6000, 2003.

[84] Heine Anton Hansen, Venkatasubramanian Viswanathan, and Jens K. Nørskov. Unifying Kinetic and Thermodynamic Analysis of 2 e and 4 e Reduction of Oxygen on Metal Surfaces. *The Journal of Physical Chemistry C*, 118(13):6706–6718, 2014.

[85] H a Harwig. On the Structure of Bismuthsesquioxide: The α, β, γ, and δ-phase. *Zeitschrift fur Anorganische und Allgemeine Chemie*, 444(1):151–166, 1978.

[86] H a Harwig and a G Gerards. Electrical properties of the alpha, beta, gamma, and delta phases of bismuth sesquioxide. *Journal of Solid State Chemistry*, 26(3):265–274, 1978.

[87] H. A. Harwig and A. G. Gerards. The polymorphism of bismuth sesquioxide. *Thermochimica Acta*, 28(1):121–131, 1979.

[88] John G. Hauck and Paul J. McGinn. Screening of novel Li-air battery catalyst materials by a thin film combinatorial materials approach. *ACS Combinatorial Science*, 17(6):355–364, 2015.

[89] T. He, E. Kreidler, L. Xiong, J. Luo, and C. J. Zhong. Alloy Electrocatalysts. *Journal of The Electrochemical Society*, 153(9):A1637, 2006.

[90] Allen Hermann, Tapas Chaudhuri, and Priscila Spagnol. Bipolar plates for PEM fuel cells: A review. *International Journal of Hydrogen Energy*, 30(12):1297–1302, 2005.

[91] Michael A. Hickner, Andrew M. Herring, and E. Bryan Coughlin. Anion exchange membranes: Current status and moving forward. *Journal of Polymer Science, Part B: Polymer Physics*, 51(24):1727–1735, 2013.

[92] Rosalie K Hocking, Robin Brimblecombe, Lan-Yun Chang, Archana Singh, Mun Hon Cheah, Chris Glover, William H Casey, and Leone Spiccia. Water-oxidation catalysis by manganese in a geochemical-like cycle. *Nature chemistry*, 3(6):461–6, 2011.

[93] Adam Holewinski, Juan-Carlos Idrobo, and Suljo Linic. High-performance AgCo alloy catalysts for electrochemical oxygen reduction. *Nature Chemistry*, 6(9):828–834, 2014.

[94] Wesley T. Hong, Marcel Risch, Kelsey A. Stoerzinger, Alexis Grimaud, Jin Suntivich, and Yang Shao-Horn. Toward the rational design of non-precious transition metal oxides for oxygen electrocatalysis. *Energy Environ. Sci.*, 8(5):1404–1427, 2015.

[95] H. S. Horowitz. Oxygen Electrocatalysis on Some Oxide Pyrochlores. *Journal of The Electrochemical Society*, 130(9):1851, 1983.

[96] H S Horowitz, J M Longo, H H Horowitz, J T Lewandowski, Science Laboratories, and Engineering Company. The Synthesis and Electrocatalytic Properties of Nonstoichiometric Ruthenate Pyrochlores. *American Chemical Society*, 1985.

[97] H.S. Horowitz, J M Longo, and J T Lewandowski. New Oxide Pyrochlores. *Materials Research Bulletin*, 16(c):489–496, 1981.

[98] H. W. Hugosson, G. E. Grechnev, R. Ahuja, U. Helmersson, L. Sa, and O. Eriksson. Stabilization of potential superhard RuO2 phases: A theoretical study. *Physical Review B*, 66(17):174111, 2002.

[99] Nika J. Ilavsky. Software for Two-Dimensional Data Reduction. *Journal of Applied Crystallography*, 45:324–328, 2012.

[100] V P Ivanov and G K Boreskov. The Chemisorption of Oxygen on the Iridium (111) Surface. *Surface Science*, 61:207–220, 1976.

[101] H. Iwahara, T. Esaka, T. Sato, and T. Takahashi. Formation of high oxide ion conductive phases in the sintered oxides of the system Bi2O3Ln2O3 (Ln = LaYb). *Journal of Solid State Chemistry*, 39(2):173–180, 1981.

[102] H. Jang, a. Zahoor, J. S. Jeon, P. Kim, Y. S. Lee, and K. S. Nahm. Sea Urchin Shaped -MnO2/RuO2 Mixed Oxides Nanostructure as Promising Electrocatalyst for Lithium-Oxygen Battery. *Journal of the Electrochemical Society*, 162(3):A300–A307, 2014.

[103] Shrisudersan Jayaraman and Andrew C. Hillier. Construction and reactivity mapping of a platinum catalyst gradient using the scanning electrochemical microscope. *Langmuir*, 17(25):7857–7864, 2001.

[104] Junhua Jiang and Anthony Kucernak. Electrochemical supercapacitor material based on manganese oxide: Preparation and characterization. *Electrochimica Acta*, 47(15):2381–2386, 2002.

[105] N. Jiang, R.M. Buchanan, D.a. Stevenson, W.D. Nix, Ji-Zhou Li, and Ji-Lian Yang. Anion ordering in aged stabilized bismuth oxide. *Materials Letters*, 22(5-6):215–219, 1995.

[106] Feng Jiao and Heinz Frei. Nanostructured cobalt and manganese oxide clusters as efficient water oxidation catalysts. *Energy & Environmental Science*, 3(8):1018, 2010.

[107] Ludwig Jörissen. Bifunctional oxygen/air electrodes. *Journal of Power Sources*, 155(1):23–32, 2006.

[108] Kevin Joseph, Taaffe Noonan, Kristina M Hugar, Henry a Kostalik, Emil B Lobkovsky, Héctor D Abruña, and Geoffrey William Coates. Phosphonium Functionalized Polyethylene : A New Class of Base Stable Alkaline Anion Exchange Membranes Phosphonium Functionalized Polyethylene : A New Class of Base Stable Alkaline Anion Exchange Membranes. *Journal of the American Chemical Society*, 134(44):18161–18164, 2012.

[109] Su-Ho Jung, Eric D. Wachsman, and Naixiong Jiang. Structural stability and conductivity of cubic (WO3)x - (Dy2O3)y-(Bi2O3)1xy. *Ionics*, 8(3-4):210–214, 2002.

[110] Suho Jung, Charles C L McCrory, Ivonne M Ferrer, Jonas C Peters, and Thomas F Jaramillo. Benchmarking nanoparticulate metal oxide electrocatalysts for the alkaline water oxidation reaction. *J. Mater. Chem. A*, 4:–, 2016.

[111] A M Kannan, A K Shukla, and S Sathyanarayana. Lead-Iridium Pyrocblore Based Bifunctional Oxygen Electrode. *Energy*, 281:339–344, 1990.

[112] Yena Kim, Young Wook Lee, Minjune Kim, and Sang Woo Han. One-pot synthesis and electrocatalytic properties of Pd@Pt core-shell nanocrystals with tailored morphologies. *Chemistry - A European Journal*, 20(26):7901–7905, 2014.

[113] Bretislav Klápste, Jirí Vondrák, and Jana Velická. MnOx/C composites as electrode materials II. Reduction of oxygen on bifunctional catalysts based on manganese oxides. *Electrochimica Acta*, 47(15):2365–2369, 2002.

[114] Jaidong Ko and Charles T. Prewitt. High-pressure phase transition in MnTiO3 from the ilmenite to the LiNbO3 structure. *Physics and Chemistry of Minerals*, 15(4):355–362, 1988.

[115] M V Kortenaar, J F Vente, D J W Ijdo, S Miiller, and R Kiitz. Oxygen evolution and reduction on iridium oxide compounds. *Journal of Power Sources*, 56(Iv), 1995.

[116] Akihiko Kudo and Yugo Miseki. Heterogeneous photocatalyst materials for water splitting. *Chem. Soc. Rev.*, 38(1):253–278, 2009.

[117] P. Lacorre, F. Goutenoire, O. Bohnke, R. Retoux, and Y. Lallgant. Designing fast oxide-ion conductors based on La2Mo2O9. *Nature*, 404(6780):856–858, 2000.

[118] K. Laurent, G. Y. Wang, S. Tusseau-Nenez, and Y. Leprince-Wang. Structure and conductivity studies of electrodeposited delta-Bi2O3. *Solid State Ionics*, 178(33-34):1735–1739, 2008.

[119] Youngmin Lee, Jin Suntivich, Kevin J. May, Erin E. Perry, and Yang Shao-Horn. Synthesis and Activities of Rutile IrO2 and RuO2 Nanoparticles for Oxygen Evolution in Acid and Alkaline Solutions. *Journal of Physical Chemistry Letters*, 3(3):399–404, 2012.

[120] Andreas Lesch, Fernando Cortés-Salazar, Victor Costa Bassetto, Véronique Amstutz, and Hubert H. Girault. Inkjet Printing Meets Electrochemical Energy Conversion. *CHIMIA International Journal for Chemistry*, 69(5):284–289, 2015.

[121] Ernest M. Levin and Robert S. Roth. Polymorphism of bismuth sesquioxide. II. Effect of oxide additions on the polymorphism of Bi2O3. *Journal of Research of the National Bureau of Standards Section A: Physics and Chemistry*, 68A(2):197, 1964.

[122] Chun Li, Xiaopeng Han, Fangyi Cheng, Yuxiang Hu, Chengcheng Chen, and Jun Chen. Phase and composition controllable synthesis of cobalt manganese spinel nanoparticles towards efficient oxygen electrocatalysis. *Nature Communications*, 6:7345, 2015.

[123] Da Li, Habib Baydoun, Claudio N. Verani, and Stephanie L. Brock. Efficient Water Oxidation Using CoMnP Nanoparticles. *Journal of the American Chemical Society*, 138(12):4006–4009, 2016.

[124] Ming Li, Martha J. Pietrowski, Roger A. De Souza, Huairuo Zhang, Ian M. Reaney, Stuart N. Cook, John A. Kilner, and Derek C. Sinclair. A family of oxide ion conductors based on the ferroelectric perovskite Na0.5Bi0.5TiO3. *Nature Materials*, 13(1):31–35, 2014.

[125] Yanguang Li, Wu Zhou, Hailiang Wang, Liming Xie, Yongye Liang, Fei Wei, Juan-Carlos Idrobo, Stephen J. Pennycook, and Hongjie Dai. An oxygen reduction electrocatalyst based on carbon nanotubegraphene complexes. *Nature Nanotechnology*, 7(6):394–400, 2012.

[126] Yongye Liang, Hailiang Wang, Jigang Zhou, Yanguang Li, Jian Wang, Tom Regier, and Hongjie Dai. Covalent Hybrid of Spinel ManganeseCobalt Oxide and Graphene as Advanced Oxygen Reduction Electrocatalysts. *Journal of the American Chemical Society*, 134(7):3517–3523, feb 2012.

[127] Fabio H.B. Lima, Marcelo L Calegaro, and Edson A Ticianelli. Investigations of the catalytic properties of manganese oxides for the oxygen reduction reaction in alkaline media. *Journal of Electroanalytical Chemistry*, 590(2):152–160, 2006.

[128] Fabio H.B. Lima, Marcelo L. Calegaro, and Edson a. Ticianelli. Electrocatalytic activity of manganese oxides prepared by thermal decomposition for oxygen reduction. *Electrochimica Acta*, 52(11):3732–3738, 2007.

[129] Hsiu Li Lin, T. Leon Yu, and Fang Hsin Han. A method for improving ionic conductivity of nafion membranes and its application to PEMFC. *Journal of Polymer Research*, 13(5):379–385, 2006.

[130] Xiaomei Lin, Liyan Zheng, Gongmin Gao, Yuwu Chi, and Guonan Chen. Electrochemiluminescence imaging-based high-throughput screening platform for electrocatalysts used in fuel cells. *Analytical Chemistry*, 84(18):7700–7707, 2012.

[131] Shizhong Liu, Michael G. White, and Ping Liu. Mechanism of Oxygen Reduction Reaction on Pt(111) in Alkaline Solution: Importance of Chemisorbed Water on Surface. *Journal of Physical Chemistry C*, 120(28):15288–15298, 2016.

[132] Xiaonao Liu, Tzyh-Jong Tarn, Fenfen Huang, and Jie Fan. Recent advances in inkjet printing synthesis of functional metal oxides. *Particuology*, 19:1–13, 2015.

[133] Xien Liu, Minjoon Park, Min Gyu Kim, Shiva Gupta, Xiaojuan Wang, Gang Wu, and Jaephil Cho. High-performance non-spinel cobalt-manganese mixed oxide-based bifunctional electrocatalysts for rechargeable zinc-air batteries. *Nano Energy*, 20:315–325, 2016.

[134] M.M. Lohrengel, a. Moehring, and M. Pilaski. Electrochemical Surface Analysis with the Scanning Droplet Cell. *Fresenius' Journal of Analytical Chemistry*, 367(4):S. 334–339, 2000.

[135] J.M. Longo, P.M. Raccah, and John B. Goodenough. Pb2M2O7-x (M=Ru, Ir, Re) - Preparation and Properties of Oxygen Deficient Pyrochlores. *Materials Research Bulletin*, 4, 1969.

[136] Mary W. Louie and Alexis T. Bell. An investigation of thin-film Ni-Fe oxide catalysts for the electrochemical evolution of oxygen. *Journal of the American Chemical Society*, 135(33):12329–12337, 2013.

[137] Guojin Lu, James S. Cooper, and Paul J. McGinn. SECM imaging of electrocatalytic activity for oxygen reduction reaction on thin film materials. *Electrochimica Acta*, 52(16):5172–5181, 2007.

[138] P. Lunca Popa, S. Sønderby, S. Kerdsongpanya, J. Lu, N. Bonanos, and P. Eklund. Highly oriented δ-Bi2O3 thin films stable at room temperature synthesized by reactive magnetron sputtering. *Journal of Applied Physics*, 113(4):2013–2016, 2013.

[139] Neelima Mahato, Amitava Banerjee, Alka Gupta, Shobit Omar, and Kantesh Balani. Progress in material selection for solid oxide fuel cell technology: A review. *Progress in Materials Science*, 72:141–337, 2015.

[140] F. Maillard, A. Bonnefont, and F. Micoud. An EC-FTIR study on the catalytic role of Pt in carbon corrosion. *Electrochemistry Communications*, 13(10):1109–1111, 2011.

[141] S. Malkhandi, P. Trinh, a. K. Manohar, K. C. Jayachandrababu, A. Kindler, G. K. Surya Prakash, and S. R. Narayanan. Electrocatalytic activity of transition metal oxide-carbon composites for oxygen reduction reaction in alkaline batteries and fuel cells. *Journal of the Electrochemical Society*, 160(9):F943–F952, 2013.

[142] N. Mamaca, E. Mayousse, S. Arrii-Clacens, T. W. Napporn, K. Servat, N. Guillet, and K. B. Kokoh. Electrochemical activity of ruthenium and iridium based catalysts for oxygen evolution reaction. *Applied Catalysis B: Environmental*, 111-112:376–380, 2012.

[143] Isabela C. Man, Hai Yan Su, Federico Calle-Vallejo, Heine A. Hansen, José I. Martínez, Nilay G. Inoglu, John Kitchin, Thomas F. Jaramillo, Jens K. Nørskov, and Jan Rossmeisl. Universality in Oxygen Evolution Electrocatalysis on Oxide Surfaces. *ChemCatChem*, 3(7):1159–1165, 2011.

[144] Rohini Mani, Michael Fischer, Joby E. Joy, J. Gopalakrishnan, and Martin Jansen. Ruthenium(IV) pyrochlore oxides: Realization of novel electronic properties through substitution at A- and B-sites. *Solid State Sciences*, 11(1):189–194, jan 2009.

[145] Lanqun Mao, Dun Zhang, Tadashi Sotomura, Kenichi Nakatsu, Nobuharu Koshiba, and

Takeo Ohsaka. Mechanistic study of the reduction of oxygen in air electrode with manganese oxides as electrocatalysts. *Electrochimica Acta*, 48(8):1015–1021, apr 2003.

[146] Lanqun Q Mao, Tadashi Sotomura, Kenichi Nakatsu, Nobuharu Koshiba, Dun Zhang, and Takeo Ohsaka. Electrochemical characterization of catalytic activities of manganese oxides to oxygen reduction in alkaline aqueous solution. *Journal of the Electrochemical Society*, 149(4):A504–A507, 2002.

[147] N. M. Markovic and P. N. Ross Jr. Surface science studies of model fuel cell electrocatalysts. *Surface Science Reports*, 45(4-6):117–229, 2002.

[148] N. M. Marković, T. J. Schmidt, V. Stamenković, and P. N. Ross. Oxygen Reduction Reaction on Pt and Pt Bimetallic Surfaces: A Selective Review. *Fuel Cells*, 1(2):105–116, 2001.

[149] Justus Masa, Wei Xia, Ilya Sinev, Anqi Zhao, Zhenyu Sun, Stefanie Grützke, Philipp Weide, Martin Muhler, and Wolfgang Schuhmann. MnxOy/NC and CoxOy/NC nanoparticles embedded in a nitrogen-doped carbon matrix for high-performance bifunctional oxygen electrodes. *Angewandte Chemie - International Edition*, 53(32):8508–8512, 2014.

[150] James McBreen. The electrochemistry of β-MnO2 and -MnO2 in alkaline electrolyte. *Electrochimica Acta*, 20(3):221–225, 1975.

[151] Charles C L McCrory, Suho Jung, Jonas C. Peters, and Thomas F. Jaramillo. Benchmarking heterogeneous electrocatalysts for the oxygen evolution reaction. *Journal of the American Chemical Society*, 135(45):16977–16987, 2013.

[152] Paul J. McGinn. Combinatorial electrochemistry Processing and characterization for materials discovery. *Materials Discovery*, 1:38–53, 2015.

[153] Géraldine Merle, Matthias Wessling, and Kitty Nijmeijer. Anion exchange membranes for alkaline fuel cells: A review. *Journal of Membrane Science*, 377(1-2):1–35, 2011.

[154] M. H. Miles, E. A. Klaus, B. P. Gunn, J. R. Locker, W. E. Serafin, and S. Srinivasan. The oxygen evolution reaction on platinum, iridium, ruthenium and their alloys at 80C in acid solutions. *Electrochimica Acta*, 23(6):521–526, 1978.

[155] Alessandro Minguzzi, Mario A. Alpuche-Aviles, Joaquin Rodríguez López, Sandra Rondinini, and Allen J. Bard. Screening of oxygen evolution electrocatalysts by scanning electrochemical microscopy using a shielded tip approach. *Analytical Chemistry*, 80(11):4055–4064, 2008.

[156] Mogens Bjerg Mogensen. Materials for fuel cells. *40 years of research at Risø: A platform*

for the future - interacting with industry and society. Summary of presentations, Risø-R-106(March):24–29, 1998.

[157] Masayuki Morita, Chiaki Iwakura, and Hideo Tamura. The anodic characteristics of modified Mn oxide electrode: Ti/RuOx/MnOx. *Electrochimica Acta*, 23(4):331–335, 1978.

[158] Masayuki Morita, Chiaki Iwakura, and Hideo Tamura. The anodic characteristics of massive manganese oxide electrode. *Electrochimica Acta*, 24(4):357–362, 1979.

[159] S. Mukerjee and S. Srinivasan. Enhanced electrocatalysis of oxygen reduction on platinum alloys in proton-exchange membrane fuel-cells. *Journal of Electroanalytical Chemistry*, 357(1-2):201–224, 1993.

[160] Sanjeev Mukerjee. Role of Structural and Electronic Properties of Pt and Pt Alloys on Electrocatalysis of Oxygen Reduction. *Journal of The Electrochemical Society*, 142(5):1409, 1995.

[161] Janice L. Musfeldt. *Handbook of Applied Solid State Spectroscopy*, volume 129. 2007.

[162] T.H. Muster, a. Trinchi, T.a. Markley, D. Lau, P. Martin, a. Bradbury, a. Bendavid, and S. Dligatch. A review of high throughput and combinatorial electrochemistry. *Electrochimica Acta*, 56(27):9679–9699, nov 2011.

[163] Mohammad Mahdi Najafpour, Gernot Renger, Małgorzata Hołyńska, Atefeh Nemati Moghaddam, Eva Mari Aro, Robert Carpentier, Hiroshi Nishihara, Julian J. Eaton-Rye, Jian Ren Shen, and Suleyman I. Allakhverdiev. Manganese Compounds as Water-Oxidizing Catalysts: From the Natural Water-Oxidizing Complex to Nanosized Manganese Oxide Structures. *Chemical Reviews*, 116(5):2886–2936, 2016.

[164] L. Napoli, J. Franco, H. Fasoli, and A. Sanguinetti. Conductivity of Nafion 117 membrane used in polymer electrolyte fuel cells. *International Journal of Hydrogen Energy*, 39(16):8656–8660, 2014.

[165] Radha Narayanan and Mostafa A. El-Sayed. Shape-dependent catalytic activity of platinum nanoparticles in colloidal solution. *Nano Letters*, 4(7):1343–1348, 2004.

[166] M. A. Nicolet. Diffusion Barriers in Thin Films. *Thin Solid Films*, 52:415–443, 1978.

[167] V Nikolova, P Iliev, K Petrov, T Vitanov, E Zhecheva, R Stoyanova, I Valov, and D Stoychev. Electrocatalysts for bifunctional oxygen/air electrodes. *Journal of Power Sources*, 185:727–733, 2008.

[168] Hong Nhan Nong, Lin Gan, Elena Willinger, Detre Teschner, and Peter Strasser. IrOx core-shell nanocatalysts for cost- and energy-efficient electrochemical water splitting. *Chem. Sci.*, 5(8):2955–2963, 2014.

[169] Hong Nhan Nong, Hyung Suk Oh, Tobias Reier, Elena Willinger, Marc Georg Willinger, Valeri Petkov, Detre Teschner, and Peter Strasser. Oxide-supported IrNiOx core-shell particles as efficient, cost-effective, and stable catalysts for electrochemical water splitting. *Angewandte Chemie - International Edition*, 54(10):2975–2979, 2015.

[170] J. K. Nørskov, J. Rossmeisl, A. Logadottir, L. Lindqvist, J. R. Kitchin, T. Bligaard, and H. Jónsson. Origin of the overpotential for oxygen reduction at a fuel-cell cathode. *Journal of Physical Chemistry B*, 108(46):17886–17892, 2004.

[171] W.E. O'Grady and A.K. Goel. Cyclic Voltammetry on RuO2 (100), (101), (001) and (110) "as-grown" Single-Crystal Surfaces. *Journal of Electroanal*, 151:295–303, 1983.

[172] Milton Ohring. *Materials Science of Thin Films: Deposition and Structure*. Academic Press, 2nd edition, 2002.

[173] Takeo Ohsaka, Lanqun Mao, Kazuki Arihara, and Tadashi Sotomura. Bifunctional catalytic activity of manganese oxide toward O2 reduction: Novel insight into the mechanism of alkaline air electrode. *Electrochemistry Communications*, 6(3):273–277, 2004.

[174] Takeo Ohsaka, Lanqun Mao, Kazuki Arihara, and Tadashi Sotomura. Bifunctional catalytic activity of manganese oxide toward O2 reduction: Novel insight into the mechanism of alkaline air electrode. *Electrochemistry Communications*, 6(3):273–277, 2004.

[175] J. Orava, A. L. Greer, B. Gholipour, D. W. Hewak, and C. E. Smith. Characterization of supercooled liquid Ge2Sb2Te5and its crystallization by ultrafast-heating calorimetry. *Nature Materials*, 11(4):279–283, 2012.

[176] H. Over, Y. D. Kim, A. P. Seitsonen, and S. Wendt. Atomic-Scale Structure and Catalytic Reactivity of the RuO2 (110) Surface. *Science*, 287:1474–1476, 2000.

[177] Herbert Over. Surface Chemistry of Ruthenium Dioxide in Heterogeneous Catalysis and Electro Catalysis : From Fundamental to Applied Research. *Chemical Reviews*, 112:3356–3426, 2012.

[178] Dimitrios Papageorgopoulos. Fuel Cells Sub-Program Overview. Technical report, U.S. Department of Energy, 2015.

[179] Shin-Ae Park, Hankwon Lim, and Yong-Tae Kim. Enhanced Oxygen Reduction Reaction

Activity Due to Electronic Effects between Ag and Mn 3 O 4 in Alkaline Media. *ACS Catalysis*, pages 3995–4002, 2015.

[180] Y. Pauleau. Reactive sputter-deposition and characterization of lead oxide films. *Journal of Vacuum Science & Technology A: Vacuum, Surfaces, and Films*, 14(4):2207, 1996.

[181] Linus Pauling. *The Nature of the Chemical Bond*. Cornell University Press, third edition, 1960.

[182] Jonathan Petrie. *Combinatorial Search for Non-Pt Catalysts for Oxygen Reduction at Low Temperatures*. PhD thesis, 2010.

[183] Valery Petrykin, KateÅina MacOunová, Maki Okube, Sanjeev Mukerjee, and Petr Krtil. Local structure of Co doped RuO2 nanocrystalline electrocatalytic materials for chlorine and oxygen evolution. *Catalysis Today*, 202(1):63–69, 2013.

[184] Valery Petrykin, Katerina MacOunova, Jiri Franc, Oleg Shlyakhtin, Mariana Klementova, Sanjeev Mukerjee, and Petr Krtil. Zn-doped RuO2 electrocatalyts for selective oxygen evolution: Relationship between local structure and electrocatalytic behavior in chloride containing media. *Chemistry of Materials*, 23(2):200–207, 2011.

[185] J A I Prakash, Donald Tryk, and Ernest Yeager. Electrocatalysis for oxygen electrodes in fuel cells and water electrolyzers for space applications. *Journal of Power Sources*, 29:413–422, 1990.

[186] Jai Prakash. Kinetic Investigations of Oxygen Reduction and Evolution Reactions on Lead Ruthenate Catalysts. *Journal of The Electrochemical Society*, 146(11):4145, 1999.

[187] Mark Prochaska, Jing Jin, Dominic Rochefort, Lin Zhuang, Francis J. Disalvo, Hctor D. Abruna, and R. B. Van Dover. High throughput screening of electrocatalysts for fuel cell applications. *Review of Scientific Instruments*, 77(5):1–8, 2006.

[188] Mark Prochaska, Jing Jin, Dominic Rochefort, Lin Zhuang, Francis J. Disalvo, Hctor D. Abruna, and R. B. Van Dover. High throughput screening of electrocatalysts for fuel cell applications. *Review of Scientific Instruments*, 77(5), 2006.

[189] Liangti Qu, Yong Liu, Jong Beom Baek, and Liming Dai. Nitrogen-doped graphene as efficient metal-free electrocatalyst for oxygen reduction in fuel cells. *ACS Nano*, 4(3):1321–1326, 2010.

[190] V. Raghuveer and B. Viswanathan. Nanocrystalline pyrochlore bonded to proton exchange membrane electrolyte as electrode material for oxygen reduction. *Journal of Materials Science*, 40(23):6249–6255, 2005.

[191] V. Raghuveer and B. Viswanathan. Nanocrystalline pyrochlore bonded to proton exchange membrane electrolyte as electrode material for oxygen reduction. *Journal of Materials Science*, 40(23):6249–6255, sep 2005.

[192] A. Sahaya Raja, S. Rajendran, and P. Satyabama. Inhibition of corrosion of carbon steel in well water by DL-phenylalanine-Zn 2+ system. *Journal of Chemistry*, (October), 2013.

[193] Erik Reddington, Anthony Sapienza, Bogdan Gurau, Rameshkrishnan Viswanathan, S. Sarangapani, Eugene S Smotkin, and Thomas E Mallouk. Combinatorial Electrochemistry: A Highly Parallel, Optical Screening Method for Discovery of Better Electrocatalysts. *Science*, 280(5370):1735–1737, jun 1998.

[194] Arthur L Robinson. Laser Annealing: Processing Semiconductors Without a Furnace. *Science*, 201(4353):333–335, 1978.

[195] I Roche, E Chanet, M Chatenet, and J Vondrk. Carbon-Supported Manganese Oxide Nanoparticles as Electrocatalysts for the Oxygen Reduction Reaction (ORR) in Alkaline Medium:łPhysical Characterizations and ORR Mechanism. *The Journal of Physical Chemistry C*, 111(3):1434–1443, 2006.

[196] Ph Roquiny, F. Bodart, and G. Terwagne. Colour control of titanium nitride coatings produced by reactive magnetron sputtering at temperature less than 100C. *Surface and Coatings Technology*, 116-119:278–283, 1999.

[197] Nancy L. Ross, Jaidong Ko, and Charles T. Prewitt. A new phase transition in MnTiO3: LiNbO3-perovskite structure. *Physics and Chemistry of Minerals*, 16(7):621–629, 1989.

[198] R. K. Roy, J. I. Njagi, B. Farrell, I. Halaciuga, M. Lopez, and D. V. Goia. Deposition of continuous platinum shells on gold nanoparticles by chemical precipitation. *Journal of Colloid and Interface Science*, 369(1):91–95, 2012.

[199] C. G. Ryan. Developments in dynamic analysis for quantitative PIXE true elemental imaging. *Nuclear Instruments and Methods in Physics Research, Section B: Beam Interactions with Materials and Atoms*, 181(1-4):170–179, 2001.

[200] C. G. Ryan, D. R. Cousens, S. H. Sie, W. L. Griffin, G. F. Suter, and E. Clayton. Quantitative pixe microanalysis of geological matemal using the CSIRO proton microprobe. *Nuclear Inst. and Methods in Physics Research, B*, 47(1):55–71, 1990.

[201] C. G. Ryan, B. E. Etschmann, S. Vogt, J. Maser, C. L. Harland, E. Van Achterbergh, and D. Legnini. Nuclear microprobe - Synchrotron synergy: Towards integrated quantitative real-time elemental imaging using PIXE and SXRF. *Nuclear Instruments and Methods in*

Physics Research, Section B: Beam Interactions with Materials and Atoms, 231(1-4):183–188, 2005.

[202] C. G. Ryan and D. N. Jamieson. Dynamic analysis: on-line quantitative PIXE microanalysis and its use in overlap-resolved elemental mapping. *Nuclear Inst. and Methods in Physics Research, B*, 77(1-4):203–214, 1993.

[203] C. G. Ryan, D. N. Jamieson, C. L. Churms, and J. V. Pilcher. A new method for on-line true-elemental imaging using PIXE and the proton microprobe. *Nuclear Inst. and Methods in Physics Research, B*, 104(1-4):157–165, 1995.

[204] C. G. Ryan, D. P. Siddons, R. Kirkham, Z. Y. Li, M. D. De Jonge, D. J. Paterson, A. Kuczewski, D. L. Howard, P. A. Dunn, G. Falkenberg, U. Boesenberg, G. De Geronimo, L. A. Fisher, A. Halfpenny, M. J. Lintern, E. Lombi, K. A. Dyl, M. Jensen, G. F. Moorhead, J. S. Cleverley, R. M. Hough, B. Godel, S. J. Barnes, S. A. James, K. M. Spiers, M. Alfeld, G. Wellenreuther, Z. Vukmanovic, and S. Borg. Maia X-ray fluorescence imaging: Capturing detail in complex natural samples. *Journal of Physics: Conference Series*, 499(1), 2014.

[205] Jens W. Saalfrank and Wilhelm F. Maier. Doping, selection and composition spreads, a combinatorial strategy for the discovery of new mixed oxide catalysts for low-temperature CO oxidation. *Comptes Rendus Chimie*, 7(5):483–494, 2004.

[206] Tomokazu Sakamoto, Koichiro Asazawa, Jean Sanabria-Chinchilla, Ulises Martinez, Barr Halevi, Plamen Atanassov, Peter Strasser, and Hirohisa Tanaka. Combinatorial discovery of Ni-based binary and ternary catalysts for hydrazine electrooxidation for use in anion exchange membrane fuel cells. *Journal of Power Sources*, 247:605–611, 2014.

[207] N.M. Sammes, G.A. Tompsett, H. Näfe, and F. Aldinger. Bismuth based oxide electrolytes structure and ionic conductivity. *Journal of the European Ceramic Society*, 19(10):1801–1826, 1999.

[208] Simone Sanna, Vincenzo Esposito, Jens Wenzel Andreasen, Johan Hjelm, Wei Zhang, Takeshi Kasama, Søren Bredmose Simonsen, Mogens Christensen, Søren Linderoth, and Nini Pryds. Enhancement of the chemical stability in confined δ -Bi 2 O 3. *Nature Materials*, 14(5):500–504, 2015.

[209] Kotaro Sasaki, Hideo Naohara, Yun Cai, Yong Man Choi, Ping Liu, Miomir B. Vukmirovic, Jia X. Wang, and Radoslav R. Adzic. Core-protected platinum monolayer shell high-stability electrocatalysts for fuel-cell cathodes. *Angewandte Chemie - International Edition*, 49(46):8602–8607, 2010.

[210] Sunita Satyapal. Introduction; DOE Hydrogen and Fuel Cells Program FY 2016 Annual Progress Report. Technical report, 2016.

[211] Jens Scheidtmann, Pierre A. Weiß, and Wilhelm F. Maier. Hunting for better catalysts and materials-combinatorial chemistry and high throughput technology. *Applied Catalysis A: General*, 222(1-2):79–89, 2001.

[212] Florian Schröder, Nikolai Bagdassarov, and Lkhamsuren Bayarjargal. Temperature dependence of Bi2O3 structural parameters close to the $\alpha\delta$ phase transition. *Phase Transitions*, 83:311–325, 2010.

[213] Selim Senkan. Combinatorial heterogeneous catalysis - A new path in an old field. *Angewandte Chemie - International Edition*, 40(2):312–329, 2001.

[214] D. Sepa, M. Vojnovic, and A Damjanovic. Kinetics and Mechanism of O2 Reduction at Pt in Alkaline Solutions. *Electrochimica Acta*, 25:1491–1496, 1980.

[215] Min-hua Shao, Ping Liu, and Radoslav R Adzic. Superoxide anion is the intermediate in the oxygen reduction reaction on platinum electrodes. *Journal of the American Chemical Society*, 128(23):7408–9, 2006.

[216] S. Sharma and L. Hines. Oxidation of Ruthenium. *IEEE Transactions on Components, Hybrids, and Manufacturing Technology*, 6(1):89–92, mar 1983.

[217] Tatsuya Shinagawa, Angel T. Garcia-Esparza, and Kazuhiro Takanabe. Insight on Tafel slopes from a microkinetic analysis of aqueous electrocatalysis for energy conversion. *Scientific Reports*, 5(1):13801, 2015.

[218] P Shuk. Oxide ion conducting solid electrolytes based on Bi2O3. *Solid State Ionics*, 89(3-4):179–196, 1996.

[219] A. K. Shukla, A. M. Kannan, M. S. Hegde, and J. Gopalakrishnan. Effect of counter cations on electrocatalytic activity of oxide pyrochlores towards oxygen reduction/evolution in alkaline medium: an electrochemical and spectroscopic study. *Journal of Power Sources*, 35(2):163–173, 1991.

[220] D. P. Siddons, R. Kirkham, C. G. Ryan, G. De Geronimo, A. Dragone, A. J. Kuczewski, Z. Y. Li, G. A. Carini, D. Pinelli, R. Beuttenmuller, D. Elliott, M. Pfeffer, T. A. Tyson, G. F. Moorhead, and P. A. Dunn. Maia X-ray microprobe detector array system. *Journal of Physics: Conference Series*, 499(1), 2014.

[221] Archana Singh and Leone Spiccia. Water oxidation catalysts based on abundant 1st row transition metals. *Coordination Chemistry Reviews*, 257(17-18):2419, 2013.

[222] N. V. Skorodumova, a. K. Jonsson, M. Herranen, M. Strømme, G. a. Niklasson, B. Johans-

son, and S. I. Simak. Random conductivity of δ- Bi2O3 films. *Applied Physics Letters*, 86(24):1–3, 2005.

[223] Donald L. Smith. *Thin-Film Deposition: Principles and Practice*. McGraw-Hill, 1995.

[224] Ya Song, Ji Yang, and Xue-Qing Gong. Prediction of Ir0.5M0.5O2 (M = Cr, Ru or Pb) Mixed Oxides as Active Catalysts for Oxygen Evolution Reaction from First-Principles Calculations. *Topics in Catalysis*, 58(10):675–681, 2015.

[225] Jacob S Spendelow and Andrzej Wieckowski. Electrocatalysis of oxygen reduction and small alcohol oxidation in alkaline media. *Physical chemistry chemical physics : PCCP*, 9(21):2654–2675, 2007.

[226] Jacob S. Spendelow and Andrzej Wieckowski. Electrocatalysis of oxygen reduction and small alcohol oxidation in alkaline media. *Physical Chemistry Chemical Physics*, 9(21):2654, 2007.

[227] Jacob S. Spendelow and Andrzej Wieckowski. Electrocatalysis of oxygen reduction and small alcohol oxidation in alkaline media. *Physical Chemistry Chemical Physics*, 9(21):2654, 2007.

[228] A. D. Spong, G. Vitins, S. Guerin, B. E. Hayden, A. E. Russell, and John R. Owen. Combinatorial arrays and parallel screening for positive electrode discovery. *Journal of Power Sources*, 119-121:778–783, 2003.

[229] John Stacy, Yagya N. Regmi, Brian Leonard, and Maohong Fan. The recent progress and future of oxygen reduction reaction catalysis: A review. *Renewable and Sustainable Energy Reviews*, 69(November 2016):401–414, 2017.

[230] Vojislav Stamenkovic, Bongjin Simon Mun, Karl J.J. Mayrhofer, Philip N. Ross, Nenad M. Markovic, Jan Rossmeisl, Jeff Greeley, and Jens K. Nørskov. Changing the Activity of Electrocatalysts for Oxygen Reduction by Tuning the Surface Electronic Structure. *Angewandte Chemie*, 118(18):2963–2967, 2006.

[231] Vojislav R. Stamenkovic, Bongjin Simon Mun, Karl J.J. Mayrhofer, Philip N. Ross, and Nenad M. Markovic. Effect of surface composition on electronic structure, stability, and electrocatalytic properties of Pt-transition metal alloys: Pt-skin versus Pt-skeleton surfaces. *Journal of the American Chemical Society*, 128(27):8813–8819, 2006.

[232] Brian C. H. Steele. Materials for fuel-cell technologies. In *Materials for Sustainable Energy: A Collection of Peer-Reviewed Research and Review Articles from Nature Publishing Group*, pages 224–231. 2010.

[233] D. A. Stevens, J. M. Rouleau, R. E. Mar, A. Bonakdarpour, R. T. Atanasoski, A. K. Schmoeckel, M. K. Debe, and J. R. Dahn. Characterization and PEMFC Testing of Pt[sub 1x]M[sub x] (M=Ru,Mo,Co,Ta,Au,Sn) Anode Electrocatalyst Composition Spreads. *Journal of The Electrochemical Society*, 154(6):B566, 2007.

[234] E.R. Stobbe, B.A. de Boer, and J.W. Geus. The reduction and oxidation behaviour of manganese oxides. *Catalysis Today*, 47(1-4):161–167, 1999.

[235] Peter Strasser, Shirlaine Koh, Toyli Anniyev, Jeff Greeley, Karren More, Chengfei Yu, Zengcai Liu, Sarp Kaya, Dennis Nordlund, Hirohito Ogasawara, Michael F. Toney, and Anders Nilsson. Lattice-strain control of the activity in dealloyed coreshell fuel cell catalysts. *Nature Chemistry*, 2(6):454–460, 2010.

[236] M a Subramanian, G Aravamudan, and G V Subba Rao. Oxide Pyrochlores - A Review. *Progress in Solid State Chemistry*, 15:55–143, 1983.

[237] Michio Sugawara, Masamichi Ohno, and Kenzo Matsuki. Oxygen reduction catalysis of MnCo spinel oxides on a graphite electrode in alkaline solution. *Journal of Materials Chemistry*, 7(5):833–836, 1997.

[238] Jin Suntivich, Hubert A. Gasteiger, Naoaki Yabuuchi, Haruyuki Nakanishi, John B. Goodenough, and Yang Shao-Horn. Design principles for oxygen-reduction activity on perovskite oxide catalysts for fuel cells and metalair batteries. *Nature Chemistry*, 3(7):546–550, jul 2011.

[239] Jin Suntivich, Kevin J. May, Hubert A. Gasteiger, John B. Goodenough, and Yang Shao-Horn. A Perovskite Oxide Optimized for Oxygen Evolution Catalysis from Molecular Orbital Principles. *Science*, 334(2011):1383–1385, 2011.

[240] L. Swette, N. Kackley, and S. A. McCatty. Oxygen electrodes for rechargeable alkaline fuel cells. III. *Journal of Power Sources*, 36(3):323–339, 1991.

[241] J. A. Switzer. Electrodeposited Ceramic Single Crystals. *Science*, 284(5412):293–296, 1999.

[242] Michele Tague. *A Combinatorial Approach for Exploring Fuel Cell Electrocatalysts*. PhD thesis, 2011.

[243] L. W. Tai, M. M. Nasrallah, H. U. Anderson, D. M. Sparlin, and S. R. Sehlin. Structure and electrical properties of La1-xSrxCo1-yFeyO3. Part 1. The system La0.8Sr0.2Co1-yFeyO3. *Solid State Ionics*, 76(3-4):259–271, 1995.

[244] Kazunori Takada, Kenjiro Fujimoto, Takayoshi Sasaki, and Mamoru Watanabe. Combinatorial electrode array for high-throughput evaluation of combinatorial library for electrode materials. *Applied Surface Science*, 223(1-3):210–213, 2004.

[245] Takehiko Takahashi and Hiroyasu Iwahara. Oxide ion conductors based on bismuth-sesquioxide. *Materials Research Bulletin*, 13(12):1447–1453, 1978.

[246] Takashi Takeda, Ryoji Kanno, Yoji Kawamoto, Yasuo Takeda, and Osamu Yamamoto. New Cathode Materials for Solid Oxide Fuel Cells Ruthenium Pyrochlores and Perovskites. *Journal of The Electrochemical Society*, 147(5):1730, 2000.

[247] T. Takeyama, N. Takahashi, T. Nakamura, and S. Itoh. Growth and characterization of high-quality δ-Bi2O3 thin films grown by carbothermal evaporation. *Materials Letters*, 60(13-14):1733–1735, 2006.

[248] Tomoharu Takeyama, N. Takahashi, T. Nakamura, and S. Itoh. δ-Bi2O3 thin films deposited on dense YSZ substrates by CVD method under atmospheric pressure for intermediate temperature SOFC applications. *Surface and Coatings Technology*, 200(16-17):4797–4801, 2006.

[249] Kwan Wee Tan, Byungki Jung, Jörg G Werner, Elizabeth R Rhoades, Michael O Thompson, and Ulrich Wiesner. Transient laser heating induced hierarchical porous structures from block copolymer directed self-assembly. *Science*, 349(6243):54–59, 2015.

[250] Yueming Tan, Chaofa Xu, Guangxu Chen, Xiaoliang Fang, Nanfeng Zheng, and Qingji Xie. Facile synthesis of manganese-oxide-containing mesoporous nitrogen-doped carbon for efficient oxygen reduction. *Advanced Functional Materials*, 22(21):4584–4591, 2012.

[251] B Tesche, H Schulenburg, B Spliethoff, and M T Reetz. Pt/C catalysts for the oxygen reduction reaction: correlation of carbon support morphology and catalytic activity. *Microscopy and microanalysis : the official journal of Microscopy Society of America, Microbeam Analysis Society, Microscopical Society of Canada*, 11 Suppl 2(Suppl 2):1522–3, 2005.

[252] Takako Toda. Enhancement of the Electroreduction of Oxygen on Pt Alloys with Fe, Ni, and Co. *Journal of The Electrochemical Society*, 146(10):3750, 1999.

[253] J. R. Varcoe and R. C T Slade. Prospects for alkaline anion-exchange membranes in low temperature fuel cells. *Fuel Cells*, 5(2):187–200, 2005.

[254] John R. Varcoe, Plamen Atanassov, Dario R. Dekel, Andrew M. Herring, Michael a. Hickner, Paul. a. Kohl, Anthony R. Kucernak, William E. Mustain, Kitty Nijmeijer, Keith Scott, Tongwen Xu, and Lin Zhuang. Anion-exchange membranes in electrochemical energy systems. *Energy & Environmental Science*, 7:3135–3191, 2014.

[255] M.J. Verkerk, G.M.H. van de Velde, and a.J. Burggraaf. Structure and ionic conductivity of Bi2O3 substituted with lanthanide oxides. *Solid State Communications*, 44(9):i, 1982.

[256] Ayfer Veziroglu and Rosario MacArio. Fuel cell vehicles: State of the art with economic and environmental concerns. *International Journal of Hydrogen Energy*, 36(1):25–43, 2011.

[257] E. D. Wachsman and K. T. Lee. Lowering the Temperature of Solid Oxide Fuel Cells. *Science*, 334(6058):935–939, 2011.

[258] Eric D Wachsman, Sai Boyapati, and Michael J Kaufman. Modeling of Ordered Structures of Phase-Stabilized Cubic Bismuth Oxides. *Journal of the American Ceramic Society*, 83(8):1964–1968, 2000.

[259] C.D. Wagner, W.M. Riggs, L.E. Davis, and J.F. Moulder. *Handbook of X-Ray Photoelectron Spectroscopy*. 1979.

[260] Ryo Wakabayashi. *Transition Metal (Oxy)Nitrides and Oxides for Energy Materials*. PhD thesis, 2016.

[261] Michael G Walter, Emily L Warren, James R McKone, Shannon W Boettcher, Qixi Mi, Elizabeth A Santori, and Nathan S Lewis. Solar Water Splitting Cells. *Chemical Reviews (ACS Publications)*, 110(11):6446–6473, 2010.

[262] Mingyong Wang, Zhi Wang, Xuzhong Gong, and Zhancheng Guo. The intensification technologies to water electrolysis for hydrogen production - A review. *Renewable and Sustainable Energy Reviews*, 29:573–588, 2014.

[263] Yifei Wang, Dennis Y.C. Leung, Jin Xuan, and Huizhi Wang. A review on unitized regenerative fuel cell technologies, part B: Unitized regenerative alkaline fuel cell, solid oxide fuel cell, and microfluidic fuel cell. *Renewable and Sustainable Energy Reviews*, 75(November 2015):775–795, 2017.

[264] Yun Wang, Ken S. Chen, Jeffrey Mishler, Sung Chan Cho, and Xavier Cordobes Adroher. A review of polymer electrolyte membrane fuel cells: Technology, applications, and needs on fundamental research. *Applied Energy*, 88(4):981–1007, 2011.

[265] Nathan A.S. Webster, Chris D. Ling, Colin L. Raston, and Frank J. Lincoln. The structural and conductivity evolution of fluorite-type Bi2O3-Er2O3-PbO solid electrolytes during long-term annealing. *Solid State Ionics*, 179(19-20):697–705, 2008.

[266] Weifeng Wei, Xinwei Cui, Weixing Chen, and Douglas G. Ivey. Manganese oxide-based materials as electrochemical supercapacitor electrodes. *Chem. Soc. Rev.*, 40(3):1697–1721, 2011.

[267] He Weidong, Qin Wei, Wu Xiaohong, and Ning Hailong. Thin bismuth oxide films prepared through the sol-gel method. *Materials Letters*, 61(19-20):4100–4102, 2007.

[268] J. F. Whitacre, W. C. West, and B. V. Ratnakumar. A Combinatorial Study of Li[sub y]Mn[sub x]Ni[sub 2x]O[sub 4] Cathode Materials Using Microfabricated Solid-State Electrochemical Cells. *Journal of The Electrochemical Society*, 150(12):A1676, 2003.

[269] Jay F. Whitacre, T. Valdez, and S. R. Narayanan. Investigation of Direct Methanol Fuel Cell Electrocatalysts Using a Robust Combinatorial Technique. *Journal of The Electrochemical Society*, 152:A1780, 2005.

[270] C. W. White, J. Narayan, and R. T. Young. Laser annealing of ion-implanted semiconductors. *Science*, 204(4392):461–468, 1979.

[271] Jianbo Wu, Miao Shi, Xi Yin, and Hong Yang. Enhanced stability of (111)-surface-dominant core-shell nanoparticle catalysts towards the oxygen reduction reaction. *ChemSusChem*, 6(10):1888–1892, 2013.

[272] Matthias Wuttig and Noboru Yamada. Phase-change materials for rewriteable data storage. *Nature Materials*, 6(11):824–832, 2007.

[273] Chengxiang Xiang, Santosh K. Suram, Joel A. Haber, Dan W. Guevarra, Ed Soedarmadji, Jian Jin, and John M. Gregoire. High-throughput bubble screening method for combinatorial discovery of electrocatalysts for water splitting. *ACS Combinatorial Science*, 16(2):47–52, 2014.

[274] Hong Yang. Platinum-based electrocatalysts with core-shell nanostructures. *Angewandte Chemie - International Edition*, 50(12):2674–2676, 2011.

[275] Jingsi Yang and Jun John Xu. Nanoporous amorphous manganese oxide as electrocatalyst for oxygen reduction in alkaline solutions. *Electrochemistry Communications*, 5(4):306–311, 2003.

[276] Ivelina Zaharieva, Petko Chernev, Marcel Risch, Katharina Klingan, Mike Kohlhoff, Anna Fischer, and Holger Dau. Electrosynthesis, functional, and structural characterization of a water-oxidizing manganese oxide. *Energy & Environmental Science*, 5:7081, 2012.

[277] J. M. Zen, R. Manoharan, and J. B. Goodenough. Oxygen reduction on Ru-oxide pyrochlores bonded to a proton-exchange membrane. *Journal of Applied Electrochemistry*, 22:140–150, 1992.

[278] Ruizhong Zhang and Wei Chen. Non-precious IrV bimetallic nanoclusters assembled on

reduced graphene nanosheets as catalysts for the oxygen reduction reaction. *Journal of Materials Chemistry A*, 1(37):11457, 2013.

[279] Wenxu Zhang, Ye Liu, Aaron C. Jackson, Alice M. Savage, S. Piril Ertem, Tsung Han Tsai, Soenke Seifert, Frederick L. Beyer, Matthew W. Liberatore, Andrew M. Herring, and E. Bryan Coughlin. Achieving Continuous Anion Transport Domains Using Block Copolymers Containing Phosphonium Cations. *Macromolecules*, 49(13):4714–4722, 2016.

[280] Yuan Zhang and Paul J. McGinn. Combinatorial screening for methanol oxidation catalysts in alloys of Pt, Cr, Co and v. *Journal of Power Sources*, 206:29–36, 2012.

[281] J. P. Zheng, P.J. Cygan, and T.R. Jow. Hydrous Ruthenium Oxide as an Electrode Material for Electrochemical Capacitors. *Journal of The Electrochemical Society*, 142(8):2699–2703, 1995.

[282] Zhi-You Zhou, Na Tian, Jun-Tao Li, Ian Broadwell, and Shi-Gang Sun. Nanomaterials of high surface energy with exceptional properties in catalysis and energy storage. *Chemical Society Reviews*, 40(7):4167, 2011.

[283] Yinlong Zhu, Wei Zhou, and Zongping Shao. Perovskite/Carbon Composites: Applications in Oxygen Electrocatalysis. *Small*, 13(12):1–25, 2017.

[284] G. Cynthia Zoski. *Handbook of Electrochemistry*. Elsevier.